High-Pressure Synthesis of Electronic Materials

George B. S. Penny

A thesis submitted in fulfilment of the requirements
for the degree of Doctor of Philosophy
to the
University of Edinburgh
2009

Declaration

I do hereby declare that this thesis has been composed by myself alone, and that the work presented in this thesis is my own, or where it is the work of another they are duly credited. Furthermore I confirm that this work has not been submitted for any other degree or professional qualification than this doctorate. Some of the research herein has already been published, these publications are included in the appendix.

George B. S. Penny
November 18$^{\text{th}}$, 2009

Acknowledgements

I must acknowledge a number of people for their help and support, which have made the completion of this thesis possible. Firstly my supervisor, Paul Attfield whose guidance has been invaluable to any successes of this research, and whose door has (almost) always been ajar for an unannounced discussion on any topic. More recently I am indebted to Paul for readily acting as *Yin* to my *Yang* during the painful generation of this thesis itself.

Thanks to all those who have been members of the Attfield group at any stage of my time here in Edinburgh, In particular Jenny Rodgers whose dedication to the running of the press has underpinned all of the results in this thesis, and my second supervisor, Jan-Willem Bos, who has been generous with his help for this research. Collaborations are a key part of all science, I am lucky enough to be able to thank many collaborators. The Takano lab in Kyodai were very welcoming and helpful during my two weeks there (and thanks again Paul for trusting me in an ambassadorial rôle), particularly Shimakawa-sensei, Saito-sensei, and Oka-san. *Domo Arigato.* For the oxypnictides thanks, in no particular order, go to Andrea Marcinkova, Anya Kusmartseva, Andrew Huxley, Dmitry Sokolov, and Wuzong Zhou. The mag-lab is kept operational by the exceptionally hard work of Gaétan Giriat so thank you Gaétan, and thanks to Gaétan's predecessor Javier Sanchez-Benitez, I am one of many in your debt. Central facilities instrument scientists Michela Brunelli, Emmanuelle Suard at the *ILL* and Paolo Radaelli and Winfried Kockelmann at ISIS were helpful in various experiments, I'm sorry you had to deal with such small samples. These scientific acknowledgments must include all of the many technicians who have laboured to ensure a steady stream of press parts, it is an ever-changing list of names but in particular I am grateful to Bob Gusthart, who provided wide-ranging assistance, both pastoral and technical. Also thank you to all who I have had interesting scientific discussions with, whether they were fruitful or not, specifically Iain, Adrian, Wei-Tin, Luis, Tony, Minghui, Mark Senn, Anya, and Conglin, amongst others. Thanks to the EPSRC for funding.

People who must be mentioned for reasons outwith the realm of science: Sandra, Simon, Tony, Al, Chris, Adrian, Iain, Nic, David, Big Rob, Derek, Anthony, and Mark Senn, for lunch and/or Friday night enthusiasm, Rob you get a special extra mention for giving me so much money as well. Thanks to the tuesday footballers, who I'm sure have gone some way to maintaining my sanity, and *REBCO* for other reasons. I have been looked after by several flatmates, so thank you Nat, R. O. B. John & Kirstie, Graham (you put me back on track!), Vicky, and most recently Lee, (I wasn't always this way, Lee). A special mention goes to Mark Symes, A fine contradiction of a man whose *joie de vivre* defies belief and is an inspiration. Thank you, my son. The last and most important of my Edinburgh *connexions* is Charlotte, Thank you, C, for all the support and understanding you've shown me over the past eight months.

The most important people of all are my family, so thanks Mum, Dad, Jean (for all those letters and biscuits!), and Jemima, I am lucky to have such a base.

Finally, thanks to you, the reader, whoever you may be. This is for you.

Abstract

High-pressure techniques have become increasingly important in the synthesis of ceramic and metallic solids allowing the discovery of new materials with interesting properties. In this research dense solid oxides have been synthesised at high pressures, and structural investigations have been conducted using x-ray and neutron diffraction.

The perovskite $LaPdO_3$ has been synthesised at pressures of 6–10 GPa. Neutron diffraction studies have been carried out from 7–260 K to investigate any structural distortions, particularly related to the possibility of charge order at low temperatures. No reduction in symmetry associated with charge ordering has been observed; the material appears to remain metallic with only one unique Pd site down to 7 K. $LaPdO_3$ adopts the $GdFeO_3$-type $Pbnm$ structure. The PdO_6 octahedra exhibit a tetragonal distortion throughout the temperature range with a shortening of the apical Pd–O bonds of $\sim$2.5 % relative to the equatorial bonds. Attempts to prepare analogues of the perovskite containing smaller rare earths have resulted in multi-phase samples, and further $R PdO_3$ perovskites remain inaccessible although there is evidence for a small amount of the perovskite phase in the products of synthesis attempts with neodymium.

Three new oxypnictide superconductors, $R FeAsO_{1-x}F_x$ (R = Tb, Dy and Ho) have been synthesised at 7–12 GPa. The materials are isostructural with other recently discovered iron arsenide superconductors and have T_c's of 52.8 K, 48.5 K and 36.2 K respectively, demonstrating a downturn in T_c in the series for smaller R. Systematic studies on $TbFeAsO_{0.9}F_{0.1}$ and $HoFeAsO_{0.9}F_{0.1}$ show negative values of dT_c/dV in contrast to those reported for early R containing materials. Low-temperature neutron diffraction measurements on both materials, and synchrotron studies on $HoFeAsO_{0.9}F_{0.1}$ reveal no tetragonal to orthorhombic transitions as observed in early R-containing materials with lower doping levels. Magnetic reflections are evident but they are shown to be from R_2O_3 and RAs impurities with T_N's of 5.5 K for Tb_2O_3, 6.5 K for HoAs and 1.7 K $< T_N <$ 4 K for Ho_2O_3. The implications of these results for superconductivity in the iron arsenides are discussed.

Contents

List of Figures

List of Tables

Chapter 1

Introduction

1.1 Overview

The current level of understanding of the electronic properties of solids has generated technologies unrecognisable a century ago, from lighting and display applications to energy storage. It has contributed to the miniaturisation and reduction in cost of consumer electronics, allowed the realisation of new research equipment and in general has greatly advanced the technological sector. This understanding is by no means complete, with existing technologies utilising materials whose properties are still not fully explained: high-T_c cuprate superconductors and materials which exhibit colossal magnetoresistance are two examples. The continued exploration of the properties of new and existing systems is therefore of fundamental importance, whether they have obvious potential applications or simply act as model systems.

The term 'electronic materials' as used in the title of this thesis refers to materials with the potential to exhibit the interesting properties which allow such technologies. In particular, this work concerns dense, metal-containing solids, in which extended orbital overlap gives rise to correlated electron states. This orbital overlap, combined with the presence of unpaired electrons, often results in materials with competing ground states which can exhibit exotic material phenomena.

High-pressure techniques are suited to the synthesis of dense electronic materials, indeed, the materials presented in the results of this work were all synthesised under high pressures using large-volume presses. Whilst the application of pressure has been the principal synthetic method employed, the first recourse when searching for the reasons behind the behaviour of a solid has been to study its structure. A detailed knowledge of the structure of a material can give information regarding the electronic state of the elements within it. Changes in structure with temperature or doping, be they obvious or subtle, may be informative regarding the onset of interesting physical properties and provide useful insights into the nature of the material.

1.2 High pressure

1.2.1 High-pressure science

High-pressure science encompasses many fields, from investigations into the fundamental properties of elements and simple systems, to materials chemistry and the geological and biological sciences. Various transitions in conductivity with pressure exhibited by the elements, which were among the first pressure-induced changes in behaviour to be observed, are still used to calibrate large-volume pressure devices. At extreme pressures atoms can be forced into geometries which would be highly unstable at ambient pressures and this can lead to interesting behaviour. Research into the nature of the elements at high pressure in terms of their structure and properties is still ongoing, some elements adopt complex crystal structures at high pressure including incommensurate modulations of atom positions,[1] and high pressures have been used to bring about such changes in the properties of elements as the metallisation of hydrogen under shock-induced pressures[2] and superconductivity in sulfur, a typical insulating element at ambient pressure. Sulfur undergoes a phase change at 93 GPa to a high-pressure polymorph which is metallic and superconducting with a T_c of 10 K, which increases to 17 K at 160 GPa, the record T_c for any element.[3] A material need not necessarily be subject to a phase change for its properties to be altered by high pressure: the record-holding high-T_c cuprate superconductor, HBCCO, has a T_c of 136 K which increases to 164 K (the record for any material) at a pressure of 30 GPa without a phase change.[4]

In the geological and planetary sciences, the reproduction of conditions within the earth and other planets requires the use of high pressures for the study of mineralogy, and the phase diagrams of planetary ices of methane, ammonia and water have been established over a wide range of pressures and temperatures.[5] In the pharmaceutical industry, the study of polymorphs of molecular crystals at high pressure is pursued.[6] The study of biological systems at pressures similar to those found at the bottom of the ocean has provided details of 'extremophile' life forms which require such pressures to live, and high pressures are being implemented as an alternative to thermal methods for preserving foodstuffs.

1.2.2 High-pressure materials synthesis

Densification is a universal property of materials under high pressure. The increase in density can be due to a simple shortening of interatomic distances or due to a more efficient packing of atoms. The latter often leads to polymorphs with increased

Table 1.1: Simple high-pressure polymorphs. The materials' structure types and coordination numbers are given at ambient pressure (AP) and high pressure (HP), transition pressures (P_{trans}) and temperatures (T_{trans}) are given.[8, 9]

Solid	AP	P_{trans} (GPa)	T_{trans} (°C)	HP
C	Graphite, 3	13	3000	Diamond, 4
CdS	Wurtzite, 4:4	3	20	Rock salt, 6:6
KCl	Rock salt, 6:6	2	20	CsCl-type, 8:8
SiO_2	Quartz, 4:2	12	1200	Rutile, 6:3
Li_2MnO_4	Phenacite, 4:4:3	1	400	Spinel, 6:4:4
$NaAlO_2$	Wurtzite, 4:4:4	4	400	Rock salt, 6:6:6
BN	Graphite, 3:3	5	1500	Sphalerite, 4:4
$(Mg,Fe)_2Si_2O_6$	Pyroxene, 6:4:4	26	1600	Perovskite, 8:6:6

coordination numbers for each atom. Sulfur provides an example of a material changing to a high-pressure polymorph which is not recoverable to ambient conditions, however, in many cases high-pressure polymorphs can be recovered to ambient conditions as metastable materials. An important example of such a material is diamond. In the middle part of the twentieth century the pursuit of the synthesis of diamond led to great improvements in high-pressure equipment. Diamonds were known to be formed in the earth at high pressures and temperatures, and to be indefinitely stable at ambient pressure, they are harder and denser than other forms of pure carbon. Some other examples of simple solids which transform to recoverable structures with increased coordination numbers are given in Table 1.1. More bonds per unit volume lead to harder materials and an important section of the current work in high pressure synthesis targets the synthesis of ultra-hard materials (the goal being materials harder than diamond). Promising systems are B-N-C-O containing materials and composites formed by treating C_{60} or C_{70} at high pressure. For an overview see [7].

The formation of polymorphs involves a local rearrangement of atoms. Reactions between different phases require the rearrangement of atoms over much larger length scales. High pressures can be beneficial to these reactions: using La_2O_3 and Fe_2O_3 as precursors, the perovskite $LaFeO_3$ can be prepared at ambient pressure via the conventional ceramic method by heating to 1000 °C for 70 h. The same reaction at 5 GPa is complete in just 5 minutes. This is a stark example of the increase in reactivity and kinetics of reactions at high pressure, the application of which increases contact between grains and ion mobility. This results in conditions that are closer to the conditions in solution and that allow a greater scope for reactivity throughout solid samples. Typically high-pressure solid state reactions occur in the timescale of a few

minutes to a few hours, rather than over several days at ambient pressure.

The improvement in kinetics at high pressures does not necessarily mean reactions are under thermodynamic control, with the global minimum-energy phase or mixture of phases being achieved at a certain set of conditions. Reactions are often strongly dependent on the nature of the precursors used. Chemical reactions occur along trajectories on the potential surface which are negative overall in terms of free energy. The thermodynamic parameter of temperature provides the impetus to a system for navigation of the peaks and valleys of the potential surface. Pressure, a separate thermodynamic parameter, provides a small amount of energy to a system (relative to temperature) but more importantly it alters the shape of the potential surface with respect to its nature at ambient pressure. The positions of minima shift based on certain lattice parameters (equilibrium bond lengths shorten, for example) and entirely new minima can be obtained. Products are typically quenched from high to room temperatures whilst the pressure is maintained in an attempt to 'freeze' atoms into structures stable at high pressures which may or may not be preserved to ambient conditions. If the material occupies a structure which is in a local minimum of potential energy at ambient pressure then it may be recoverable.

Metastable polymorphs of ambient-pressure materials and entirely new materials can be recovered to ambient pressures. Not only do atoms occupy coordinations which may be increased relative to their usual ambient-pressure states, but they also may be found in unusual oxidation states. Copper, commonly found in +1 and +2 oxidation states, has been stabilised in oxides as Cu^{III} using high pressure, *e.g.* in a distorted perovskite phase $LaCuO_3$,[10] as has the usually unstable Cr^{IV} ion in various perovskite phases *e.g.* $SrCrO_3$.[11] The stabilisation of another metal in an unusual oxidation state, Pd^{III}, by high-pressure synthesis of a perovskite is discussed in Chapter 3. The perovskites are a class of material well suited to high-pressure synthesis; their dense structure is very stable at high pressure and thus highly metastable oxidation states and coordinations may be achieved and recovered to ambient conditions, leading to unusual physical properties. The transition of magnesium and iron silicates to the perovskite structure, an example of which is given in Table 1.1, is thought to make perovskite minerals the most abundant in the earth, and to cause the discontinuity in the mantle at 670 km depth.[9] Rodgers *et al.* present a review of more than 60 novel perovskites and related materials synthesised by high-pressure methods from 1995-2006.[12] $MgSiO_3$ undergoes a further transition to a more dense, post-perovskite phase at pressures similar to those near the base of the mantle, giving rise to another discontinuity in the earth.[13]

There are drawbacks to high-pressure synthesis, it is costly and the application and removal of pressure, combined with the intricacies of setting up high-pressure devices means that a reaction which may take only 5 minutes requires a whole day of laboratory time. There are constraints on sample volume and whilst most modern measurements can be made on the product of one high-pressure run, if large volumes are required many runs may have to be made. Many of the components of sample assemblies cannot be re-used and need to be fashioned for each press run. The reactions cannot be monitored as they can with re-grinding and x-ray analysis for the ceramic method, and the metastable nature of some desirable products means they may be difficult to synthesise free from impurity phases with which they can exist in equilibria. Nonetheless, the opportunities which high-pressure synthesis offers make it an increasingly popular and important technique in the field of materials chemistry.

1.3 Perovskites

A large family of materials are the perovskites, so called after the mineral of the same name, which is comprised of $CaTiO_3$. There are many variations of perovskite and a full discussion of their properties and peculiarities is beyond the scope of this work, however the basic structure will be introduced. The prototype structure ABX_3 consists of a cubic arrangement of corner-sharing BX_6 octahedra, interspersed with A cations. By far the most common anion is oxygen, and only oxide perovskites will be discussed henceforth. A diagram of the structure is shown in Figure 1.1. A cations are larger than B, and many elements can be incorporated into the perovskite structure. The structure has simple connectivity, with each of the B cations connected to another through an oxygen, with the B–O–B angle equal to 180°.

The large number of elements which can be included within the basic structure combined with possible structural distortions result in these materials boasting a vast range of properties and a large number of applications. Simple ferromagnetic ordering as in the rare earth manganites[14] is less common than antiferromagnetic order as in $LaCrO_3$[15]. $BaTiO_3$ provides a classic example of a ferroelectric material,[16] a net dipole arises from titanium ion displacements from the centre of the TiO_6 octahedra, the material is used in capacitors. The recently popular field of multiferroics (materials which exhibit a coexistence of more than one of spin, orbital, and dipole ordering) is mainly based on perovskites *e.g.* $BiFeO_3$[17] and $BiMnO_3$.[18] High ion-mobility in rare earth manganite perovskites leads to their use in solid oxide fuel cells and $LaCoO_3$ is used as an interconnect in fuel cells due to its electrical conductivity and high-temperature stability.

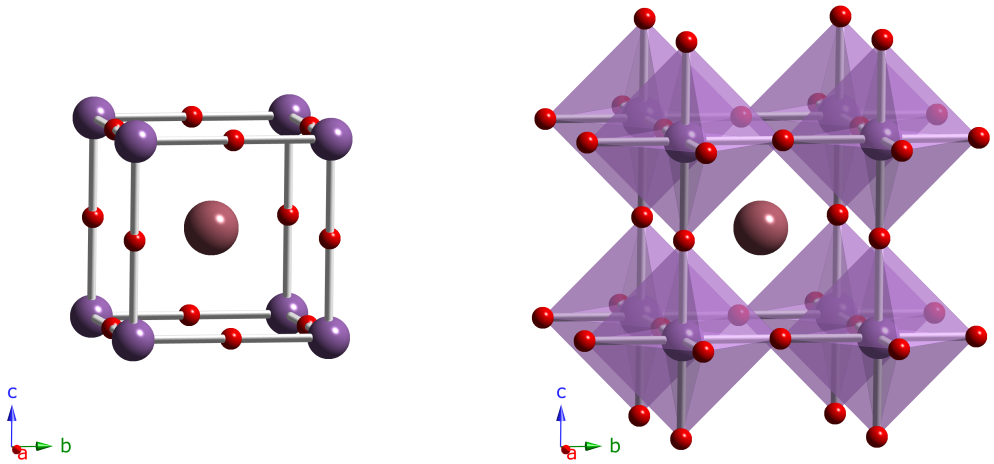

(a) Unit cell **(b)** BO_6 octahedra

Figure 1.1: The prototype $ABO3$ perovskite structure. A is shown in pink, B in purple and O in red. The cubic structure has space group $Pm\bar{3}m$, $a \approx 4$ Å. The unit cell is shown in (a), an expanded view showing the BO_6 octahedra is given in (b).

1.3.1 Structural distortions

1.3.1.1 Octahedral tilting

The most common of the structural distortions undergone by perovskites is octahedral tilting. The inherent instability of oxygen in a linear geometry means deviations in the B–O–B angle from 180° are often seen in perovskites, and the various tilting and twisting of octahedra which result were described by Glazer in 1972.[19] The system Glazer introduced describes the tilting of a general BO_6 octahedron about three Cartesian axes, x, y and z which are coincident with the three crystallographic axes a, b and c, and how the rest of the structure relates to the tilting. Three letters describe the angles of rotation about each axis and their superscripts describe whether the tilting in subsequent layers perpendicular to the axis is in phase (+) or out of phase(-). A superscript of '0' indicates that there is no tilting about an axis. The ideal cubic structure has a tilt system of $a^0a^0a^0$. The tilting affects the coordination of the A cation, some tilt systems and their space groups and A-site coordinations are shown in Table 1.2.

Tilting can occur to accommodate cations which are not of an appropriate size to pack in a cubic structure, how close the ratio of sizes of ions is to that required for

Table 1.2: Glazer tilt systems for perovskites showing the tilt system and corresponding space group, and the A-site coordination and geometry.[21]

Tilt system	Space group	A coordination	A geometry
$a^0a^0a^0$	$Pm\bar{3}m$	12	Cubo-octahedral
$a^0a^0c^-$	$I4/mcm$	4+4	Distorted tetrahedral
$a^0a^0c^+$	$P4/mbm$	4+4	Rectangular planar
$a^0b^-b^-$	$Imma$	5+2	Square pyramidal
$a^0b^+b^-$	$Cmcm$	4+2	Distorted tetrahedral
		6+2	Face centered trigonal prismatic
$a^0b^+b^+$	$I4/mmm$	4	Square planar
		8	Square prismatic
		4+4	Rectangular planar
$a^-a^-a^-$	$R\bar{3}c$	3+6	Trigonal planar
$a^+a^-a^-$	$Pnma$	4+4	Distorted tetrahedral
$a^+a^+a^-$	$P4_2/nmc$	4+4	Distorted tetrahedral
		4+4	Square planar
		6+4	Face centered trigonal prismatic
$a^+a^+a^+$	$Im\bar{3}m$	12	Distorted Cubo-octahedral
		4+4	Square planar

cubic packing is described by Goldschmidt's tolerance factor, t:[20]

$$(R_{\mathrm{O}} + R_A) = t\sqrt{2}(R_{\mathrm{O}} + R_B) \tag{1.1}$$

Where R_A, R_B and R_{O} are the ionic radii of A, B, and O respectively, and t is the tolerance factor. A value of 1 corresponds to ions with the necessary radii for cubic packing in the perovskite structure, this is not to say they will form a cubic perovskites. Given the correct valences, combinations of cations which yield tolerance factors $0.85 < t < 1$ are usually stable, perovskites with lower values of t may be stabilised by high pressures. As can be seen from Equation 1.1, a decrease in the size of A relative to B results in a lower value of t.

1.3.1.2 Charge order

The term charge order (CO) refers to a situation in which a metal, M, on one crystallographic site with some average charge, c, exhibits a disproportionation of this charge at low temperature resulting a breaking of symmetry and two distinct metal sites *i.e.* $2\,M^{c+} \longrightarrow M^{(c+\delta)+} + M^{(c-\delta)+}$. This is a special, localised instance of a general ordering phenomenon known as a charge density wave (CDW) in which there is a modulation of charge usually incommensurate with the crystal structure. Two examples of charge-ordered perovskites, $La_{0.5}Sr_{0.5}MnO_3$ and $BaBiO_3$ are given in the perovskite case study section below, and a further example of the rare earth nickelates in the introduction of Chapter 3. In perovskites CO usually results in a structural distortion which can be viewed as a frozen breathing vibrational mode of, *e.g.*, the B-site octahedra, where slightly larger and slightly smaller octahedra correspond to $M^{(c-\delta)+}$ and $M^{(c+\delta)+}$ metals respectively. This gives rise to often subtle superstructures in the material and typically opens a gap in the electronic structure causing a switch from conducting to insulating properties.

1.3.1.3 Orbital ordering and Jahn-Teller distortions

The Jahn-Teller effect is the spontaneous distortion from regular geometry of an element which acts to minimise the energy of a system. In an octahedral coordination the five d orbitals of a metal are split into two degenerate sets, the lower t_{2g} set which comprises of the d_{xy}, d_{xz} and d_{yz} orbitals, and the upper e_g set which comprises of the $d_{x^2-y^2}$ and d_{z^2} orbitals. The lobes of the e_g orbitals point towards the six ligands, those of the t_{2g} orbitals point between the ligands. Where a set of degenerate orbitals is asymmetrically occupied, a distortion which removes the degeneracy of the set by lowering the energy of some and raising the energy of other orbitals may occur. For example, an elongation of the bonds on the z axis and contraction of the bonds in the xy plane of the octahedron will lower the energy of the d_{z^2} orbital and raise the energy of the $d_{x^2-y^2}$ orbital by the same amount, also a smaller effect is seen on the t_{2g} orbitals (smaller since they do not point directly at the ligands): the d_{xz} and d_{yz} orbitals would be lowered whilst the d_{xy} orbital would be raised in energy. This specific distortion is referred to as a tetragonal elongation. A tetragonal compression is also possible with the opposite effect on the perturbation of the energies of each of the orbitals. These effects are shown in Figure 1.2.

As is the case with charge order, the distortion of one octahedron from its regular geometry can give rise to superstructures in the crystal if the octahedral distortions are orientationally ordered with respect to one another. The phenomenon is referred

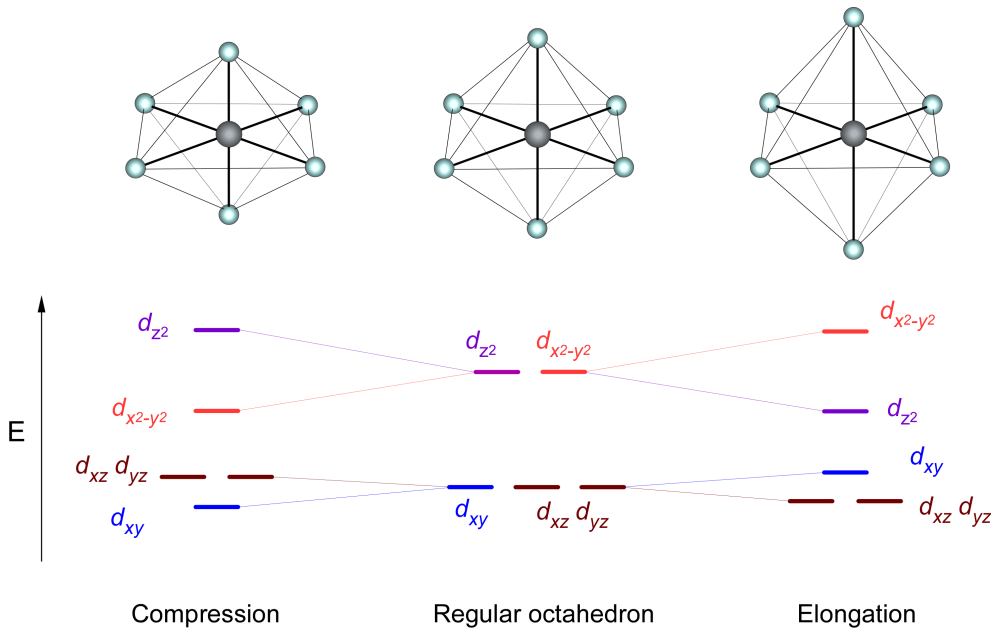

Figure 1.2: Octahedral Jahn-Teller distortions compared to a regular octahedron and the corresponding metal *d*-orbital relative energies.

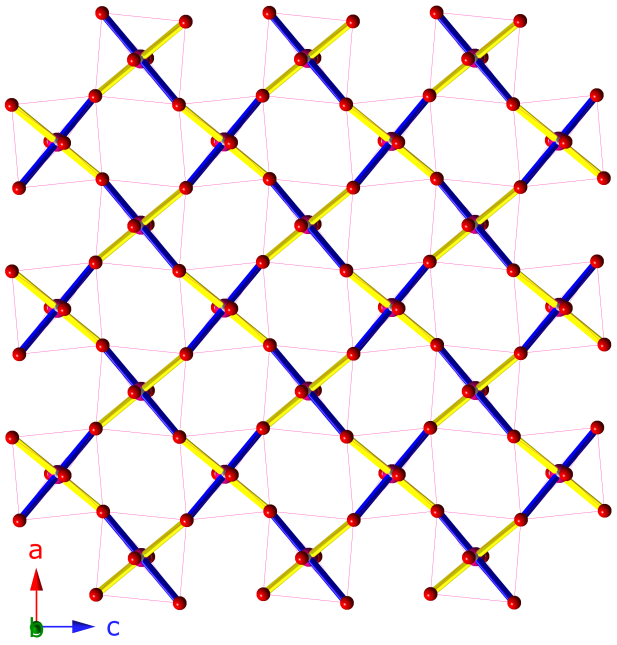

Figure 1.3: Orbital ordering in $LaMnO_3$. A single layer of MnO_6 octahedra is shown with long bonds (blue) and short bonds (yellow). The *A*-site lanthanum ions are omitted for clarity.

to as orbital ordering and is seen in perovskites, *e.g.* in $LaMnO_3$ which has an ordered tetragonal elongation as shown in Figure 1.3. This stabilises the high spin d^4 manganese electronic configuration. The single electron in its e_g orbitals occupies the reduced-energy d_{z^2} orbital, thus in Figure 1.3 the z direction of each specific octahedron is coincident with the direction of the long (blue) bonds *i.e.* the direction in which the d_{z^2} orbital is oriented is that of the blue bonds. In this case long and short octahedral axes alternate. Cases such as this are sometimes referred to as cooperative Jahn-Teller distortions.

In the case of charge order two slightly differently sized octahedra are positionally crystallographically ordered, whilst in the case of orbital ordering all the octahedra are identical, but they can give rise to superstructures through orientational crystallographic order of their unique axes.

1.3.2 Magnetic and transport properties

The diverse range of magnetic and electric transport properties exhibited by perovskites was alluded to in the introduction of this section. These properties are dependent on the nature of dominant interactions in the perovskite structure, the B–O–B interactions. Weak overlap between B-site and oxygen orbitals tends to result in insulating properties. B-sites are too far apart from one another for direct exchange so any interaction between localised unpaired electrons is via superexchange, *i.e.* the unpaired electrons on one B cation couple with the localised oxygen p-orbital electrons, which are also coupled to the unpaired electrons on their other B-site nearest neighbour. This communication between B-site unpaired electrons is usually antiferromagnetic, its strength is dependent on the geometry of the B–O–B bonds.

Conversely, when there is relatively strong B–O–B orbital overlap wide conduction bands are formed. If these bands are partially filled, metallic behaviour is seen. In these cases magnetic exchange between any B-site unpaired electrons is via Stoner exchange, *i.e.* exchange between itinerant electrons. In this instance ferromagnetic exchange can occur as seen in $SrRuO_3$.[22]

Due to structural distortions not all B–O–B geometries will necessarily be the same in a given perovskite and hence not all interactions will be the same. As well as ferromagnetic ordering, several types of overall antiferromagnetic order are seen in the perovskites, with differences brought about by different exchange interactions in each direction. Three types of antiferromagnetism are illustrated in Figure 1.4. *A*-

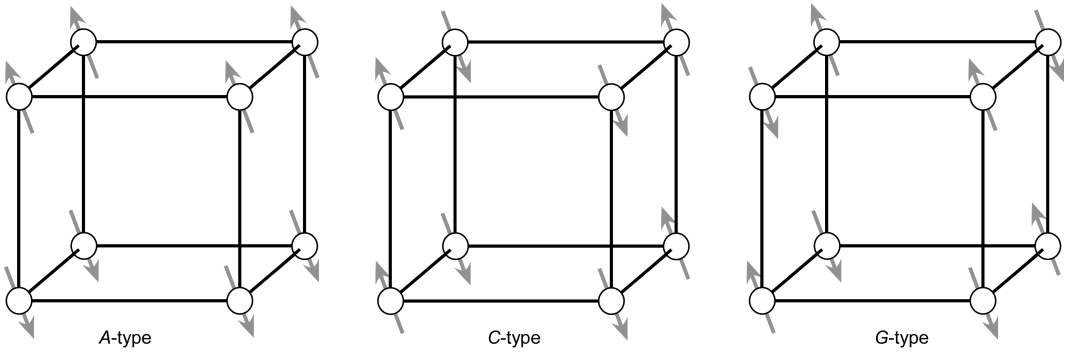

Figure 1.4: Types of antiferromagnetic order showing spin directions on atoms at the vertices of a simple cubic cell. Examples of perovskites with each of the types of ordering are given in the text.

type consists of spins which are arranged in planes, with ferromagnetic intra-plane alignment and antiferromagnetic inter-plane alignment, this is the type of alignment in $LaMnO_3$.[23] *C*-type ordering consists of lines or columns of ferromagnetically aligned spins, with adjacent columns exhibiting antiferromagnetic interactions with one another. This is the type of ordering seen in $BiCoO_3$.[24] *G*-type ordering consists of a rock salt type of alignment, with each spin aligned antiferromagnetically to all its nearest neighbours, this is common in cubic perovskites and is the type of ordering seen in $LaFeO_3$[25] and $LaCrO_3$.[15]

1.3.3 Case Studies

1.3.3.1 Manganite perovskites

Notable as the materials for which the term 'colossal magnetoresistance' (CMR) was coined, members of the series $R_{1-x}M_xMnO_3$ (R = rare earth, M = divalent metal) undergo orders-of-magnitude drops in resistivity upon the application of a magnetic field.

In the undoped end member of the $La_{1-x}M_xMnO_3$ series, $LaMnO_3$, the lanthanum ions occupy a trivalent state as do the manganese ions which are high-spin d^4. The manganese ions are antiferromagnetically coupled as is expected from the Mn–O–Mn geometry and the material is semiconducting. Doping of the *A*-site with a divalent metal such as calcium or strontium causes some manganese ions (one per divalent substitution) to occupy a d^3 tetravalent state in order to balance the change in *A*-site charge. The material becomes ferromagnetic when $0.13 < x < 0.45$. It has been shown that the resistivity behaviour (without magnetic field) above the Curie temperature is semiconductive and below the Curie temperature the resistivity drops

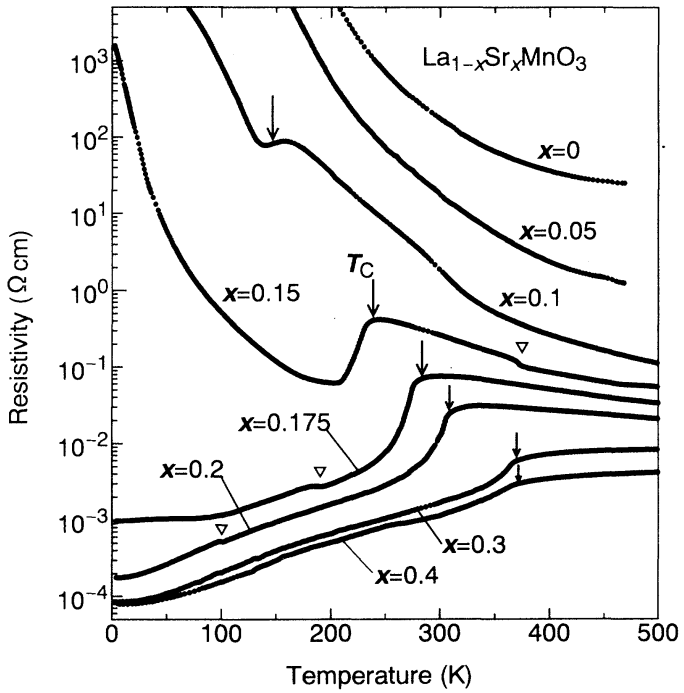

Figure 1.5: The resistivity of $La_{1-x}Sr_xMnO_3$ with temperature for various x showing a drop in resistivity at the Curie temperature, T_C, marked by an arrow.[26]

and metallic behaviour is observed,[14] illustrated in Figure 1.5. In 1950 Zener proposed a mechanism called Double Exchange to explain these phenomena, in which the conductive transport occurs via hopping of electrons between e_g^1 Mn^{III} sites and e_g^0 Mn^{IV} sites.[28] A summary of the double exchange mechanism is that the manganese ions have appreciable spins (S = 2 or $\frac{3}{2}$ respectively) and it is much easier for an electron to hop from one e_g orbital to another if the ions' spins are parallel, hence the drop in resistivity below the ferromagnetic Curie temperature or in a magnetic field where the spins have a tendency to align parallel.

Near $x = 0.5$ the ratio of Mn^{III} : Mn^{IV} is close to 1:1 and charge order is observed when the material becomes insulating. In the ferromagnetic state the material exhibits CMR with the largest changes of resistivity occurring for x values close to those required for CO. The magnitude of the decrease in resistivity of the manganites cannot be explained by the double exchange mechanism alone.[29] The currently accepted explanation for the CMR cites percolative transport between spin-aligned, conducting regions which are phase-separated from CO insulating regions as shown in Figure 1.6. This transport is greatly enhanced when neighboring regions' spin directions are aligned to each other hence the drop in resistivity in a magnetic field.[27] Thus CO underpins a remarkable physical property in the rare earth manganites.

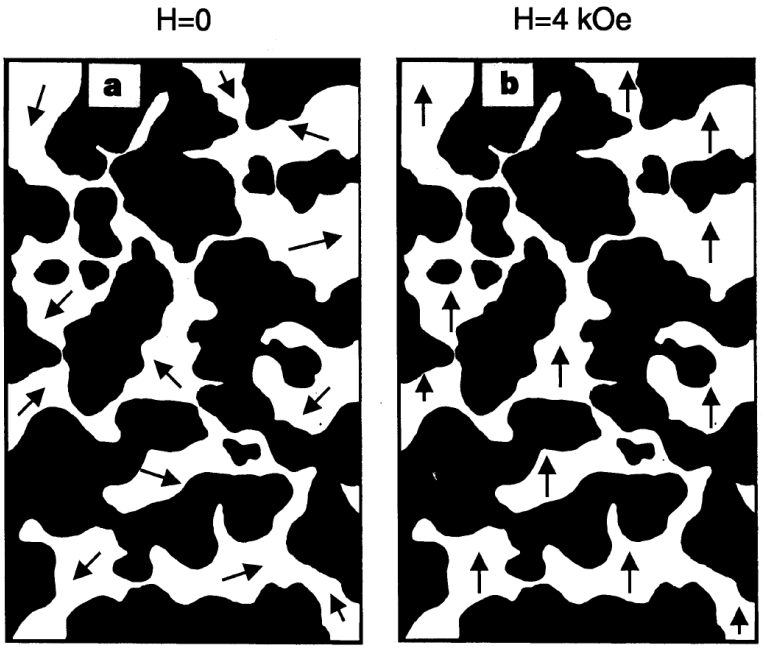

Figure 1.6: Sub-micron phase separation for CMR. The insulating CO phase is shown in black and conducting phase in white, without field (a) and with field (b).[27]

1.3.3.2 Barium bismuthate

The perovskite $BaBiO_3$ is a good example of a charge-ordered system, it can be written as ideally $Ba_2Bi^{III}Bi^{V}O_6$, or more realistically $Ba_2Bi^{(4-\delta)+}Bi^{(4+\delta)-}O_6$.[30] The structure is shown in Figure 1.7. The CO is of high stability and apparently persists up to 873 K. The CO phase has tilted octahedra, interestingly this tilting is eliminated along with the charge order and the structure becomes cubic above 873 K.[31] $BaPb_xBi_{1-x}O_3$ was shown to be superconducting with a maximum temperature of the onset of the superconductive transition (T_c) of ~12 K in 1975.[32] In 1988 it was reported that potassium doping on the *A*-site induced superconductivity with a T_c of 30 K which at the time was the maximum T_c of any oxide-containing non-cuprate material.[33] Increasing the amount of substitution of monovalent potassium for divalent barium (x in $Ba_{1-x}K_xBiO_3$) causes the ratio of $Bi^{(4-\delta)+}$: $Bi^{(4+\delta)+}$ to depart from 1:1 and so acts to suppress CO. As x is increased the structure first changes to one which is charge disproportionated but not charge ordered at $x \approx 0.1$, then to a cubic structure at $x \approx 0.35$ in which each bismuth is equivalent and has a charge of +4, at which point there is a change from insulating to conducting properties in the normal state. Optimum doping for superconductivity (*i.e.* that which gives the maximum T_c) is at $x \approx 0.4$.

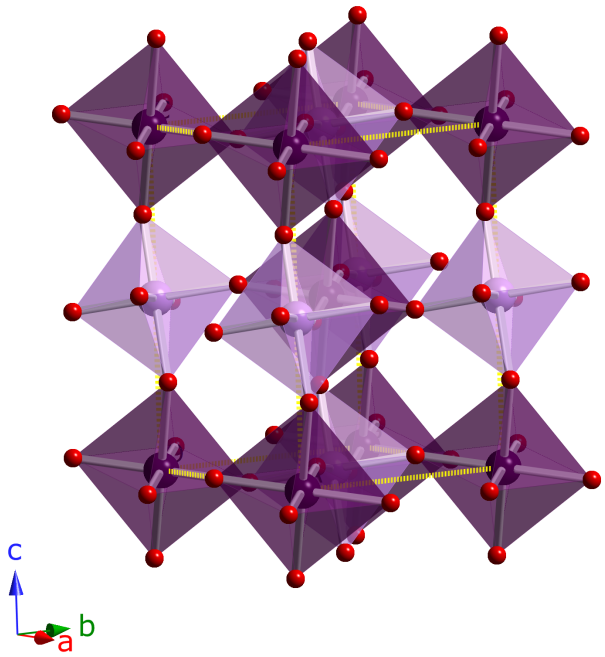

Figure 1.7: The structure of $BaBiO_3$ viewed roughly along the 110 direction showing the tilting of the BiO_6 octahedra. The unit cell is indicated by a yellow dashed line and barium is omitted for clarity. The $Bi^{(4+\delta)+}$ ions occupy the smaller light purple octahedra and the $Bi^{(4-\delta)+}$ ions occupy the larger deep purple octahedra. They are ordered in a rock salt fashion. The structure has space group $I2/m$.

The mechanism of superconductivity in this system is unconventional and not well understood, high-resolution structural analysis has suggested some degree of charge disproportionation persists into the cubic region and is involved with the causes of the superconducting behaviour.[34] The material continues to draw attention and provides a good illustration of the necessity of a fuller understanding of charge order and its associated properties. In this case the associated property is superconductivity, which features in the second part of this thesis and which is introduced below.

1.4 Superconductivity

The main and most obvious property of a material in a superconducting state, the property after which the phenomenon was named, is electrical conduction with zero resistance. A second property of note is the Meissner effect: in a superconducting state, materials will exclude magnetic field.

Superconductivity was first observed in elemental mercury in 1911 by Heike Kamerlingh Onnes who, exploiting his recent achievement of liquefying helium, showed a transition

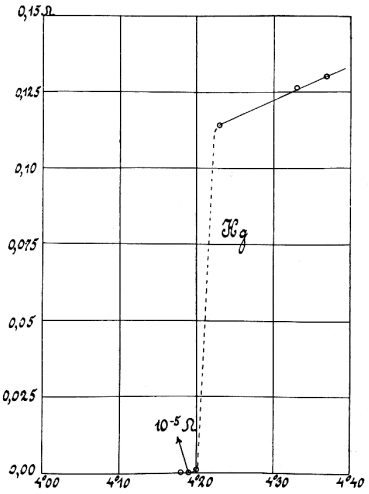

Figure 1.8: The resistivity with temperature of mercury showing a superconductive transition above 4.2 K. The x axis represents temperature (Kelvin) and the y axis resistance (Ohms). The diagram is a reproduction of that in Onnes's original report.[35]

to zero resistance in the metal at 4 K (Figure 1.8).[35] The second element to be shown to superconduct was lead, which was observed to have a T_c of 7 K in 1913. Approximately half of the pure elements have now been shown to be superconductors given the right conditions (low temperatures, high pressure, thin film *etc.*), the highest T_c of the elements (at ambient pressure) is exhibited by niobium which has a T_c of 9.25 K. The Meissner effect - the expulsion or exclusion of magnetic flux from superconducting materials, was described in 1933,[36] it is a consequence of this effect which leads to the images of magnets levitating above cooled superconductors which are near-ubiquitous in popular media connected to superconductivity.

Various compounds were found to have higher T_c's than their constituent elements and over the first three quarters of the twentieth century the record T_c was gradually increased. A successful model of the mechanisms behind superconductivity was proposed in 1957 John Bardeen, Leon Cooper and John Schrieffer, which is known as BCS theory.[37] A qualitative explanation of this theory is given below, superconductors which obey it are known as 'conventional'. BCS theory puts an upper limit on T_c of approximately 30 K, and the highest T_c conventional superconductor, Nb_3Ge (T_c = 23 K) was discovered in 1973.[38]

The BCS paradigm was challenged in the late 80's by one of the most significant discoveries of the twentieth century. In 1986 Bednorz and Müller reported an onset T_c of 30 K in the perovskite-related Ba-La-Cu-O system.[39] Within in six months T_c's

had been raised above the boiling point of nitrogen, 77 K, in the related Y-Ba-Cu-O material ($T_c = 93$ K).[40] This was an important step as liquid nitrogen is much cheaper than liquid helium, and it opened up a large field of commercial applications. These materials are collectively referred to as the 'cuprates' since the electronically active part consists of copper oxide and they constitute a large research field in themselves. There have been few non-cuprate unconventional superconductors (*i.e.* superconductors which do not obey BCS theory). $Ba_{1-x}K_xBiO_3$ with a T_c of 30 K is described above, C_{60} has been shown to superconduct up to 38 K in the presence of caesium and rubidium[41, 42] and until 2008 the record for a non-cuprate superconductor was held by MgB_2 which has a T_c of 39 K[43]. 2008 saw the discovery of the iron arsenide superconductors, which have T_c's in excess of 50 K and are introduced in Chapter 4.

Apart from being classified as conventional (BCS) or unconventional, superconductors fall in to two types, Type I and Type II, distinguished by the behaviour of the materials in increasing magnetic fields. Type I superconductors undergo an abrupt loss of superconductivity above a critical field (H_c), whilst Type II superconductors show a gradual loss of superconductivity around H_c.

1.4.1 BCS Theory and conventional superconductivity

Superconductivity is not just a gradual decrease in resistivity to zero, there is a clear phase transition to the superconducting state. When classically good conductors are cooled, their resistivity drops with temperature, but levels off at temperatures of a few kelvin to give some residual resistance. The mechanism of normal conductivity is that electrical transport is mediated by charge carriers (electrons) in bands formed by combinations of the orbitals of the atoms in a lattice (*i.e.* delocalised electrons). The motion of these electrons is hindered by lattice vibrations causing an increase of resistivity with temperature. Lattice vibrations are not eliminated at base temperature, and combined with defects such as impurities, grain boundaries *etc.* they account for the residual resistivity.

In their 1957 report on the theory of superconductivity, Bardeen, Cooper and Schrieffer sought to account for five key properties of superconductors:

> "The main facts which a theory of superconductivity must explain are (1) a second-order phase transition at the critical temperature, T_c, (2) an electronic specific heat varying as $\exp(-T_0/T)$ near $T = 0$ K and other evidence for an energy gap for individual particle-like excitations, (3) the Meissner-Ochsenfeld effect ($B = 0$), (4) effects associated with infinite conductivity ($E = 0$), and (5) the dependence of T_c on isotopic mass, $T_c\sqrt{M}$

= const."

The authors succeeded in explaining all of these properties. Metallic conduction was described by Bloch in 1928 by modifying the free-electron gas description with the addition of a periodic lattice[44]. In Bloch's model a wavefunction on each lattice point is modified by an overall wavefunction which extends throughout the lattice. Correlations between electrons are ignored and the lattice is fixed, the electrons move in a field defined by the other electrons and ions which is immutable. Electrons are fermions and all the energy levels are filled from the ground state up to the Fermi energy, E_F. All the energy levels above E_F are empty.

The discovery of the isotope effect,[45] listed as (5) in the quotation above, was of great importance in the search for a theory of superconductivity. It hinted that lattice vibrations or phonons were linked to electrical transport in superconductors. The second property listed above, the apparent existence of an energy gap near E_F in the superconducting state implies a key realisation which lead BCS theory: that there is an attractive interaction between conduction electrons. First proposed by Fröhlich[46] and Bardeen[47] independently in 1950 this can be explained by considering interactions between electrons and a flexible metal lattice. As a negatively charged electron moves through a solid it distorts the positive lattice around it causing lattice vibrations. This leads to areas of increased positive charge and hence the lowering of energy of another electron in the vicinity. Referred to as the phonon interaction, this results in the formation of pairs of electrons in the superconducting state known as 'Cooper pairs'. The pairs are coupled over a distance called the correlation length, typically of the order of 100 nm, a range of many times the space between atoms in the lattice. The cooper pairs contain electrons of opposite spin and can be treated as individual charge carriers. In contrast to individual electrons these cooper pairs have zero overall spin and are bosons, meaning they can all occupy the same energy level, thus they condense at low temperatures giving rise to the phase transition observed at the onset of superconductivity.

The phonon interaction results in a "cooperative many particle state" formed of bosonic Cooper pairs of electrons. The individual particle-like excitations referred to above consist of the breaking of a pair, and since the pairs form a many-body condensate, breaking one will effect the energies of all the others. This causes the BCS ground state to be separated from higher energy states by a gap. The Meissner effect is explained since the bosonic pairs cannot exist if a magnetic field causes the electron spins to align in any way other than antiparallel. In the superconducting state the energy gap

Table 1.3: Cuprate summary giving the chemical formula, abbreviation, T_c and year of discovery of seven cuprates.

Compound	Abbreviation	T_c (K)	Year
$La_{2-x}Ba_xCuO_4$	LBCO	30	1986[39]
$La_{2-x}Sr_xCuO_4$	LSCO	36	1986[48]
$YBa_2Cu_3O_7$	YBCO	92	1987[40]
$Bi_2Sr_2Ca_2Cu_2O_{10}$	BSCCO	107	1988[49]
$Tl_2Ba_2Ca_2Cu_3O_{10}$	TBCCO	120	1988[50]
$HgBa_2Ca_2Cu_3O_8$	HBCCO	133	1993[51]
$Hg_{0.8}Tl_{0.2}Ba_2Ca_2Cu_3O_{8+\delta}$	HBCCO	136	1995[52]

means the charge carriers cannot absorb phonons in 'collision interactions', the normal mechanism of resistivity, since the phonons have less energy than the gap, hence there is conduction with zero resistance. The opening of a gap also serves to explain the exponential suppression of the specific heat of superconductors at low temperatures, since thermal excitations below the energy of the gap cannot occur.

Bardeen, Cooper and Schrieffer's seminal theory earned them the Nobel Prize in 1972. It was a complete mathematical description which they described as "an extension of the Bloch theory to superconductors". The theory agreed with the experimental data available at the time and made several predictions, not least that T_c's had a maximum close to 30 K. It was therefore a cause of great excitement in the scientific community when the high-T_c cuprate superconductors were discovered in the late '80s.

1.4.2 The high-T_c cuprate superconductors

In their 1986 paper[39] Bednorz and Müller cited superconductivity in $BaPb_xBi_{1-x}O_3$[32] as one of the reasons for their research into perovskite-related cuprates. They refer to the Ba-La-Cu-O 'system' since their samples consisted of three phases, the superconducting phase is a multi-layered perovskite based on $La_{2-x}Ba_xCuO_4$. The discovery of superconductivity with an onset T_c of 30 K was followed by a large number of reports of related materials with the maximum T_c's rapidly increasing, summarised in Table 1.3. It quickly became apparent that BCS theory could not account for these high T_c values. Pairing of electrons remained the accepted mechanism of superconductivity in the materials, the challenge was to explain correlations strong enough to survive to such high temperatures.

The materials in general occupy tetragonal or close-to-tetragonal orthorhombic structures with large c axes, they are layered, the layers stretching out in the ab direction

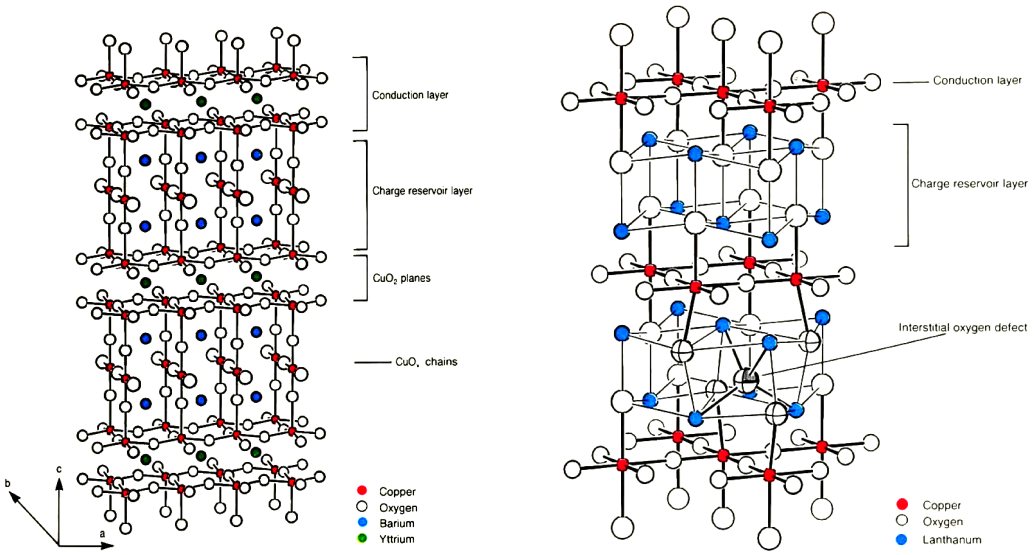

(a) $YBa_2Cu_3O_{6+\delta}$

(b) $La_2CuO_{4+\delta}$

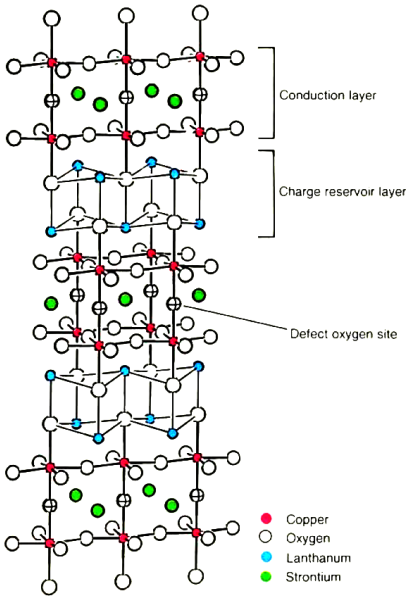

(c) $La_2SrCu_2O_{6+\delta}$

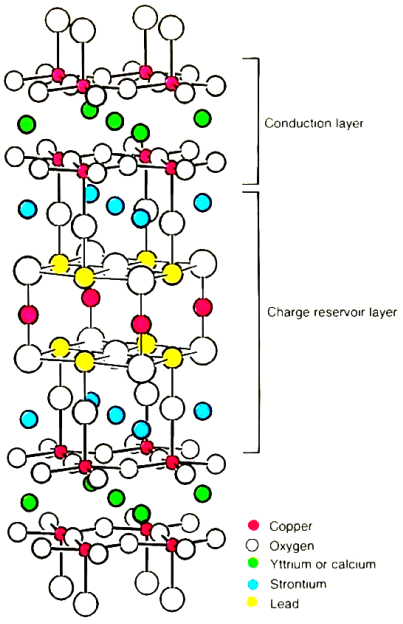

(d) $Pb_2Sr_2Y_{1-x}Ca_xCu_3O_{8+\delta}$

Figure 1.9: The structures of four cuprates. (b) and (c) show interstitial and defect oxygen sites. Conduction and charge-reservoir layers are labelled.[53]

and stacking in the c direction. The electronically active layer, the layer through which the superconductive transport occurs, is a planar or near-planar CuO_2 layer, with the copper in a square-planar coordination. One or more adjacent CuO_2 layers are separated by various other layers which act as charge reservoirs. Superconductivity is induced by electron or hole doping: Substituting ions in the charge-reservoir layers for other ions of higher or lower valencies introduces electrons or holes into the electronically active layer, causing the square-planar copper ions to depart from a $2+$ d^9 state. Doping can also be brought about by oxygen inclusions or vacancies. Specifically, oxygen vacancies or the replacement of a cation with one of higher valence in the charge-reservoir layer causes electron doping, inclusions of oxygen or the replacement of a cation with one of lower valence causes hole doping. The structures of four cuprates are shown in Figure 1.9.

The undoped parent materials are antiferromagnets, doping suppresses the antiferromagnetic ordering, decreasing T_N to zero, after which superconductivity emerges. In general lower values of hole doping are required than those of electron doping for the same effect. A phase diagram is shown in Figure 1.10. High-temperature superconductivity is accompanied by unusual normal-state properties, a 'pseudogap' (an area with a very low density of states near E_F) occurs in the low hole-doped region of the phase diagram above superconducting temperatures. This is not well understood but is thought to originate either from some ordering within the material *e.g.* a SDW or some charge ordering, or from correlations above T_c.

Soon after the first report of the cuprate superconductors, Anderson suggested the origin of the electron correlation may be magnetic rather than phonon based.[54] In the 1992 Monthoux proposed that the pairing of electrons via antiferromagnetic fluctuations, a 'paramagnon' mediated correlation, could give rise to a superconductive transition[55] and would lead to a superconductive gap of $d_{x^2-y^2}$ symmetry, that is to say the Cu $d_{x^2-y^2}$ and oxygen p orbitals give rise to the bands in which the correlated pairs form.[56] The original BCS theory described spherical or s-wave superconductivity, it is now accepted that the cuprates are d-wave superconductors, and has been suggested that BCS theory when phrased to accommodate d and higher-wave superconductivity can account for the high-T_c behaviour (*e.g.* [57]) although this is not established.

A full discussion of the proposed mechanisms of superconductivity in the cuprates would be a considerable undertaking and will not be attempted here, but it is important to note that no superconducting systems with comparable T_c's were reported in the

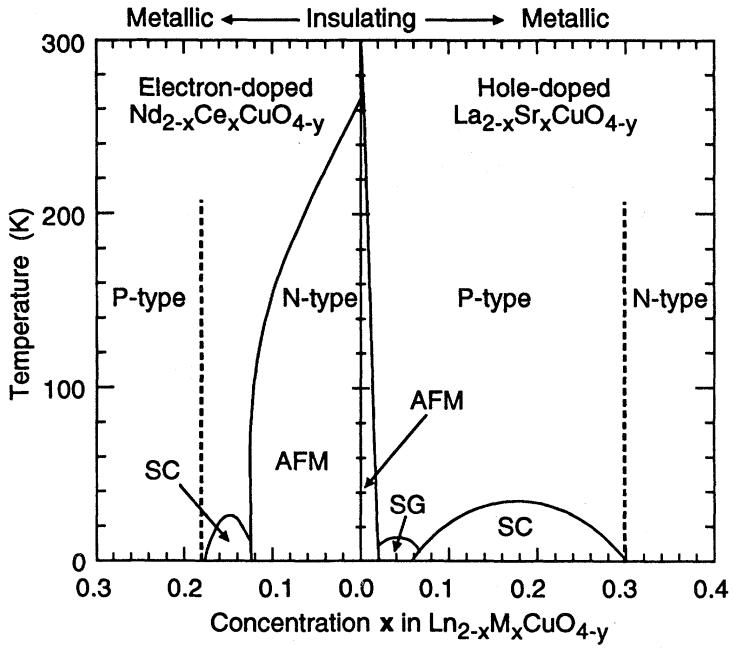

Figure 1.10: Cuprate phase diagram showing the anitferromagnetic (AFM) region suppressed by doping, and the emergence of superconductivity at higher doping levels.[58]

twenty years following the discovery of the cuprates. The iron-based superconductors discovered in 2008 are introduced in Chapter 4, it remains to be seen quite how similar they are to the cuprate system but their discovery will surely help to shed new light on some of the significant unanswered questions of condensed matter physics.

Chapter 2

Experimental techniques

High-pressure synthesis has been of great importance in this work and will be introduced in this chapter along with ambient-pressure solid state synthesis techniques. A brief discussion of the principles and theory which form the basis of powder crystallography is then followed by an examination of the analytical methods that have been used.

2.1 Synthesis

2.1.1 Ambient-pressure solid state synthesis: the ceramic method

The materials which are the subject of this research are dense ceramic and metallic solids consisting of extended lattices. In order to react with one another, two chemical species must come into close proximity on an atomic scale which is a problem when dealing with chemical species which are strongly bound in an extended lattice. One of the requisites of solid state synthesis is to facilitate the mixing of chemical species in order for reactions to occur.

The ceramic method offers a basic solution: to grind the solids to fine powders which are mixed, pressed into pellets and heated. Despite its simplicity the ceramic method is an effective one; many important materials have been produced by the ceramic method including the cuprate superconductors and rare earth manganite CMR materials. The first step is diligent manual grinding typically in an agate pestle and mortar. Key to the reaction process is as intimate a mixing as possible of the reactants since thoroughly ground powders with small grain sizes result in more contact between the reactants than course powders do. Other methods of combining solids exist, including the use of solution precursors, the evaporation of which can leave gels or residues of small particles. The aim of these methods is to combine reactants more thoroughly than by manual grinding. Pressing the powders into pellets increases contact between grains further: the mixed powders are placed in a steel pellet die, which is subjected to a load of several tonnes to pelletise the mixture. Even if powders are well ground on

a macroscopic level and the mixture appears homogeneous, on an atomic level the material is largely a heterogeneous mixture of solids. Reactions will occur at grain boundaries first but take a long time to occur in the bulk of grains. High temperatures promote ion mobility through the solids resulting in reactions over a larger volume, but solid state reactions are still slow at ambient pressure; pelleted samples are placed in alumina crucibles and heated at several hundred degrees for several days in high-temperature furnaces. Intermediate regrinding helps re-distribute unreacted portions of the mixture and brings new grains together. The reaction can be monitored by x-ray diffraction at the intermediate grinding stages until confirmed as complete when there is no further change in the diffraction pattern.

This method tends to produce the thermodynamic product at a given set of conditions. Theoretically it should not matter what starting materials are used as long as the correct stoichiometry of elements is present. The ceramic method can be supplemented by the tailoring of the gaseous environment which surrounds the pelleted samples. Dry, oxygen-free inert gases such as nitrogen or argon provide a mildly reducing environment, which can be enhanced by the addition of hydrogen. Pure oxygen can be used for oxidation. Different phases or mixtures of phases may be thermodynamically stable at different temperatures, and quenching the reaction from high temperature to room temperature is intended to preserve the thermodynamic products from the high-temperature conditions.

Once the reaction is finished the product may be single or multi-phase. It is very difficult to separate or purify single phases out of a mixture of solids so many repetitions may be necessary to find synthesis conditions which produce a single-phase sample. High temperatures are necessary to facilitate reactions but the melting or decomposition points of reactants cannot be exceeded. Solid state synthesis has become a large field with many innovative methods employed to various ends including crystal and thin film growth. Ambient-pressure methods have only been used for the synthesis of precursors and specific methods are described in the results chapters. The main synthesis steps for all the materials reported in this thesis have been carried out at high pressures.

2.1.2 Historical development of high-pressure synthesis equipment

The effective application of high pressures for experiment and synthesis has been practiced for throughout the twentieth century. Early interest existed in the geological sciences to investigate the properties and formation of naturally occurring minerals within the earth's interior, particularly diamond, and in physics to investigate the

fundamental physical properties of elements at high pressures. The use of high pressures has steadily spread into the myriad fields in which it is exploited today. Improvements in available materials and in the design of research equipment have led to ever-higher accessible pressures.

In general high pressures are generated by two distinct techniques; static and dynamic. Static techniques can generate high pressures and hold them for arbitrary lengths of time, dynamic techniques involve the application of high pressures over microsecond timescales via impacts or shockwaves. Dynamic techniques allow the highest pressures but are not usually accurately reproducible, however they are useful as the only way of accessing pressures significantly above 300 GPa. Dynamic techniques are mainly used for measurements on materials at very high pressure rather than for synthesis, however they were used for microcrystalline diamond synthesis as early as 1961.[59] Static techniques are of more relevance to this work and will be the focus of this section, henceforth 'high pressure' will refer to static high pressure.

2.1.2.1 Opposed-anvil devices

Percy Williams Bridgman was the pioneer of high-pressure physics and made great advances in the field in the first half of the 20th century. He increased attainable pressures from 0.3 to 10 GPa in his lifetime and won the Nobel prize for physics for his work on high pressures in 1946. In his 1950 lecture, 'Physics above 20 000 kg cm^{-2}',[60] Bridgman described an opposed-anvil device for measuring electrical resistivity at high pressure. This design was to become very influential in the field of high-pressure equipment. The other advance that allowed such an increase in available pressures at the time was the unsupported area seal which is now known as the 'Bridgman Seal'. An unsupported area allowed deformable material to reach higher pressures than the intended pressure vessel, effectively sealing the pressure vessel. The designs are shown in Figure 2.1. Bridgman's devices made use of 'Carboloy' which is tungsten carbide cemented with cobalt, the hardness and small compressibility of tungsten carbide made it ideal for use as a piston or anvil material, and it is still widely used in high-pressure equipment as will be discussed. The work Bridgman undertook on the compressibility of elements was carried out in large assemblies of series of rams in cylinders using Bridgman seals. These 'supported' rams or pistons had much greater strength under compression than the ram material would have if unsupported. Using a small device with opposing pistons made of tungsten carbide within a steel device capable of applying pressures of 3 GPa on its own, pressures of 10 GPa could be achieved. Soft metals such as lead or iridium were used as pressure-transmitting media intended to convert

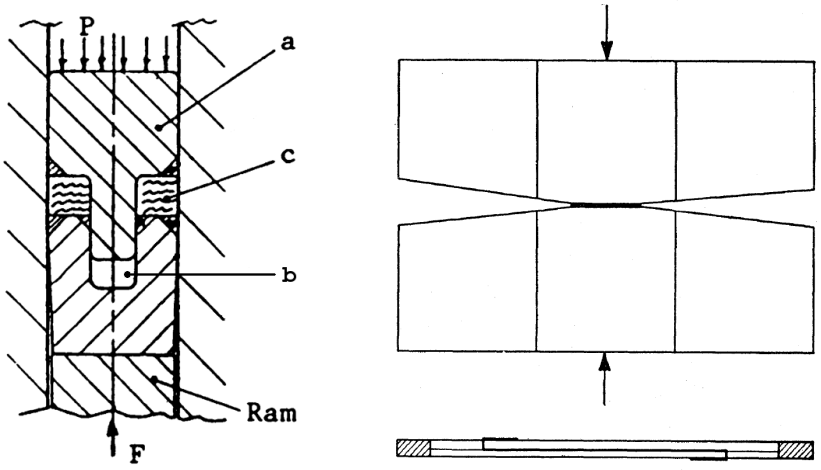

(a) Bridgman's unsupported area seal

(b) Bridgman's opposed-anvil apparatus for resistivity measurements with sample environment below.

Figure 2.1: Bridgman apparatus. In (a), the Bridgman seal, the initial ram is separated from a second floating ram, 'a' by an unsupported area labeled 'b' such that a sealant 'c' is under higher pressure than the sample area at the top, 'P'. In (b) the two opposed anvils' outer sections are steel and inner sections are tungsten carbide. The sample environment below consists of soap stone (hatched) enclosing a silver chloride pressure-transmitting medium with thin sample strip.[60]

uniaxial into hydrostatic pressures. With a knowledge of the elasticity of the materials he employed, Bridgman could work out the change in volume of the samples he was measuring upon the application of pressure.

There were obvious problems with measuring resistivities in these large piston-cylinder assemblies, the change in volume could be inferred from outside the equipment but it was unfeasible to connect samples to an electrical circuit. The much more simple opposed-anvil assembly provided a solution. The opposed anvils were made of tungsten carbide contained in a shrunk-on steel ring. Between the flat, opposed, truncated faces the sample (typically a thin metal strip) was embedded in insulating silver chloride, which acted as the pressure-transmitting medium. The sample was oriented such that it contacted each of the opposed anvils. The sample and silver chloride layer was surrounded by an insulating pipe stone (catlinite) ring. Named 'pipe stone' as it was traditionally used to carve pipes by Native Americans the material well suits the function of a gasket – it is a clay which is deformable enough to allow even load throughout the ring but becomes very strong under compression in a direction transverse to that of the compression. Sub-micron sized grit provides very high friction in contact with tungsten carbide, hence it prevents lateral extrusion of the

silver chloride. Since the sample-containing materials and gasket were insulating, the transport properties of the sample could be measured. Tungsten carbide is conducting, and a measuring circuit was formed connecting one of the anvils with the other, providing one of the anvils was insulated from the press used to apply load.

The system worked for metal strips up to 10 GPa but required nearly two-dimensional samples or very small volumes, and was only used for temperatures close to room temperature. The race to produce synthetic diamonds was ongoing at the time and prompted advancement of the heating capabilities of the equipment Bridgman had produced for high-pressure work. The General Electric scientists Francis Bundy, Herbert Strong, H. Tracy Hall *et al.* produced the first report of a reliable, reproducible synthesis of diamond in 1955[1].[61] Bundy had already modified Bridgman's opposed anvils to include two recesses, increasing the sample volume and allowing for a heater, although this did weaken the anvils. The first report on diamond synthesis by Bundy *et al.* was restrictive with the details it provided about the pressure equipment used, they merely stated that they had developed some new ways of distributing stress and given support to critical parts of Bridgman's piston-cylinder devices. Their second report in 1959[62] gave more details of the 'Belt' device they had used which was attributed to one of their co-workers, H. Tracy Hall. The details of the sample-containing assemblies for the diamond experiments were given in this paper, a detailed report of the belt apparatus itself was published in 1960[63]. The belt apparatus can be viewed as an amalgam of piston-cylinder and opposed-anvil systems, a schematic diagram is shown in Figure 2.2. The opposed anvils are reminiscent of Bridgman's original resistivity measurement setup, the 'belt' acts as the supporting cylinder would in the piston-cylinder systems or as a supplement to the gaskets used in opposed-anvil systems, allowing much bigger sample volumes than before. The centres of the anvils and belt were made from tungsten carbide and separated from each other by pyrophyllite, an alumino-silicate material with properties similar to pipe stone but more readily available. The belt apparatus was designed specifically for the synthesis of diamond but represented a significant breakthrough in high-pressure research allowing reproducible static pressures of up to 10 GPa for relatively large volumes of material which could be heated to temperatures in excess of 3000° when combined with appropriate sample assemblies. It also allowed a greater degree of access to the sample than in previous piston-cylinder systems providing the possibility of *in situ* measurements. Hall remarked it would be "of particular interest to geologists since

[1]It is now accepted that the Swedish electric company ASEA succeeded in synthesising diamond using a split-sphere device designed by Baltzar von Platen in 1953, but the company were secretive about their success and did not publish the result before the success of the General Electric scientists.

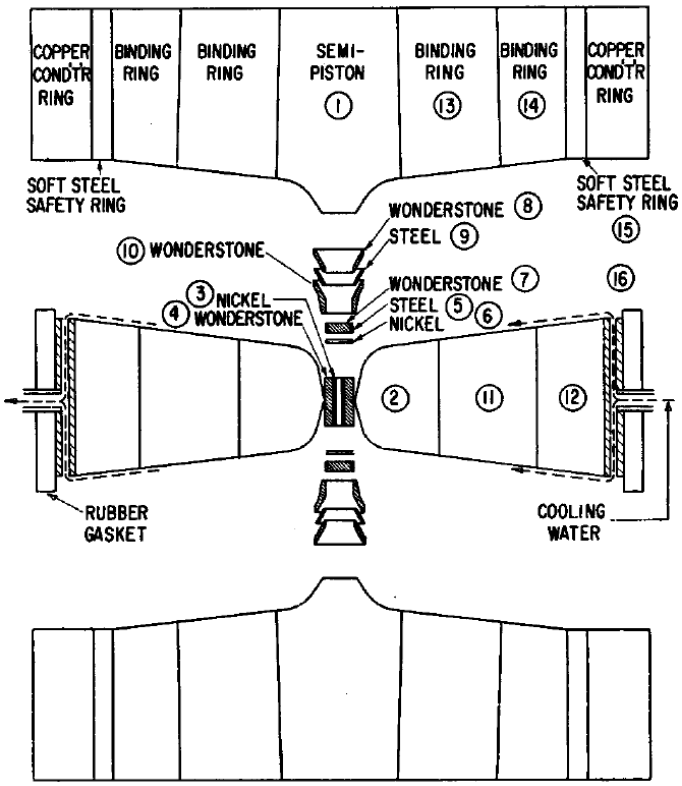

Figure 2.2: A section through Hall's 'Belt' apparatus, which was circular. (1) and (2) are tungsten carbide, (3) is the sample containing metal tube which acts as a heater when current is passed through it. (4) is the pressure-transmitting medium, wonderstone (pyrophyllite). A small steel ring (5) and metal disk (6) provide an electrical connection from the piston to the heater. a pyrophyllite plug (7) provides thermal insulation and a gasket is made from two funnel shaped pyrophyllite pieces (8) and (10) with steel between them (9) Hardened steel binding rings, (11)-(14), are "strained near their elastic limits by forced on tapered fits [to] greatly strengthen the chamber".[63]

100000 atmos correspond to a depth of about 240 miles in the earth". The pressure was calibrated by observing the load on the anvils and checking changes in the resistivity accompanying phase transitions as originally observed by Bridgman. The same method is used in modern devices and will be discussed later.

2.1.2.2 The diamond anvil cell

Since a significant factor governing the pressure available to a system is the compressive strength of the components used by the system it makes sense to use diamonds, the hardest known material, to build a high-pressure device. Two diamonds, using the same principle as Bridgman's opposed anvils, formed the basis of a diamond 'squeezer' pressure cell described in 1959[64] which, since the diamonds were transparent, could

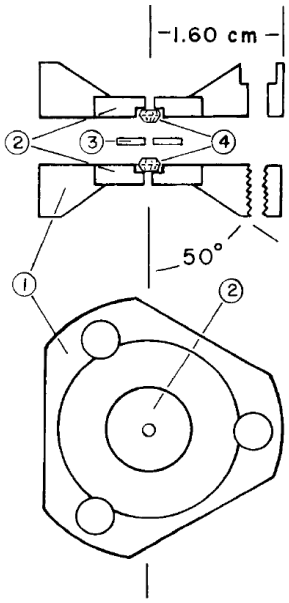

Figure 2.3: The Merrill-Bassett cell diamond anvil cell. (1) is a steel backing plate, (2) are beryllium disks (these hold the diamonds but are transparent to x-rays), (3) is an inconel gasket, (4) are two opposed diamonds. A load is applied via three screws.[66]

be used to make visual observations of small amounts of liquid under high pressures.[65] The transparency of diamond to a large portion of the electromagnetic spectrum allowed more than just visual observations to be made. In 1974 Bassett and Merrill described a diamond anvil cell which could be used on standard x-ray diffractometers.[66] This came to be known as the 'Merrill-Bassett' diamond anvil cell (DAC). The original design is shown in Figure 2.3. A further breakthrough came in 1972 with the use of the shift in ruby luminescence with pressure to accurately measure the pressure the within the DAC[67] (before this pressure in the cell had been estimated). The Merrill-Bassett cell and variations of it have become the principle tool for high-pressure measurements, today pressures of $\sim$3.5 MPa are attainable in DACs, close to the pressure at the centre of the earth. Normally a methanol/ethanol mix is used as a pressure-transmitting medium. A large and expanding number of uses now exists for DACs, with 'designer diamonds' available which have components set within them for various measurements including resistivity and magnetisation studies. DACs can be heated using lasers to high temperatures, but they are principally used for measurements rather than synthesis. They have not been used in this work, nonetheless, they are of great importance in the context of high-pressure equipment hence the inclusion of this subsection. For a review see [68].

2.1.2.3 Multi-anvil devices

So far all the devices described apply a uniaxial load, which may or may not be transfered into a hydrostatic pressure through a pressure-transmitting medium. A static system is obtained as the force in one direction along the axis is balanced by a force in the opposite direction. In order to contain a plastic pressure-transmitting medium and prevent off-axis extrusion, force must be applied from directions other than those of the anvils. In the case of the opposed-anvil systems this is provided by the compressed and strengthened gaskets, in simple piston-cylinder systems it is provided by the walls of the cylinder and in the belt apparatus it is provided by the gaskets and the belt itself. No loads are applied from these off-axis directions, the force is simply a reaction force from the components of the equipment.

In theory we would like to apply a load from every direction, to have infinitely many anvils arranged in a sphere, each one pointing inwards at the sample. This is not possible but to have more than two anvils is. The positioning of the anvils must lead to no net force. The principle of 'massive support' described by Bridgman relating to his opposed-anvil device is one of the reasons his anvils were made as truncated cones; the support is greater when the cone angle is larger. This would suggest that in a multi-anvil device it is desirable to have the anvils spaced at as wide an angle as possible. These two considerations lead to the intuitive ideal positioning of anvils of a multi-anvil device at the vertices of the platonic solids.

Hall, who had had such success with the belt apparatus also designed a tetrahedral multi-anvil apparatus.[69] Four hydraulic rams drove anvils which instead of truncated cones were truncated triangular-pyramids such the the flat faces would touch one another when extended together. The truncation of the tip resulted in a small tetrahedral void in the middle of the apparatus where the sample could be put in a tetrahedral assembly. This system could access pressures up to 10 GPa. Other multi-ram presses in trigonal bi-pyramid and cubic arrangements for six anvils were made but the complex nature of the many-ram presses meant they were never widely used.

A more simple way of introducing an increased number of anvils is to convert some of the uniaxial force of a standard one-ram press into force in other directions with angled metal blocks. This was very successfully applied to a cubic setup described by Lloyd and Hutton in 1959[70] using wedge-shaped outer ends of the four 'equatorial' anvils combined with angles in the upper and lower rams to create a simultaneous force from six anvils. This is known as the DIA setup after 'diamond' since it was originally used as

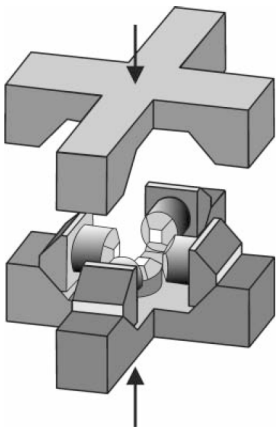

(a) A Schematic of the standard DIA-type apparatus.[72]

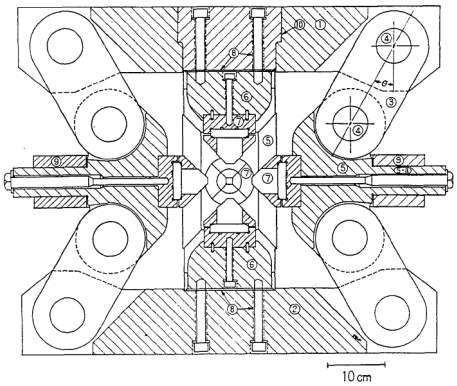

(b) A 'linked-DIA' apparatus.[71]

Figure 2.4: DIA apparatus where uniaxial load is converted to triaxial pressure via equatorial anvils with tapered outer edges (a) or with hinged linking arms (b).

a yet another piece of equipment to synthesise diamond. The anvils are similar to those used in Hall's tetrahedral press but this time are truncated square pyramids resulting in a cubic void in the centre for a cubic sample assembly. A schematic diagram of the DIA system is shown in Figure 2.4a. The wedges of the equatorial anvils slide along inclined surfaces around the edges of the upper and lower rams to create a situation with a pair of opposed anvils on each of the three orthogonal axes. An interesting variation has all six anvils linked together by massive steel hinged linking 'arms'[71]. A diagram is shown in Figure 2.4b. Some of the synthesis in this research was performed using a DIA-type press, the system will be re-visited in a later section.

The devices described above are single-stage, which means the anvils driven by the presses are directly applied to the sample assembly. It was well known that nesting small pressure assemblies inside larger ones could multiply the attainable pressure, this was exploited by Bridgman in his early compressibility studies using a small tungsten carbide piston cylinder within a larger steel assembly to reach pressures of 10 GPa.[60] Hall had discussed nesting in his 1958 report, 'Some High-Pressure, High-Temperature Design Considerations' (the same report in which he described his tetrahedral multi-ram press)[69] but was discouraged by the difficulties in making an electrical circuit and connecting a thermocouple to the sample in such a device. He noted in the same report that Bridgman had managed to extend the pressures achieved in his opposed-anvil device from 10 GPa in normal conditions to ∼45 GPa when the whole device was surrounded with 3 GPa hydrostatic pressure. The method of surrounding the

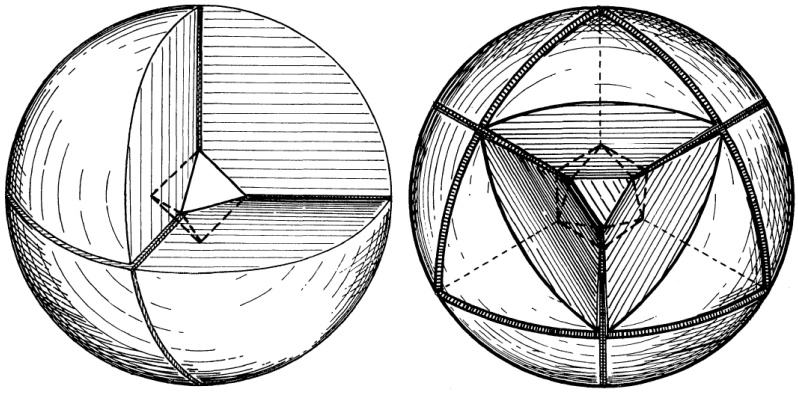

Figure 2.5: Kawai's split spheres. A sphere is split into eight (left) and twenty (right) anvils. The spheres were initially 80 mm in diameter, later variations used 250 mm spheres.[73]

whole system with hydrostatic pressure was utilised by a notable contributer to the development of large-volume high-pressure systems, Naoto Kawai, who in 1966 used anvils in the shape of sphere segments. These split spheres were truncated at the centre to give a polyhedral cavity allowing a sample assembly with the same number of faces as there were anvils. A diagram is shown in Figure 2.5. The whole system was covered in a rubber membrane and immersed in oil which would be pressurised. The anvils were separated from one another by soft insulating spacers, and partial extrusion of the central pyrophyllite assembly provided an effective gasket. Using an eight-anvil system Kawai obtained reproducible pressures up to at least 16 GPa and by extrapolation estimated the ability to reach more than 20 GPa. Considering the pressure that had been reached in previous systems, Kawai reached the conclusion that in principle the more anvils a system employed, the higher the pressure that could attained. Experiments with a sphere split into 20 segments and an icosahedral sample assembly were thus undertaken but did not share the success of the octahedral setup. Significant improvements in the attainable pressure were made by Kawai and Endo in 1970 by including a second set of anvils within the first. This '6-8 anvil type' comprised of a split sphere with 6 segment-shaped steel outer anvils, their truncated tips forming a cubic void, within which sat 8 truncated tungsten carbide cubes.[2] This could achieve a maximum pressure estimated to be between 30 and 50 GPa.[74] The device was modified to sit in two opposed rigid hemispherical cavities in a press due to problems with oil attacking the rubber membrane, a variation of this is shown in Figure 2.6a.[75] A very similar device to Endo and Kawai's 6-8 sphere in oil was employed from 1997 onwards in Russia for the synthesis of diamonds and other minerals.[76]

[2] A benefit of multi-stage apparatus is that the outer anvils do not have to apply such large pressure so can be made of steel, with inner anvils of tungsten carbide or harder materials.

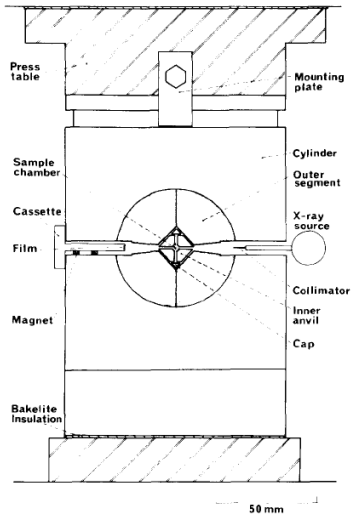

(a) Kawai's sphere in a rigid press instead of an oil bath.

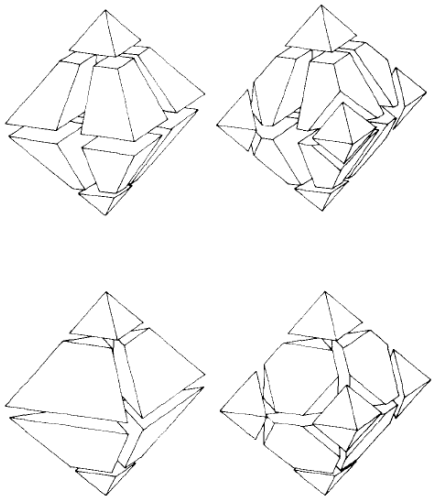

(b) Split octahedra

Figure 2.6: Kawai's two-stage split-octahedron device (a). The outer stage is a split sphere which encloses an inner split octahedron. The system is modified for x-ray diffraction by leaving gaps in the sphere and press. The central split octahedra are shown in (b) with two variations of 10 anvils on the left and two variations of 14 anvils on the right.[78]

More complicated systems with anvils comprising of split octahedra exist (*e.g.* used by Prikhna and Bromski for diamond synthesis[77]) either for an increase of pressure or for making *in situ* x-ray diffraction measurements of which a remarkable example is given by Kawai.[78] The outer anvils are segments of a sphere as with earlier designs, but there are 8 of them instead of 6, leading to an octahedral void in the centre. This is filled by anvils which make up a split octahedron, truncated at the centre to leave a octahedral void for the sample assembly. The pressure-transmitting medium is diamond powder in epoxy resin. The octahedron is split into anvils in various ways, the system is shown in Figure 2.6b.

These complex split-octahedron devices, dependent on the materials used, are suitable for pressures up to ∼25 GPa. They do not present a significant advantage over the variety of 6-8 devices which exist. The development of original and specific large-volume high-pressure devices is expensive and time consuming, and in 1990 Walker reported a device which could be retro-fitted into most large uniaxial presses. The original design is shown in Figure 2.7 It is based on a modification made by Ohtani in 1987 which replaced hemispherical nests with cylindrical clusters of wedges in movable equatorial steel rings.[79] The outer stage in the 'Walker module' is made of 6 steel wedges, a nest

of 3 above and below the standard inner split cube of 8 truncated tungsten carbide cubes. The wedges are free to move within a constraining ring. The Walker module is an inexpensive and practical way of achieving high pressures for large volumes. A modification was used for the majority of the synthesis in this work and information specific to this device will be given in the following section.

2.1.3 High-pressure equipment used in this research

The majority of the synthesis in this work was carried out using a high-pressure setup at Edinburgh University consisting of a two-stage 6-8 Walker-type module, supplemented with a small amount using one and two stage DIA-type presses at Kyoto University.

2.1.3.1 Two-stage Walker module

The press design used at Edinburgh was developed in Munich by Hubert Huppertz. It incorporates a modification of the Walker module with a thickened steel ring more than double the size of Walker's original design which was fabricated in collaboration with the press-manufacturer Voggenreiter to be loadable up to 1000 t. A detailed description is provided in Huppertz's useful review of multi-anvil devices.[72] A schematic of the 6-8 setup is shown in Figure 2.8.

The inner diameter of the steel ring is 17.8 cm, The steel wedges have square faces with 6 cm edges. There is a 1 mm gap between the steel wedges in each of the nests (upper and lower) and a larger gap (∼1 cm) between the upper and lower nests. The eight tungsten carbide cubes are have 32 mm edges. The attainable pressure is defined by the load applied by the press and the truncation of the cubes which in turn defines the sample-assembly volume. The truncation of the cubes and the sample-assembly volume are commonly discussed in terms of the truncation edge length (TEL) and octahedral edge length (OEL). Typical 6-8 assemblies are (OEL(mm)/TEL(mm)) 26/17, 19/12, 18/11, 14/8, 10/5, 10/4, and 7/3. Smaller truncations and sample assemblies attain higher pressures at a cost of smaller sample volumes. The maximum pressure for 18/11 is approximately 10 GPa, 15 GPa for 14/8 and 25 GPa for 7/3. This research has employed a 14/8 setup.

Samples are heated with electric resistance heaters in the sample assembly so certain parts must be electronically isolated from others: The lower nest of steel wedges is in contact with the base of the Walker module, but the upper nest must be isolated from the steel containment ring and is in electrical contact with the steel lid of the module. This is achieved by insulating all the wedges from the steel ring. One layer

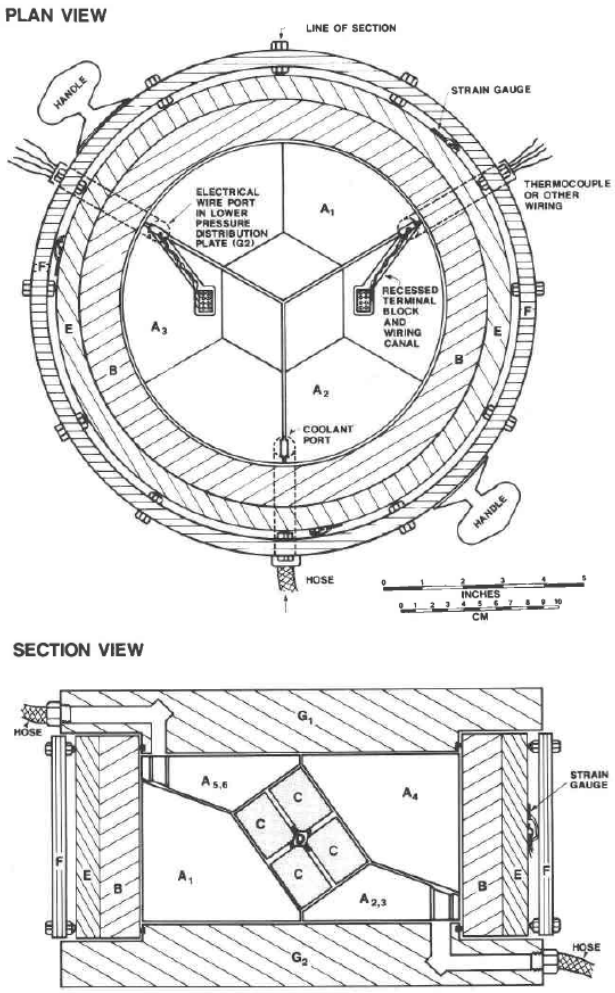

Figure 2.7: The original design of the Walker module. The upper view is drawn with with the top pressure distribution plate (G,), the top three wedges ($A_{4\text{-}6}$), and the cubes plus the pressure medium assembly (C, D) removed. The containment ring is made from two layers of steel (E, B), inner diameter ∼20 cm and there is an outer shatter guard (F). The outer diameter of the module is ∼30 cm.[80]

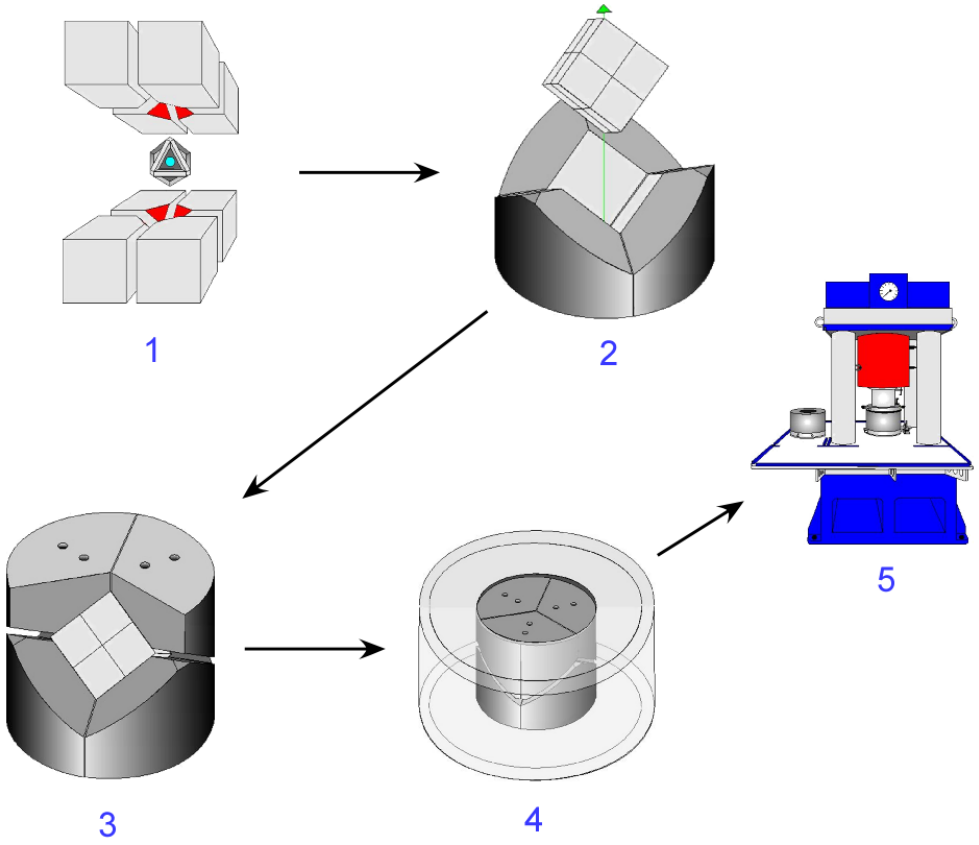

Figure 2.8: Schematic of the Walker module used at Edinburgh. The 8 32 mm tungsten carbide cubes with 8 mm inner truncations enclose a 14 mm octahedron (1). They form a split cube which sits in a lower nest of three steel wedges with one of its three-fold rotation axes vertical (2). a further nest of three wedges sits above the cube (3), with a 1 mm gap between each steel wedge and a 1 cm gap between the upper and lower nests. The system is enclosed in a steel containment ring (4), inner diameter 17.8 cm, outer diameter 37.8 cm. The modules sits in a Voggenreiter 1000 t press (5). The images were provided by Hubert Huppertz.

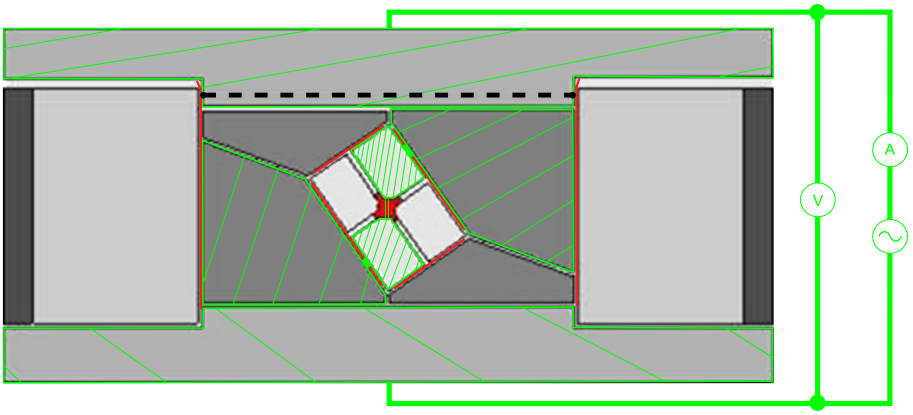

Figure 2.9: Section of the Walker module showing electrically connected parts. Electrical insulation is shown by red lines (fibreglass around the cubes, mylar sheets around the wedges, and the insulating MgO octahedral sample assembly), the electric circuit is shown in green. Green cross hatched parts are an example of parts connecting to form the circuit. The rubber o-ring is shown by a black dashed line.

of plastic (mylar film, 75 µm thick) is placed round the inner edge of the containment ring and the outer, curved edge of each steel wedge has another layer of plastic (mylar film, 50 µm thick) affixed with Polytetrafluoroethane (PTFE) spray, which also acts as a lubricant. The cylindrical outer layer of plastic extends above the containment ring and, in addition to a rubber O-ring, electronically isolates the lid from the rest of the module. The eight tungsten carbide cubes are held together by a square of fibreglass (0.8 mm thick) on each face of the larger split cube which they form. This acts as electrical insulation, two opposed inner cubes are connected to the upper and lower nests of steel wedges by small copper sheets which are passed through cuts in two opposite fibreglass squares. All the inner cubes are insulated from one another with sheets of PTFE in case they come into contact, thus two opposite truncated faces form two electrical contacts which connect with two opposite faces of the octahedral sample assembly. A schematic of the parts which connect to make an electric circuit through the Walker module is shown in Figure 2.9. The module is connected to a water supply and during heating its upper and lower plates are water-cooled through internal pipes.

For each press run the tungsten carbide cubes are aligned carefully by hand, and attached with superglue to the insulating fibreglass sheets. They are separated from one another at the centre by pyrophyllite gaskets and the octahedral sample assembly.

2.1.3.2 The octahedral sample assembly

The sample assembly at Edinburgh consists of a sintered, chromite-doped MgO octahedron (OEL = 14 mm) which acts as a pressure-transmitting medium, containing

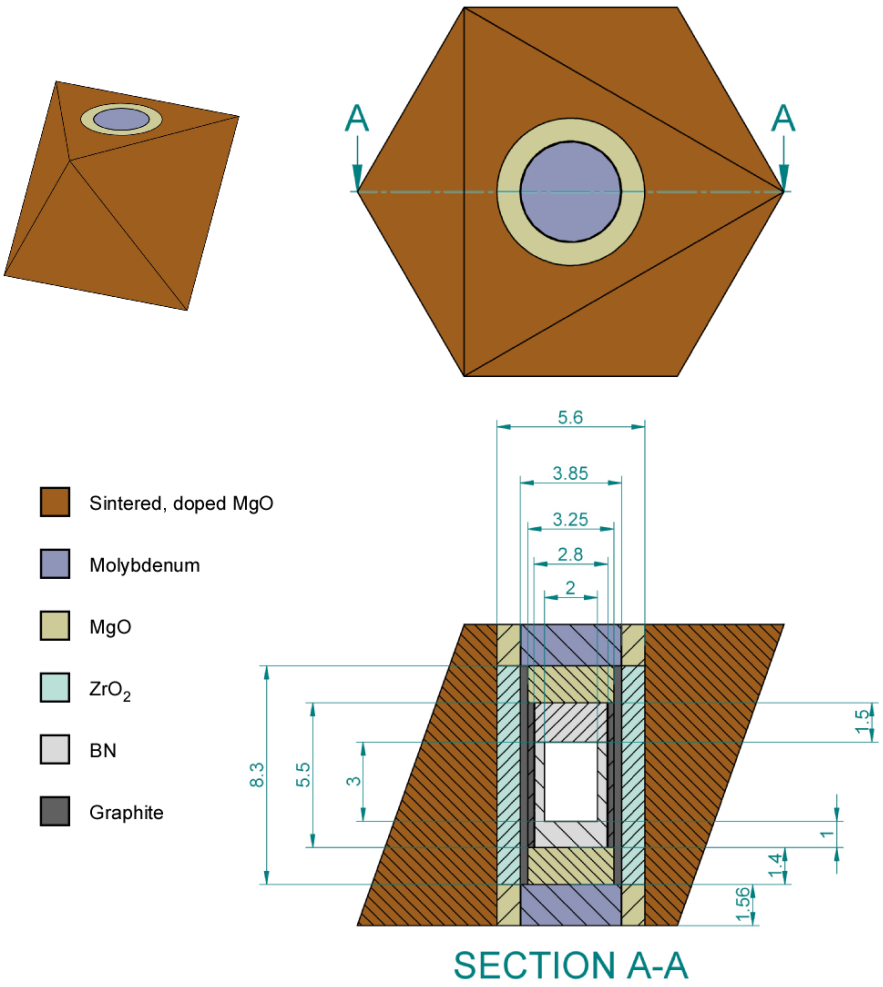

Figure 2.10: The octahedral sample assembly used at Edinburgh showing a top view and section. A key to the materials and triclinic view are shown on the left. Measurements are given in millimetres.

various cylindrical layers shown in Figure 2.10. The outer zirconia sleeve acts as a thermal insulator as do MgO rings and plugs at each end of the BN sample container. Two concentric graphite heaters surrounding the sample container are connected to two opposing anvils by molybdenum electrodes. The sample volume is 9.4 mm^3. Two samples can be run simultaneously by including a BN spacer in the sample container. For oxidation reactions the BN capsule is lined with 0.1 mm gold foil.

2.1.3.3 Calibrations

Neither the pressure nor the temperature are measured directly in synthesis runs, they are inferred from the load on the module and the power outputted by the electrical heating circuit respectively. The pressure is calibrated by measuring the resistivity

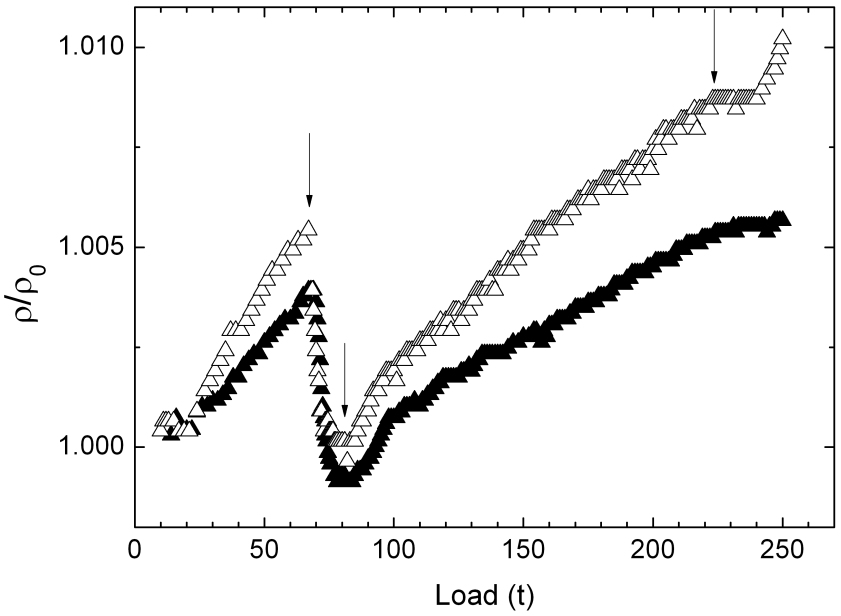

Figure 2.11: Pressure calibrations. Two measurements of the resistivity of bismuth with varying load are shown. The three known transitions are indicated with arrows. A load of 300 t corresponds to a pressure of 10 GPa in the sample assembly.

of a bismuth sample at room temperature with varying load; there are three known transitions at specific pressures. The temperature is calibrated by inserting a Pt-Rh thermocouple into a standard assembly with normal graphite heaters and measuring the temperature compared to the power outputted by the circuit, which is known. Both methods involve feeding wires through the walker module, which is challenging, especially in the case of temperature calibrations which involve thin thermocouple wires. Slippage of the anvils often breaks the wires.

All calibrations of the press used at Edinburgh have been carried out by Dr. Jenny Rodgers. Two pressure calibrations are shown in Figure 2.11, showing the three transitions in the resistivity of bismuth with increasing load. Temperature calibrations show a linear dependence of temperature on power output, and the temperature is inferred from measurements of the power from the heating circuit.

2.1.3.4 DIA presses

Syntheses up to 8 GPa in Kyoto were carried out in a one stage DIA-type press with a cubic sample assembly, shown in Figure 2.12. The sample assembly in Kyoto can accommodate samples up to $\sim$31 mm^3 in volume, the larger sample volume is partly due to the use of a single graphite heater rather than two in Edinburgh. A thermocouple

is routinely used to measure the temperature of the sample container during syntheses, it is the fact that all six anvils are electronically isolated in the DIA system, rather than arranged in an upper and lower nest, that allows the routine use of a thermocouple. A small hole is drilled through the centre of the assembly perpendicular to the direction of the cylinders of the sample container and heater, and a Pt-Rh thermocouple is inserted which sits outside the sample container but within all the other layers of the assembly. The heating circuit is passed through the anvils on the vertical axis, and the thermocouple circuit is passed through a pair of equatorial opposing anvils. A schematic of the DIA-type press setup was shown earlier in Figure 2.4a.

One run of higher pressure was attempted in Kyoto using a larger DIA-type press (the 'Elephant' press) containing a split cube, *i.e.* a standard 6-8 setup using a DIA press for the outer stage instead of a Walker module. The inner tungsten carbide cubes had 26 mm edge lengths as opposed to the 32 mm cubes used in Edinburgh, the OEL/TEL was 14/8, the same as the in the Walker module used at Edinburgh. A 15 GPa run was attempted using this system but the tungsten carbide cubes failed.

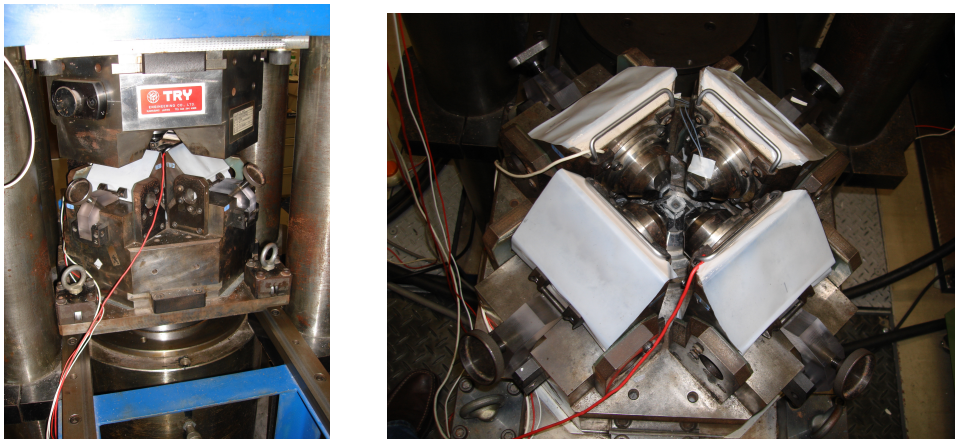

(a) The DIA setup **(b)** Lower section and equatorial anvils

Figure 2.12: The 'Infinite' DIA press, Kyoto. The lower section under the upper anvil is shown in (a) and the lower section, equatorial anvils and cubic sample assembly in (b). The white material on the outer edges of the equatorial anvil wedges is Teflon which allows the even application of pressure from the off-axis anvils. The thermocouple circuit travels through two equatorial anvils, they are shown connected to a red and a white wire. The temperature of the anvils is monitored using another thermocouple, which can be seen taped to one of the anvils in (b). When necessary, for very high temperatures, the anvils are cooled with an air-gun.

2.2 Diffraction Methods

2.2.1 Theory

2.2.1.1 Bragg's law

Diffraction is familiar as the effect on waveforms of travelling past obstacles. Here the specific behaviour of wavelike radiation interacting with a periodic lattice, the concern of the field of crystallography, will be introduced.

The first consideration is the condition for constructive interference in radiation reflected by atoms on a series of equally spaced parallel planes, distance d apart. The situation is shown schematically in Figure 2.13.

Considering monochromatic radiation, constructive interference will occur when the 'phase shift' of the beam of light reflected from an atom in the lower plane is zero relative to a beam reflected from an atom in the upper plane. This occurs when the extra distance travelled by the lower beam is equal to an integer value of the wavelength,

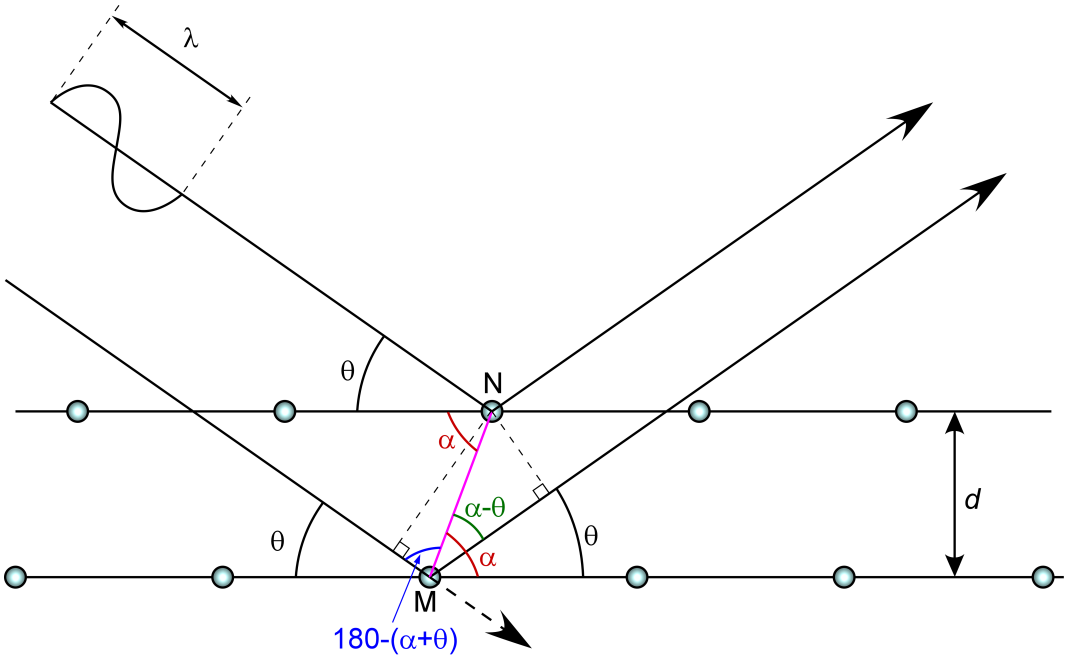

Figure 2.13: Scattering of radiation from consecutive planes of atoms with an arbitrary offset of the atoms in one plane with respect to those in the other.

as given by Equation 2.1:

$$\begin{aligned} n\lambda &= MN\cos(180-(\alpha+\theta)) + MN\cos(\alpha-\theta) \\ &= MN[-\cos(\alpha+\theta)+\cos(\alpha-\theta)] \end{aligned} \tag{2.1}$$

Standard trigonometric relationships are given in Equation 2.2:

$$\begin{aligned} \cos(\alpha+\theta) &= \cos\alpha\cos\theta - \sin\alpha\sin\theta \\ \cos(\alpha-\theta) &= \cos\alpha\cos\theta + \sin\alpha\sin\theta \end{aligned} \tag{2.2}$$

using which Equation 2.1 can be written as:

$$n\lambda = MN(2\sin\alpha\sin\theta) \tag{2.3}$$

An inspection of the geometry in Figure 2.13 gives:

$$d = MN\sin\alpha \tag{2.4}$$

Equation 2.3 and 2.4 can be combined to write Bragg's law:

$$n\lambda = 2d\sin\theta \tag{2.5}$$

where n is any integer, λ is the wavelength of the radiation, d the distance between planes and θ is the angle of reflection. Note the equation does not include α, which means the offset of atoms in one plane relative to another is not important, all that matters is the spacing between planes. If the equation is not satisfied the waves do not line up in reflected beams from consecutive planes, and if the radiation can penetrate such that it is reflected off many planes, overall there will be destructive interference, hence radiation diffracted off a series of parallel planes will result in a series of sharp peaks when intensity is measured with varying θ.

The periodicity of a crystal is given by its unit cell dimensions and symmetry, there are many overlapping series of planes in many different directions for each lattice. To distinguish them they are described by Miller indices. Consider a plane in a volume defined by three axes, x, y, and z (the axes need not necessarily be orthogonal). The orientation of any plane can be described by the points at which it crosses the axes, which also give the coefficients of a vector in a direction normal to the plane. Three examples are shown in Figure 2.14. In a crystal system it is conventional to define the planes in terms of the unit cell (whose dimensions are given as a, b, and c) as

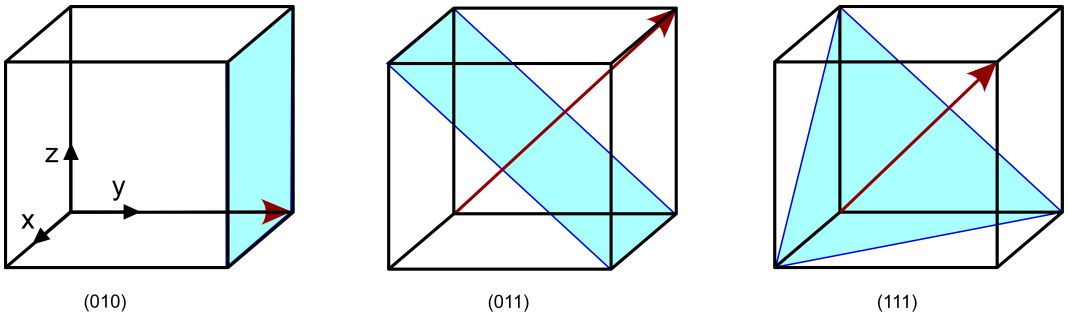

Figure 2.14: Three Miller index examples and their normal vectors in simple cubic cells.

Miller indices whose general form is (hkl) such that the plane cuts the axes at $\frac{a}{h}$, $\frac{b}{k}$, and $\frac{c}{l}$. Each (hkl) refers to an orientation which, since we are in a crystal lattice, will have many equally separated planes associated with it. As we have shown above equally spaced planes give rise to peaks in reflected radiation at specific angles defined by Bragg's law, these 'Bragg peaks' can thus be assigned with an (hkl) value of the set of equally spaced planes which were their cause and origin. The position of each Bragg peak refers, via Bragg's law given in Equation 2.5, to a d-spacing. This is given by the (hkl) value and the unit cell dimensions *e.g.* for unit cells with orthogonal axes:

$$\frac{1}{d_{hkl}^2} = \frac{h^2}{a^2} + \frac{k^2}{b^2} + \frac{l^2}{c^2} \tag{2.6}$$

Thus, given a set of unit cell dimensions the positions of the Bragg reflections for any given hkl are known. High values of hkl give small d-spacings; the planes with high hkl values are close together.

2.2.1.2 Structure Factors

So far we have considered only the unit cell spacing and not atoms within it. The introduction of atoms into the unit cell increase the complexity of the situation we are dealing with. For every atom there will be a set of planes generated by the unit cell periodicity, with d-spacings given by Equation 2.6, however the set of planes generated by one atom will be offset in space relative to the set generated by another. This offset, which is not described with the above equation, can lead to destructive or constructive interference, indeed, complete absences of intensity may occur for certain hkls. Only when all the atom positions are known can the intensity of each Bragg peak be calculated. The relative intensity of any Bragg peak, I_{hkl} is proportional to $|F_{hkl}|^2$ where F_{hkl} is the structure factor. It is related to the atom positions in a crystal as

follows:

$$F_{hkl} = \sum_{j=1}^{N} f_j \exp\left[2\pi i(hx_j + ky_j + lz_j) - \left(\frac{B_j \sin^2\theta}{\lambda^2}\right)\right] \tag{2.7}$$

This equation introduces some important factors. It is a sum over all atoms in the unit cell, a general atom is labelled j and there are N atoms. x_j, y_j and z_j are the fractional coordinates of the atom in the unit cell. f_j is the scattering factor of the j^{th} atom. This describes the degree to which the atom j interacts with the radiation being diffracted, and is known for each atom. In the case of x-ray diffraction this scattering of light occurs via an interaction of x-ray photons with the electron density of an atom. The more electrons an atom has the more it can interact with x-rays, hence the average scattering factor increases with atomic number (Z); heavier atoms are easier to 'see' by x-ray diffraction than light atoms. The electrons of an atom are not localised on one point, electron density is spread around the atom. X-rays can be scattered from any part of the electron cloud and, again, there is constructive and destructive interference of the diffracted light from an electron cloud to the effect that the scattering factor falls off with $\frac{\sin\theta}{\lambda}$. As such the scattering intensity of x-rays for any atom falls off with increasing θ (see Figure 2.15a).

The term on the right of the exponent in Equation 2.7 relates to the thermal motion of the atoms: B is the atomic temperature factor, a common alternative to B is U where:

$$B = 8\pi^2 U \tag{2.8}$$

U is the mean squared displacement of an atom from its average position, it assumes the position of the atom has a Gaussian distribution about its average position which is spherically symmetric (isotropic). Anisotropic temperature factors can be used with different components in different directions, but they do not feature in this thesis. The temperature factor depends on the sample environment and the nature of the lattice and crystal. Note the temperature factor's effect on the structure factor, and hence on the intensity, depends on θ. A large temperature factor implies the intensities will be reduced as θ increases (for $\theta < 90°$). From Equation 2.6 and 2.7 we can see that the positions of Bragg peaks depend on the unit cell dimensions and the intensities depend the contents of the unit cell; which atoms it contains and their positions.

A beam of neutrons can be treated in a similar way to other radiation and the diffraction principles above can be applied equally to x-ray and powder neutron diffraction (PND). A significant difference is in the structure factor. Neutrons, which have a spin of $\frac{1}{2}$, interact with the nuclei of atoms and with magnetic moments. If magnetic moments are

ordered neutrons will be diffracted by them just as they are by nuclei. For unpolarised neutron diffraction the total structure factor, F_{hkl} is given by

$$|F_{hkl}|^2 = |F_{hkl}^{nuc}|^2 + |\vec{F}_{hkl}^{mag}|^2 \tag{2.9}$$

where F_{hkl}^{nuc} is the nuclear structure factor and $\vec{F}_{hkl}^{mag}$ the magnetic structure factor. The nuclear structure factor is similar to the structure factor for x-rays:

$$F_{hkl}^{nuc} = \sum_{j=1}^{N} b_j \exp\left[2\pi i(hx_j + ky_j + lz_j) - \left(\frac{B_j \sin^2\theta}{\lambda^2}\right)\right] \tag{2.10}$$

The only difference between this and Equation 2.7 is the use of the neutron scattering length, b, instead of the x-ray form factor, f, but it is a difference which has important consequences. For the purposes of physical structure determination, neutrons can be considered as not interacting with electrons, they are scattered by the nuclei of the atoms in a lattice. The nuclei occupy a volume the dimensions of which are negligible compared to the wavelength of the neutrons at attainable energies so they can be considered as points. There is none of the constructive and destructive interference associated with differences in phase which are observed in x-rays diffracting from electron clouds as a fall-off in intensity; the intensity of scattered neutrons is independent of angle. A diagram of relative scattering intensities is shown in Figure 2.15a. Since less of the volume of a crystal is occupied by nuclei than by electrons, neutrons interact less strongly with matter than x-rays, in general longer counting times are required to get Bragg reflections with a reasonable intensity for neutrons than for x-rays. In addition, b does not increase smoothly with atomic number, the overriding factors controlling its magnitude being complex interactions between neutrons and nuclei which result in an irregular variation with increasing Z. These effects are illustrated in Figure 2.15b.

The magnetic structure factor is slightly different from nuclear structure factors:

$$\vec{F}_{hkl}^{mag} = \sum_{j=1}^{N} \vec{S}_{(hkl)j} f_j^{mag} \exp\left[2\pi i(hx_j + ky_j + lz_j) - \left(\frac{B_j \sin^2\theta}{\lambda^2}\right)\right] \tag{2.11}$$

In this case $\vec{S}_{(hkl)}$ is the component of a magnetic moment in a specific hkl plane, and f^{mag} is the magnetic form factor. Since magnetic moments are located on electrons, not nuclei, this does exhibit a fall-off with θ, just like the x-ray form factor. Magnetic Bragg peaks only occur when a phase is magnetically ordered. Comparing PND patterns above and below the transition temperature of a phase which magnetically orders allows

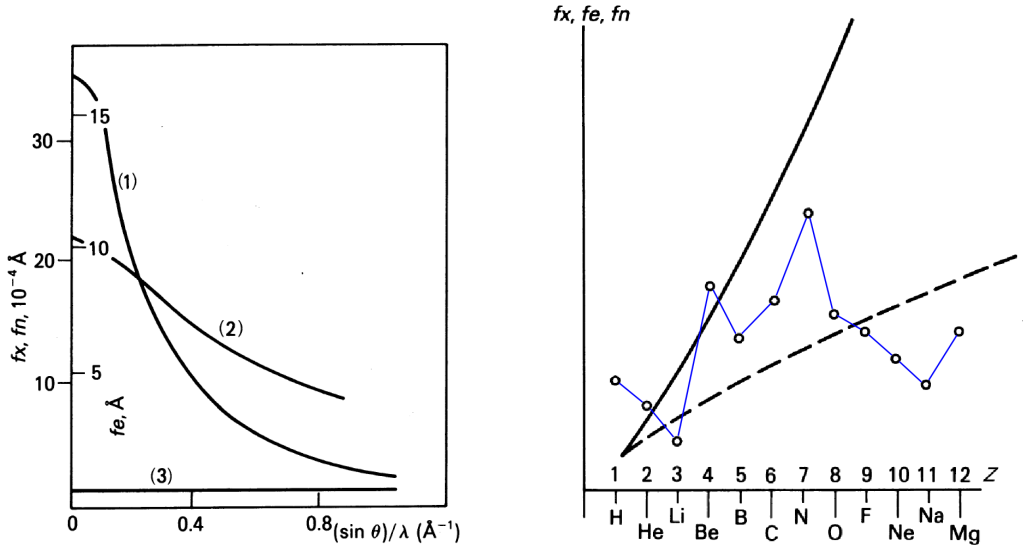

(a) Scattering factors of lead.

(b) Scattering factor for elements 1–12.

Figure 2.15: (a) shows the scattering factors vs. $\frac{\sin\theta}{\lambda}$ of lead, the factors for electrons, x-rays and neutrons are given by (1), (2) and (3) respectively. (b) shows the scattering factors averaged over $\frac{\sin\theta}{\lambda}$ for the first 12 elements. The factors for electrons, x-rays and neutrons are given by dashed black, black, and blue line respectively. Adapted from '*International Tables for Crystallography C*'.

the extra low-temperature peaks to be assigned as magnetic and allows the magnetic structure to be solved. In this work, magnetic structures are described relative to the nuclear structure of the material which exhibits magnetic order using a reciprocal-space propagation vector, k, whose components are in terms of the nuclear unit cell dimensions.

2.2.2 Powder techniques

The specific diffraction techniques used in this research are powder x-ray diffraction (PXRD) and powder neutron diffraction (PND). Figure 2.13 and the derivation of Bragg's equation which follows are valid for planes of atoms orthogonal to the plane which the incident and reflected beam occupy, which is the plane of the illustration. In a single crystal the *hkl* planes have many orientations and reflections appear at specific points on an imaginary sphere whose centre is the sample. A polycrystalline powder can be viewed as, ideally, a superposition of all orientations of a single crystal. The resulting diffraction occurs as cones radiating from the sample, termed 'Debye-Scherrer' cones, which are centered on the incident beam. A diagram illustrating the difference is shown in Figure 2.16. The angles of these cones from the incident beam correspond to the angle 2θ, described above. The results from a powder diffraction measurements

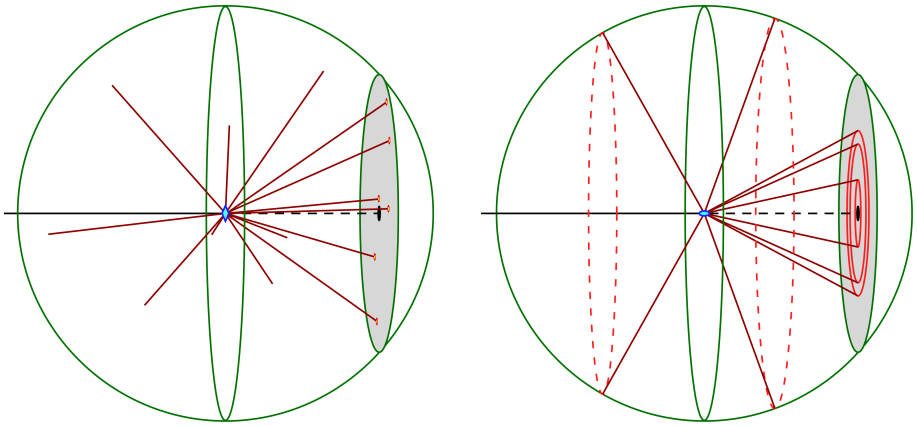

Figure 2.16: Debye-Scherrer cones. A single crystal (left) diffracts an incident beam (horizontal and black in these diagrams) at specific directions in a sphere centred on the sample whereas a powder (right) diffracts light in Debye-Scherrer cones (diffracted light is shown in red). Hence an area detector (pictured in grey) will see spots for a single crystal and rings for a powder.

can therefore simply be given as a variation of intensity with 2θ, rather than having to be described in terms of the position on the surface of a sphere. Information is lost compared to single crystal diffraction since separate reflections which are the same angle from the incident beam may be resolved in diffraction from single crystals but will overlap in a powder pattern.

2.2.2.1 Laboratory x-ray diffractometry

The diffractometer used for in-house measurements for this research is a Bruker D8 Advance diffractometer typical of many lab diffractometers. X-ray production is via an 'x-ray tube': a high voltage (in the case of our machine 40 kV which drives a current of 40 mA) produces electrons from a cathode which accelerate through an evacuated tube towards an anodal target. When electrons of sufficient energy hit the target they ionise core the core electrons of the metal. The relaxation of electrons in higher-energy orbitals to the core is accompanied by the emission of x-rays with defined wavelengths which depend on the metal of the anode. The machine used in this work has a copper x-ray tube which produces emission lines Kα_1, Kα_2, (which correspond to electrons in the copper $2p$ orbital decaying to the $1s$ orbital) and Kβ_1. The beam is monochromated by an angled crystal of germanium, which is oriented such that only the desired Bragg reflection is used to measure a sample, which consists solely of Cu Kα_1 radiation (λ = 1.540 562 Å). The machine is set up in 'Bragg-Brentano' geometry whereby the sample is irradiated from a fixed source with a divergent beam which converges post-diffraction at a fixed radius from the sample, where the detector is located. Various anti-scatter

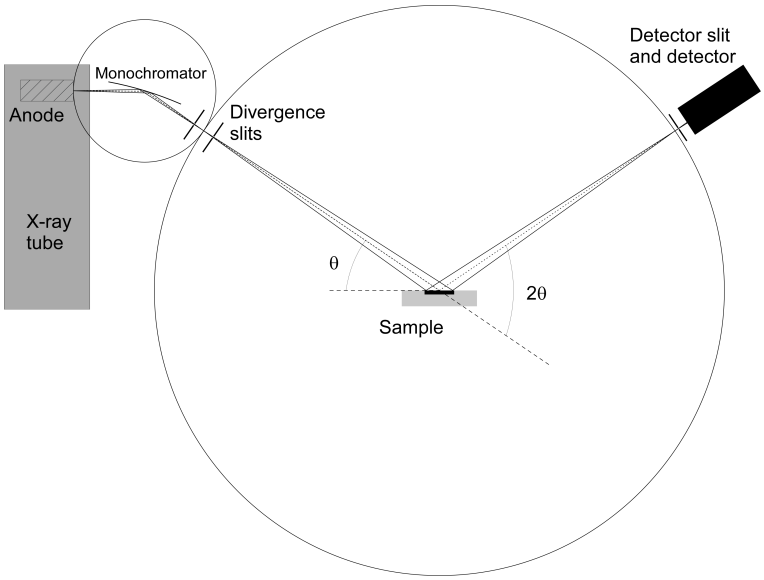

Figure 2.17: Bragg-Brentano geometry for a laboratory diffractometer using an x-ray tube source and a pre-sample monochromator. The focus loci of the x-ray beam are shown as circles.

and anti-divergence slits ensure the beam is only incident on the sample, and minimise any chance of radiation scattered from anything other than the sample reaching the detector. A schematic diagram is shown in Figure 2.17. The sample is usually spun to get the best powder average. The sample and the detector's motions are 'locked-coupled' which in this case means for every degree moved by the sample, the detector moves two degrees. Since they are both calibrated with a zero-point aligned with the incident beam, the sample surface orientation will be at an angle of θ and the detector at 2θ from the incident beam. It is conventional to report measurements of intensity relative to 2θ. The D8 at Edinburgh uses a Braun position sensitive detector (PSD) in which a potential exists across a volume of methane gas. X-rays ionise the methane and the resulting current can be measured, giving the x-ray intensity. The PSD measures 8° 2θ at once. Short identification scans are possible in half an hour using step sizes of 0.068 956° 2θ for 1 s at each step, long scans employ smaller step sizes of 0.006 859° 2θ scanning for ∼3 s per step, resulting in scans lasting from 7–15 h depending on the 2θ range and time per step.

2.2.2.2 Synchrotron diffractometry

Synchrotron x-ray diffraction (SXRD) in this research has been carried out at ID31, a high-resolution diffractometer situated on one of 32 beamlines at the European Synchrotron Radiation Facility (ESRF) in Grenoble, which uses a synchrotron to

produce high-energy, high-intensity x-rays.

When charged particles travelling at relativistic speeds[3] are accelerated they produce radiation. At the ESRF electrons are confined in a precise orbit in a large containment ring which is under ultrahigh vacuum. The electron beam has a width of the order of 0.5 mm and the containment ring has a circumference of ∼850 m. The path of the electron beam is controlled by arrays of magnets. The electrons go through curved sections and straight sections. At the curved sections, bending magnets alter the course of the electrons directing them from one straight section to the next. At each change of course of the electron beam high-intensity x-rays are produced tangentially in the direction of the original course of the beam, thus the bending magnets act as x-ray sources for experiments producing a fan of highly vertically collimated light. Insertion devices in the straight sections of the ring can also act as x-ray sources. Two such devices are undulators and wigglers. These are arrays of magnets with sinusoidally alternating magnetic fields. Wigglers have a relatively long period of oscillation causing a wide amplitude of the oscillations of the electrons. X-rays produced from wigglers add together incoherently and the flux is proportional to the number of the magnetic periods. A fan of vertically collimated light is produced. Undulators have a shorter period of oscillation resulting in smaller deflections of the electron beam. Radiation from different oscillations interferes resulting in horizontal collimation of the beam as well as the normal vertical collimation, and producing a higher flux density than bending magnets or wigglers do. A schematic diagram of a general synchrotron, and the layout of instruments at the ESRF are shown in Figure 2.18. Synchrotrons produce white radiation, the ability to select a single wavelength with a monochromator appropriate to the desired purpose is a great advantage over conventional x-ray sources.

ID31 is situated at the end of a straight section of the electron beam, with x-rays produced by undulator magnets. The instrument has a similar geometry to conventional laboratory diffractometers, but has a bank of 9 detectors, each of which has a silicon crystal between it and the sample. These crystals define the angle of light accepted by the detectors to a much higher degree of accuracy than the detector slits in a conventional diffractometer. A schematic diagram of the detector is shown in Figure 2.19. Information is combined from each of the detectors in the bank and with a movement of 2.3° of the detector bank, 18° 2θ is measured.

[3] At ESRF the electrons in the synchrotron travel at $\sim 0.9999999964c$, which gives them a mass of $11742m_e$, equivalent to just over the mass of a ^{6}Li atom at rest. The electrons are travelling at a speed sufficient to make 355000 circuits of the synchrotron ring per second.[81]

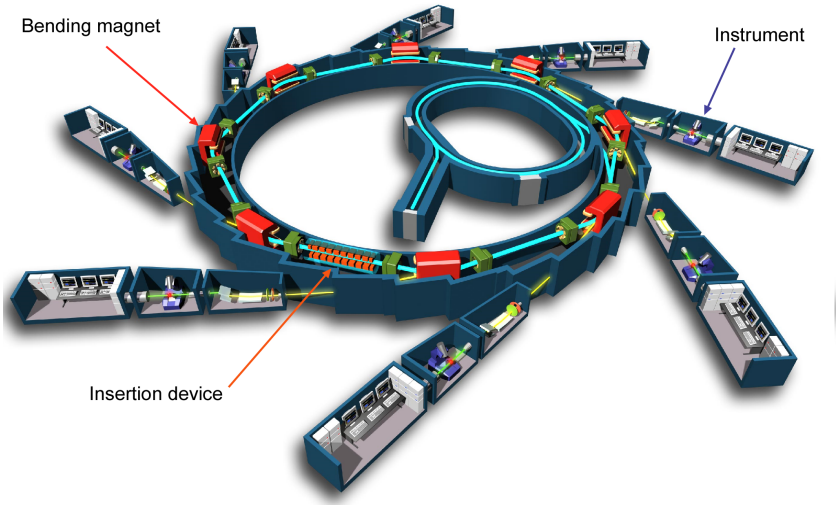

(a) General synchrotron schematic showing bending magnets and insertion devices and the tangential situation of the instruments around the synchrotron

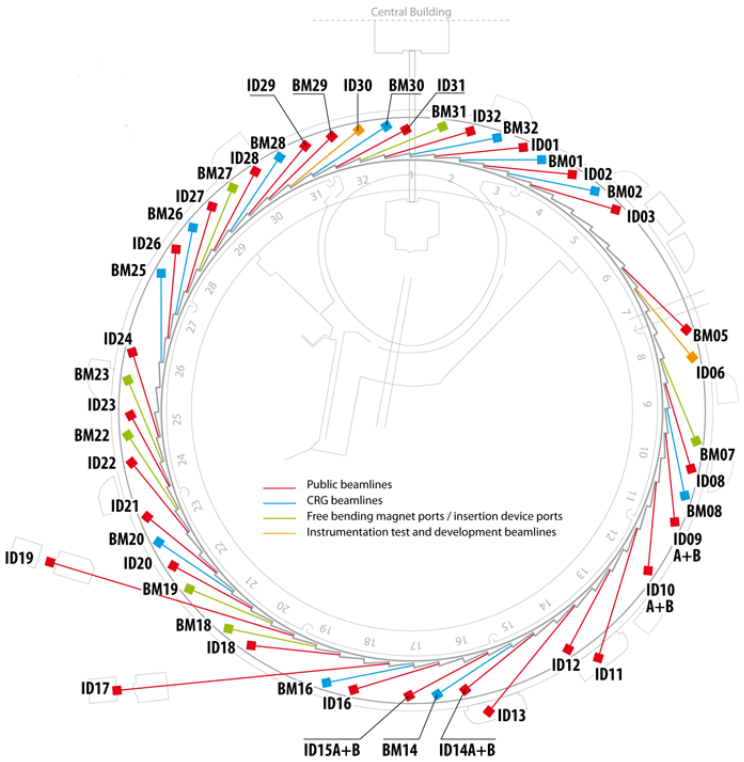

(b) Layout of instruments at the ESRF

Figure 2.18: A generic diagram of a synchrotron (a) and the layout of instruments at the ESRF (b) taken from the ESRF website.

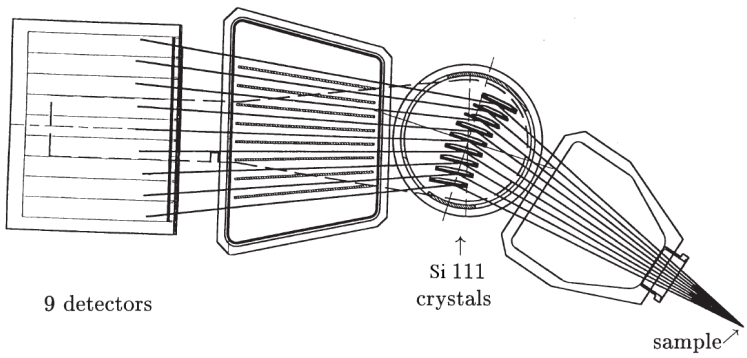

Figure 2.19: ID31 detector bank. The Si crystals have a very small angle of acceptance and so define the angle of the light from the sample very precisely.[82]

The analyser crystals, combined with a highly collimated, very bright beam and the high mechanical sensitivity and accuracy of the machine (in terms of the positioning of the detector bank relative to the sample) make much higher resolution diffraction images possible from ID31 than from laboratory x-ray diffractometers.

2.2.2.3 Constant-wavelength neutron diffraction experiments

The constant-wavelength PND experiments in this work were all performed at D20, a neutron powder diffractometer at the Institut Laue-Langevin (ILL) which is a neutron facility on the same site as the ESRF in Grenoble. The source is a nuclear reactor which is optimised to produce a high flux of neutrons, The ILL produces the highest continuous neutron flux for research use in the world. Fission of several kilograms of enriched ^{235}U produces the neutrons, which are cooled in heavy water to moderate their velocity and hence their wavelength. The heavy water also concentrates the neutrons in a small volume, these are known as 'thermal neutrons' (the D_2O is kept at ~35 °C, though some moderator sections are kept at higher or lower temperatures to produce 'hot' and 'cold' neutrons).

Various instruments are located radially from the core of the reactor, supplied with neutrons through guide tubes from the reactor itself. A diagram of the layout of the instruments is shown in Figure 2.20. Since neutrons do not interact with matter to the extent that x-rays do, relatively large samples or long counting times are needed to get reasonable structural information. D20 is one of the highest flux neutron diffractometers at the ILL, making it a desirable instrument when limited sample volumes are available. A choice of wavelengths exists from 1–2.41 Å (typical of thermal neutrons). Depending on the d-spacing range of interest, the wavelengths are selected with graphite, copper or germanium monochromators. A large detector bank can

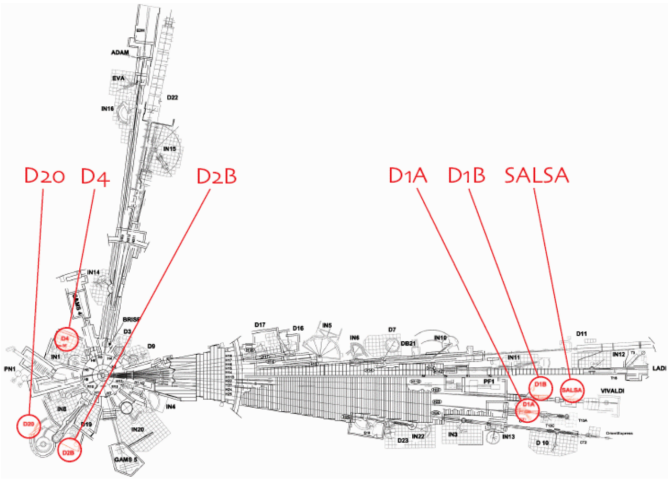

Figure 2.20: ILL instrument layout showing the radial distribution of instruments around the reactor core. The powder diffractometers are marked in red. The image is taken from the ILL website.

measure 153.6° 2θ simultaneously using 1536 separate detection cells. Samples are housed in vanadium cans (vanadium has a neutron scattering length close to zero), and the $\theta - 2\theta$ plane is horizontal, rather than vertical in the x-ray devices described above. A schematic diagram is shown in Figure 2.21. For the experiments in this research D20 was set up with $\lambda = 2.41\,\text{Å}$, the most appropriate wavelength for the observation of magnetic reflections which are most obvious at high d-spacing.

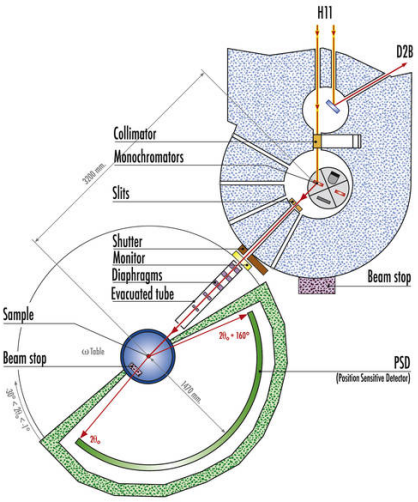

Figure 2.21: D20 schematic showing the neutron path from the reactor (top right) and the instrument (bottom left) with the large PSD bank shown as a green arc. The image is taken from the ILL website.

2.2.2.4 Time-of-flight neutron diffraction experiments

An alternative method to constant-wavelength diffraction is time-of-flight neutron diffraction. A neutron's wavelength is defined by its momentum and hence its velocity. If a pulse of neutrons with various energies, (*i.e.* various velocities) is released at one instant from one point, and the time each neutron takes to reach a second point a known distance away is measured, this so-called time of flight can be used in place of the wavelength. The de Broglie relationship states:

$$\lambda = \frac{h}{p} \tag{2.12}$$

Combining 2.12 with Bragg's law, given by Equation 2.5 we can write an alternative condition for constructive interference which does not include λ:

$$t = \frac{2mL}{h} d \sin\theta \tag{2.13}$$

where h is Plank's constant, p, v, and m are a neutron's momentum velocity and mass, L the total distance it travels and t the time of flight. Given a knowledge of the geometry of an instrument and the timings of the release of neutron pulses, Bragg peaks at specific d-spacing can be measured. Detectors are at fixed θ and measure a range of d-spacings which depends on the range of wavelengths of the neutrons that they measure. The specific instrument used in this research is GEM (from 'General materials diffractometer'), a time-of-flight neutron powder diffractometer at the ISIS pulsed neutron and muon source which is situated at the Rutherford-Appleton Laboratories, Oxfordshire. Neutrons are produced at ISIS by spallation: Protons are accelerated to high energies in a small synchrotron ring (163 m circumference), and extracted in pulses or 'packets' by powerful magnets. The high energy proton packets are directed into one of two tungsten targets where they eject neutrons from the tungsten nuclei. The neutrons are slowed to useful velocities with hydrogenous moderators. They are then directed to a variety of instruments distributed radially around the two target stations. A diagram of the layout of instruments at ISIS is shown in Figure 2.22.

GEM uses a methane moderator and is situated with an incident flight path of 17 m and a post sample flight path to the various detectors of 1.0–2.9 m. The detector array has 7270 elements located in six banks which are positioned between 1.1° and 169.3° 2θ. Choppers between the instrument and the spallation target select neutrons with wavelengths varying from 0.05–3.40 Å. A schematic diagram showing the positioning of the detector banks relative to the sample is shown in Figure 2.23

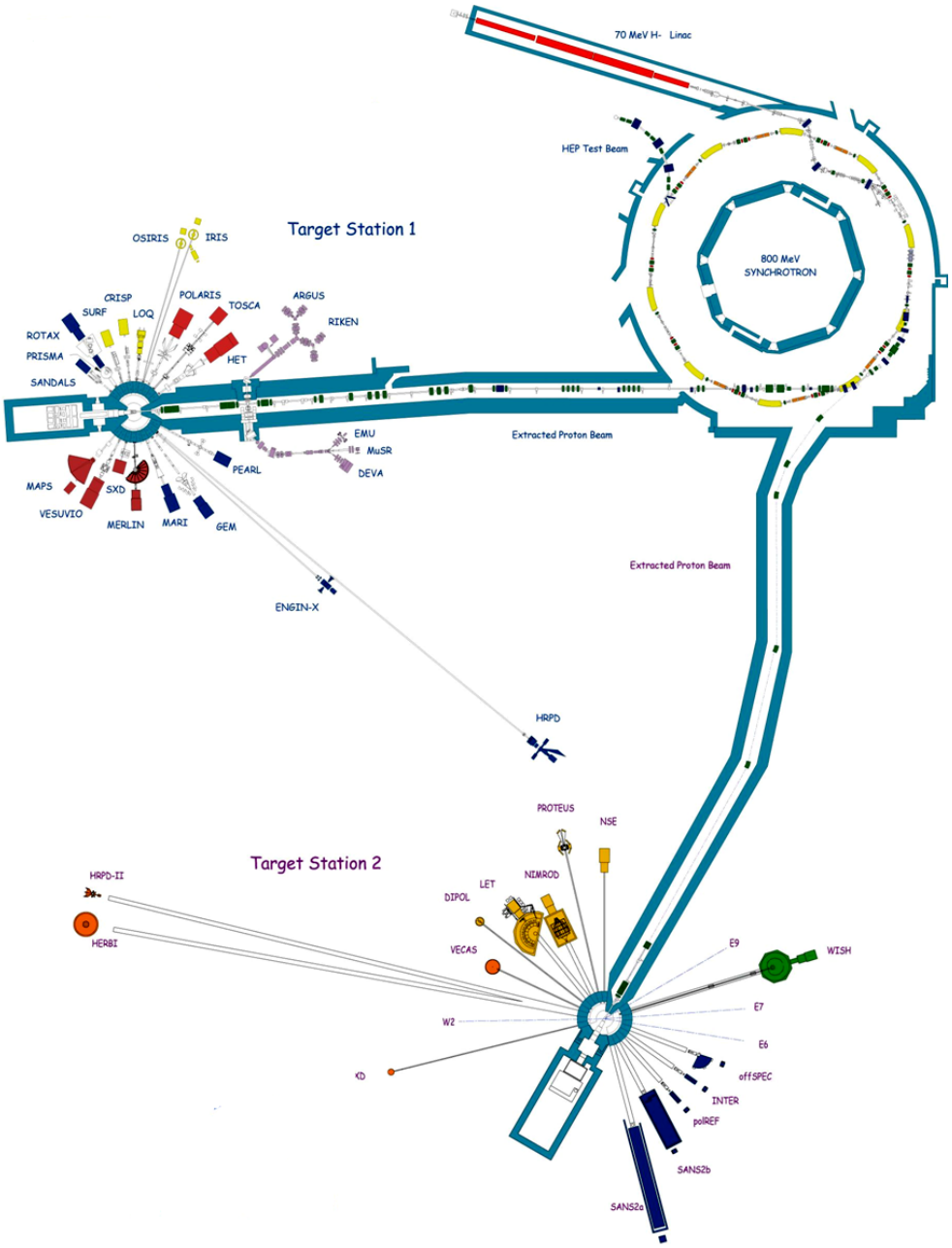

Figure 2.22: The layout of instruments at ISIS. The proton-accelerating synchrotron is shown at the top right, target station 1 is at the top left and target station 2 below. GEM is below target station 1 on the diagram. The image is taken from the ISIS website.

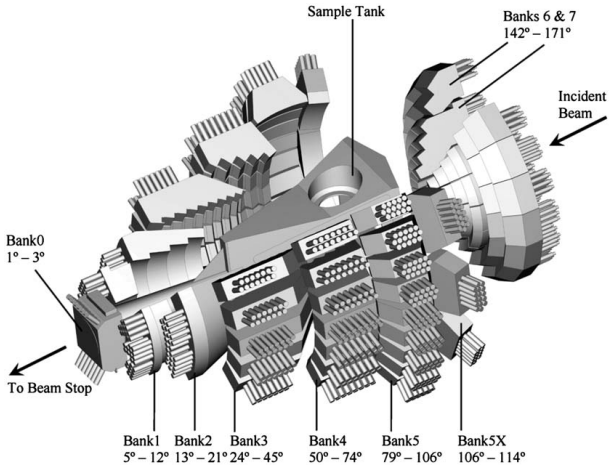

Figure 2.23: The GEM diffractometer showing the incident beam and the positions of the detector banks.[83]

2.2.2.5 Profile fitting methods for structure refinement

The Rietveld method, proposed in 1969,[84] works by generating a calculated powder diffraction pattern from a structural model, the parameters of which can be altered or 'refined' over a number of cycles to obtain the minimum difference between the calculated pattern some observed powder diffraction pattern. Peak positions and relative intensities are generated using the equations referred to above, in the diffraction methods section, and the total generation of a calculated powder pattern is arrived at as follows:

$$y_{i(calc)} = s \sum_{hkl} L_{hkl} |F_{hkl}|^2 \phi(2\theta_i - 2\theta_{hkl}) + y_{i(bkg)} \tag{2.14}$$

Where $y_{i(calc)}$ is the calculated intensity at point i, s is the scale factor, (hkl) refers to the set of miller indices the reflections of which contribute to the intensity at point i, F_{hkl} is the structure factor of those reflections, L_{hkl} is a term which contains various correction factors (Lorentz polarisation, absorption, preferred orientation, *etc.*), ϕ is a peak shape function which describes the variation of the intensity between the Bragg angle of reflection (hkl), θ_{hkl}, and the current point, θ_i, and $y_{i(bkg)}$ is the intensity of the background at point i.

Rietveld refinement minimises the residual S_y where

$$\begin{aligned} S_y &= \sum_i \frac{(y_{i(obs)} - y_{i(calc)})^2}{y_{i(obs)}} \\ &= \sum_i w_i (y_{i(obs)} - y_{i(calc)})^2 \end{aligned} \tag{2.15}$$

in which $y_{i(obs)}$ is the observed intensity at point i, and the difference is weighted by $\frac{1}{y_{i(obs)}} = w_i$. The minimisation of this residual is known as 'least squares' refinement. Minimisation is achieved by the variation of crystallographic, peak shape, background, and other correction parameters allowing the structure to be known to a high degree of accuracy, however, for a refinement to be successful, the starting model must be close to the final structure.

Le Bail fitting, a distinct profile fitting method from the Rietveld method, does not require the contents of a unit cell or the structure factor to be known, it merely generates peak positions from a set of unit cell dimensions using, *e.g.* Equation 2.6. The method then simply adjusts pre-set (or refined) peak-shapes in size to minimise difference in observed and calculated patterns (in a similar way to Rietveld refinement). This way the relative intensities at different peak positions can be found. This is not a structure solution or refinement method, but it is a useful way of checking if unit cell parameters are close to their true values, and for checking peak-shape profiles. It is often used as an early step in solving unknown structures from powder diffraction data.

The visual inspection of a plot of the overlaid observed and calculated patterns, in combination with a difference curve, provides a good qualitative indication of the 'goodness' of the fit of a model to experimental data, but there are several quantitative results that are commonly reported in conjunction with structure refinement. R_p and R_{wp} are the 'pattern' and 'weighted pattern' residuals respectively, they are given in Equation 2.16 and 2.17:

$$R_p = \frac{\sum_i |y_{i(obs)} - y_{i(calc)}|}{\sum_i y_{i(obs)}} \tag{2.16}$$

$$R_{wp} = \sqrt{\frac{S_y}{\sum_i w_i y_{i(obs)}^2}} \tag{2.17}$$

Note R_{wp} includes the factor which is minimised by refinement, as such it is the more statistically relevant residual. The reduced χ^2 or 'goodness of fit' is given by:

$$\chi^2 = \frac{S_y}{N_{obs} - N_{var}} \tag{2.18}$$

with N_{obs} and N_{var} being the number of observations and number of refined variables. The optimum value of χ^2 will be a small amount larger than 1 where the only difference between the model and the data is from noise.

The refinement in this work has been carried out using two different suites of programs, GSAS[85], and FullProf[86]. Backgrounds to patterns have usually been modelled using a shifted Chebyschev function with 4–6 variables or linear interpolation between points with refineable heights. For constant wavelength diffraction a pseudo-Voigt peak shape has been used which is a sum of Gaussian and Lorentzian profiles. The variations of the full width at half maximum (FWHM) of the Gaussian and Lorentzian contributions are given by Equation 2.19 and 2.20:

$$\mathrm{FWHM}_g = U\tan^2\theta + V\tan\theta + W \tag{2.19}$$

$$\mathrm{FWHM}_l = \frac{X}{\cos\theta} + Y\tan\theta \tag{2.20}$$

Where U, V and W are refineable coefficients for the Gaussian, and X and Y for the Lorentzian components of the peak profile. For time-of-flight data a more complicated peak function has been used, which has pseudo-Voigt and exponential decay components to better model the tail in each peak typical of time-of-flight instruments, which is an consequence of the pulse profile.

2.2.3 Electron microscopy

In contrast to x-ray and neutron diffraction methods, which focus on the bulk of a sample, electron microscopy techniques apply to relatively small areas of samples, providing a images of areas a few tens of nanometers in diameter. Local structural variations can be observed in this way with direct real-space images of the lattice, or, with the simple insertion of an appropriate aperture, reciprocal-space electron diffraction images can be observed. Electrons are focused with electromagnetic lenses, it is these lenses which allow real-space images to be obtained, distinguishing electron diffraction from the x-ray and neutron techniques above for which lenses cannot easily be manufactured. A schematic diagram of an electron microscope in diffraction and microscopic imaging modes is shown in Figure 2.24. The ability to analyse local areas of a material is an advantage compared to x-ray and neutron methods for investigating distortions, but the unit cell parameters provided by electron diffraction are of lower accuracy for the same reason. Only thin sections of samples can be used due to the strong absorption and scattering of electrons. HRTEMs are capable of resolving the positions of atoms in real space images and as such provide an attractive structural analysis method complementary to PXRD and PND.

All the electron microscopy for this work was carried out in St. Andrews by Dr.

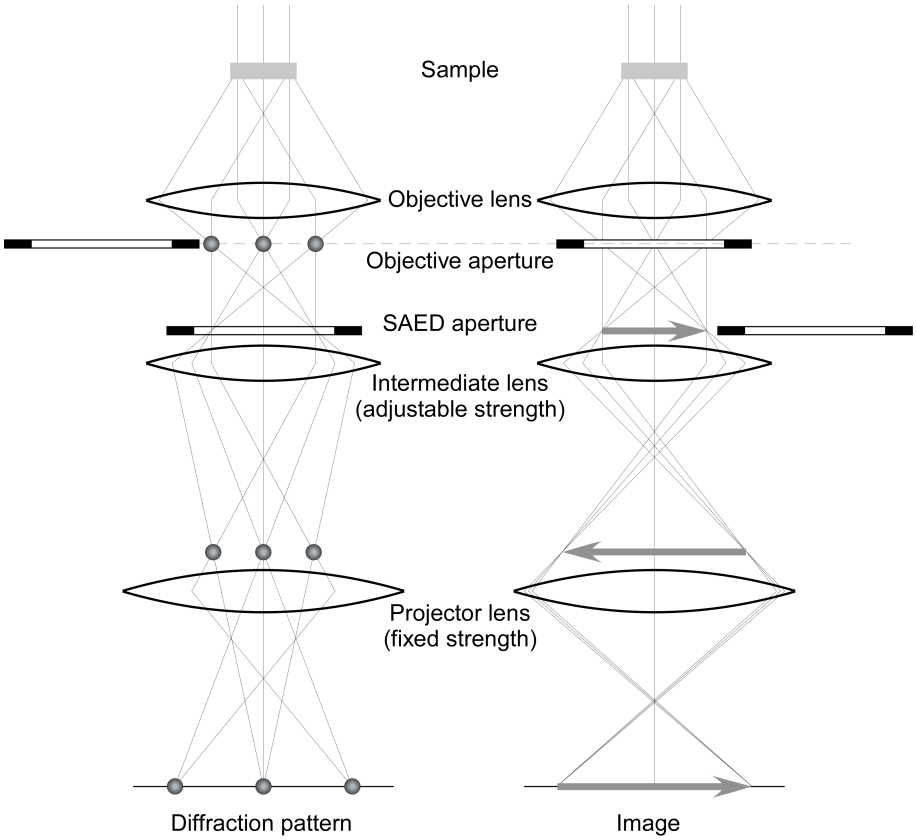

Figure 2.24: Schematic diagram of an electron microscope in diffraction mode (left) and imaging mode (right). Switching between modes is a simple matter of removing and inserting appropriate apertures

Wuzong Zhou so the technique is only briefly introduced here. A JOEL JEM 2011 electron microscope was used to collect selected-area electron diffraction (SAED) and high-resolution transmission electron microscope (HRTEM) images.

2.3 Physical property measurements

2.3.1 Magnetisation measurements

Magnetisation measurements can give information about the magnetic susceptibility of a sample and hence information about its magnetic behaviour. The behaviour of the spins of electrons defines the magnetic properties of a material, all materials exhibit a small diamagnetism, *i.e.* magnetisation in a direction opposite to that of an external magnetic field, the cause of which is related to the magnetic field altering the orbits of electrons about the nuclei of atoms.

Paramagnetism refers to the magnetisation of a material parallel to a magnetic field. 'Curie Paramagnetism' occurs when a material contains localised unpaired electrons. Electron states with angular momentum aligned to a magnetic field are stabilised in energy relative to those which are not aligned. This paramagnetic contribution is inversely dependent on temperature, increasing at low temperatures as the thermal randomisation of spins decreases (*i.e.* the stabilised energy-states become more populated). The behavior is given by the Curie law:

$$\chi = \frac{C}{T} \tag{2.21}$$

Where χ is the paramagnetic susceptibility, C is the Curie constant (containing the effective paramagnetic moment) and T is the temperature. If there are exchange interactions between unpaired electrons spontaneous alignment of spins can occur, as was discussed for the perovskites in Chapter 1. This alignment occurs below certain critical temperatures known as the Curie Temperature (T_C) for ferromagnets and the Néel Temperature (T_N) for antiferromagnets. Below these temperatures alignment of spins is seen (parallel for ferromagnets, antiparallel for antiferromagnets), above the critical temperatures the magnetisation of the materials exhibits Curie-Weiss behaviour:

$$\chi = \frac{C}{T - \theta} \tag{2.22}$$

where θ is the Weiss constant. Normally itinerant electrons are arranged with an equal number of up and down spin-states resulting in no net magnetisation. In a magnetic field a small imbalance between the populations of up and down spin-states can occur which results in 'Pauli paramagnetism'. Pauli paramagnetism is temperature independent and, in general, a smaller effect than Curie paramagnetism since only a small proportion of the itinerant electrons' spins can align compared to the number of localised spins which are free to align.

For superconductors, a large increase in diamagnetism is observed at the onset of superconductivity, T_c, (ideally the exclusion of all magnetic field from the sample) due to the Meissner effect.

In this research, magnetisation measurements were made with a Quantum Design magnetic properties measurement system (MPMS) which utilises a SQUID (superconducting quantum interference device) to measure the magnetisation of a sample at temperatures controlled by a cryostat. The system employs a superconducting electromagnet which can apply a tuneable magnetic field. Measurements can be made

within a temperature range of 2–400 K and a field range of ±7 T. The magnetisation measurements are made by passing the sample through a Josephson junction. The current transported by a Josephson junction is highly sensitive to magnetic field and hence the magnetisation of a sample can be inferred by comparing a measurement of the current when the sample is in the junction to when it is not. AC and DC measurements are possible, where the type of current is referring to that in the superconducting solenoid, such that DC measurements are of a sample in a constant field in one direction and AC measurements are of a sample in a magnetic field which switches direction at the AC frequency used. AC measurements give two values of magnetisation per measurement, an in-phase and out-of-phase or real and imaginary part referred to as M' and M'' respectively.

From the measured magnetisation at a magnetic field H the susceptibility is given by:

$$\chi = \frac{M}{H} \tag{2.23}$$

χ is usually converted using the mass and molar mass of the sample to the molar susceptibility, χ_m. An alternative which is useful for superconductors is the volume susceptibility, χ_{vol}, which can be used to estimate the diamagnetic fraction of a sample in the superconducting state.[87]

2.3.2 Electrical transport measurements

The behaviour of resistivity with varying temperature gives information on whether a material is metallic or insulating and regarding any superconductivity, hence variable-temperature resistivity measurements have been important within this work. Electrical transport or resistivity measurements have been made using a Quantum Design physical properties measurement system (PPMS) using sintered blocks direct from high pressure syntheses. Measurements were made using the standard four-point configuration in which an electrode is applied to each end of a sample providing a current which can be measured, and the voltage between two more electrodes a known distance apart on the sample is measured to give the resistance. A photograph of the setup is shown in Figure 2.25.

The electrodes are attached with silver paint or welded on for smaller samples and since the transport properties of the measuring circuit are known, the resistance of the sample can be measured. This gives the resistivity, ρ, by:

$$\rho = \frac{RA}{L} \tag{2.24}$$

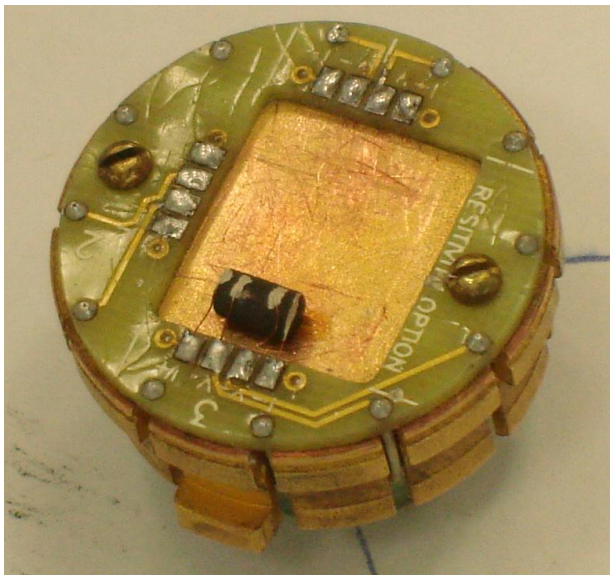

Figure 2.25: Four point resistivity measurement: A high-pressure sample sits on the resistivity measurement puck before insertion into the PPMS. The electrodes are attached with silver paint.

where L is the distance over which the potential difference is measured and A is the cross sectional area of the sample. Temperature is controlled in the PPMS using a cryostat and a magnetic field can be applied for field-dependent resistivity measurements. The sample sits on a puck which is capable of taking three samples at a time for three simultaneous resistivity measurements.

Chapter 3

High-pressure synthesis of $R\mathrm{PdO_3}$

3.1 Introduction

First synthesised by Kim *et al.* in 2001, $\mathrm{LaPdO_3}$ is the first oxide to contain $\mathrm{Pd^{III}}$.[88] Usually $\mathrm{Pd^{III}}$ is unstable with respect to disproportionation to $\mathrm{Pd^{II}}$ and $\mathrm{Pd^{IV}}$, so $\mathrm{LaPdO_3}$ may be expected to adopt a charge-ordered state at low temperatures, as in the $R\mathrm{NiO_3}$ (R = rare earth) series which exhibit charge order in all but the end member $\mathrm{LaNiO_3}$.[89] We have synthesised $\mathrm{LaPdO_3}$ at high pressure and conducted structural studies at a range of temperatures to investigate the possibility of any low-temperature structural transitions. In addition, we have attempted the synthesis of other $R\mathrm{PdO_3}$ analogues, R = Pr and Nd.

3.1.1 Rare earth nickelates

The $R\mathrm{NiO_3}$ (R = Rare earth) series attracted a good deal of interest in the latter part of the 20th century as it is provides an opportunity to investigate charge disproportionation in a simple (in terms of the physical, and band structure), undoped environment. The variation in the system comes from changing the rare earth element, R. The ionic radii of R^{III} vary by some 15 % across the group whilst the metals maintain reliable trivalency. With the exception of R = La, the materials (in their metallic states) adopt the orthorhombic distorted $GdFeO_3$-type perovskite structure, space group $Pbnm$, with tilted $\mathrm{Ni^{III}}$ octahedra. The d^7 nickel ions are low spin. As the series is crossed and the A-site R^{III} ion decreases in size, the structure departs further from that of the aristotypical perovskite, and the distortion (in this case the octahedral tilting) increases. In turn the Ni–O–Ni bond angles move further from 180°, *i.e.* the Ni–O–Ni bonds become more 'bent'.

$\mathrm{LaNiO_3}$ is exceptional. It is rhombohedral, space group $R\bar{3}c$, and is a paramagnetic metal down to the lowest temperatures, the partly occupied Ni e_g orbitals forming a narrow σ^* conduction band.[90] In contrast, the other members of the series exhibit antiferromagnetic ordering of the Ni ions at low temperatures and undergo a metal—

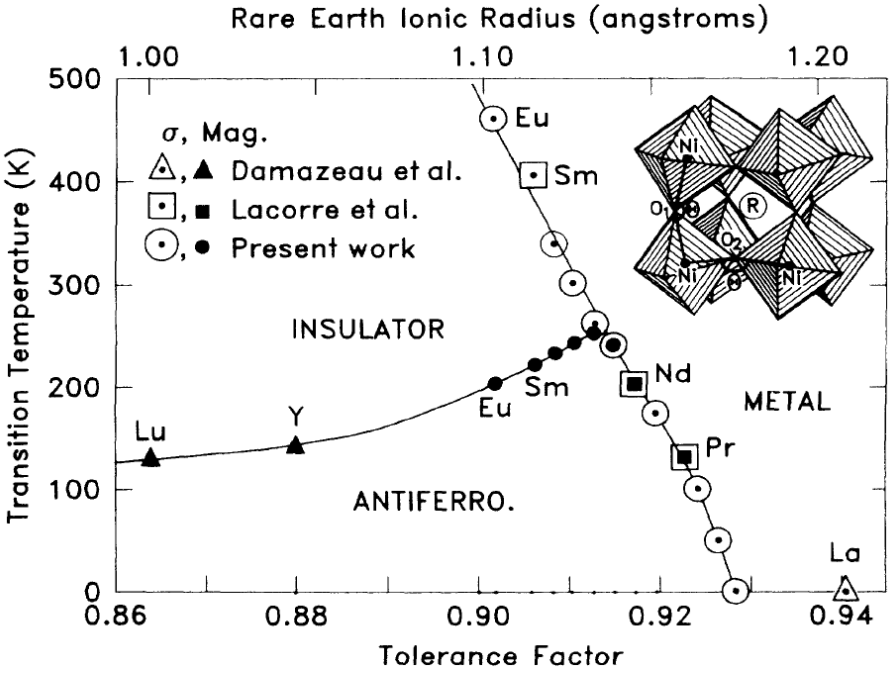

Figure 3.1: Phase diagram of $R\mathrm{NiO_3}$ showing the metal-insulator and magnetic transition temperatures with tolerance factor and rare earth ionic radius. The $GdFeO_3$-type orthorhombic structure of $R\mathrm{NiO_3}$ is inset in the top right.[89]

insulator (MI) transition at some critical temperature, T_{MI}, which increases across the group. A phase diagram is shown in Figure 3.1.

For R = Pr and Nd the Néel temperatures coincide with T_{MI}'s of 135 K and 200 K respectively.[91] T_{MI} continues to increase monotonically across the series but the slope of T_{N} reverses after neodymium and for samarium T_{N} = 220 K and T_{MI} = 400 K.[92] Thus the samarium and later rare earth containing compounds exist in three distinct phases: insulating and antiferromagnetic at low temperatures, insulating and paramagnetic at intermediate temperatures, and metallic and paramagnetic at high temperatures.

Synthesis of the later R-containing nickelates allowed a subtle structural transition at T_{MI} to be observed from $Pbnm$ (metal) to monoclinic $P2_1/c$ (insulator). This is accompanied by the emergence of two distinct ordered nickel sites with slightly shortened or lengthened Ni–O bonds compared to those of $\mathrm{Ni^{III}}$, which is interpreted as charge ordering (CO): $2\,\mathrm{Ni}^{3+} \longrightarrow \mathrm{Ni}^{(3+\delta)+} + \mathrm{Ni}^{(3-\delta)+}$.[93] This CO explains the opening of a gap in the σ^* conduction band, and the transition from metallic to insulating properties. The magnitude of δ and the extent of this transition decrease

approaching the itinerant limit *i.e.* moving to lighter R, making CO more difficult to detect.

3.1.2 Nickel-group transition metals

The properties of the members of any particular group of the periodic table are broadly similar, but they are not the same. The neutral nickel-group elements (we will consider nickel, palladium and platinum) all have different frontier-orbital configurations: nickel is $3d^8\ 4s^2$, palladium $4d^{10}\ 5s^0$, and platinum $5d^9\ 6s^1$. They can access different oxidation states and geometries. Nickel is found in +4, +3 and +2 oxidation states, +2 being the most common. Indeed, d^8 Ni^{II} provides a classic example of the effects of the ligand on the geometry of transition metal complexes: $[Ni(H_2O)_6]^{2+}$, $[NiCl_4]^{2-}$, and $[Ni(CN)_4]^{2-}$ adopt octahedral, tetrahedral and square-planar geometries respectively depending on ligand field strength. The +3 oxidation state is less flexible in terms of geometry, d^7 Ni^{III} forms a limited number of low-spin octahedral complexes, and is the configuration of nickel in $R NiO_3$. Low-spin Ni^{III} is $t_{2g}^6\ e_g^1$, the asymmetric degeneracy of the e_g orbitals suggests the ion should be susceptible to Jahn-Teller distortion, but this is not seen in any of the $R NiO_3$ series, unlike in the electronically similar Mn^{III} ($t_{2g}^3\ e_g^1$) in $LaMnO_3$ which exhibits a first order Jahn-Teller effect that is enhanced by substitution of smaller rare earth elements onto the A-site.[94] Ni^{IV} has been isolated in $BaNiO_3$, synthesised at 0.2 GPa,[95] and in a small number of complexes featuring highly electronegative ligands, it is octahedral low-spin d^6.

As the group is descended the d-orbitals become more radially diffuse which lends greater stability to higher oxidation states. The +3 oxidation state was viewed as common for palladium and platinum compounds until structural examination of many apparently trivalent compounds in the middle part of the 20th century revealed chains of M^{II} + M^{IV} dimers.[96] A typical example is the platinum compound, Wolfram's Red Salt,[97] shown in Figure 3.2. Wolfram's Red Salt contains alternating Pt^{II} and Pt^{IV} ions in Pt−Cl−Pt chains, each platinum coordinated by four $C_2H_5NH_2$ ligands normal to the the chain. The divalent platinums are effectively square-planar with long contacts to their neighboring chlorines and the tetravalent platinums are octahedrally coordinated by their two neighbouring chlorines and four surrounding organic ligands.

The +2 oxidation state is the most common of palladium, but in contrast to Ni^{II}, Pd^{II} and Pt^{II} are almost always found in square-planar coordinations. Pd^{IV} is more stable than Ni^{IV}, and is usually found in octahedral coordinations. The paucity of Pd^{III} compounds can be rationalised by the relative stabilities of the square-planar

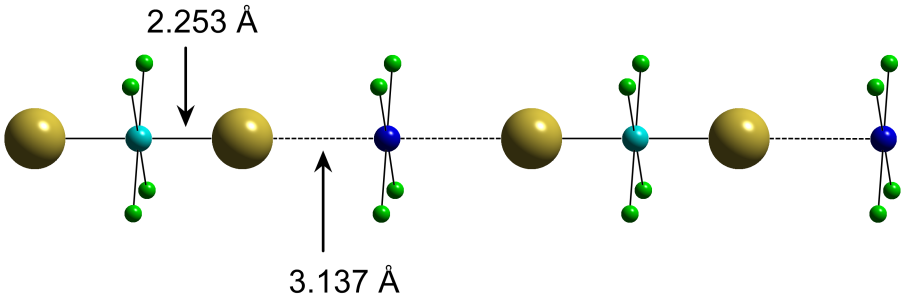

Figure 3.2: Wolfram's Red Salt: $[Pt(C_2H_5NH_2)_4Cl]Cl_2 \cdot H_2O$. Pt^{IV} is shown in cyan, Pt^{II} in dark blue, Cl in mustard, and N in green, with carbons, hydrogens, and the uncoordinated Cl_2 and H_2O omitted for clarity.

d^8 Pd^{II} and octahedral d^6 Pd^{IV} configurations compared to that of d^7 Pd^{III} in either geometry. Most studies of Pd^{III} compounds have involved halides rather than oxides. PdF_3 is an interesting example of a dimer of Pd^{II} and Pd^{IV}[98] in which the average valence state can be stabilised at high pressures.[99]

Platinum has similar atomic and ionic radii to palladium. This is due to the inefficacy of the shielding of the f-shell relative to that of lower-order atomic orbitals. It has largely similar properties to palladium adopting the same geometries in the +2 and +4 oxidation states, and rarely appearing as Pt^{III}. The highest available oxidation state available to platinum is +6, PtF_6 is the last and least stable of the series of third row transition metal hexa-halide salts.

3.1.3 Ternary Palladates

There are several ternary oxides containing lanthanum and palladium which serve to provide further examples of the behaviour of palladium in different coordination environments. Brief details of some palladium compounds are shown in Table 3.1 including Kim's report of $LaPdO_3$. In complex oxides palladium occurs as square-planar coordinated Pd^{II} much more frequently than it does in higher oxidation states. The only exclusively Pd^{IV} oxides known other than those reported in the table are PdO_2, and the pyrochlore system $R_2Pd_2O_7$ for R = Gd, Dy, Er, Tb, Sc, Y.[100] It is interesting to note that with the exception of the alkali metal oxides *e.g.* Na_2PdO_3, materials with palladium in higher oxidation states than +2 all require synthesis conditions with high oxygen pressures. Of these 'high-pressure' materials $LaPd_2O_4$ was synthesised under relatively mild conditions[101] resulting in palladium with a nominal oxidation state of +2.5. This is a mixed-valence, metallic material. The series has been synthesised up to

Table 3.1: Ternary palladium compounds with details of the palladium oxidation state, geometry and bond distances. Na_2PdO_3 also exists for K and Rb. Ca_4PdO_6 also exists for Sr. The 'Geometry' refers to the local geometry of Pd, S.P. is square-planar, Tet. tetrahedral and Oct. octahedral.

Compound	Pd Ox.	Geometry	Pd—O (Å)	Synth. pressure	Ref.
La_4PdO_7	+2	S.P.	(x2) 2.0131(1) (x2) 2.060(9)	Ambient	[104]
$La_2Pd_2O_5$	+2	S.P.	(x2) 2.05(2) (x2) 2.07(2)	Ambient	[104]
La_2PdO_4	+2	S.P.	(x4) 2.028	Ambient	[105]
$LaPd_2O_4$	+2.5	S.P.	(x2) 2.001(4) (x2) 2.009(3)	2.5 GPa	[101]
Na_2PdO_3	+4	Oct.	(x1) 1.993(10) (x1) 2.033(10) (x1) 1.979(9) (x1) 2.041(14) (x1) 2.024(13) (x1) 2.082(15)	Ambient	[106]
Zn_2PdO_4	+4	Tet.	(x4) 1.842	6 GPa	[107]
Ca_4PdO_6	+4	Oct.	(x6) 2.08(1)	10 GPa	[108]
$LaPdO_3$	+3	Oct.	(x2) 2.087(7) (x2) 2.12(2) (x2) 2.04(2)	5 GPa	[88]

$LuPd_2O_4$, and trends include increased conductivity across the group as the rare earth elements decrease in size and the palladium ions move closer together.[102, 103]

As expected, Pd^{IV}-containing octahedra do not exhibit any obvious tetragonal distortions; the $t_{2g}^6\ e_g^0$ configuration is not Jahn-Teller active. In contrast, the most commonly studied Pd^{III} compounds *e.g.* A_2BPdF_6 (A and B = alkali metals) undergo strong Jahn-Teller distortions stabilising the $t_{2g}^6\ e_g^1$ configuration.[109] Previous work on $LaPdO_3$ has indicated that it contains Pd^{III} but is not Jahn-Teller distorted, the nearly isotropic nature of the palladium octahedra is consistent with a $t_{2g}^6\ \sigma^{*1}$ electronic configuration (*i.e.* instead of being localised in a metal e_g orbital, one electron is in a delocalised σ^* band).[110] It has not included low-temperature structural studies and

attempts at synthesising heavier rare earth containing analogues of the perovskite were unsuccessful. The synthesis of these materials is desirable to further investigate the behaviour and properties of trivalent palladium.

3.2 Synthesis

$R\mathrm{PdO_3}$ synthesis attempts followed Kim's method[88] by oxidising $R_2\mathrm{Pd_2O_5}$ precursors at high pressure.

To make $R_2\mathrm{Pd_2O_5}$ a stoichiometric ratio of $R_2\mathrm{O_3}$ and PdO was suspended and partly dissolved in concentrated nitric acid, which was then boiled to dryness. The resulting residue was thoroughly ground and pelleted, and heated in an alumina boat-type crucible at a temperature of 1000 °C for two weeks with intermittent re-grinding and PXRD analysis. The product, a brick-red powder, was made up of $R_2\mathrm{Pd_2O_5}$ and small impurities of palladium metal. Reactions were typically carried out in batches of ∼300 mg of material.

For high-pressure reactions the $R_2\mathrm{Pd_2O_5}$ precursor was mixed with $\mathrm{KClO_3}$ in a 1:1 molar ratio. The mixture was packed into a gold capsule: attempts with unlined boron nitride capsules led to difficulties in recovering the sample, which reacted with the BN capsule, the BN did not seal the sample as required for $\mathrm{KClO_3}$ to produce a high oxygen pressure. Consequently when oxidising samples the BN capsule was lined with 0.1 mm gold foil to produce an effective gold capsule. The reactants were subjected to temperatures of 1000–1100 °C for 20 minutes at pressures ranging from 6–10 GPa using the Walker module in Edinburgh and DIA-type presses in Kyoto. The high pressures were applied over 3 hours, held constant for the duration of the reaction, and removed over 9 hours. Specific details are given in the results section. The syntheses produced black, sintered cylinders comprised of polycrystalline R-Pd-O and KCl products. KCl removal from some samples was achieved by grinding the products to a powder, then sonicating in distilled water. The solution was poured off and the process repeated to wash the samples thoroughly.

3.3 Results

3.3.1 $R\mathrm{PdO_3}$ phases

Precursors $R_2\mathrm{Pd_2O_5}$ were synthesised for the first half of the rare earth series and characterised by PXRD. PXRD patterns of $R_2\mathrm{Pd_2O_5}$ with R = La, Pr, Nd, and Sm

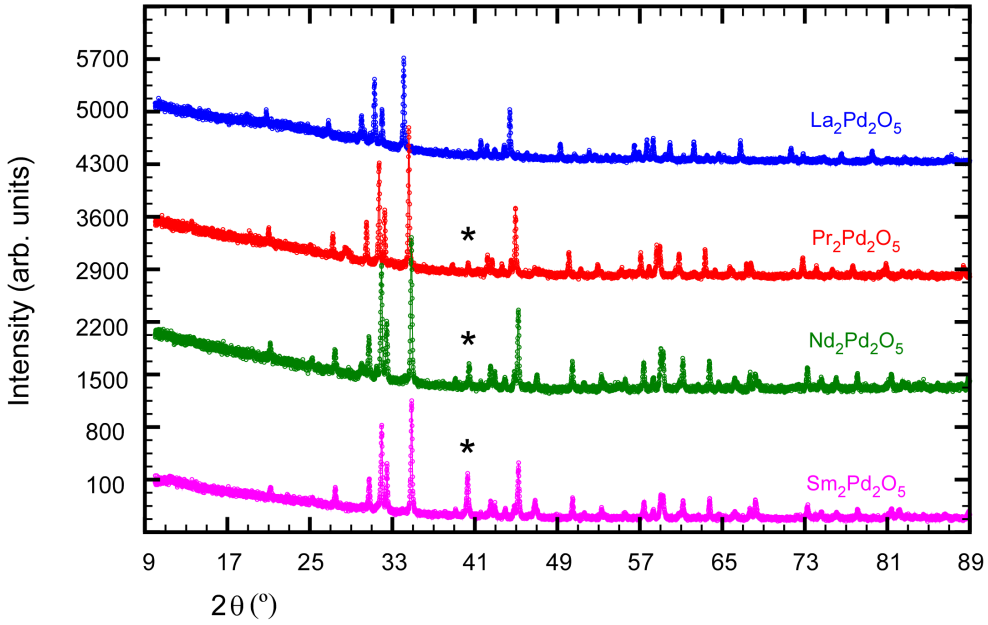

Figure 3.3: PXRD patterns of $R_2Pd_2O_5$. The main impurity was a small amount of palladium metal which is marked with an asterisk.

are shown in Figure 3.3. Attempts at the synthesis of RPdO$_3$ with R = La, Pr and Nd with pressures of 6–10 GPa succeeded for LaPdO$_3$ but failed for other R analogues, resulting in multi-phase samples. Further results for LaPdO$_3$ are reported in the following sections. Successful syntheses were carried out at 6, 8 and 10 GPa with the temperature held at 1100 °C for 20 minutes. The structure of LaPdO$_3$ was analysed by Laboratory PXRD, Rietveld refinements of the data were performed using the GSAS suite of programs with the EXPGUI interface.[111] The data were fitted to the *GdFeO$_3$*-type perovskite structure, space group *Pbnm*, as was reported for the nickelates. A fitted pattern of combined synthesis runs is shown in Figure 3.4. The removal of KCl by washing with distilled water is illustrated in Figure 3.5. Rietveld refinements gave the statistics $R_{wp} = 5.27\,\%$, and $\chi^2 = 3.03$. The unit cell parameters were $a = 5.5856(2)$ Å, $b = 5.8270(2)$ Å, and $c = 7.8720(2)$ Å. Atom positions are given in Table 3.2 and bond details in Table 3.3.

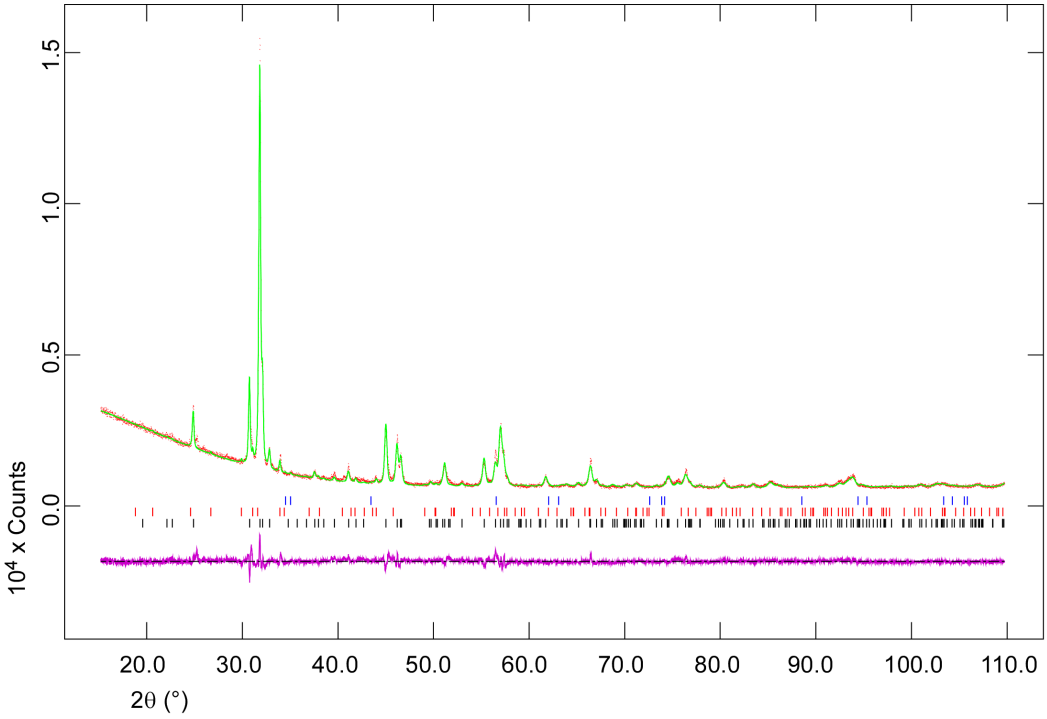

Figure 3.4: PXRD pattern of $LaPdO_3$. The experimental data are red points, the generated model is the green line and the purple line is the difference between them. The main phase is denoted by the black tick marks with minor impurities of the starting material $La_2Pd_2O_5$ (4.6(2) % by mass) and a high pressure phase of PdO (0.37(8) % by mass) given by the red and blue tick marks respectively.

Table 3.2: Atom positions for $LaPdO_3$ from room-temperature PXRD. Thermal parameters are isotropic and were constrained to be identical for the two oxygen atoms.

Atom	x	y	z	U (Å^2)
La	0.9880(7)	0.0597(3)	$\frac{1}{4}$	0.0253(7)
Pd	$\frac{1}{2}$	0	0	0.0203(8)
O1	0.144(3)	0.447(3)	$\frac{1}{4}$	0.003(3)
O2	0.718(3)	0.304(2)	0.048(2)	0.003(3)

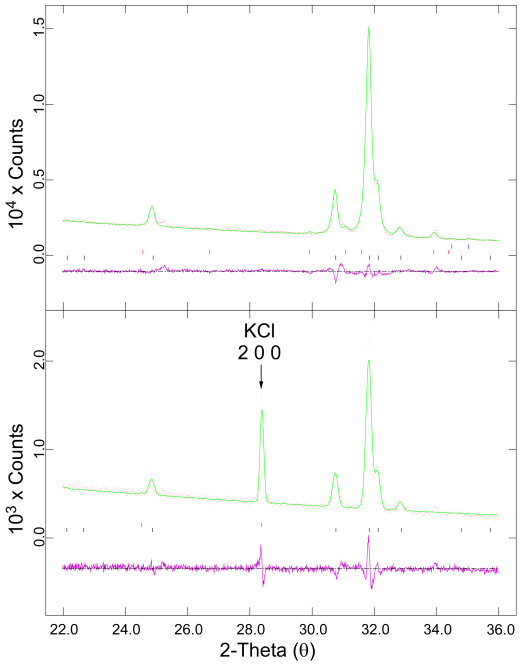

Figure 3.5: KCl comparison. The lower and upper panels show sections of PXRD diffraction patterns of $LaPdO_3$ samples before and after washing with distilled water respectively. The samples were ground and sonicated in several washes of distilled water before being dried for several hours at 60 °C. The upper panel shows a combination of several samples (it is from the same pattern as shown in Figure 3.4), the lower panel shows a sample from one individual synthesis run. Note the disappearance of the KCl (2 0 0) reflection, the most prominent KCl reflection, indicating the removal of the KCl from the sample.

Table 3.3: Bond details and angles for $LaPdO_3$ from room-temperature PXRD. Different values between equivalent atoms are distinguished by superscript numerals *e.g.* Pd—$O2^{i}$ and Pd—$O2^{ii}$ which are orthogonal bonds in the PdO_6 octahedra.

Bond Lengths	(Å)	Bond Angles	(°)
La—O1	2.42(2)	Pd–O1–Pd	132.7(8)
La—O1	2.16(2)	Pd–O2–Pd	151.4(6)
La—O2 (x2)	2.62(1)		
La—O2 (x2)	2.46(1)	O1–Pd–$O2^{i}$	99.7(5)
La—O2 (x2)	2.79(1)	O1–Pd–$O2^{ii}$	92.4(6)
		O1–Pd–$O2^{iii}$	80.3(5)
Pd—O1 (x2)	2.148(7)	O1–Pd–$O2^{iv}$	87.6(7)
Pd—$O2^{i}$ (x2)	2.18(1)	O2–Pd–$O2^{i}$	89.5(2)
Pd—$O2^{ii}$ (x2)	1.98(1)	O2–Pd–$O2^{ii}$	90.5(2)

Praseodymium samples synthesised at pressures of 5.5, 6, 8 and 10 GPa and temperatures of 800, 1000, and 1100 °C (all with heating times of 20 minutes) contained a mixture of $PrPd_2O_4$ and PrO_2 as well as KCl. A Rietveld fit of a praseodymium attempt at 8 GPa is shown in Figure 3.6.

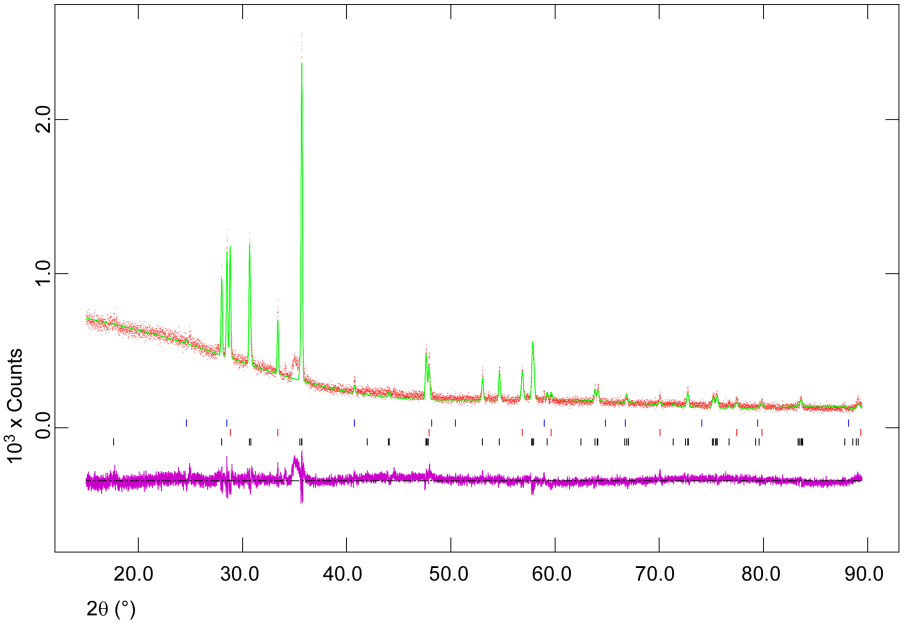

Figure 3.6: Rietveld fit of a high-pressure Pr-Pd-O sample. The data are fitted by a model of $PrPd_2O_4$ (lower tickmarks), PrO_2, and KCl (upper tickmarks).

Synthesis attempts with Nd at 8, 10, and 12 GPa and 1100 °C with the temperature held for 20 minutes resulted in samples containing $NdPd_2O_4$ and other mixed phases. The parameter most effective on the composition of the products was the cooling time. All samples contained a majority of $NdPd_2O_4$ but those which were quenched to room temperature showed Bragg reflections in the region expected for a perovskite structure. A comparison of quenched and 'slow cooled' samples (*i.e.* samples cooled in 10 min), and the $LaPdO_3$ perovskite PXRD patterns is shown in Figure 3.7. The multi-phase nature of the sample makes structural refinement difficult, however approximate unit cell parameters may be obtained. A Rietveld refinement of region of interest of the quenched sample is shown in Figure 3.8, The $NdPdO_3$ perovskite structure fitted to the data has unit cell parameters which are given in Table 3.4 with the $LaPdO_3$ unit cell parameters for comparison.

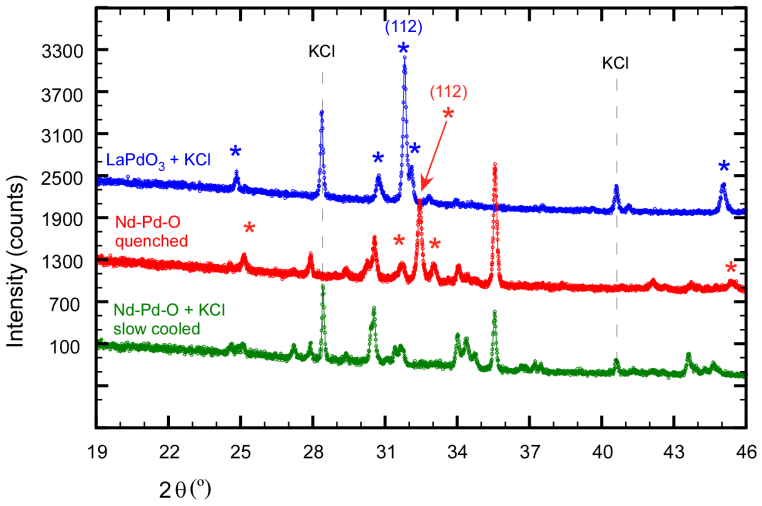

Figure 3.7: Comparison of high-pressure Nd-Pd-O samples and $LaPdO_3$. The 'quenched' Nd-Pd-O sample (middle pattern) has had KCl removed by sonicating in distilled water.

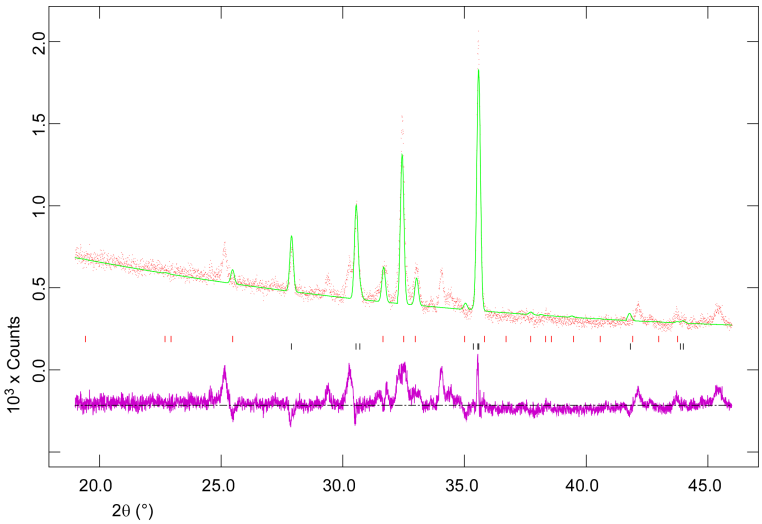

Figure 3.8: Rietveld fit of a quenched high-pressure Nd-Pd-O sample. The data are fitted by a model of $NdPd_2O_4$ (lower tickmarks), and $NdPdO_3$ (upper tickmarks), the structure of which has been assumed to be a simple expansion of the orthorhombic $LaPdO_3$ structure.

Table 3.4: $LaPdO_3$ and $NdPdO_3$ unit cell comparison

	a (Å)	b (Å)	c (Å)	V (Å^3)
$LaPdO_3$	5.5856(2)	5.8270(2)	7.8720(2)	256.210(9)
$NdPdO_3$	5.6375(4)	5.4141(6)	7.7679(6)	237.10(3)

3.3.2 $LaPdO_3$ physical property measurements

3.3.2.1 Magnetic measurements

Magnetisation measurements were made using a Quantum Design PPMS. The results of DC susceptibility measurements are shown in Figure 3.9. The measurements were carried out on 140 mg of $LaPdO_3$ powder. The data show paramagnetic behaviour and can be fitted to Equation 3.1.[110, 112]

$$\chi_m = \chi_0 - aT^2 + C/T \tag{3.1}$$

The fit gives values of $\chi_0 = 0.6 \times 10^{-4}$ emu mol^{-1} and $a = 0.93 \times 10^{-10}$ emu K^{-2} mol^{-1}. These terms represent Pauli paramagnetic susceptibility and its (small) temperature dependence respectively. $C = 1.3 \times 10^{-3}$ emu K mol^{-1} and represents a Curie component which can be attributed to impurities, its magnitude is equivalent to that of 0.3 % spin $\frac{1}{2}$ impurity. The values are similar to those reported in by Kim *et al.*[110]

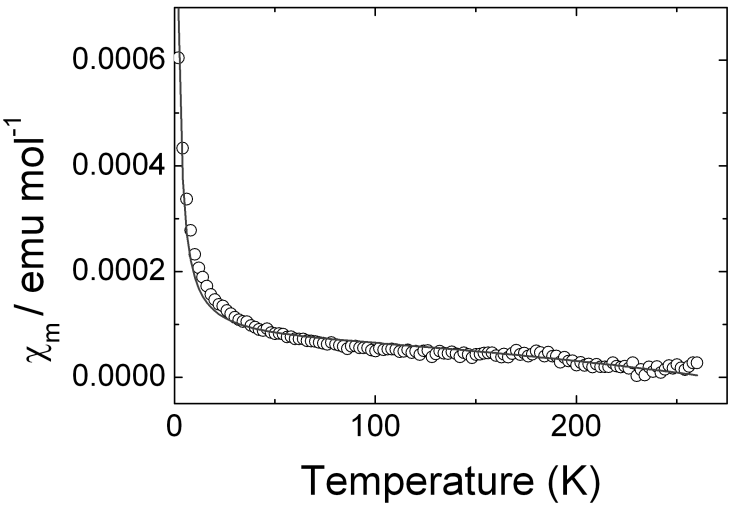

Figure 3.9: The molar magnetic susceptibility of $LaPdO_3$ taken at 10 kOe (open circles). The data are fitted by Equation 3.1 (black line).

3.3.2.2 Resistivity measurements

Resistivity measurements were carried out using the standard four probe method on a 30 mg sintered block of $LaPdO_3$ using a Quantum Design PPMS without magnetic field and at 10 kOe. The sample was taken directly from a synthesis run and as such still contained KCl. The results are shown in Figure 3.10.

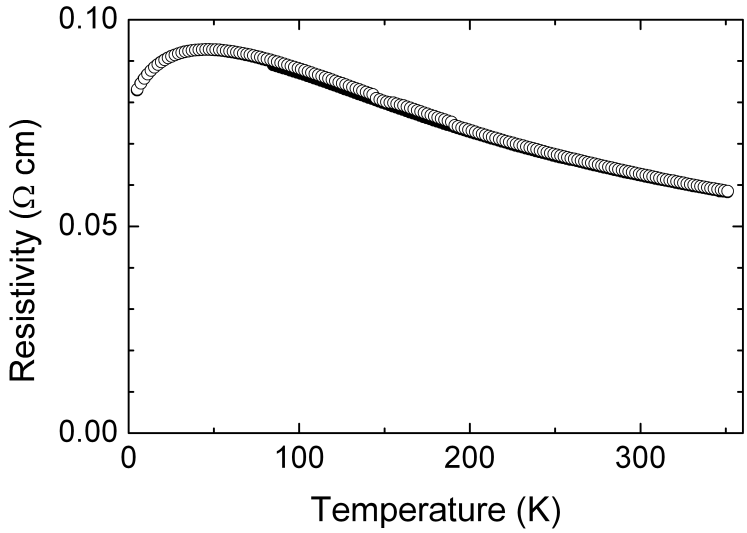

Figure 3.10: Resistivity of $LaPdO_3$ + KCl sample vs. temperature. Measurements without field are closed circles, open circles indicate measurements taken at 10 kOe.

The data indicate a smooth curve with no sharp jumps in resistivity, the material is metallic. Since the KCl in the sample is insulating, it should not qualitatively effect the data. A small increase of resistivity with temperature is seen at low temperatures follow by a negative temperature dependency of the resistivity throughout the rest of the temperature range. This behaviour is typical of resistivity measurements on solid oxide samples made up of grains of metallic material separated by insulating grain boundaries, which are responsible for the negative temperature dependence of the resistivity. A transition from metallic to insulating properties is not observed, indicative of a lack of charge ordering transition in the temperature range measured. The resistivities in zero and applied field are very similar so the sample is not appreciably magnetoresistive.

3.3.3 Variable-temperature neutron diffraction study

Powder neutron diffraction (PND) measurements were carried out on $LaPdO_3$ using the time-of-flight instrument GEM at ISIS. The sample was approximately 500 mg in mass made from combining the washed products of seven high-pressure runs in Kyoto and three in Edinburgh. Data were recorded at 14 temperatures between 7 and 263 K. Rietveld refinements were performed using GSAS, backgrounds were fitted using shifted Chebyschev polynomials and peak shapes modelled with pseudo-Voigt functions. A typical fit of all 6 banks is shown in Figure 3.11. Zero points for each bank and phase fractions were set to be equal for each of the temperature runs. The *Pbnm* $LaPdO_3$ structure fitted the data to the lowest temperatures, there was no evidence of any structural distortion in the temperature range measured. The impurities were significantly more abundant than found by PXRD, they were $La_2Pd_2O_5$ (16(2) % by mass) and PdO (8.2(3) %). Refinement parameters and unit cell dimensions for $LaPdO_3$ are given in Table 3.5. The variation of a, b, and c with temperature is shown in Figure 3.12. Selected bond distances and angles are given in Table 3.6 and atom positions are given in Table 3.7 at high and low temperatures. A comparison of the crystal structure information from PND and PXRD is given in Table 3.8.

Table 3.5: Refinement and structural details for $LaPdO_3$ from PND data.

Temp (K)	Charge (μAh)	R_{wp} (%)	χ^2	a (Å)	b (Å)	c (Å)
7	360	7.1	8.4	5.5836(2)	5.8293(2)	7.8631(3)
22	180	7.5	4.9	5.5838(2)	5.8293(2)	7.8631(3)
41	180	7.5	5.0	5.5839(2)	5.8291(2)	7.8632(3)
62	180	7.4	4.8	5.5844(2)	5.8283(2)	7.8644(3)
82	180	7.5	4.9	5.5852(2)	5.8275(2)	7.8654(3)
103	180	7.3	4.7	5.5861(2)	5.8261(2)	7.8672(3)
123	180	7.4	4.8	5.5867(2)	5.8250(2)	7.8691(3)
143	180	7.5	4.9	5.5877(2)	5.8240(2)	7.8711(3)
163	180	7.4	4.9	5.5886(2)	5.8226(2)	7.8739(3)
183	180	7.4	4.9	5.5896(2)	5.8215(2)	7.8761(3)
204	180	7.5	5.0	5.5907(2)	5.8201(2)	7.8784(3)
224	180	7.4	5.0	5.5915(2)	5.8193(2)	7.8806(3)
243	180	7.5	5.1	5.5925(2)	5.8180(2)	7.8826(3)
263	130	7.8	4.0	5.5939(3)	5.8168(3)	7.8851(4)

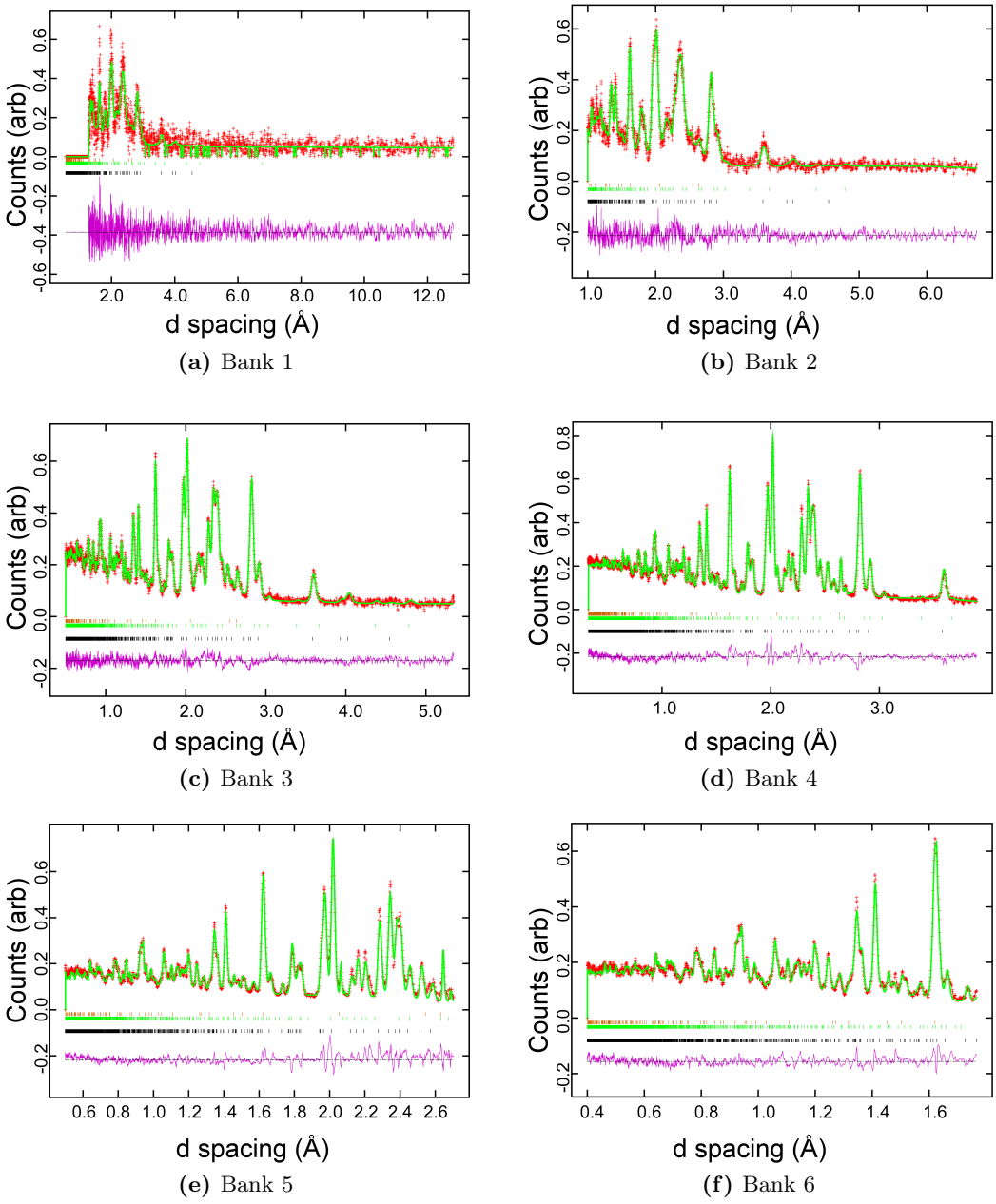

(a) Bank 1 **(b)** Bank 2

(c) Bank 3 **(d)** Bank 4

(e) Bank 5 **(f)** Bank 6

Figure 3.11: Rietveld refinements of all six banks of the GEM diffractometer at ISIS. Bank 1 is situated at the lowest angle and consequently deals with the longest *d*-spacing. Bank 6 which is at the highest angle and deals with short d-spacings. The tickmarks represent, from bottom to top, $LaPdO_3$ (75.58(4) % by mass), $La_2Pd_2O_5$ (16(2) %) and PdO (8.2(3) %).

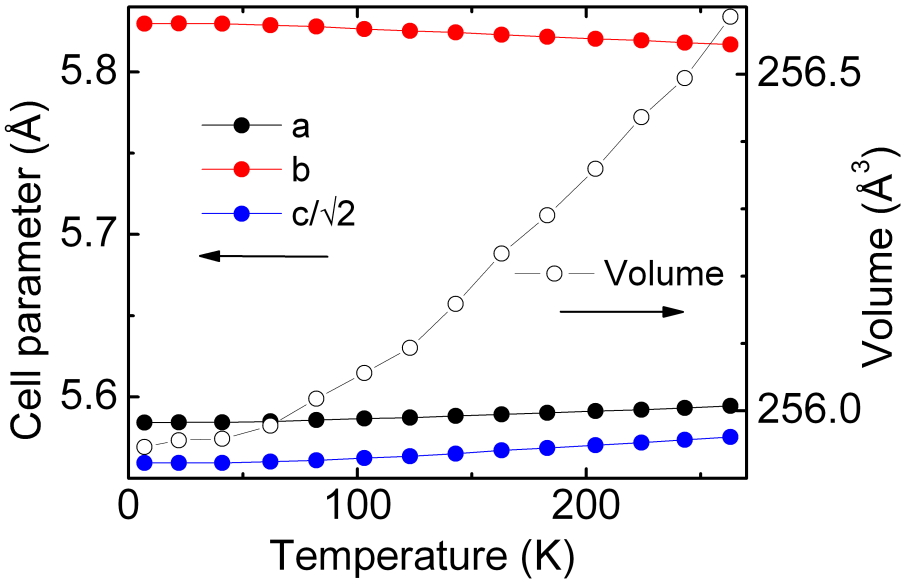

Figure 3.12: Variation of unit cell parameters with temperature of $LaPdO_3$.

Table 3.6: Bond details for $LaPdO_3$ at 7 K (top) and 263 K (bottom) from PND data.

Bond Lengths	(Å)	Bond Angles	(°)
La—O1	2.488(1)	Pd–O1–Pd	148.80(7)
La—O1	2.413(2)	Pd–O2–Pd	150.37(5)
La—O2 (x2)	2.649(1)		
La—O2 (x2)	2.442(1)	O1–Pd–O2^{i}	92.03(5)
La—O2 (x2)	2.747(1)	O1–Pd–O2^{ii}	89.95(5)
		O1–Pd–O2^{iii}	87.97(5)
Pd—O1 (x2)	2.0407(4)	O1–Pd–O2^{iv}	90.05(5)
Pd—O2^{i} (x2)	2.0895(9)	O2–Pd–O2^{i}	89.32(1)
Pd—O2^{ii} (x2)	2.0857(9)	O2–Pd–O2^{ii}	90.69(1)
La—O1	2.486(2)	Pd–O1–Pd	148.96(9)
La—O1	2.420(2)	Pd–O2–Pd	150.72(6)
La—O2 (x2)	2.653(1)		
La—O2 (x2)	2.446(1)	O1–Pd–O2^{i}	92.16(5)
La—O2 (x2)	2.756(1)	O1–Pd–O2^{ii}	89.82(6)
		O1–Pd–O2^{iii}	87.84(5)
Pd—O1 (x2)	2.0458(4)	O1–Pd–O2^{iv}	90.18(6)
Pd—O2^{i} (x2)	2.085(1)	O2–Pd–O2^{i}	89.50(2)
Pd—O2^{ii} (x2)	2.085(1)	O2–Pd–O2^{ii}	90.50(2)

Table 3.7: Atom positions for $LaPdO_3$ at 7 K (top) and 263 K (bottom) from PND data.

Atom	x	y	z	U (Å^2)
La	0.9833(2)	0.0599(1)	$\frac{1}{4}$	0.000 73(4)
Pd	$\frac{1}{2}$	0	0	0.000 73(4)
O1	0.0943(2)	0.473 29(2)	$\frac{1}{4}$	0.000 73(4)
O2	0.6991(2)	0.2972(2)	0.0456(1)	0.000 73(4)
La	0.9832(2)	0.0584(2)	$\frac{1}{4}$	0.001 92(7)
Pd	$\frac{1}{2}$	0	0	0.001 92(7)
O1	0.0935(3)	0.4723(2)	$\frac{1}{4}$	0.001 92(7)
O2	0.6999(2)	0.2963(2)	0.0451(1)	0.001 92(7)

Table 3.8: Comparison of $LaPdO_3$ refinement results. The material adopts the orthorhombic *$GdFeO_3$*-type perovskite structure, space group *Pbnm*. Further structural details can be found in earlier tables.

Instrument	D8 (x-ray)	GEM (neutron)	GEM (neutron)
T(K)	298	7	263
Scan time (h)	15	–	–
Charge (µh)	–	360	130
R_{wp} (%)	5.3	7.1	7.8
χ^2	3.0	8.4	4.0
$LaPdO_3$ (%)	95.07(2)	75.58(4)	75.58(4)
$La_2Pd_2O_5$ (%)	4.6(2)	16(2)	16(2)
PdO (%)	0.37(8)	8.2(3)	8.2(3)
a (Å)	5.5856(2)	5.5836(2)	5.5939(3)
b (Å)	5.8270(2)	5.8293(2)	5.8168(3)
c (Å^3)	7.8720(2)	7.8631(3)	7.8851(4)

3.4 Discussion

Syntheses were successful for $LaPdO_3$ but not for further members of the series. The ability of praseodymium to adopt a +4 oxidation state makes the stabilisation of trivalent Pd in the perovskite structure difficult and the Pr-Pd-O high-pressure products were all dominated by PrO_2 and $PrPd_2O_4$ suggesting that this synthesis method is unlikely to be effective in stabilising the $PrPdO_3$ perovskite. Neodymium is more reliably trivalent than praseodymium so may be expected to be more likely to be able to stabilise the Pd^{III} ion in a perovskite structure. An attempt was made to fit a perovskite model structure to the Nd-Pd-O PXRD data (Figure 3.8), the resulting unit cell parameters are compared to those of $LaPdO_3$ in Table 3.4. The difference in unit cell volume is much larger than expected for a simple substitution of neodymium for lanthanum.

The lack of discontinuities in the changes of resistivity and unit cell parameter with temperature suggest there is no transition between room and low temperatures in $LaPdO_3$, this is confirmed by PND measurements to which a *Pbnm* orthorhombic structure could be fitted throughout the temperature range. The unit cell undergoes simple thermal expansion from low to high temperatures, There is a small convergence of a and b but it is not large enough to predict a phase transition to a tetragonal perovskite at reasonable temperatures. The magnetisation and resistivity measurements are consistent with trivalent palladium ions adopting a $t_{2g}^6\ \sigma^{*1}$ configuration. Neutron diffraction data resolve oxygen positions with greater precision than PXRD and give a good model of the palladium local environments. The structure is shown in Figure 3.13.

The PdO_6 octahedra merit examination: They are oriented with the oxygens labelled O2 arranged approximately in the ab plane and chains of O1–Pd–O1 in the c direction. The Pd–O2–Pd chains in the ab plane are made of alternating pairs of $Pd–O2^{i}$ and $Pd–O2^{ii}$ bonds. A tetragonal distortion is evident – the Pd–O1 bonds are roughly 2.5 % shorter than the two sets of Pd–O2 bonds as shown in Figure 3.14. This is contrary to PXRD data which indicate a shortening in one of the pairs of Pd–O2 bonds, which is probably unreliable due to the low degree of accuracy of the oxygen positions from this method. The delocalisation of the e_g electron into a σ^* conduction band causes the tetragonal distortion to be small in magnitude. The shortening of the Pd–O1 (apical) bonds suggests, from a localised orbital point of view, the stabilisation of the $d_{x^2-y^2}$ orbital. The conduction band is formed from this orbital mixing with the oxygen p orbitals, hence the electric transport is likely to have a two-dimensional character, with relatively good conductivity in the ab plane compared to that in the c direction.

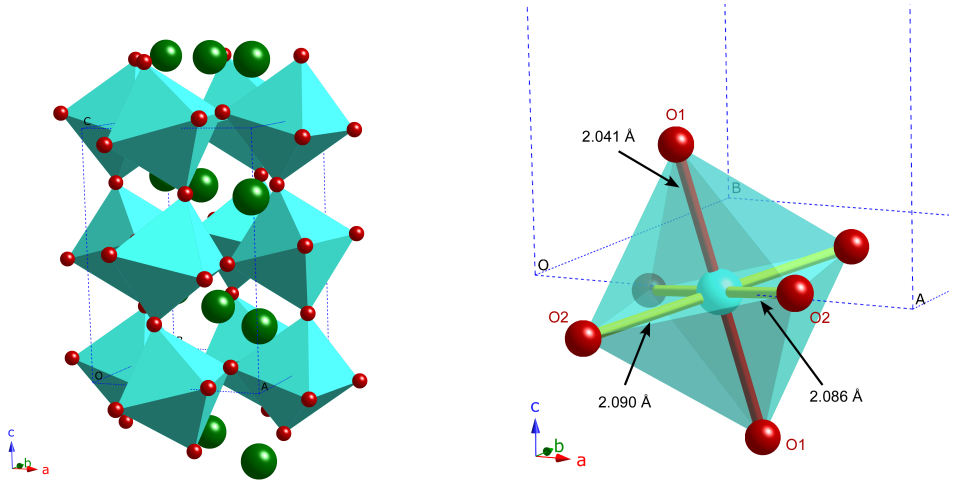

(a) $LaPdO_3$ structure **(b)** PdO_6 octahedron detail

Figure 3.13: The structure of $LaPdO_3$ at 7 K. (a) shows the tilting of PdO_6 octahedra (cyan) and La^{III} ions (dark green) (b) shows a detail of the lowest foreground octahedron in (a), with shorter bonds shown in red and longer bonds in yellow. The unit cell is marked with a blue dashed line.

There is not a significant change in the magnitude of the tetragonal distortion in the temperature range of the measurements.

This orbital ordering in $LaPdO_3$ has not previously been reported. It can be compared to the situation in $M MnO_3$, a perovskite system which is categorised into three distinct types of orthorhombic structure, O, O' and O'', where O is a phase without Jahn-Teller distortion in which (in the $Pbnm$ setting) $a < \frac{c}{\sqrt{2}} < b$ (exhibited by $CaMnO_3$), O' is Jahn-Teller distorted with orbital ordering and $\frac{c}{\sqrt{2}} < a < b$ (as seen in $LaMnO_3$), and O'' is Jahn-Teller distorted but not orbitally ordered with $\frac{c}{\sqrt{2}} < b < a$.[113] The magnitudes of the unit cell parameters of $LaPdO_3$ place it in the O' category, and it is orbitally ordered but the orbital ordering is different from that in $LaMnO_3$. A comparison of the two materials is shown in Figure 3.15. $LaMnO_3$ has a tetragonal elongation with one long and two short pairs of bonds in the MnO_6 octahedra, $LaPdO_3$ has a tetragonal contraction with one short and two long pairs of bonds in the PdO_6 octahedra, and yet the orbital ordering in each case results in the same O'-type orthorhombic structure. The reason for the similarity in the effects of the orbital ordering on the unit cell parameters is the orientation of the octahedra in each case.

In $LaMnO_3$ the unique long pair of bonds in the MnO_6 octahedra lies in the plane of the two short crystallographic axes, alternating with one of the short pairs of bonds in each

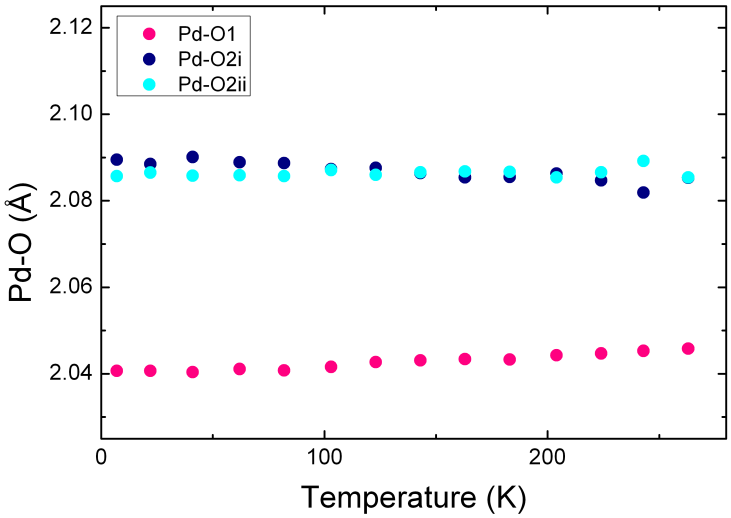

Figure 3.14: Pd—O bond lengths from PND data showing a tetragonal contraction of the PdO_6 octahedra which is approximately constant throughout the temperature range.

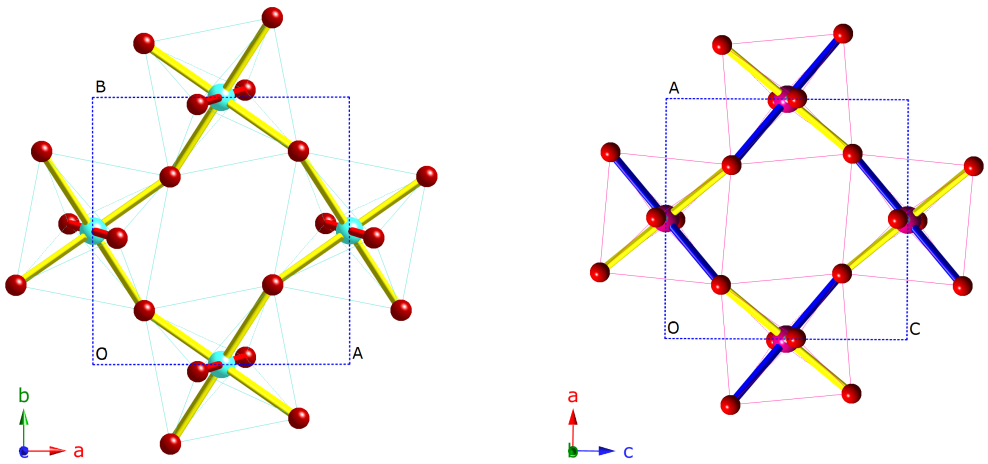

(a) $LaPdO_3$ *ab* plane **(b)** $LaMnO_3$ *ac* plain

Figure 3.15: Comparison of $LaPdO_3$ (a) in which the unique shortened pairs of bonds in the octahedra are in red, and $LaMnO_3$ (b) in which the unique lengthened pairs of bonds in the octahedra are in blue. The unique pair of bonds in each case is the direction of the d_{z^2} orbital of the *B*-site metals. *A*-site metals are omitted and the unit cell axes are given by blue dashed lines.

direction in chains of octahedra in this plane (Figure 3.15b). Thus the bonds in the plane of the short crystallographic axes can viewed as an average of some intermediate bond length between the long and short bonds in the octahedra, while the pairs of bonds in the c axis direction are uniquely short. In $LaPdO_3$ PdO_6 octahedra are oriented with the uniquely short bonds in the direction of the c axis (Figure 3.15a), hence the effect of the orbital ordering in both systems on the relative magnitudes of the unit cell axes is the same, although the d_{z^2} orbitals are oriented differently in both systems.

3.5 Conclusions

$LaPdO_3$ has been synthesised at pressures of 6, 8, and 10 GPa. Magnetisation and resistivity measurements are consistent with palladium adopting the +3 oxidation state. No evidence of charge order has been found. Neutron powder diffraction measurements indicate a small (∼2.5 %)[1] tetragonal contraction of the PdO_6 octahedra which are ordered with their short axes in the c direction. The palladium ions are in a $t_{2g}^6\ \sigma^{*1}$ configuration with the σ^* band formed from oxygen p and palladium $d_{x^2-y^2}$ orbitals. The distortion of palladium octahedra and the delocalisation of the $d_{x^2-y^2}$ electron both remove degeneracy in the e_g orbitals, the phenomena occur separately in other systems: delocalisation in $LaNiO_3$ and Jahn-Teller distortion in $LaMnO_3$. The simultaneous occurrence of both in this system is predicted to lead to two-dimensional electrical conduction. $LaPdO_3$ is an orbitally ordered metallic oxide from room to low temperatures.

No single-phase samples of further members of the $R PdO_3$ series have been successfully synthesised. The ability of Pr to form the +4 oxidation state generates difficulties in high-pressure oxidation syntheses due to a tendency to form PrO_2. Neodymium does not form the +4 oxidation state so remains a promising candidate for the second member of the series. Some of the phase may have been formed at 10 GPa with unit cell parameters $a = 5.6375(4)$ Å, $b = 5.4141(6)$ Å, and $c = 7.7679(6)$ Å. A concerted effort at optimisation of the reaction conditions utilising higher pressures could yield a phase-pure sample. It would be very interesting to see if charge order existed in this material.

[1] This is a small Jahn-Teller effect when compared to *e.g.* a ∼10 % elongation in the unique axis of the MnO_6 octahedra in $LaMnO_3$.

Chapter 4

High-pressure synthesis of new oxypnictide superconductors

4.1 Introduction

The discovery of superconductivity up to 26 K in fluoride-doped LaFeAsO in 2008[114] triggered a flurry of research into oxypnictides. It was the first example of a class of material some members of which would be found to superconduct to temperatures above 50 K, a remarkable property which for more than twenty years had been boasted exclusively by the cuprates. Thus a new group of high-T_c superconductors had been found.

Several families of iron arsenide superconductor have been discovered since. The original family, based on RFeAsO or MFeAsF is referred to as the 1111 family. The other main types are the MFe$_2$As$_2$ (R = Ca, Sr, Ba) 122 family and the AFeAs (A = Li, Na) 111 family. All the materials contain two-dimensional layers of edge-sharing iron arsenide tetrahedra through which the superconductive transport occurs. That the electronically active layer is based on iron, the archetypical magnetic element, is remarkable and the existence of these materials puts an end to the dogma that such elements are unsuitable as candidates for high-T_c superconductors. We have synthesised members of the 1111 family for late rare earth elements R = Tb, Dy, and Ho at high pressures and investigated the implications their properties have for the whole series.

The results which follow were obtained in collaboration with several people. The ambient-pressure precursor synthesis was carried out by Andrea Marcinkova, and help was received with high-pressure synthesis from Jenny Rodgers. Dmitry Sokolov assisted with magnetisation and resistivity measurements, and performed the shape corrections for estimates of diamagnetic fractions. Anna Kusmartseva also helped with resistivity measurements. Any other assistance has been indicated in the results sections.

4.1.1 Families of iron-based superconductor

4.1.1.1 1111

The original family of iron arsenide superconductors is now referred to as the 1111 family. Kamihara *et al.* discovered superconductivity in the quaternary oxypnictides LaFePO ($T_c \approx 5\,K$)[115] and LaNiPO ($T_c \approx 3\,K$)[116].[1] It was their discovery of superconductivity in $LaFeAsO_{0.89}F_{0.11}$ that heralded the birth of the high-T_c iron arsenide field.[114] The materials' structure is tetragonal, space group $P4/nmm$ and consists of tetrahedral iron arsenide layers alternating with ionic rare earth oxide layers (Figure 4.1). The general atom positions are given in Table 4.1.

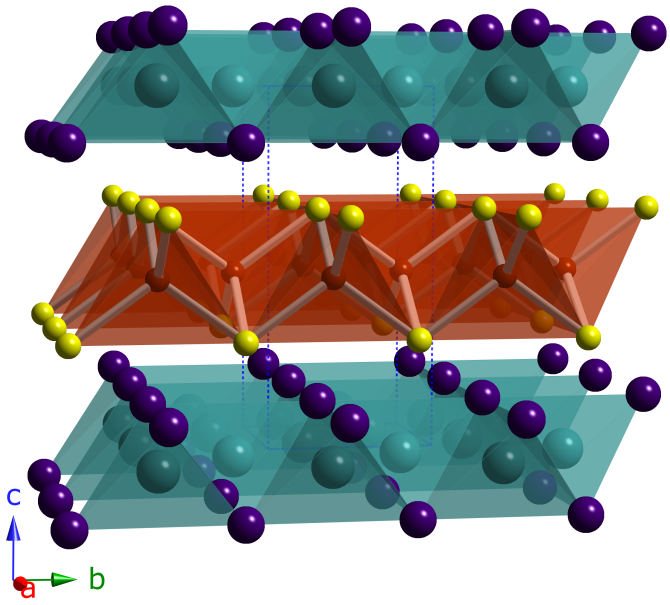

Figure 4.1: The layered structure of LaFeAsO which consists of covalent tetrahedral iron arsenide layers (iron is shown in brown, arsenic in yellow) alternating with ionic LaO layers (lanthanum is in purple, oxygen in blue). The structure is tetragonal, space group $P4/nmm$.

The majority of early reports which followed Kamihara's discovery focused on synthesising other members of the $RFeAsO_{1-x}F_x$ (R = rare earth) series. Within three months of the first report materials with R = Ce,[117] Nd,[118] Pr,[119] Sm[120] and Gd[121] were synthesised with T_c = 41, 52, 52, 55 and 36 K respectively. The amount of

[1] Some analogues of the other families with metals other than iron and/or pnictogens other than arsenic exist but they remain relatively low in T_c compared to the iron arsenides.

Table 4.1: Tetragonal 1111 atom positions

atom	x	y	z
R	1/4	1/4	R:z
Fe	3/4	1/4	1/2
As	1/4	1/4	As:z
O/F	3/4	1/4	0

fluoride doping required to generate the maximum T_c's for these materials was quoted as (nominally) $0.1 \leq x \leq 0.17$. Each fluoride doped onto the oxygen site introduces one extra electron into the tetrahedral layer. Of the first reports $CeFeAsO_{1-x}F_x$ was synthesised at ambient pressure, R = Pr, Nd and Sm-containing materials were synthesised at 6 GPa and $GdFeAsO_{1-x}F_x$ at ambient pressure. More recently R = Pr, Nd and Sm materials have been synthesised at ambient pressure with higher phase purities than in the original reports.[122–124] The undoped parent materials are not superconducting but an alternative to fluoride substitution as a method of electron doping is to leave oxygen vacancies as in the $RFeAsO_{1-\delta}$ materials. This method was first reported by Ren *et al.* for R = La, Ce, Pr, Nd, Sm[125] and Gd,[126] T_c = 31, 47, 51, 54, 55, and 54 K respectively.

A phase diagram of $CeFeAsO_{1-x}F_x$ is shown in Figure 4.2 which can be taken as representative of the phase diagrams of other early R containing 1111 materials. On cooling the undoped parent material transforms from tetragonal to orthorhombic (space group $Cmma$) at T_s then at a lower temperature, T_N(Fe), a spin density wave (SDW) emerges - the irons become magnetically ordered. At very low temperatures (~4 K) the ceriums also become magnetically ordered (T_N(Ce)). As electron doping is increased (either by fluoride doping or oxygen deficiency) the structural transition and iron magnetic ordering is suppressed, T_s and T_N (Fe) decrease. At some doping level the SDW is destroyed and superconductivity emerges, typically at around x (or δ) = 0.05. The orthorhombic structural transition persists into a low-doped portion of the superconducting region but is also destroyed by doping above $x \approx 0.1$.[128] T_c reaches a maximum and levels off at around $x = 0.1$ or $\delta = 0.15$, with overdoped samples inaccessible thus far. Values for δ can be refined by powder neutron diffraction but it is very difficult to determine x experimentally,[2] and usually values quoted are nominal only *i.e.* the composition of the starting materials is assumed to be the composition of the product.

[2] Fluoride content cannot be measured by PXRD as F^- is isoelectronic with O^{2-} and unfortunately the two elements have very similar neutron scattering lengths (^{16}O = 4.232 b and ^{19}F = 4.017 b) making distinction by PND difficult.

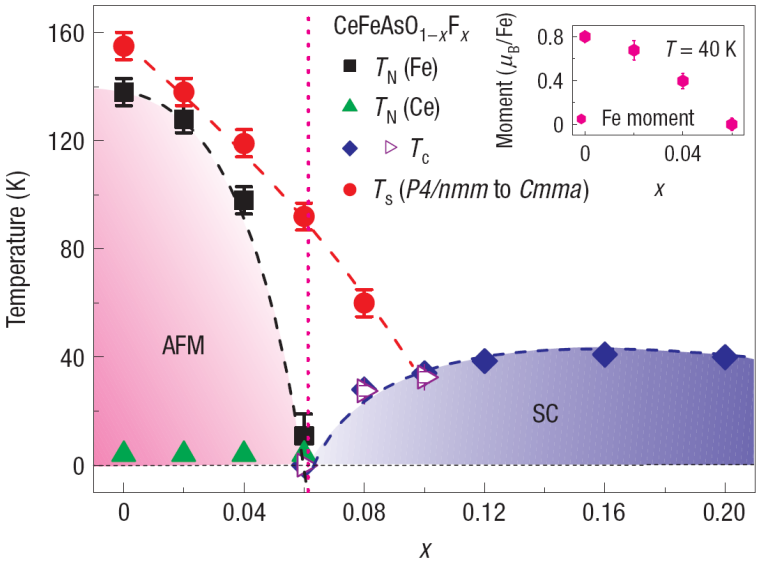

Figure 4.2: Phase diagram of $CeFeAsO_{1-x}F_x$ showing the variation of the Néel temperatures of Ce (T_N(Ce)) and Fe (T_N(Fe)), the tetragonal to orthorhombic transition temperature (T_s) and the superconducting critical temperature (T_c) with x.[127]

An alternative method to electron doping by changing the composition of the insulating ionic layer is to dope directly onto the FeAs layer. The first report was in $LaFe_{1-x}Co_xAsO$[129] which was synthesised at ambient pressure. The introduction of cobalt directly onto the FeAs layer was claimed to be a more effective method of doping but it introduces disorder into the electronically active layer and the maximum T_c in this compound is ∼14 K. Further studies on La and Sm materials suggest the phase diagram is largely similar to that of the fluoride doped 1111 materials, with the SDW being destroyed by doping and superconductivity appearing at $x \approx 0.03$, and T_c reaching a maximum (15.2 K in the samarium compound) at $x \approx 0.1$. In this case overdoped samples can be synthesised, and superconductivity is suppressed above $x \approx 0.2$.[130]

Early studies into hole doping to induce superconductivity in the 1111 oxypnictides are somewhat conflicted. Kamihara's initial report mentioned that doping LaFeAsO with Ca^{2+} (replacing La^{3+}) instead of F^- did not induce superconductivity.[115] Hole doping was then reported to successfully produce superconductivity up to 25 K in $La_{1-x}Sr_xFeAsO$ with symmetric behaviour to the electron doped variants,[131] however this material was later claimed to be oxygen deficient and hence electron doped.[132] It is now accepted that hole doping can induce superconductivity in 1111 oxypnictides, it has been reported in $Nd_{1-x}Sr_xFeAsO$ with a T_c of 13.5 K for $x = 0.2$,[133] and

$Pr_{1-x}Sr_xFeAsO$ which has a maximum T_c of 16.3 K at $x = 0.25$.[134]

An oxygen-free 1111 material isostructural with the oxypnictide 1111 compounds was recently reported to be superconducting: the parent material MFeAsF (isostructural to LaFeAsO) becomes superconducting when Co is doped onto the Fe site in $CaFe_{1-x}Co_xF$ with a T_c of 22 K at $x = 0.1$.[135] An alternative electron-doping method is to replace the divalent metal with a trivalent one as in $Sr_{1-x}La_xFeAsF$, which has a T_c of 29.5 K at $x = 0.4$.[136] These materials are very similar to the 1111 oxypnictides with the same tetragonal to orthorhombic structural transition and SDW formation at lower temperatures. Both transition temperatures decrease with increasing doping. For $CaFe_{1-x}Co_xF$ the orthorhombic structure extends into the superconducting region and there is some evidence for overlapping magnetic order and superconductivity in $CaFe_{0.94}Co_{0.06}F$, mesoscopic phase separation is cited as the explanation.[137] The record for the highest T_c of the iron arsenides is 56 K, and is held jointly by two materials, both from the 1111 family: $Sr_{0.5}Sm_{0.5}FeAsF$, the most recent,[138] and $Gd_{0.8}Th_{0.2}FeAsO$[139]. Both materials use similar methods of electron doping with one metal on the ionic layer being replaced by another with a higher valence *i.e.* Sr^{II} is replaced by Sm^{III} or Gd^{III} is replaced by Th^{IV}. Thorium doping has also been suggested to successfully induce superconductivity in $Tb_{1-x}Th_xFeAsO$[140], but ThO_2 impurities are evident in both the thorium-doped materials and the real source of electron doping could be oxygen deficiency.

4.1.1.2 122

The second family of iron arsenide materials to exhibit superconductivity is the 122 MFe_2As_2 family. $BaFe_2As_2$ was shown to be superconducting in May 2008 with a T_c of 38 K when doped with 40 % potassium on the barium site.[141] Strontium, europium and calcium analogues followed with T_c's of 37, 32, and 26 K respectively.[142–145] Barium, strontium and europium materials were prepared at ambient pressures but inclusion of the smaller calcium ions required syntheses under a pressure of 2 GPa. Undoped materials undergo antiferromagnetic ordering to display SDWs. An example of the materials' room-temperature tetragonal structure is shown in Figure 4.3.

In contrast to the early work on the 1111 family, which centred on electron doping of the negatively charged iron arsenide layer, hole doping was initially used to induce superconductivity in the 122 materials. Doping a monovalent metal, typically an alkaline metal, onto the M^{II} site introduces 0.5 holes to the tetrahedral layer per substitution. This is the mechanism described in the first reports, above. More recently

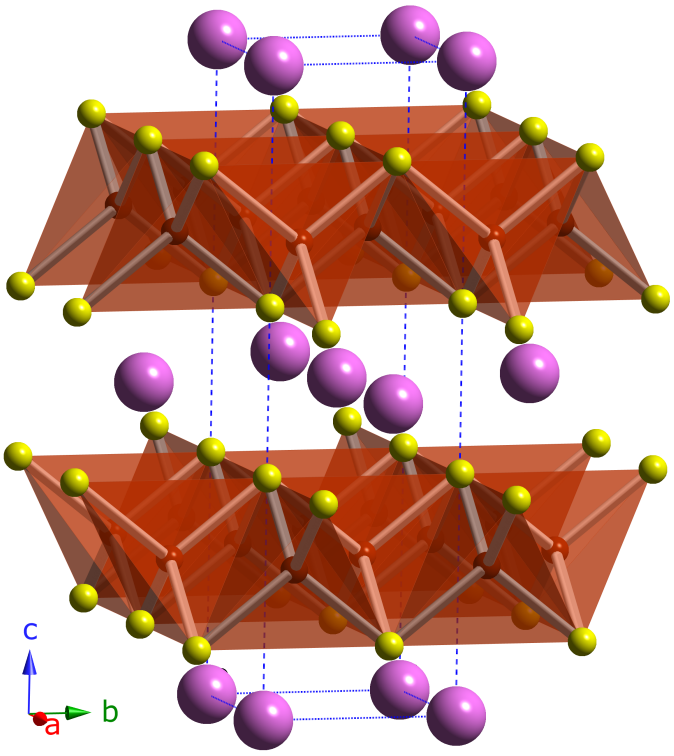

Figure 4.3: The structure of $BaFe_2As_2$. Ba^{II} ions are shown in pink, Fe^{II} in brown and As^{3-} in yellow. The structure is tetragonal occupying the space group $I4/mmm$, it was first reported in 1980.[147]

superconductivity has been induced with electron doping: Fe^{II} is replaced by Co^{III} in the tetrahedral layer *e.g.* in $BaFe_{1.8}Co_{0.2}As_2$ which has a T_c of 22 K.[146]

The undoped parent materials, MFe_2As_2, are not superconductors at ambient pressure but reports of superconductivity at increased pressure have triggered debate: between 0.2 and 0.9 GPa, $CaFe_2As_2$ was reported to have a T_c of 12 K,[148] and $SrFe_2As_2$ and $BaFe_2As_2$ were reported to superconduct up to temperatures of ∼28 K at around 4 GPa.[149] Further reports claim a suppression of magnetism in $SrFe_2As_2$ accompanies the onset of superconductivity at 3.6 GPa with a T_c of 34 K,[150] whereas the $BaFe_2As_2$ material has been reported to maintain a SDW up to 9 GPa and although a drop in resistivity appears at temperatures around 25 K above 3.5 GPa it is not to a state without resistance.[151] Pressure-dependent neutron diffraction measurements on $CaFe_2As_2$ revealed a large anisotropic structural "collapse" in the material (a 10 % decrease in c and small increase in a and b) coincident with the pressure-induced superconductivity.[152] Since the high-pressure resistivity studies reporting

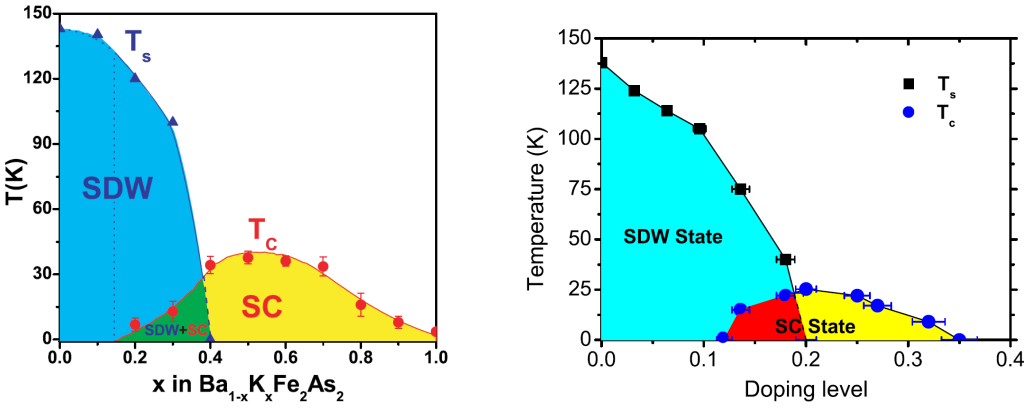

(a) $Ba_{1-x}K_xFe_2As_2$[157] **(b)** $BaFe_{2-x}Co_xAs_2$[158]

Figure 4.4: 122 Phase diagrams. The magnetically ordered (SDW) orthorhombic regions are in blue with superconducting (SC) regions in yellow. The white regions are tetragonal normal-state materials.

superconductivity were made using a single crystal and solid pressure medium the pressure would have been anisotropic in line with the nature of the structural transition. Subsequent studies performed under isotropic pressure did not result in a superconducting state despite the presence of the collapsed phase.[153] The transport properties of the 122 parent materials at high pressures remain contentious.

Two phase diagrams of the 122 material are shown in Figure 4.4. On cooling undoped materials undergo a structural transition from tetragonal $I4/mmm$ (Figure 4.3) to orthorhombic $Fmmm$ at T_s which is accompanied by SDW formation.[154] As the doping increases in both the $Ba_{1-x}K_xFe_2As_2$ and $BaFe_{2-x}Co_xAs_2$ systems this transition is suppressed and T_s decreases in magnitude, however the SDW does appear to persist into the early part of the superconducting region in the phase diagrams of both materials. This coexistence has been clarified by μSR measurements as phase segregation into separate superconducting and magnetic regions in $Ba_{1-x}K_xFe_2As_2$[155] and $CaFe_{2-x}Co_xAs_2$.[156]

The $Ba_{1-x}K_xFe_2As_2$ solid solution can be synthesised for $x = 0$–1 with superconductivity emerging at $x \approx 0.2$, reaching a maximum T_c at $x \approx 0.5$ and diminishing at higher doping levels. The unit cell volume does not change with x, a linear increase in c is compensated by a decrease in a and b, and the Ba–As and Fe–As bond lengths do not change. This structural evolution can be viewed as the layers concertinaring - they become thicker in c but compress in the ab plane as the As–Fe–As tetrahedral angle decreases in magnitude.[159]

The cobalt-doped system can only be synthesised up to $x = 0.6$ but in this case each substitution introduces one electron to the tetrahedral layer (compared to 0.5 holes per substitution in $Ba_{1-x}K_xFe_2As_2$). The phase diagram is superficially similar to that of the hole-doped 122 materials with a transition to a magnetically ordered orthorhombic phase being suppressed by increased doping and a superconducting region emerging, reaching a maximum T_c and then decreasing again as the material becomes overdoped. The unit cell decreases in volume with increasing x, with the c parameter decreasing linearly while a and b remain approximately constant.[160] It has been reported that the structural and magnetic transitions are not coincident as they are in $Ba_{1-x}K_xFe_2As_2$ occurring at similar but distinct temperatures although it was not initially clear what order the transitions are in.[161]

4.1.1.3 111

A third family of superconductors based on LiFeAs is labelled as the 111 family. Three reports appeared within two weeks in September 2008, the first claiming superconductivity up to 18 K in samples of nominal composition $Li_{0.6}FeAs$ synthesised at $\sim$ 1 GPa[162] in which the FeAs layers are doped with one hole per lithium vacancy. In the second report two approximately stoichiometric samples of LiFeAs synthesised at ambient pressure and characterised by powder neutron diffraction were shown to superconduct below 16 and 10 K.[163] The third claims a T_c of 18 K in another ambient-pressure stoichiometric sample.[164] The properties are clearly sensitive to synthetic conditions. The materials occupy the same tetragonal space group as the 1111 family, $P4/nmm$, the structure is show in Figure 4.5. The analogue NaFeAs was first reported to show a small diamagnetic transition below 9 K but is not a bulk superconductor, with a low diamagnetic fraction of $\sim$10 %.[165] Single crystal measurements have indicated T_c's of 23 K in $Na_{1-\delta}FeAs$ and given evidence of a structural transition at 50 K.[166] Both reports give evidence for magnetic ordering in NaFeAs which is not present in LiFeAs. These materials are difficult to synthesise and highly air sensitive, hence they are less well documented than the other families.

4.1.1.4 Iron chalcogenides

The most structurally simple of the iron-based superconductors does not include arsenic, it is based on tetragonal β-FeSe but can be included within the umbrella of the new iron arsenide superconductors due the structural and electronic similarity it shares with them. Superconductivity up to 8 K was reported in $FeSe_{0.88}$.[169] It appears that a surplus of iron is required for superconductivity. The structure, which consists of tetrahedral FeSe layers without any inter-layer atoms, is shown in Figure 4.6. It has

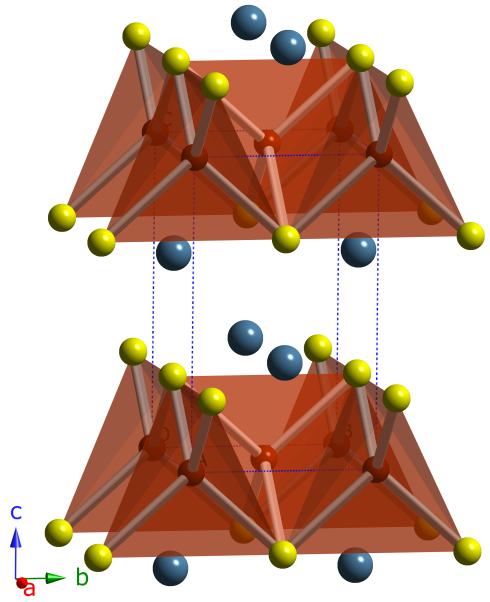

Figure 4.5: The structure of LiFeAs. Li ions are shown in blue, Fe^{II} in brown and As^{3-} in yellow. The structure is tetragonal occupying the space group $P4/nmm$, it was first reported in 1968.[167]

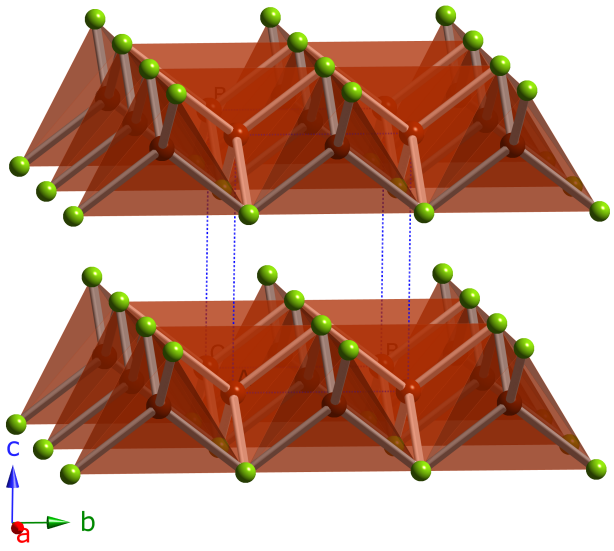

Figure 4.6: The structure of FeSe. Fe^{II} in brown and Se^{2-} in green. The structure is tetragonal occupying the space group $P4/nmm$, it was first reported in 1933.[168]

since been suggested that a surplus of iron results not in selenium vacancies but in interstitial inclusions of iron, *i.e.* $Fe_{1+\delta}Se$, and that there is a strong dependence of T_c on stoichiometry with that closest to 1:1 FeSe resulting in the highest T_c. There is no apparent magnetic order in the material[170] but there is a structural transition to orthorhombic *Cmma* at ∼70 K.[171] Substituting tellurium onto the selenium site enhances superconductivity raising the T_c to above 15 K in $FeSe_{0.5}Te_{0.5}$[172] although FeTe itself does not superconduct. Pressure has a significant effect on the properties of $Fe_{1+\delta}Se$, initially the T_c was shown to increase from 8 K at ambient pressure to 27 K at 1.5 GPa[173]. More recent work has shown T_c increases up to a maximum of 36.7 K at 9 GPa.[174, 175] The FeSe family still attracts a lot of attention due to the simplicity of its structure, affording a good opportunity to study the nature of superconductivity in two-dimensional tetrahedral iron layers.

4.1.2 General properties

The properties of the new iron arsenide superconductors have broad similarities, a general form is shared by the phase diagrams of each of the families: Low-doped materials do not become superconducting, they exhibit a tetragonal to orthorhombic phase transition, followed by magnetic ordering of the irons at lower temperatures. As the doping level increases, *i.e.* the formal charge of FeAs departs from -1, the temperature at which these phenomena occur decreases. Long-range magnetic order is destroyed as superconductivity emerges, the two properties do not appear to coexist except in segregated phases. The orthorhombic transition is fully suppressed by the doping levels required for maximum T_c's. It appears that there are two competing ground states in these materials - superconducting and magnetically ordered. This is, of course, highly reminiscent of the situation in the high-T_c cuprates.[176]

The magnetic structures of the different families have been extensively investigated by powder neutron diffraction. It is easier to synthesise large samples and single crystals of the 122 family than of the other families; they have received the most attention. The iron spin directions are shown in Figure 4.7. The magnetic structures of the 1111 and 122 families are identical in the *ab* plane and the inter-layer ordering (that in the *c* direction) is either ferromagnetic (in the Ce and Pr 1111 materials) or antiferromagnetic (in the La and Nd 1111 materials and the 122 materials). This magnetic structure is forbidden in a tetrahedral setting so $T_N \leq T_s$ for all materials clarifying any confusion in the order of the two transition temperatures in some 122 materials. The magnetism of FeTe is not the same as in the other families, at low temperatures there is a transition from tetragonal to monoclinic symmetry, resulting in two distinct Fe sites. This is

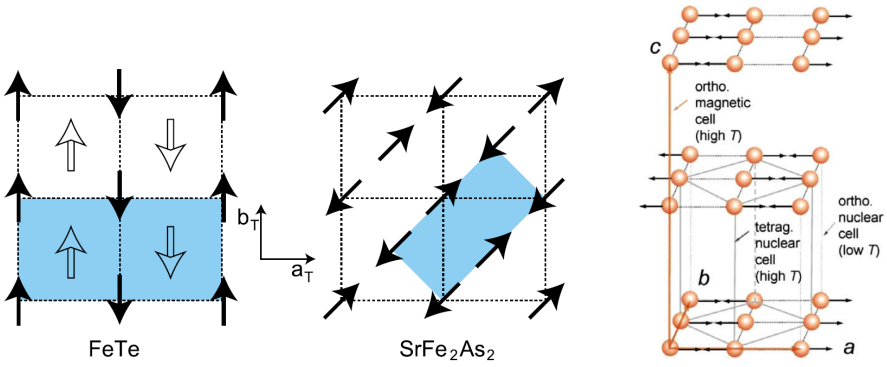

(a) 11 and 122 **(b)** 1111 and 122

Figure 4.7: Iron magnetic structure. The difference between in-plane magnetic structures of iron telluride and the 122/1111 families is shown in (a),[177] and the magnetic structure of, for example, LaFeAsO is shown in (b).[178]

accompanied by magnetic order, shown in Figure 4.7a.[177] The magnetic structures of the irons in these materials are simple and commensurate, although there is some incommensurate order in iron tellurides with excessive iron contents.[179]

The presence of magnetic ions other than Fe in *R*FeAsO is an added complication to the magnetism of these species. The rare earth spins do align at very low temperatures, the magnetic structures of Ce, Nd, and Pr materials have been studied. In underdoped compounds $T_N(Ce) = 4\,K$[127] and $T_N(Nd) = 2\,K$.[180] Pr orders at higher temperatures, up to 14 K.[122, 181] There is no evidence of long-range ordering of the rare earth ions within the superconducting region. The magnetic structure of each of the materials is similar, trios of adjacent rare earth ions are distinguished by spin direction with ferromagnetic intra-trio exchange and antiferromagnetic inter-trio exchange, as shown in Figure 4.8.

Ultimately, the electronic behaviour of these materials depends on their band structure and the occupancy of the bands. Doping has the very obvious effect of changing this occupancy *i.e.* moving the Fermi surface to higher or lower energies. A small change in Fermi energy can lead to a large change in properties if there is a large gradient in the density of states at that energy.

There is a second more subtle effect of doping; as larger or smaller ions are substituted, and electrons or holes included, the physical structure of the materials changes. The band structure is informed by the physical structure and so must be modified accordingly, hence electronic doping by chemical means not only effects the occupancy,

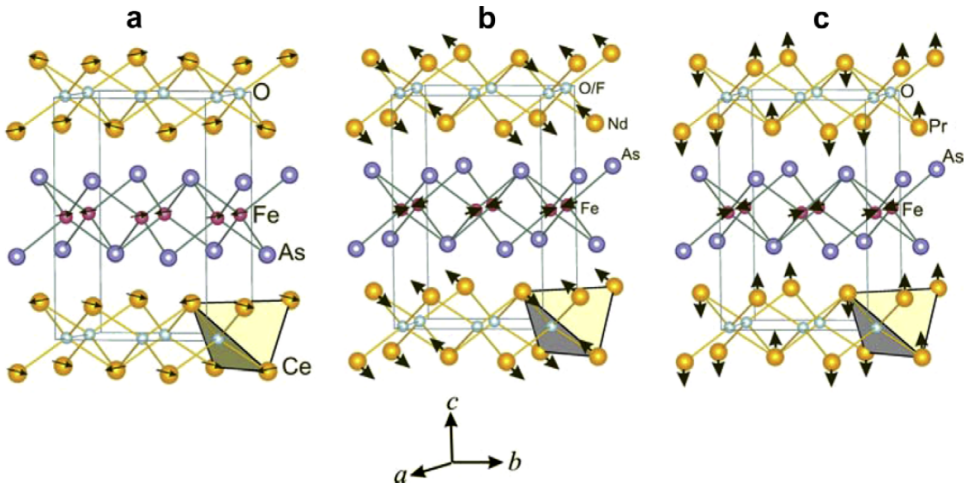

Figure 4.8: Rare earth magnetic ordering in CeFeAsO (a), NdFeAsO (b), and PrFeAsO (c). The iron magnetic structures were assumed to be the same as they are without rare earth ordering.[178]

but also the band structure itself due to these lattice effects. The variation of the band structure due to these lattice effects is evidenced by the different T_c's of different members of any one family with similar electronic doping levels. The maximum T_c's of RFeAsO for different R metals provides a good example; T_c increases for smaller R over the first half of the rare earth series as shown in Figure 4.9.

Unit cell volume is a crude measure of the lattice effect caused by variation in the

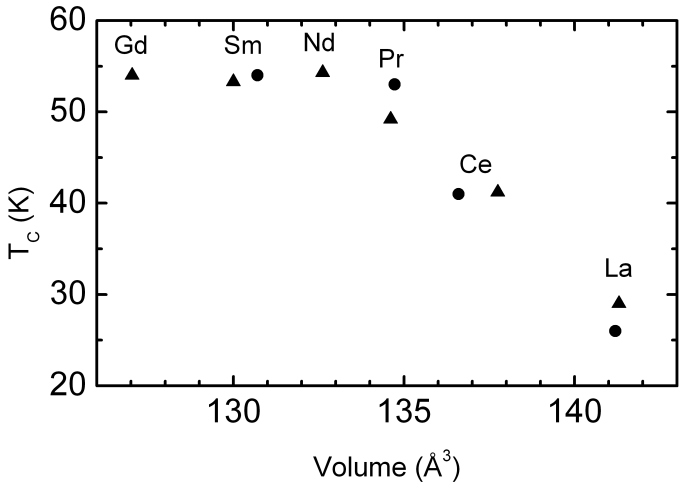

Figure 4.9: Maximum T_c's versus unit cell volume for RFeAsO$_{1-x}$F$_x$ (circles) and RFeAsO$_{1-\delta}$ (triangles). R is labelled on the figure.

rare earth metal radii and the lattice effect is responsible for the increase in T_c across the series. The doping levels of the materials with maximum T_c's are similar, yet T_c doubles from La to Sm. The same effect can be seen in individual materials: $LaFeAsO_{0.89}F_{0.11}$ has a T_c of 26 K at ambient pressure, which increases to ∼43 K at 4 GPa pressure, as the unit cell is compressed.[182] Since the electronically active part of these superconductors is the FeAs layer it is the structure of this which is of particular interest. Several connected parameters are quoted in the literature as definitive of the geometric state or distortion of this tetrahedral layer: The Fe–Fe distance is a measure of how 'stretched out' the layer is. The Fe–As distance tends to remain relatively constant within families, so distortions of the FeAs layer can be viewed as stretching and flattening, or compressing and thickening, *i.e.* concertinaring as mentioned earlier. In this case the Fe–Fe distance is a similar measure to one of the two tetrahedral angles. The angles α and β are labelled in Figure 4.10. The two angles are related so only one is needed to describe the tetrahedra.

Since doping effects the geometry of the FeAs layer as well as the Fermi level it is difficult to separate lattice effects from doping effects when studying a variation of doping in any individual material. The pressure effect on the T_c of $LaFeAsO_{0.89}F_{0.11}$

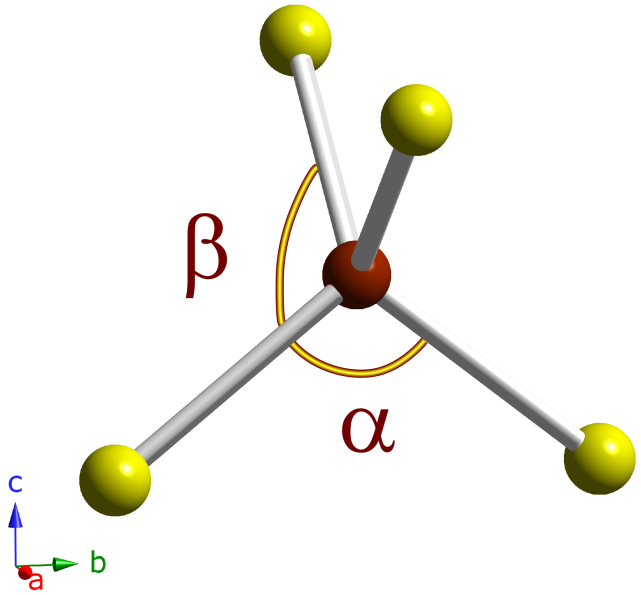

Figure 4.10: The FeAs tetrahedron with α and β labelled. As the layer is stretched in the ab plane and compressed in the c direction α increases in value and β decreases. In the extreme case, if the layer was made planar α would be 180° and β would be 90°.

and the increase in T_c from La to Sm in RFeAsO$_{1-x}$F$_x$ hint that smaller rare earth ions may have higher T_c's, however the value of T_c seems to level off for the middle rare earths. It is unclear what the lattice effect will be ultimately and the investigation of the late rare earth containing compounds is valuable in providing a deeper understanding of the properties of these materials.

4.2 Synthesis

The syntheses of the materials presented in this chapter followed a common method: polycrystalline samples of nominal compositions RFeAsO$_{1-x}$F$_x$ (R =Nd, Tb, Dy, Ho) were synthesised from stoichiometric amounts of RAs, Fe_2O_3, FeF_2 and Fe. RAs precursors were prepared from a stoichiometric mixture of the elements heated to 500 °C for 5 hours and then 900 °C for 10 hours in an evacuated quartz tube. The reactants were mixed and ground in a glove box, sealed in a BN capsule, and subjected to pressures of 6–12 GPa. Once at pressure, the samples were heated to 950–1300 °C in 10 min, held at this temperature for various lengths of time from 15 minutes to 3 hours, and then quenched to room temperature, followed by release of the pressure. The products were dense, black, sintered, polycrystalline pellets. Specific details of each of the synthesis conditions are in the separate materials' sections.

4.3 NdFeAsO$_{1-x}$F$_x$

A preliminary synthesis of the previously reported material NdFeAsO$_{0.9}$F$_{0.1}$ was attempted. The original report had cited synthesis from a mixture of Nd, As, Fe, Fe_2O_3 and FeF_3, heating the mixture to 1300 °C for 60 minutes under 6 GPa pressure.[118] We used a stoichiometric mixture as described in the previous section. The mixture was heated to 1050 °C for 15 minutes under 6 GPa pressure, then quenched to room temperature followed by a release of the pressure. The attempt was successful producing a superconducting material with a T_c of 47 K (the original report referred to above indicated that NdFeAsO$_{0.89}$F$_{0.11}$ has a T_c close to 50 K). A PXRD pattern of the material is shown in Figure 4.11 and its magnetisation in Figure 4.12. The unit cell parameters are $a = 3.9336(3)$ Å and $c = 8.5184(9)$ Å, the main impurity is NdAs (11.8(5) % by mass), there are no major unassigned impurity peaks. Subsequent synthesis attempts of other materials were based on this synthesis.

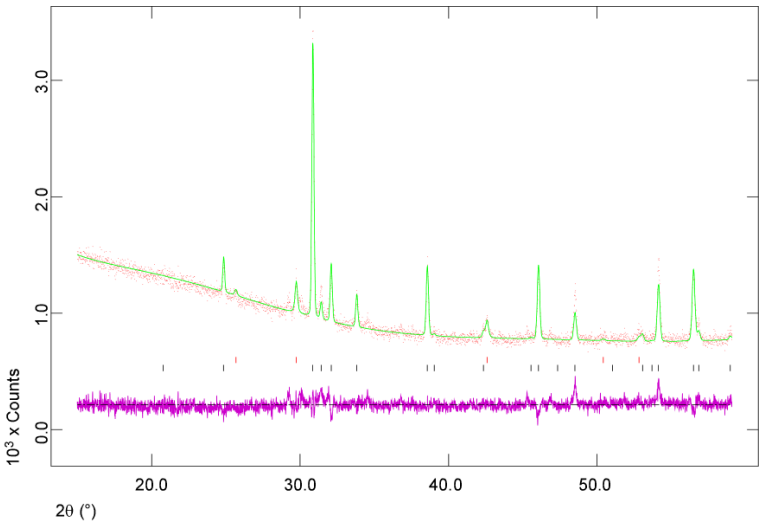

Figure 4.11: Rietveld refinement of a PXRD pattern of $NdFeAsO_{0.9}F_{0.1}$. The data are fitted by a model of the tetragonal 1111 phase (lower tickmarks, 88.23(8) % by mass) and NdAs (upper tickmarks, 11.8(5) %). A difference curve is shown at the bottom of the figure. The pattern was taken over 30 minutes and Rietveld refinement gave unit cell values of $a = 3.9336(3)$ Å, $c = 8.5184(9)$ Å, Volume $= 131.80(3)$ Å^3, with $\chi^2 = 1.705$ and $R_{wp} = 4.14$ %.

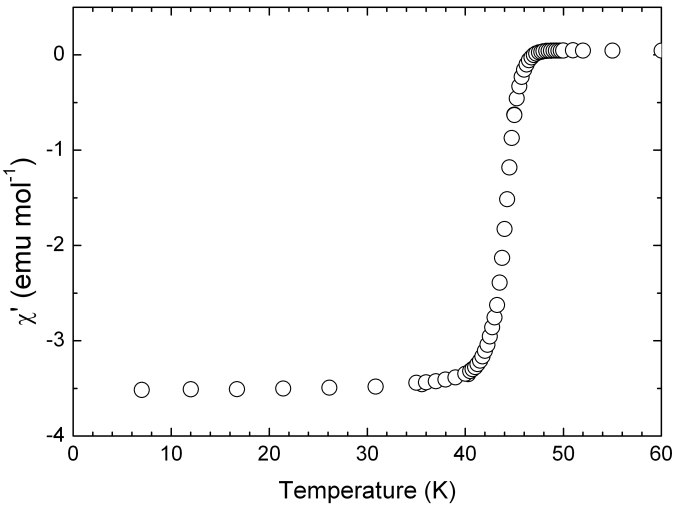

Figure 4.12: Molar AC susceptibility of $NdFeAsO_{0.9}F_{0.1}$ showing a clear transition to negative values indicative of a superconducting state. The transition is at 47 K. The measurement was carried out at 10 Oe with an AC frequency of ∼117 Hz, the same conditions were used in subsequent susceptibility measurements of other materials.

4.4 $TbFeAsO_{1-x}F_x$

4.4.1 Synthesis

$TbFeAsO_{1-x}F_x$ materials with nominal compositions of $x = 0.1$ and 0.2 have been synthesised. Superconducting materials of various purities were prepared at a variety of conditions as attempts were made to optimise the synthesis as shown in Table 4.2. Initial success was achieved with short reaction times: conditions of 10 GPa with 20 minutes heating time at 1100–1150 °C yielded materials with the tetragonal 1111 phase present. Tb-containing iron arsenide superconductors had not previously been reported. The samples were multi phase and an increase of heating time and decrease of pressure led to samples with increased phase purity.

Table 4.2: $TbFeAsO_{1-x}F_x$ and $TbFeAsO_{1-\delta}$ synthesis conditions. The main phases are listed as they appear on identification PXRD scans, 'α' and 'β' refer to α-Tb_2O_3 and β-Tb_2O_3 respectively, and 'mix' indicates an unidentified mixture of phases.

Sample	Pressure (GPa)	Temp. (°C)	Time (min)	x	δ	T_c (K)	Main phases
Tb01	10	1000	20	0.1	0.0	46	1111, β
Tb02	10	1000	20	0.2	0.0	46	α, 1111
Tb03	10	1000	20	0.2	0.0		α, TbAs
Tb04	10	1000	20	0.3	0.0		α, TbAs
Tb05	10	1050	23	0.0	0.0		β
Tb06	10	1050	23	0.0	0.1	50	1111, β
Tb07	8	1000	60	0.1	0.0		1111, α mix
Tb08	10	1000	60	0.2	0.0		1111, α mix
Tb09	7	1050	90	0.0	0.0		β
Tb10	7	1050	90	0.0	0.1		β
Tb11	6	1000	60	0.1	0.0		1111, α
Tb12	10	1000	60	0.0	0.1		β, 1111
Tb13	11	1000	60	0.0	0.1		β, 1111
Tb14	7	1000	60	0.1	0.0		1111, TbAs
Tb15	10	1100	30	0.0	0.0		β
Tb16	10	1050	15	0.0	0.1		β
Tb17	10	1050	25	0.0	0.1		β, 1111
Tb18	6	1000	60	0.1	0.0	53	1111, β
Tb19	7	1000	60	0.1	0.0		1111, β, TbAs, α
Tb20	7	1000	60	0.1	0.0	51	1111
Tb21	7	950	60	0.1	0.0	52	1111
Tb22	7	950	60	0.1	0.0	51	1111

4.4.2 Superconducting property measurement

Preliminary measurements indicated that the 1111 materials were superconducting, with T_c's of 45.5 and 45.9 K for $x = 0.1$ and 0.2. Additionally, an attempted synthesis of the parent material TbFeAsO gave a multi-phase sample with a T_c of ~50 K. This is indicative of the problems involved in quoting nominal compositions. The sample is assumed to be in fact oxygen deficient due to slightly reducing conditions associated with high-pressure synthesis. The $x = 0.1$ and 0.2 samples have similar T_c's which may suggest a more restricted doping range than the nominal values.

AC susceptibility measurements show clear transitions to diamagnetism, with estimated diamagnetic fractions close to 80 % (Figure 4.13). Resistivity measurements also show a clear transition to zero below T_c. There is a smooth negative curvature of the temperature dependence of the resistivity in the normal state as shown in Figure 4.14. There is no higher-temperature anomaly in the resistivity as is seen in some earlier R-containing materials.

There is a broadening of the superconductive transition with magnetic field, attributed to structural and electrical anisotropy.[183] The onset T_c decreases by 2 K in the highest field applied, 9 T, compared to its value in 0 T. This can be extrapolated (ignoring the

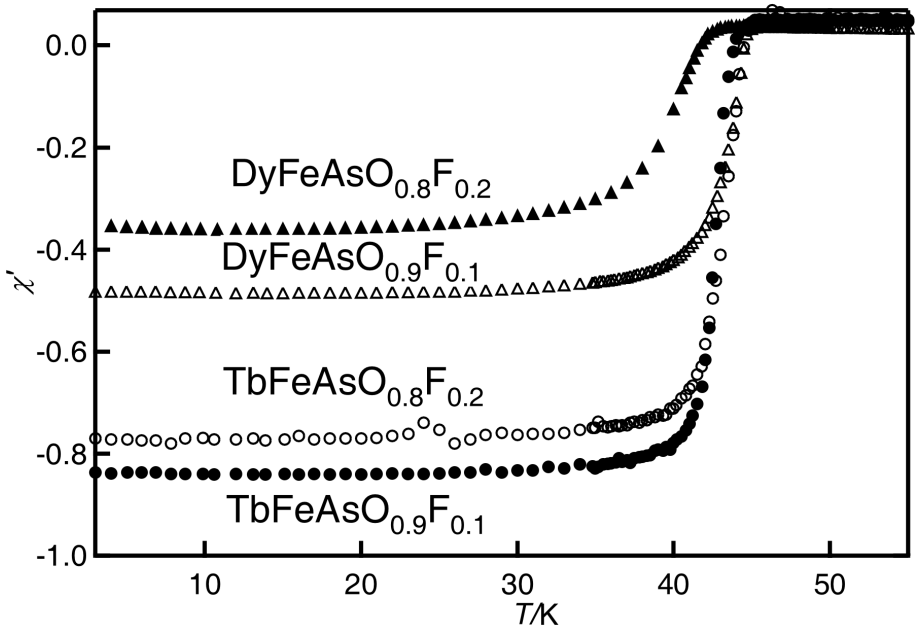

Figure 4.13: AC susceptibility of $TbFeAsO_{1-x}F_x$ and $DyFeAsO_{1-x}F_x$ with temperature. The measurement labelled $TbFeAsO_{0.9}F_{0.1}$ is of sample Tb01, that labelled $TbFeAsO_{0.8}F_{0.2}$ is of sample Tb02. Dysprosium sample details are given in the next section.

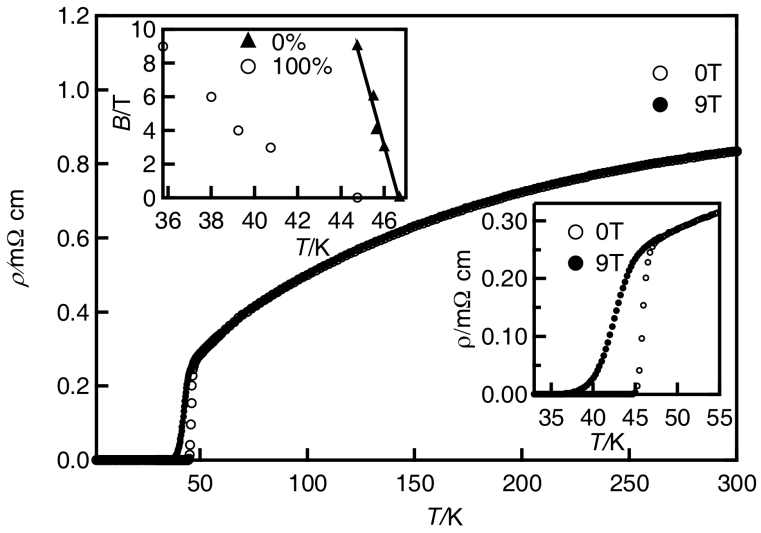

Figure 4.14: Temperature dependence of the resistivity of $TbFeAsO_{0.8}F_{0.2}$ (sample Tb02). The lower inset shows the superconducting transitions in 0 and 9 T fields, and the upper inset shows the onset (0 %) of the transition and the zero resistance point (100 %) indicative of the upper critical field (B_{c2}).

BCS paramagnetic limit) to an upper critical field $B_{c2} > 100$ T, similar to values seen in the cuprates.

Following these initial measurements the synthesis of $TbFeAsO_{0.9}F_{0.1}$ was optimised to some degree in repetitions for a sample suitable for neutron diffraction. A resistivity measurement of sample Tb18 is shown in Figure 4.15, it shows a similar sharp transition at T_c and smooth negative curvature at temperatures above T_c. The AC susceptibility measurements of five samples with $x = 0.1$ are shown in Figure 4.16. A summary of the T_c measurements is given in Table 4.3.

Table 4.3: Tb superconducting properties showing onset ($T_c(\rho_{ons})$), midpoints ($T_c(\rho_{mid})$), and zero points ($T_c(\rho_0)$) of resistive transitions and onsets of magnetic transitions ($T_c(\chi_{ons})$). Diamagnetic fractions (Dia. Frac.) are given where they have been estimated.

Sample	$T_c(\rho_{ons})$ (K)	$T_c(\rho_{mid})$ (K)	$T_c(\rho_0)$ (K)	$T_c(\chi_{ons})$ (K)	Dia. Frac. (%)
Tb01	45.8	43.8	42.2	45.5	84
Tb02	46.8	45.9	45.0	45.2	77
Tb18				50.5	
Tb20	52.3	51.7	50.3	51.2	
Tb21				51.8	
Tb22				52.8	

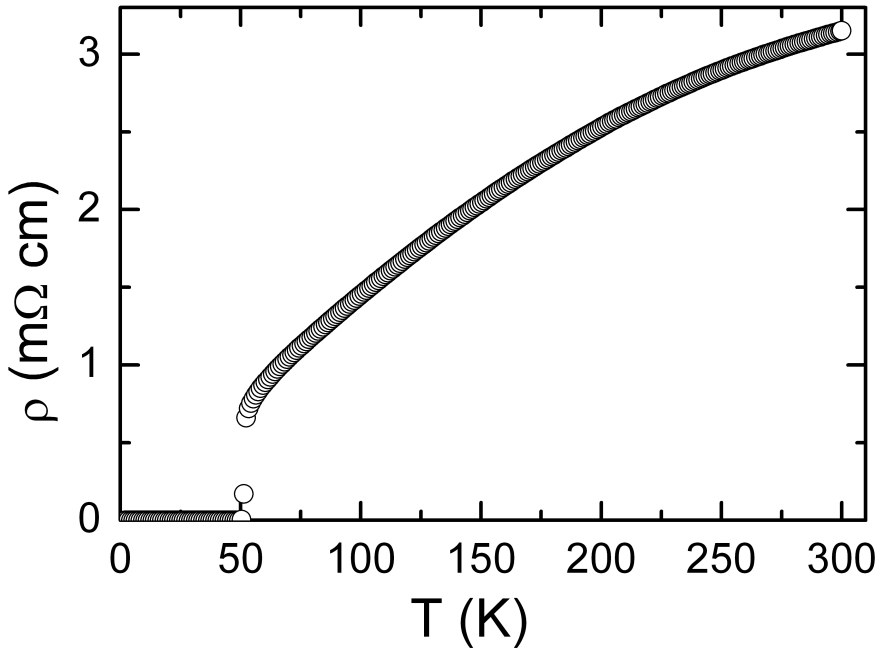

Figure 4.15: Temperature dependence of the resistivity of $TbFeAsO_{0.9}F_{0.1}$ (sample Tb20).

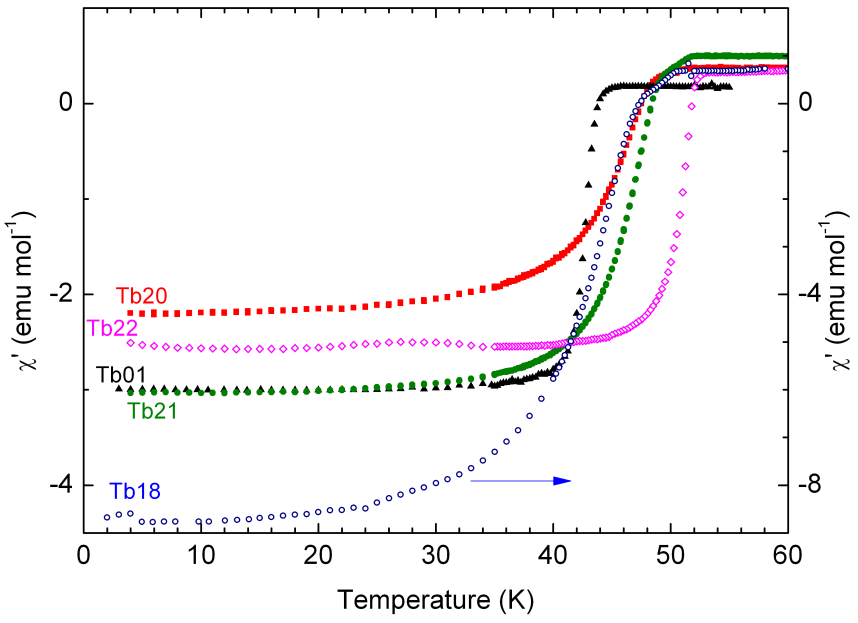

Figure 4.16: Molar AC susceptibility of five $TbFeAsO_{0.9}F_{0.1}$ samples. The samples are labelled on the diagram. The susceptibility of sample Tb018 is given by the right hand x axis, those of the other samples by the left x axis.

4.4.3 Laboratory x-ray diffraction studies

The results of laboratory x-ray studies and a review of the synthesis conditions and superconducting properties for five samples with nominally identical doping levels (x = 0.1) are summarised in Table 4.4. The materials are isostructural with the earlier tetragonal 1111 materials, with the same general atom positions (see Figure 4.1 and Table 4.1). The patterns were collected for 7 h from 10-100° 2θ and refinement was performed using GSAS. A typical Rietveld fit is shown in Figure 4.17. The five nominally identical samples have a range of structural and superconducting properties

Table 4.4: Lab PXRD results for five samples of nominal composition $TbFeAsO_{0.9}F_{0.1}$. The synthesis conditions and T_c's are shown at the top, followed by refinement statistics, phase mass fractions, unit cell parameters, atom parameters, and bond distances and FeAs tetrahedral angles. Temperature factors (U) are isotropic, where they are identical for two atoms in one sample they have been constrained to be equal.

Sample	Tb01	Tb18	Tb20	Tb21	Tb22
P_{syn} (GPa)	10	6	7	7	7
T_{syn} (°C)	1000	1000	1000	950	950
t_{syn} (min)	20	60	60	60	60
T_c (K)	45.5	52.8	50.5	51.8	51.2
R_{wp} (%)	2.52	2.19	2.56	2.38	2.13
χ^2	1.49	1.48	1.72	1.28	1.33
1111 (%)	75.0(1)	48.9(1)	83.62(8)	82.76(9)	83.46(7)
TbAs (%)	8.3(3)	8.5(3)	3.8(3)	1.5(1)	–
Tb_2O_3 (%)	9.0(2)	29.3(8)	12.5(2)	15.7(2)	11.4(2)
FeAs (%)	7.6(2)	13.3(5)	–	–	5.2(1)
a (Å)	3.8467(3)	3.8535(2)	3.8500(1)	3.8534(1)	3.8535(1)
c (Å)	8.2991(8)	8.3090(8)	8.3033(4)	8.3078(5)	8.3048(4)
V (Å^3)	122.80(3)	123.35(2)	123.08(1)	123.36(1)	123.32(1)
Tb:z	0.1450(4)	0.1445(5)	0.1437(3)	0.1427(3)	0.1424(2)
As:z	0.6641(6)	0.6585(9)	0.6643(5)	0.6656(5)	0.6670(4)
U_{Tb} (Å^2)	0.016(1)	0.002(2)	0.0072(8)	0.0004(8)	0.0029(6)
U_{Fe} (Å^2)	0.016(1)	0.002(2)	0.0072(8)	0.0004(8)	0.0029(6)
U_{As} (Å^2)	0.013(2)	0.003(3)	0.008(1)	0.008(1)	0.004(1)
$U_{O/F}$ (Å^2)	0.008(8)	0.003(3)	0.008(1)	0.008(1)	0.004(1)
Tb–O (Å)	2.269(2)	2.270(2)	2.265(1)	2.262(1)	2.261(1)
Tb–As (Å)	3.148(2)	3.180(3)	3.155(2)	3.156(2)	3.151(2)
Fe–As (Å)	2.357(3)	2.334(4)	2.359(2)	2.367(2)	2.374(2)
α (°)	109.4(2)	111.3(3)	109.4(2)	109.0(2)	108.5(1)
β (°)	109.5(1)	108.6(2)	109.52(8)	109.73(8)	109.96(6)

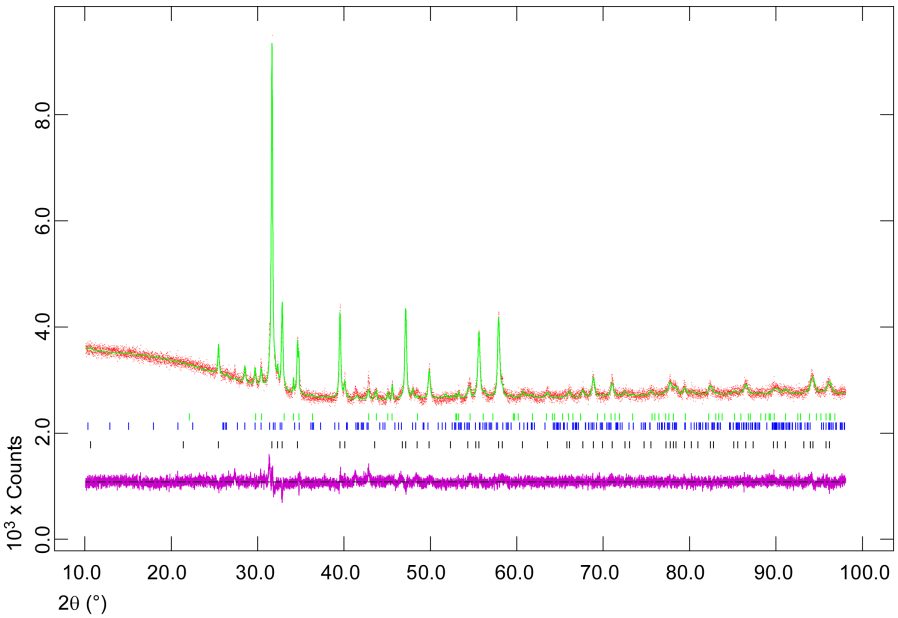

Figure 4.17: Rietveld fit to a PXRD pattern of sample Tb022. The data are fitted by a model of the tetragonal 1111 phase (lower tickmarks, 83.4 % by mass), Tb_2O_3 (11.4 %), and FeAs (upper tickmarks, 5.2 %).

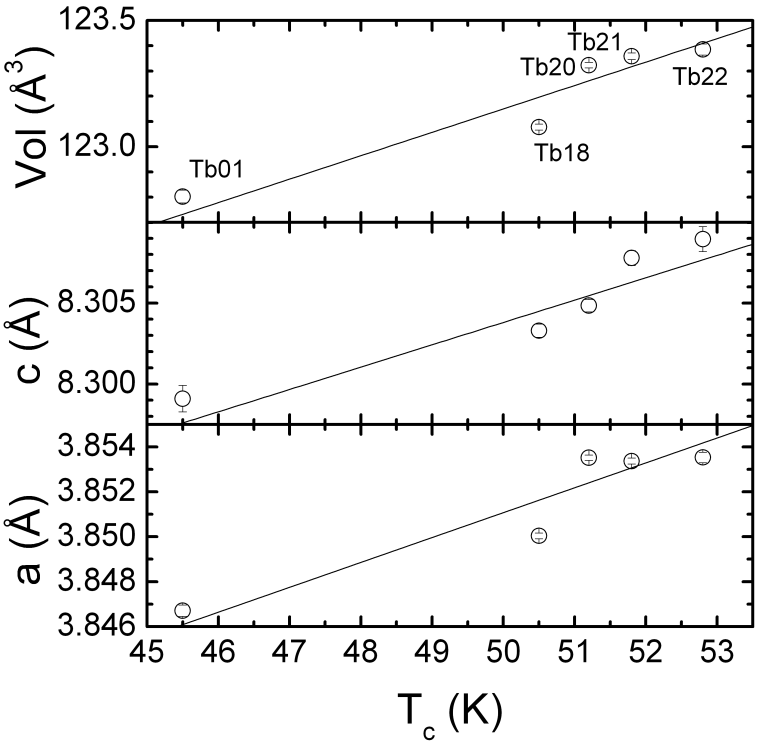

Figure 4.18: $TbFeAsO_{0.9}F_{0.1}$ unit cell parameters vs. T_c from PXRD data.

which are rationalised as a consequence of small variations in precursor stoichiometry and the various synthesis conditions resulting in a variation in x about the nominal composition. The materials exhibit a trend of unit cell parameters and T_c shown in Figure 4.18. dT_c/dV is positive, with a value of $11\,\mathrm{K\,\AA^{-1}}$. The variation in both unit cell and T_c is attributed the variation in x.

4.4.4 Neutron Diffraction

4.4.4.1 Time-of-flight temperature-dependent study

Neutron diffraction measurements were carried out on a combination of the highest purity $TbFeAsO_{0.9}F_{0.1}$ samples on GEM at ISIS to search for any evidence of structural distortions or magnetic ordering at low temperatures. Approximately 70 mg of $TbFeAsO_{0.9}F_{0.1}$ powder was collected by combining samples Tb01, and Tb20-22 listed in Table 4.4. The time and temperature of each GEM measurement, refinement statistics, unit cell parameters and atom positions are given in Table 4.5. Banks 1 and 6 gave poor data for this sample, which is small in the context of neutron diffraction measurements, and were excluded from refinements. The tetragonal $P4/nmm$ structure fitted the data throughout the temperature range, no distortion to orthorhombic symmetry was observed. High and low-temperature data with Rietveld fits are displayed in Figure 4.19. The mass fractions of the fitted phases are 81.2(1) % $TbFeAsO_{0.9}F_{0.1}$, 14.1(3) % Tb_2O_3 and 4.7(1) % FeAs. In the lowest temperature dataset one large (equivalent to the main structural reflections' intensities) and two small magnetic reflections are evident which do not appear in any of the higher-temperature data, this can be seen in the comparisons shown in Figure 4.19.

A thermal expansion of the unit cell is seen, the unit cell volume increases by ∼0.7 % from 1.7–300 K. This temperature effect is anisotropic, with the c axis changing by ∼0.49 % compared to the a axis change of 0.11 %. The change in a, c and the c/a ratio with temperature are shown in Figure 4.20. The bond lengths and tetrahedral angle α are shown in Figure 4.21. The 1.7 K dataset gives unexpected As:z values which are an artefact of the unfitted magnetic reflections altering the intensities of some of the observed nuclear Bragg reflections. This results in the lowest-temperature values for Tb–As and Fe–As bond lengths and tetrahedral angle α lying off the guide curves for the temperature variation of those parameters in Figure 4.21.

Table 4.5: $TbFeAsO_{0.9}F_{0.1}$ GEM PND details with charge (indicative of how long the sample was counted for) and refinement statistics at the top followed by unit cell parameters, atom parameters, and bond distances and FeAs tetrahedral angles. The temperature factors (U) are isotropic with iron and arsenic temperature factors constrained to be identical. The mass fractions were found to be $TbFeAsO_{0.9}F_{0.1}$ (81.2(1) %), Tb_2O_3 (14.1(3) %) and FeAs (4.7(1) %).

Temperature (K)	1.7	15	100	200	300
Charge (µAh)	1100	100	700	700	700
R_{wp} (%)	1.96	3.86	2.12	2.07	2.03
χ^2	3.67	1.29	2.68	2.54	2.45
a (Å)	3.84801(7)	3.8481(1)	3.84881(7)	3.85009(7)	3.85216(7)
c (Å)	8.2588(8)	8.2614(5)	8.2641(3)	8.2793(3)	8.2990(3)
V (Å^3)	122.289(4)	122.335(7)	122.419(4)	122.726(4)	123.150(4)
Tb:z	0.1442(2)	0.1441(5)	0.1437(3)	0.1427(3)	0.1436(3)
As:z	0.6647(3)	0.6631(5)	0.6643(5)	0.6656(5)	0.6644(3)
U_{Tb} (Å^2)	0.0024(3)	0.0028(6)	0.0031(3)	0.0040(3)	0.0063(4)
U_{Fe} (Å^2)	0.0006(1)	0.0001(3)	0.0011(2)	0.0021(2)	0.0035(2)
U_{As} (Å^2)	0.0006(1)	0.0001(3)	0.0011(2)	0.0021(2)	0.0035(2)
$U_{O/F}$ (Å^2)	0.031(1)	0.027(2)	0.036(1)	0.039(1)	0.045(1)
Tb–O (x4) (Å)	2.263(1)	2.270(2)	2.264(1)	2.263(1)	2.265(1)
Tb–As (x4) (Å)	3.146(1)	3.180(3)	3.151(1)	3.154(1)	3.156(1)
Fe–As (x4) (Å)	2.356(1)	2.334(4)	2.352(1)	2.355(1)	2.360(1)
α (°)	109.49(9)	110.0(2)	109.79(9)	109.6(1)	109.4(1)
β (°)	109.46(5)	109.21(8)	109.31(5)	109.39(5)	109.52(5)

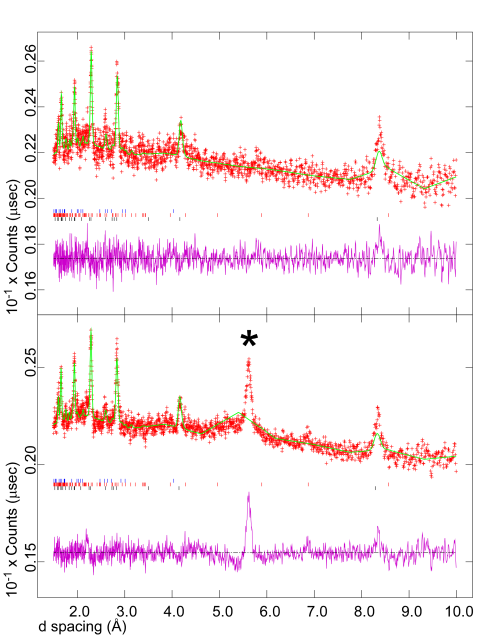

(a) Bank 2

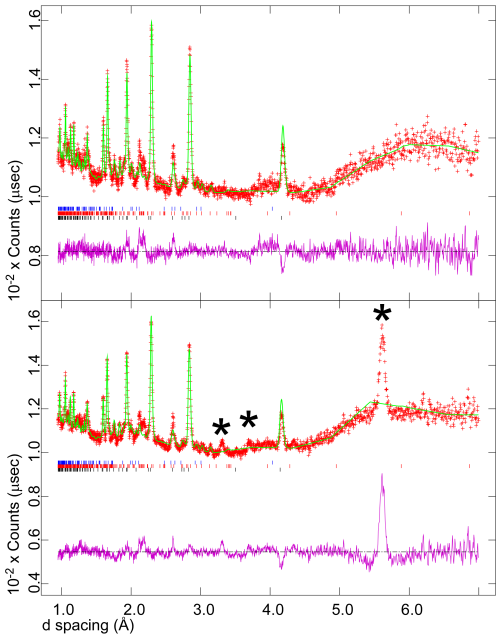

(b) Bank 3

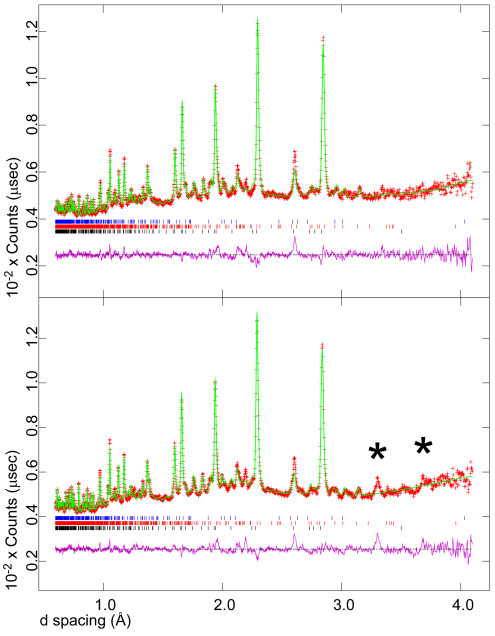

(c) Bank 4

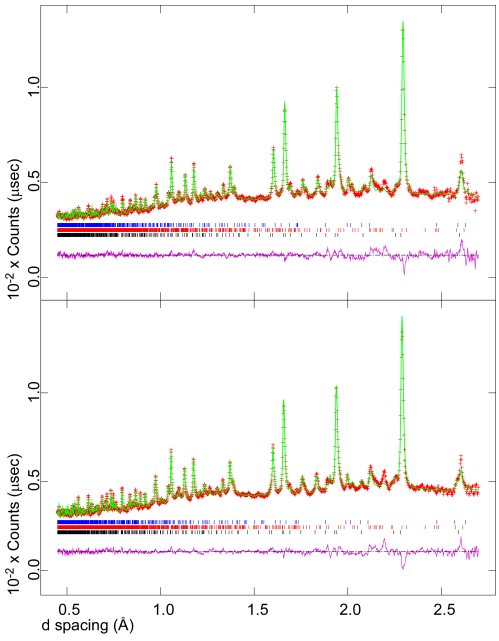

(d) Bank 5

Figure 4.19: Rietveld refinements of banks 2-5 of the GEM diffractometer at ISIS showing data collected at 1.7 K (lower panels) and 300 K (upper panels). The tickmarks are FeAs (top), Tb_2O_3 and $TbFeAsO_{0.9}F_{0.1}$ (bottom). Magnetic reflections are marked with asterisks.

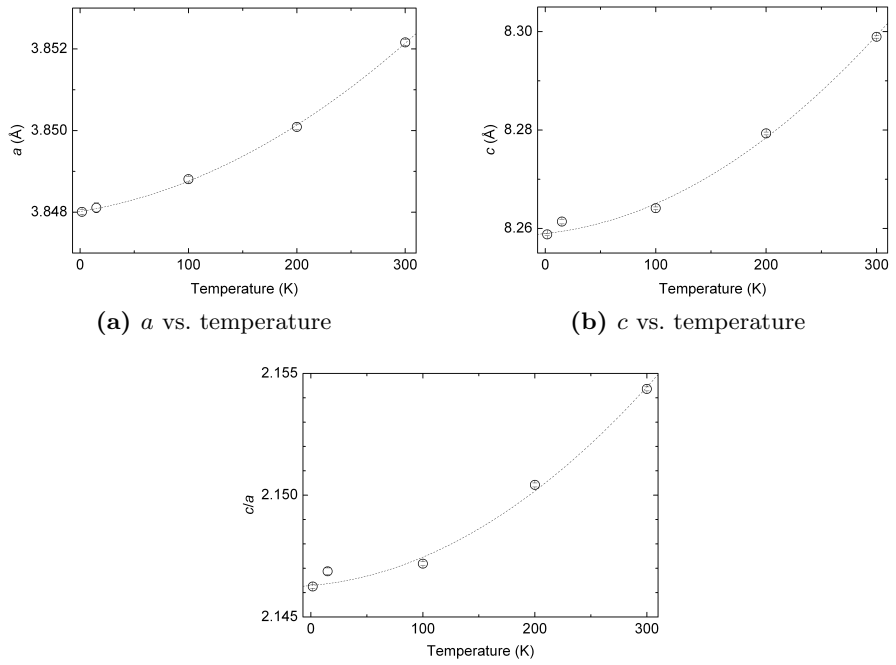

(a) a vs. temperature

(b) c vs. temperature

(c) c/a vs. temperature

Figure 4.20: $TbFeAsO_{0.9}F_{0.1}$ unit cell parameters vs. temperature from GEM PND data. The c/a ratio is given in panel (c).

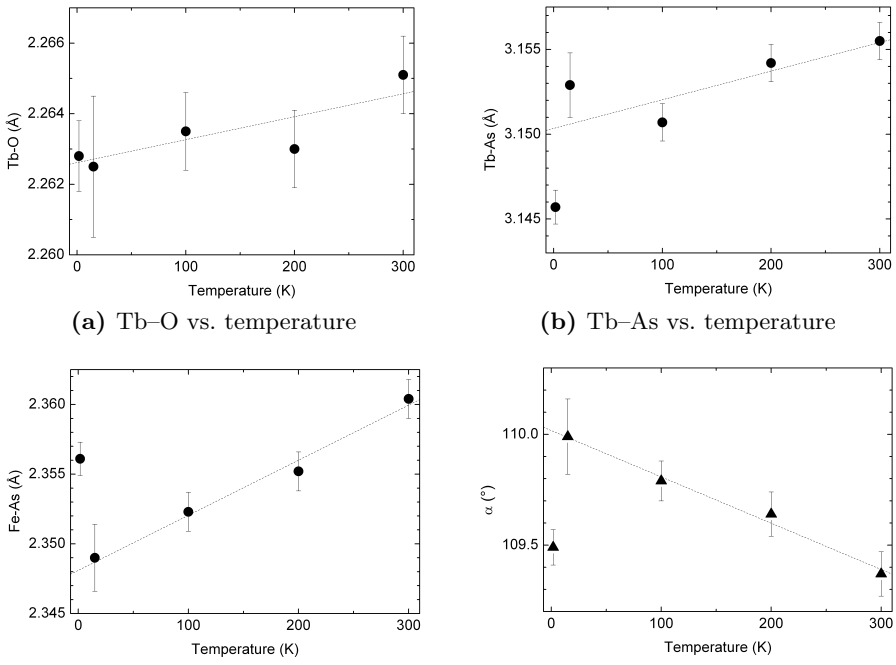

(a) Tb–O vs. temperature

(b) Tb–As vs. temperature

(c) Fe–As vs. temperature

(d) α vs. temperature

Figure 4.21: $TbFeAsO_{0.9}F_{0.1}$ bond lengths and α vs. temperature from GEM PND data.

4.4.4.2 Constant-wavelength low-temperature study

The same $TbFeAsO_{1-x}F_x$ sample was measured on D20 at the ILL in order to further investigate the magnetic reflections. Measurements were made at various temperatures below 10 K, listed in Table 4.6, using a wavelength of 2.41 Å. Due to the small nature of the sample there was a very large amorphous background and several peaks attributed to sample environment were visible, The 9 K raw data including the full background and peaks from the sample environment (which were excluded in refinements) are shown in Figure 4.22. The datasets used for analysis were normalised to a maximum intensity of 1000 arbitrary units and refinements were performed using FullProf.

The data again are fitted by the tetragonal $P4/nmm$ structure with no evidence of any structural distortion at low temperature. The mass fractions were 84.4(3) % $TbFeAsO_{0.9}F_{0.1}$, 12.3(1) % Tb_2O_3 and 3.3(3) % FeAs, similar to those from the GEM data. Table 4.6 shows the details of each dataset. The data provided reasonable unit cell values but were not suitable for attaining reliable atom positions. There is negligible thermal variation in the unit cell parameters over the temperature range of the D20 measurements. Five magnetic reflections were evident including the three seen in the GEM data, which are shown in Figure 4.23. Not present in data taken at 9 K, the reflections emerge in the 5 K dataset and increase in intensity at least until 1.7 K. Attempts to index these reflections to either of the terbium-containing phases with programs *k-search* and *supercell* were unsuccessful, attempted Le Bail fits of commensurate k vectors for both phases resulted in a successful fit for a magnetic structure of the β-Tb_2O_3 impurity phase with propagation vector k = $(\frac{1}{2}\ \frac{1}{4}\ \frac{1}{4})$ shown in Figure 4.24. The largest magnetic reflection is the $(\frac{3}{2}\ \frac{1}{4}\ \frac{5}{4})$ satellite, its intensity (relative to the background) with temperature is shown in Figure 4.24.

Table 4.6: $TbFeAsO_{0.9}F_{0.1}$ D20 PND details. Unit cell parameters, counting times and refinement statistics are given for each temperature.

T (K)	a (Å)	c (Å)	V (Å^3)	Time (min)	R_{wp} (%)	χ^2
1.7	3.8547(2)	8.2719(6)	122.91(1)	360	13.4	16.9
4.0	3.8559(2)	8.2722(8)	122.99(2)	270	14.3	12.6
4.8	3.8554(3)	8.2705(8)	122.93(1)	30	18.7	2.3
5.0	3.8559(2)	8.2703(6)	122.96(1)	270	13.5	11.9
9.0	3.8546(2)	8.2764(6)	122.97(1)	180	14.0	7.8

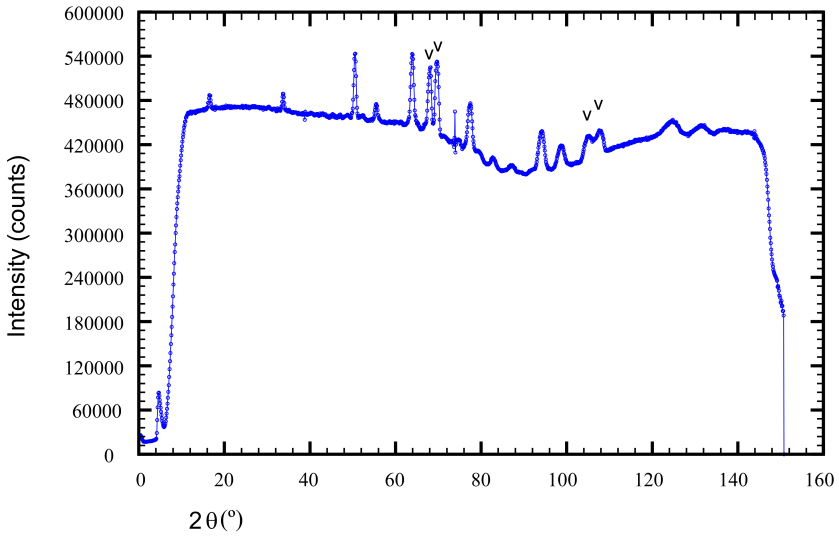

Figure 4.22: $TbFeAsO_{0.9}F_{0.1}$ D20 9 K entire pattern showing the low peak to background ratio. The reflections from sample environment are marked with a 'v'. These were excluded from refinements.

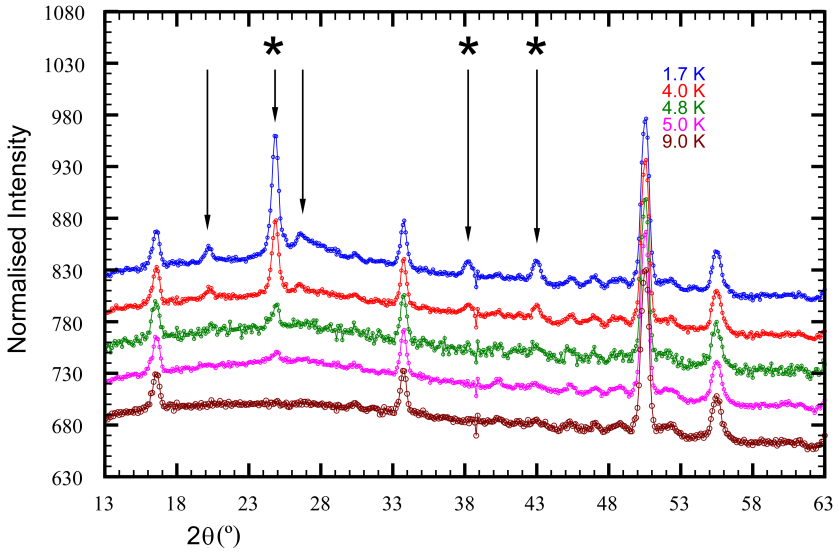

Figure 4.23: $TbFeAsO_{0.9}F_{0.1}$ magnetic reflections. All the D20 temperature runs are shown, magnetic reflections are indicated with arrows, the ones which were visible in GEM data are also marked with an asterisk.

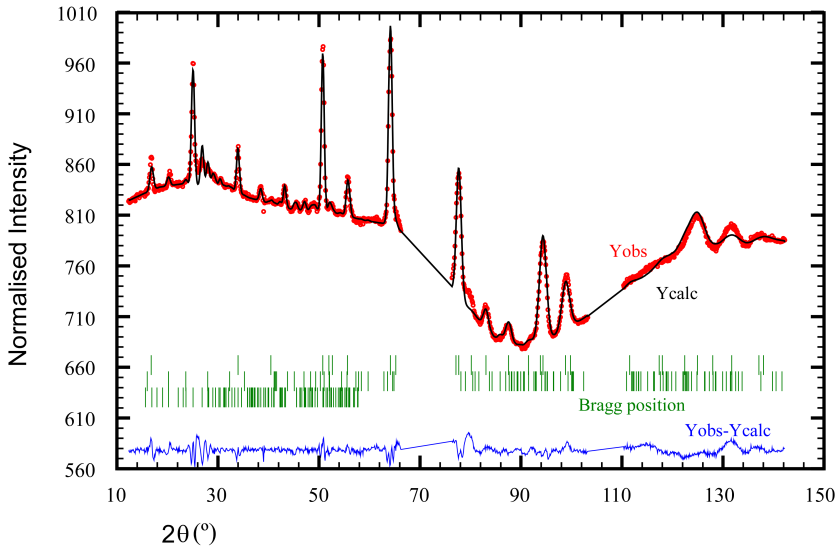

Figure 4.24: Rietveld fit to D20 1.7 K data. The tickmarks represent the positions of Bragg peaks from (top to bottom) the 1111 phase, β-Tb_2O_3, and a Le Bail fit of the magnetic satellites from β-Tb_2O_3 with k = $(\frac{1}{2}\ \frac{1}{4}\ \frac{1}{4})$.

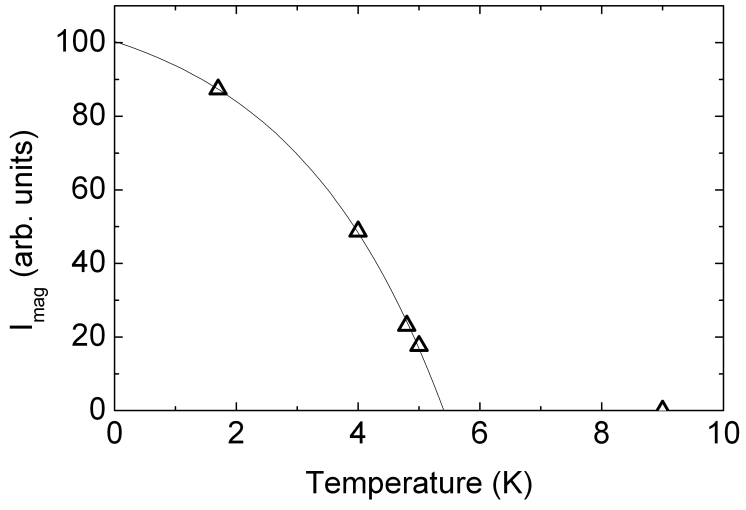

Figure 4.25: Tb_2O_3 magnetic intensity with temperature. I_{mag} is the intensity of the $(\frac{3}{2}\ \frac{1}{4}\ \frac{5}{4})$ satellite with the background subtracted.

4.4.5 Electron microscopy

After the synthesis of terbium-containing superconductors at high pressure, ambient-pressure synthesis was successfully used for the parent material, TbFeAsO, by Dr. Jan-Willem Bos. The ambient-pressure parent material has unit cell parameters a = 3.8985(1) Å, c = 8.4060(3) Å, Volume = 127.76(1) Å^3, significantly larger than those of the high-pressure fluoride-doped materials. $TbFeAsO_{0.9}F_{0.1}$ (synthesised at high pressure) and TbFeAsO (synthesised at ambient pressure) were compared by transmission electron microscopy by Dr. Wuzong Zhou and Wenbo Yue at the university of St. Andrews. Images of the (100) and (001) planes are shown for both samples in Figure 4.26. The images along the a axis show the layered nature of the structure (Figure 4.26a and Figure 4.26c), while images along the c axis show a square arrangement of atoms (Figure 4.26b and Figure 4.26d-4.26f), with an apparent modulated structure in the ambient-pressure sample which is not present in the high-pressure sample.

4.4.6 Discussion

A simple increase in pressure from that required for early rare earth materials allows the synthesis of superconducting terbium oxypnictides as shown by the first results in this section. The materials have low phase purity, however, and it was a decrease in pressure and lengthening of synthesis time compared to the first attempts which yielded samples of sufficient purity for systematic analysis. Listed in Table 4.2, samples Tb18-22 were synthesised at nominally similar conditions, yet their properties vary. This is indicative of a high sensitivity of the products to starting stoichiometry and small variations in synthetic conditions. The samples are all superconductors, with clear transitions to negative susceptibility at ∼50 K (Figure 4.16).

Neutron diffraction measurements revealed no orthorhombic distortions at low temperature, the unit cell volume increases by ∼0.7 % from 1.7–300 K with the majority of this change taken up by the change in the c axis as shown in Figure 4.20. An examination of the layered structure suggests the anisotropic nature of the thermal expansion is to be expected, with weak inter-layer interactions relative to the intra-layer ones. Displayed in Figure 4.21, the Fe–As bond distance shows a larger thermal expansion than the Tb bond distances, and combined with a decrease in α it can be seen that the FeAs layer becomes thicker with increasing temperature resulting in the increase in c.

The reflections which emerge below 9 K in both sets of neutron data are magnetic in origin, they did not convincingly index to any propagation vector of the tetragonal

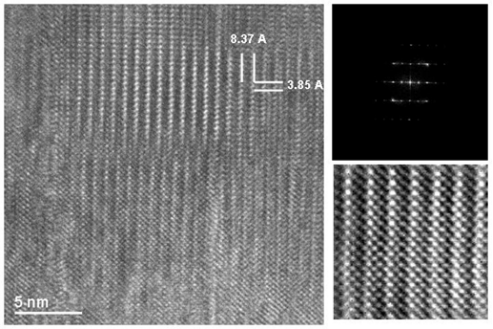

(a) HP (100)

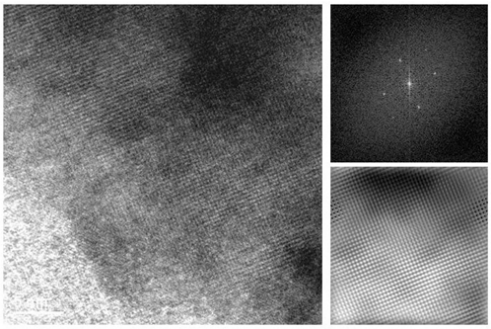

(b) HP (001)

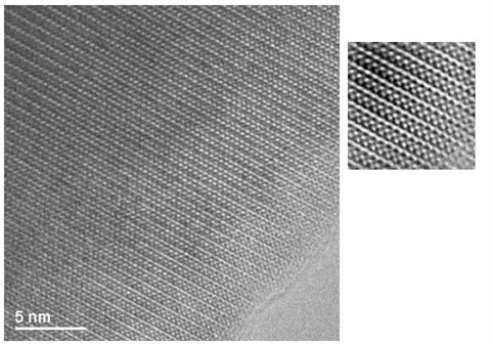

(c) AP (100)

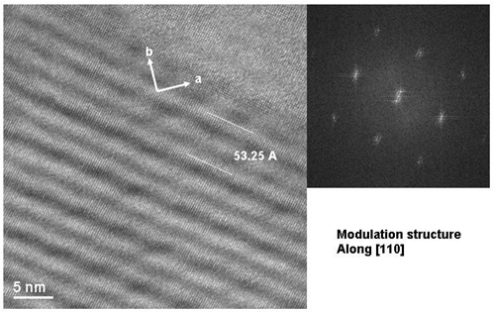

(d) AP (001)

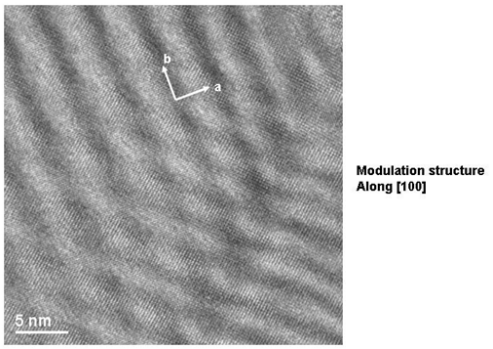

(e) AP (001)

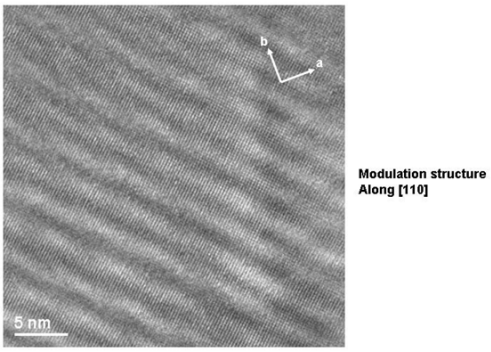

(f) AP (001)

Figure 4.26: High-pressure (HP) and ambient-pressure (AP) $TbFeAsO_{0.9}F_{0.1}$ HRTEM images of (100) and (001) planes. In the ambient pressure sample modulation of the 001 plane in various directions was observed (panels d-f), whereas the high pressure sample did not show modulation. Electron-diffraction images and microscopic image models are shown on the right hand side of the figure panels.

unit cell. The Le Bail fit of the low-temperature D20 data by a magnetic structure of Tb_2O_3 with k = ($\frac{1}{2}$ $\frac{1}{4}$ $\frac{1}{4}$) (Figure 4.24) provides strong evidence that the this is the origin of the magnetic reflections. The variation of the intensity of the strongest magnetic reflection with temperature suggests Tb_2O_3 has a T_N of ∼5.5 K, as shown in Figure 4.25.

The TEM images show a difference between high and ambient-pressure Tb-containing 1111 samples. The high-pressure samples have more regular local arrangement of atoms, the ambient-pressure samples displaying modulation or distortion within layers. This is indicative of the 1111 structure-type becoming more unstable for small R at ambient pressure than it is at high pressure. High-pressure synthesis allows a regular arrangement of atoms, which is frozen when the heating is removed and can be recovered to ambient-pressure conditions. In samples synthesised at ambient pressure this regular arrangement does not form, and the structure becomes slightly distorted to accommodate the relatively small terbium atom. PXRD only gives an average structure over large length scales relative to those of TEM images, and these distortions have not been seen by laboratory PXRD.

4.5 $DyFeAsO_{1-x}F_x$

4.5.1 Synthesis

$DyFeAsO_{1-x}F_x$ with $x = 0.1$ and 0.2 was synthesised successfully. Attempts at the parent material DyFeAsO were unsuccessful in terms of producing a sample with a majority of the 1111 phase present, which is an indication of the increased difficulty of synthesising the smaller rare earth materials. Indeed, the dysprosium-containing superconductors require more extreme synthesis conditions than the larger terbium-containing 1111 materials: The first samples were heated to 1100–1150 °C for 20 minutes under 12 GPa pressure and quenched. The attempts at $DyFeAsO_{1-x}F_x$ syntheses are shown in Table 4.7.

Table 4.7: $DyFeAsO_{1-x}F_x$ and $DyFeAsO_{1-\delta}$ synthesis conditions. The main phases are listed as they appear on identification PXRD scans, 'α' and 'β' refer α-Dy_2O_3 and β-Dy_2O_3 respectively, and 'mix' indicates an unidentified mixture of phases.

Sample	Pressure (GPa)	Temp. (°C)	Time (min)	x	δ	T_c (K)	Main phases
Dy01	6	1000	15	0.1	0.0		mix
Dy02	6	1050	15	0.1	0.0		BN
Dy03	6	1000	17	0.1	0.0		DyAs
Dy04	6	1000	15	0.1	0.0		mix
Dy05	10	950	35	0.2	0.0	43	1111, DyAs
Dy06	10	1000	20	0.1	0.0		DyAs, 1111
Dy07	11	1000	30	0.1	0.0	45	α, DyAs, 1111
Dy08	11	1000	30	0.2	0.0		DyAs, 1111
Dy09	11	1050	30	0.3	0.0		β
Dy10	11	1050	30	0.0	0.0	42	DyAs, 1111
Dy11	10	1000	30	0.1	0.0	42	DyAs, 1111
Dy12	10	1000	30	0.2	0.0		DyAs, α, 1111
Dy13	10	1000	20	0.0	0.1		β
Dy14	10	1000	15	0.0	0.0		β
Dy15	11	1000	10	0.0	0.0		β
Dy16	12	1000	20	0.1	0.0		1111, DyAs
Dy17	12	1000	20	0.2	0.0		α, DyAs, 1111
Dy18	12	1000	40	0.2	0.0		α, DyAs, 1111
Dy19	12	1000	40	0.1	0.0		DyAs, 1111, Fe_2O_3
Dy20	8	1000	60	0.1	0.0	49	1111
Dy21	8	1000	60	0.2	0.0		α, 1111
Dy22	10	1000	60	0.0	0.1		β, 1111
Dy23	8	1050	60	0.1	0.0		β, 1111
Dy24	8	1000	60	0.1	0.0		1111

4.5.2 Superconducting property measurement

Magnetic susceptibility measurements of samples Dy05 and 07 were shown in Figure 4.13. This figure is repeated alongside a comparison of the resistivities of Dy07 and Tb02 in Figure 4.27. The diamagnetic fractions are clearly lower for the dysprosium materials than for terbium, their T_c's are similar. The magnetic susceptibility of a more recently synthesised sample with a higher phase purity is shown in Figure 4.28. The superconducting property measurements are summarised in Table 4.8. Dy10 is nominally undoped but is a superconductor, this situation was also observed with terbium-containing materials and is indicative of the real composition not matching the nominal composition.

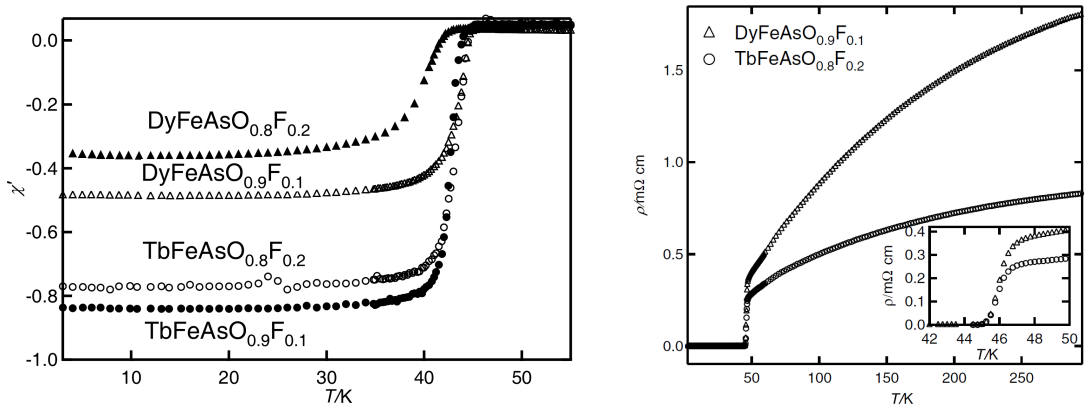

(a) AC susceptibility **(b)** Resistivity

Figure 4.27: Dysprosium 1111 magnetisation and resistivity measurements compared to those of Tb 1111 materials. Measurements labelled as $DyFeAsO_{0.9}F_{0.1}$ are sample Dy05 and those labelled $DyFeAsO_{0.9}F_{0.2}$ are sample Dy07.

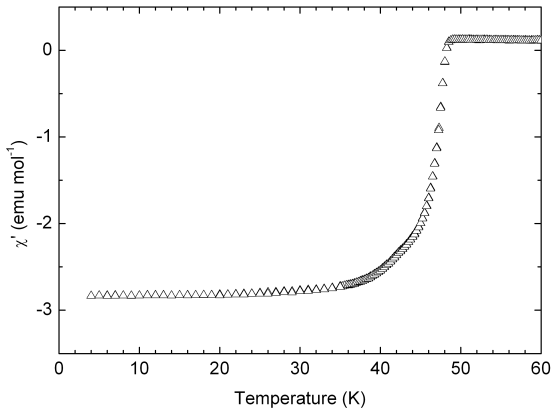

Figure 4.28: Molar AC susceptibility of $DyFeAsO_{0.9}F_{0.1}$ with temperature.

Table 4.8: $DyFeAsO_{1-x}F_x$ superconducting properties

Sample	$T_c(\rho_{ons})$ (K)	$T_c(\rho_{mid})$ (K)	$T_c(\rho_0)$ (K)	$T_c(\chi_{ons})$ (K)	Dia. Frac. (%)
Dy05	44.5	43.1	41.75	43.7	49
Dy07	76.8	45.9	45.0	45.2	36
Dy10				42.3	
Dy11				43.2	
Dy20	49.3	48.5	47.8	48.5	

4.5.3 Laboratory x-ray diffraction studies

The low purity of the early samples is evident from PXRD and good structural detail is difficult to obtain from these measurements. Higher-purity $DyFeAsO_{0.9}F_{0.1}$ was subsequently synthesised at milder conditions, sample Dy20 has a T_c of 48.5 K. A PXRD pattern is shown in Figure 4.29. The pattern was taken over 15 h and Rietveld refinement gave unit cell values of $a = 3.8360(1)$ Å, $c = 8.2740(4)$ Å, Volume = $121.75(1)$ Å^3, with $\chi^2 = 1.72$, and $R_{wp} = 1.92$ %. The atom positions are given in Table 4.9.

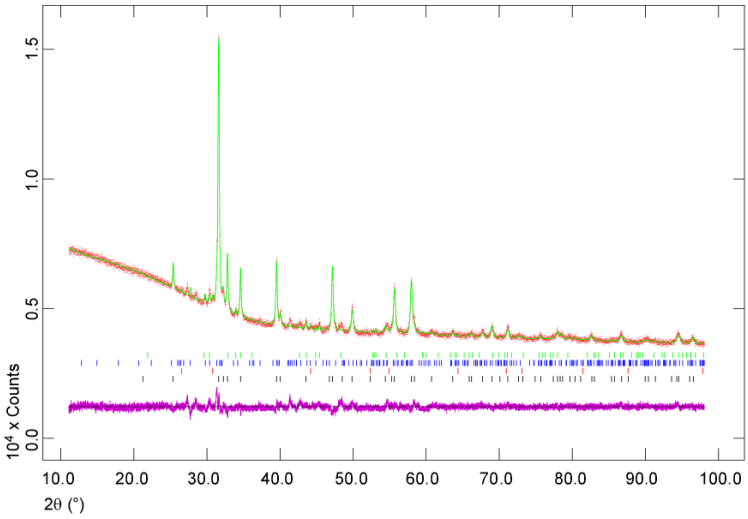

Figure 4.29: PXRD pattern of $DyFeAsO_{0.9}F_{0.1}$ sample Dy20. The tickmarks represent, bottom to top, $DyFeAsO_{0.9}F_{0.1}$ (88.00(5) % by mass), DyAs (1.38(8) %), Dy_2O_3 (7.9(2) %) and FeAs (2.8(1) %).

Table 4.9: $DyFeAsO_{0.9}F_{0.1}$ sample Dy20 PXRD atom positions. U values were constrained to be the same for Dy and Fe.

atom	x	y	z	U (Å^2)
Dy	1/4	1/4	0.1432(2)	0.018(6)
Fe	3/4	1/4	1/2	0.018(6)
As	1/4	1/4	0.6662(3)	0.016(1)
O/F	3/4	1/4	0	0.023(5)

4.5.4 Discussion

Work on dysprosium and terbium oxypnictide superconductors was carried out in parallel, hence there is a similar synthetic pattern. The first syntheses utilised high pressures and with small heating times; a direct increase in pressure from the successful method used for $NdFeAsO_{0.9}F_{0.1}$. Attempts were made at various values of nominal x and superconductors were produced for $x = 0.1$ and 0.2. These materials had lower phase purities by PXRD than the first Tb materials and slightly lower T_c's. Magnetic susceptibility measurements show a lower diamagnetic volume fraction for the early Dy materials than for Tb materials and they have higher resistivities than the Tb materials in the normal state (Figure 4.27a).

An increase in heating time and corresponding decrease in synthetic pressure afforded samples with higher phase purity, equivalent to the highest purity achieved for Tb-containing materials, and a higher T_c of 48.5 K. Fewer repeats of optimal synthesis conditions were made due to the unsuitability of Dy for neutron diffraction, so systematic studies of reasonably pure $DyFeAsO_{0.9}F_{0.1}$ samples have not been possible as they have with the Tb (and Ho) materials. We would expect the results to be similar, although the maximum T_c's of Dy materials have remained lower than $TbFeAsO_{1-x}F_x$ maximum T_c's.

4.6 $HoFeAsO_{0.9}F_{0.1}$

4.6.1 Synthesis

Of attempts at the synthesis of $HoFeAsO_{1-x}F_x$ with $x = 0$, 0.1 and 0.2, only those for $x = 0.1$ were successful. Tetragonal samples of nominal composition $HoFeAsO_{0.9}F_{0.1}$ were synthesised under varying conditions at 10 GPa pressure, a list of attempts is shown in Table 4.10.

Table 4.10: $HoFeAsO_{0.9}F_{0.1}$ synthesis conditions. The main phases are listed as they appear in identification PXRD scans, 'α' and 'β' refer to α-Ho_2O_3 and β-Ho_2O_3 respectively, and 'mix' indicates an unidentified mixture of phases.

Sample	Pressure (GPa)	Temp. (°C)	Time (min)	x	δ	T_c (K)	Main phases
Ho01	10	1000	60	0.1	0.0		HoAs, β
Ho02	10	1050	120	0.1	0.0	36	1111, mix
Ho03	12	1000	60	0.1	0.0		HoAs, mix
Ho04	11	1000	60	0.0	0.1		mix
Ho05	10	1000	180	0.1	0.0		β, mix
Ho06	10	1200	30	0.1	0.0		1111, β, mix
Ho07	10	1050	30	0.1	0.0		1111, β, mix
Ho08	12	900	60	0.1	0.0		1111, β, mix
Ho09	8	1050	60	0.1	0.0		1111, β
Ho10	10	1100	120	0.1	0.0	29	1111, β, HoAs
Ho11	10	950	120	0.1	0.0		HoAs, Fe_2O_3, 1111, mix
Ho12	10	1150	120	0.1	0.0		β, 1111
Ho13	10	1050	120	0.1	0.0	35	1111, HoAs, β
Ho14	10	1050	120	0.1	0.0	33	1111, HoAs, β
Ho15	10	1050	180	0.1	0.0	34	1111, β
Ho16	10	1050	60	0.1	0.0	33	1111, HoAs, β
Ho17	11	1050	120	0.1	0.0		HoAs, β, mix
Ho18	10	1050	120	0.1	0.0		HoAs, β, Fe_2O_3, mix
Ho19	10	1100	120	0.0	0.0		HoAs, mix
Ho20	10	1050	120	0.2	0.0		mix
Ho21	10	1050	120	0.2	0.0		mix

4.6.2 Superconducting property measurement

Magnetic susceptibility measurements were performed on six samples with an apparent majority of the 1111 phase, These measurements and the resistive transitions of two of the samples are shown in Figure 4.30. The samples are all superconducting but their T_c's vary from 29–36 K, there is even a variation of T_c in samples synthesised

at nominally identical conditions. The structural details and mass fractions were obtained from Rietveld refinements of laboratory PXRD data, a pattern is shown in Figure 4.31. The AC susceptibility measurements for all six samples, and the resistivity measurements for sample 4 and sample 6 are shown in Figure 4.30. The superconducting properties are given in Table 4.11.

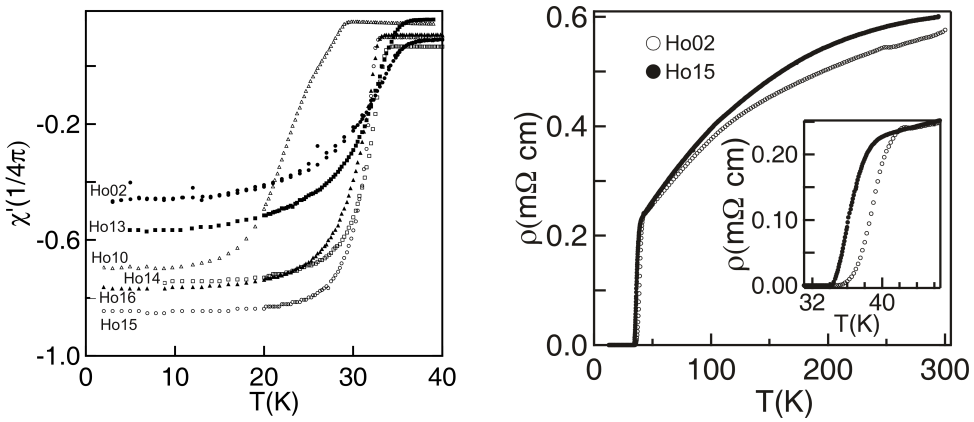

(a) AC susceptibility **(b)** Resistivity

Figure 4.30: $HoFeAsO_{0.9}F_{0.1}$ superconductive properties showing magnetisation measurements for six samples (a) and resistivity measurements for two samples (b).

Table 4.11: $HoFeAsO_{0.9}F_{0.1}$ superconducting property summary.

Sample	$T_c(\rho_{ons})$ (K)	$T_c(\rho_{mid})$ (K)	$T_c(\rho_0)$ (K)	$T_c(\chi_{ons})$ (K)	Dia. Frac. (%)
Ho02	41.0	39.0	35.5	36.2	46
Ho10				29.3	70
Ho13				35.2	57
Ho14				33.0	85
Ho15	38.1	36.2	34.3	33.7	74
Ho16				33.2	76

4.6.3 Laboratory x-ray diffraction studies

The six samples measured above were analysed by laboratory PXRD with scans of 7 h, the results and the superconducting properties of each sample are summarised in Table 4.12, Rietveld refinements were made using GSAS, a typical fit is shown in Figure 4.31. As with nominal $TbFeAsO_{0.9}F_{0.1}$ studies, the variation in structure and properties is attributed to variation in actual doping levels. The mutual dependency of a, c, and unit cell volume with T_c is shown in Figure 4.32. dT_c/dV is positive, with a

value of $7\,\mathrm{K\,\AA^{-1}}$.

Table 4.12: Room-temperature laboratory PXRD results for six samples of nominal composition $HoFeAsO_{0.9}F_{0.1}$. The synthesis details and superconducting properties are shown at the top (all materials were synthesised at 10 GPa) followed by refinement statistics, phase mass fractions, unit cell parameters, atom parameters, and bond distances and FeAs tetrahedral angles. Temperature factors (U) are isotropic, where they are identical for two atoms in one sample they have been constrained to be equal.

Sample	Ho02	Ho10	Ho13	Ho14	Ho15	Ho16
T_{syn} (°C)	1050	1100	1050	1050	1050	1050
t_{syn} (min)	120	120	120	120	180	60
T_c (K)	36.2	29.3	35.2	33.0	33.7	33.2
Dia. frac. (%)	46	70	57	85	74	76
R_{wp} (%)	5.72	3.27	3.65	3.96	3.97	4.63
χ^2	1.97	2.90	1.37	1.49	2.00	2.49
1111 (%)	39.6(6)	60.0(3)	59.1(2)	47.5(2)	55.0(4)	40.8(4)
HoAs (%)	29.5(3)	8.51(9)	12.3(3)	21.4(3)	20.5(6)	20.6(5)
β-Ho_2O_3 (%)	18.0(3)	16.3(3)	19.0(2)	20.9(2)	20.7(5)	22.6(4)
α-Ho_2O_3 (%)	5.2(1)	10.5(2)	8.6(1)	8.2(1)	10.0(3)	10.1(2)
Fe_2O_3 (%)	7.7(3)	4.7(3)	1.0(2)	2.0(2)	12.3(4)	6.0(4)
a (Å)	3.8337(4)	3.8263(2)	3.8281(2)	3.8277(2)	3.8299(3)	3.8269(3)
c (Å)	8.274(1)	8.2537(5)	8.2621(6)	8.2626(7)	8.2626(8)	8.2625(9)
V (Å^3)	121.61(3)	120.84(1)	121.07(2)	121.06(2)	121.19(2)	121.01(2)
Ho:z	0.146(1)	0.1459(4)	0.1452(3)	0.1453(4)	0.1460(6	0.1471(7)
As:z	0.669(2)	0.6734(7)	0.6710(5)	0.6715(6)	0.6758(9)	0.674(1)
U_{Ho} (Å^2)	0.048(5)	0.020(2)	0.028(1)	0.032(2)	0.008(2)	0.001(2)
U_{Fe} (Å^2)	0.016(6)	0.006(3)	0.007(2)	0.007(2)	0.008(2)	0.001(2)
U_{As}(Å^2)	0.043(6)	0.025(3)	0.022(2)	0.022(2)	0.026(4)	0.001(2)
$U_{O/F}$ (Å^2)	0.36(8)	0.11(2)	0.12(1)	0.16(2)	0.11(2)	0.001(2)
Ho–O (Å)	2.264(5)	2.261(2)	2.259(1)	2.259(2)	2.263(3)	2.267(3)
Ho–As (Å)	3.117(6)	3.090(3)	3.104(2)	3.101(2)	3.083(3)	3.082(4)
Fe–As (Å)	2.371(8)	2.389(3)	2.3789(2)	2.382(3)	2.404(4)	2.395(5)
α (°)	107.9(5)	106.4(2)	107.1(2)	107.0(2)	105.6(3)	106.1(3)
β (°)	110.3(3)	111.0(1)	110.65(8)	110.8(1)	111.4(2)	111.2(2)

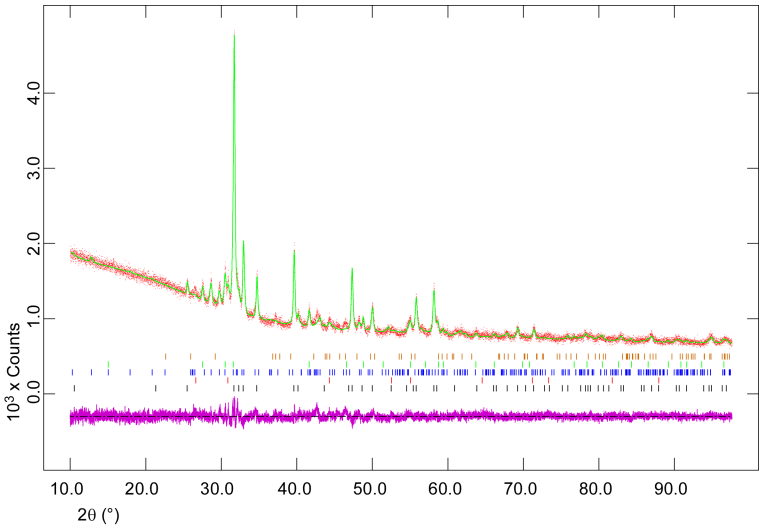

Figure 4.31: Rietveld fit to a PXRD pattern of sample Ho13. The tick marks represent (bottom to top) $HoFeAsO_{0.9}F_{0.1}$ (59.1(2) % by mass), HoAs (12.3(3) %), β-Ho_2O_3 (19.0(2) %), α-Ho_2O_3 (8.6(1) %), and Fe_2O_3 (1.0(2) %).

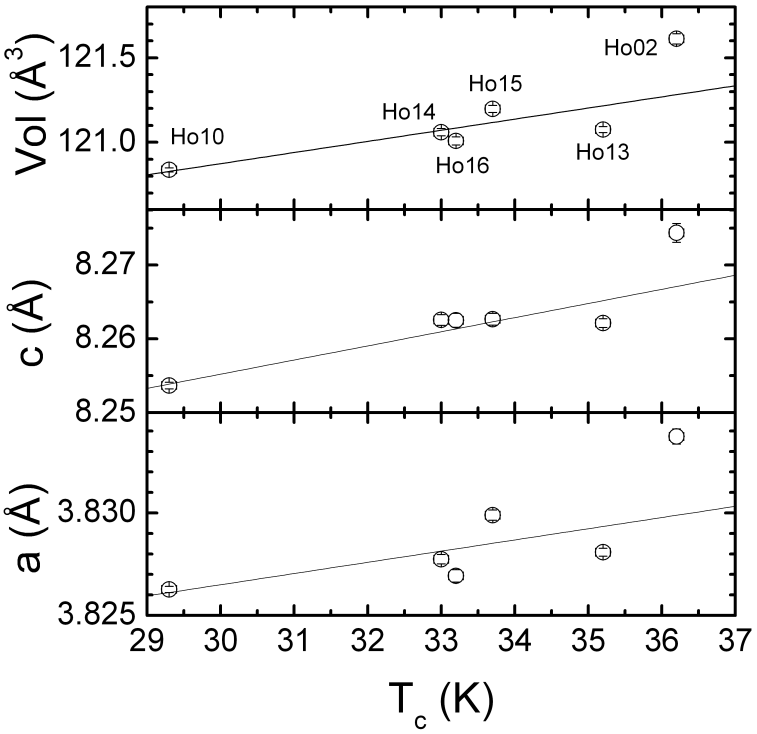

Figure 4.32: $HoFeAsO_{0.9}F_{0.1}$ unit cell parameters vs. T_c from laboratory PXRD data.

4.6.4 Temperature-dependent synchrotron-diffraction study

Approximately 50 mg of $HoFeAsO_{0.9}F_{0.1}$ was collected by combining samples Ho10 and Ho13-15 detailed in Table 4.12. The sample was measured at ID31 at the ESRF in order to identify all the impurities and so to establish accurate structural details of the 1111 phase. Measurements were carried out at ambient pressure at five temperatures from 10–200 K using a wavelength of 0.3994 Å. The experiment was kindly undertaken by Dr. Jan-Willem Bos. The results are summarised in Table 4.13. Rietveld refinement was carried out using FullProf, the background was modelled by a linear interpolation between points with refined heights. The high resolution at ID31 indicated a six-phase sample constituting of $HoFeAsO_{0.9}F_{0.1}$ (50.6(3) % by mass), β-Ho_2O_3 (22.2(2) %), Fe_2O_3 (10.9(2) %), α-Ho_2O_3 (9.42(9) %), HoAs (3.66(5) %), and FeAs (3.3(1) %). A fit to the data is shown in Figure 4.33. The data from ID31 show no transition from tetragonal to orthorhombic symmetry with temperature. A thermal expansion is seen with the majority of the change in volume taken up by a change in c, the temperature variations of the cell parameters are shown in Figure 4.34, those of the bond lengths and tetrahedral angle α are shown in Figure 4.35.

Table 4.13: $HoFeAsO_{0.9}F_{0.1}$ ID31 results. The refinement statistics are shown at the top followed by, unit cell parameters, atom parameters, and bond distances and FeAs tetrahedral angles. Temperature factors (U) are isotropic, As and O/F temperature factors were constrained to be equal. The sample consisted of $HoFeAsO_{0.9}F_{0.1}$ (50.6(3) % by mass), β-Ho_2O_3 (22.2(2) %), Fe_2O_3 (10.9(2) %), α-Ho_2O_3 (9.42(9) %), HoAs (3.66(5) %), and FeAs (3.3(1) %).

Temperature (K)	10	50	100	150	200
R_{wp} (%)	12.3	12.7	12.7	12.9	12.9
χ^2	8.6	8.9	8.9	8.8	8.7
a (Å)	3.82736(3)	3.82740(3)	3.82811(3)	3.82913(3)	3.83029(3)
c (Å)	8.2233(1)	8.2253(1)	8.2305(1)	8.2377(1)	8.2462(1)
V (Å^3)	120.461(2)	120.493(2)	120.614(2)	120.784(2)	120.981(2)
Ho:z	0.1464(1)	0.1464(1)	0.1464(1)	0.1463(1)	0.1461(1)
As:z	0.6740(3)	0.6741(3)	0.6741(3)	0.6741(3)	0.6741(3)
U_{Ho} (Å^2)	0.0030(3)	0.0035(3)	0.0041(3)	0.0048(3)	0.0057(3)
U_{Fe} (Å^2)	0.0080(8)	0.0081(8)	0.0087(9)	0.0100(9)	0.011(1)
U_{As} (Å^2)	0.0024(5)	0.0029(6)	0.0038(6)	0.0042(6)	0.0049(6)
$U_{O/F}$ (Å^2)	0.0024(5)	0.0029(6)	0.0038(6)	0.0042(6)	0.0049(6)
Ho–O (x4) (Å)	2.2609(6)	2.2612(6)	2.2618(6)	2.2623(6)	2.2626(6)
Ho–As (x4) (Å)	3.083(1)	3.083(1)	3.084(1)	3.085(1)	3.088(1)
Fe–As (x4) (Å)	2.390(2)	2.390(2)	2.391(2)	2.392(2)	2.394(2)
α (°)	106.43(5)	106.38(5)	106.36(5)	106.33(5)	106.29(5)
β (°)	111.0(1)	111.0(1)	111.1(1)	111.1(1)	111.1(1)

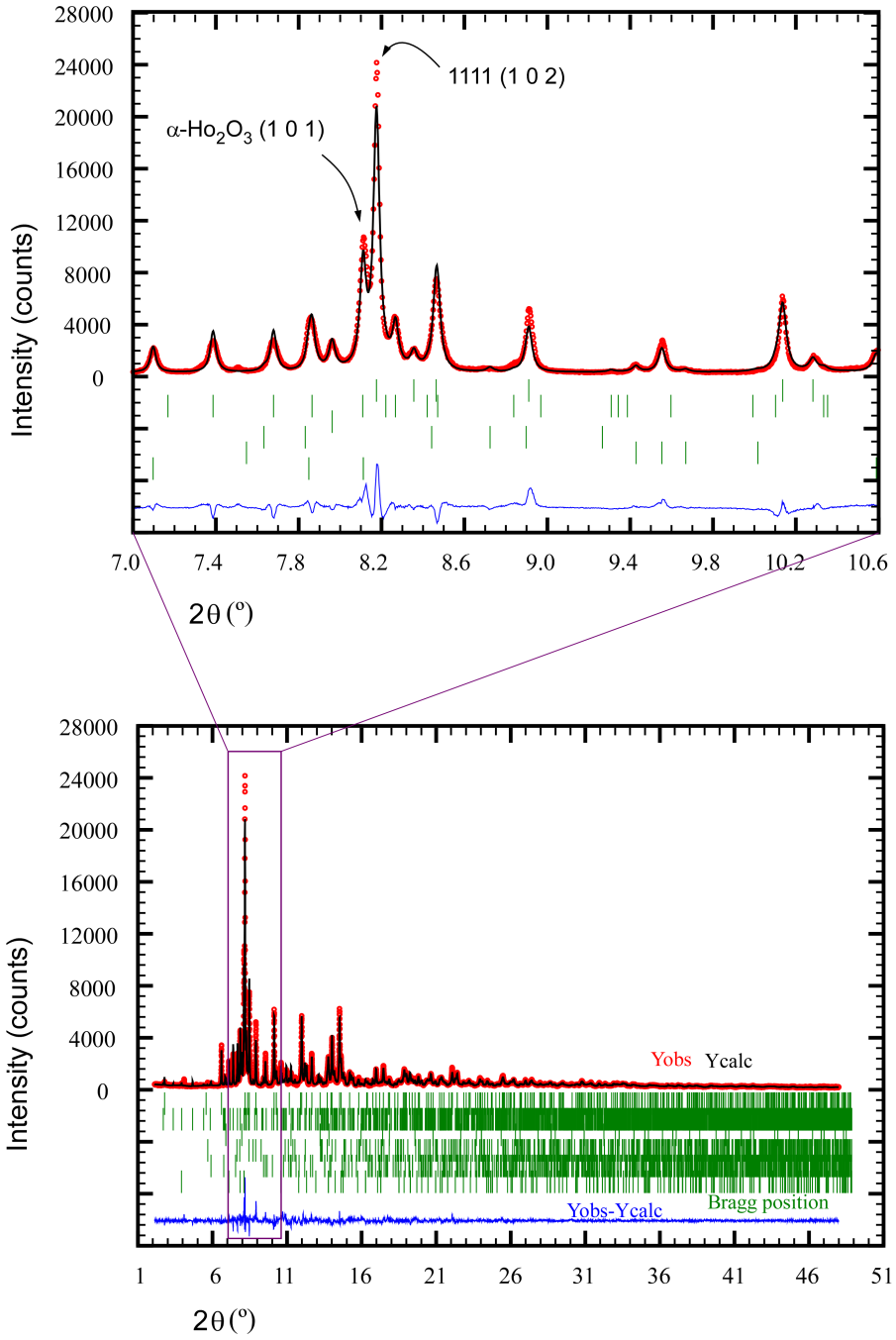

Figure 4.33: Rietveld fit to ID31 data showing an exploded view of the area around the main $HoFeAsO_{0.9}F_{0.1}$ (1 0 2) peak. Note the proximity of the main α-Ho_2O_3 (1 0 1) peak to the left of the largest peak, which was not previously resolved. The Bragg markers in green are, from top to bottom, $HoFeAsO_{0.9}F_{0.1}$ (50.6(3) % by mass), β-Ho_2O_3 (22.2(2) %), HoAs (3.66(5) %), FeAs (3.3(1) %), Fe_2O_3 (10.9(2) %), and α-Ho_2O_3 (9.42(9) %).

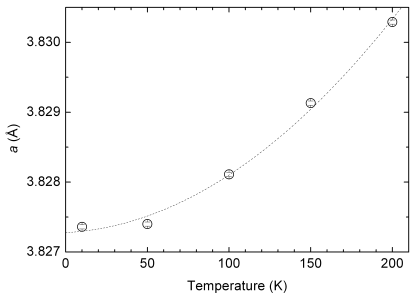

(a) a vs. temperature

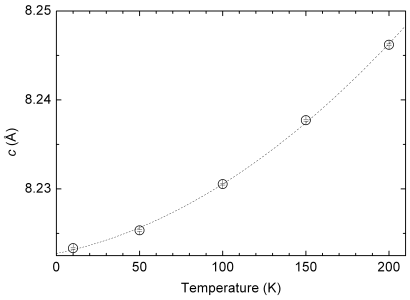

(b) c vs. temperature

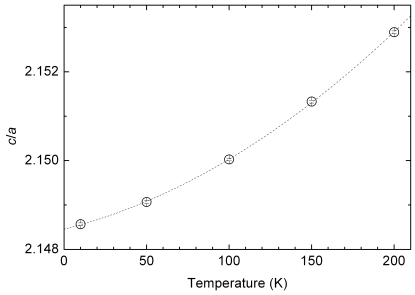

(c) c/a vs. temperature

Figure 4.34: $HoFeAsO_{0.9}F_{0.1}$ unit cell parameters and c/a ratio vs. temperature from ID31 data.

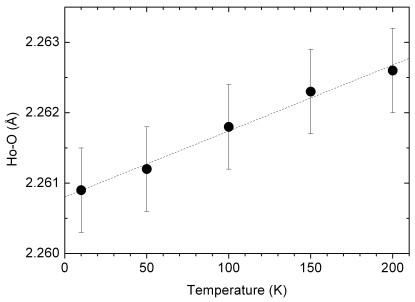

(a) Ho–O vs. temperature

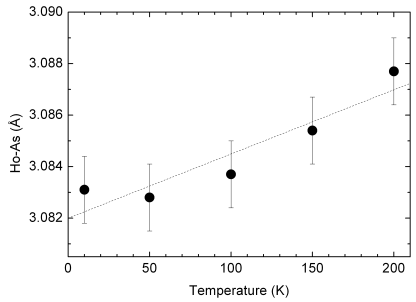

(b) Ho–As vs. temperature

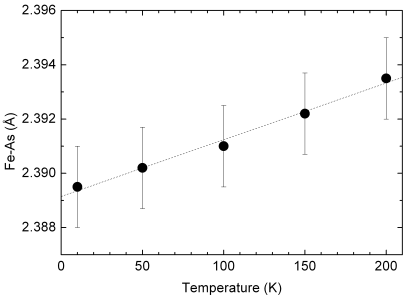

(c) Fe–As vs. temperature

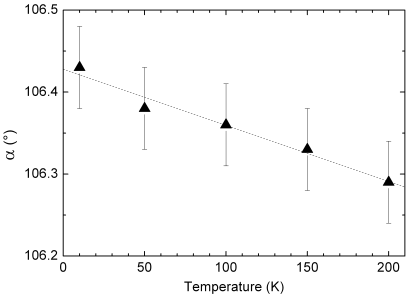

(d) α vs. temperature

Figure 4.35: $HoFeAsO_{0.9}F_{0.1}$ bond lengths and α vs. temperature from ID31 data.

4.6.5 Low-temperature neutron diffraction study

Neutron diffraction was carried out on D20 at the ILL on the same $HoFeAsO_{0.9}F_{0.1}$ sample as was measured on ID31. The small nature of the sample made data collection challenging, some reflections from the sample environment were apparent and had to be excluded. No magnetic reflections were seen on cooling to a temperature of 10 K. Measurements were made at 10 K, 6 K, 4 K and 1.7 K for 3–9 h using a wavelength of 2.41 Å. A pair of magnetic reflections emerged at 6 K and reached a maximum at 4 K. A second set of magnetic reflections appeared at 1.7 K which had not been observed at 4 K demonstrating the presence of two magnetic phases. Both sets of peaks were indexed as magnetic satellites of impurity phases, the higher temperature phase being FeAs (k = $\frac{1}{2}\frac{1}{2}\frac{1}{2}$) and the lower temperature phase being β-Ho_2O_3 (k = $\frac{1}{2}\frac{1}{2}\frac{1}{2}$). The temperature evolution of the reflections is shown in Figure 4.36 and a fit to the low-temperature data in Figure 4.37. The variation of magnetic intensity the two ordered impurity phases with temperature is given in Figure 4.38, showing HoAs has a T_N of ~6.5 K and that Ho_2O_3 begins to order somewhere between 1.7 and 4 K. The data were useful for the observation of these magnetic reflections, but were of worse quality than the $TbFeAsO_{0.9}F_{0.1}$ D20 data due to a smaller sample volume and were not suitable for detailed structure refinement.

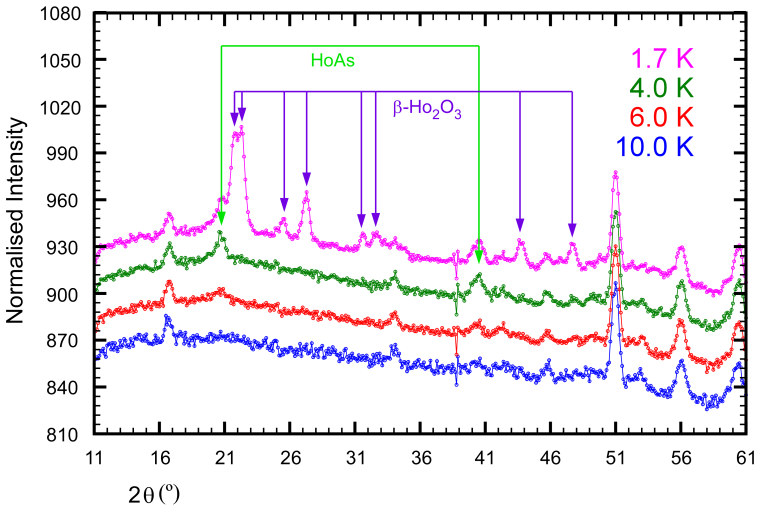

Figure 4.36: $HoFeAsO_{0.9}F_{0.1}$ magnetic reflections. All D20 temperature runs are shown, the magnetic reflections from two phases are indicated with arrows. The reflections have been indexed as being from HoAs and Ho_2O_3 both with propagation vector k = $\frac{1}{2}\frac{1}{2}\frac{1}{2}$.

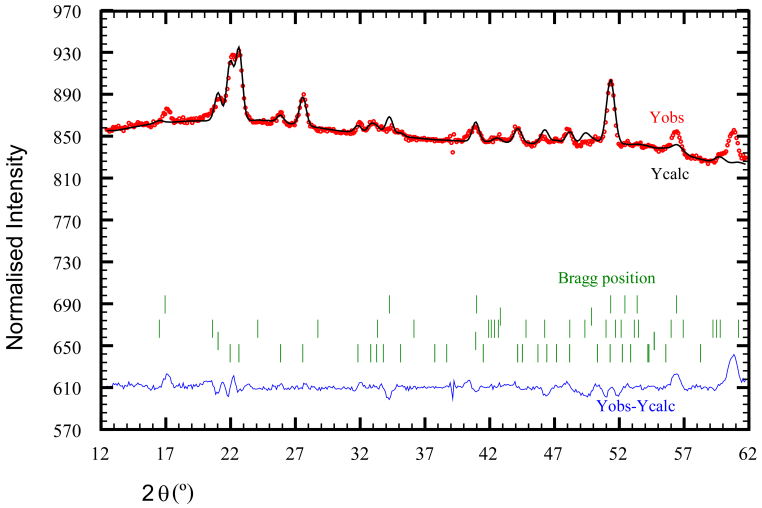

Figure 4.37: Fits to 1.7 K $HoFeAsO_{0.9}F_{0.1}$ data. The Bragg markers represent, from top to bottom, Rietveld fits of the 1111 phase, HoAs, and β-Ho_2O_3, and Le Bail fits of HoAs and β-Ho_2O_3 phases, respectively.

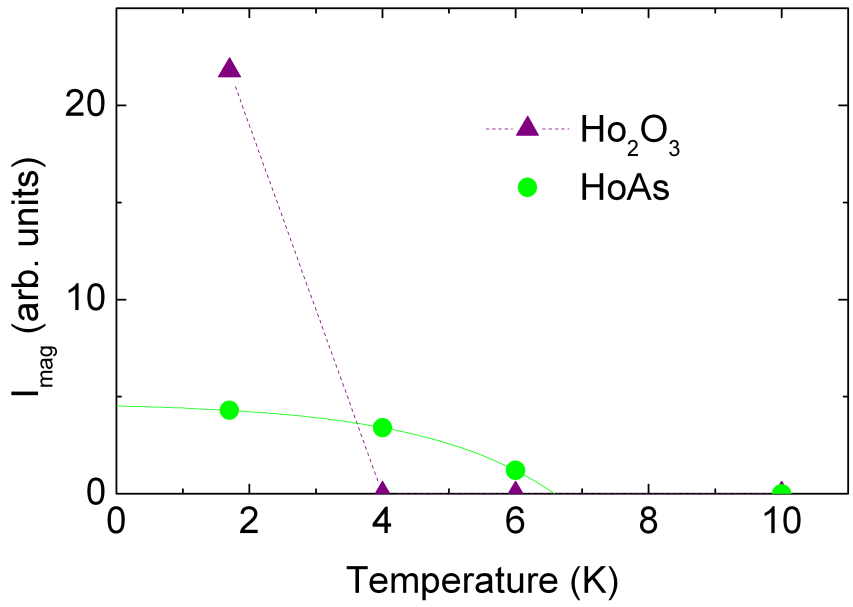

Figure 4.38: HoAs and Ho_2O_3 magnetic intensity with temperature. I_{mag} is the intensity of the $(\frac{1}{2}\ \frac{1}{2}\ \frac{1}{2})$ satellite for Ho_2O_3 (purple) and the $(\frac{1}{2}\ \frac{1}{2}\ \frac{1}{2})$ satellite for HoAs (green).

4.6.6 Discussion

A direct increase in pressure from that required for early rare earth materials with short heating times proved unsuccessful in the synthesis of superconducting holmium oxypnictides. All the Ho materials were synthesised with heating times $\geq 1\,\mathrm{h}$. Only syntheses of $x = 0.1$ materials were successful. This is clear evidence of the increasing difficulty in the synthesis of ever-smaller R-containing 1111 materials. Comparisons of nominal $x = 0.1$ samples reveal a mutual trend of unit cell parameters and T_c shown in Figure 4.32. dT_c/dV is positive, with a value of $7\,\mathrm{K\,\AA^{-1}}$, slightly lower than the Tb materials' value. The variation in both unit cell and T_c is again attributed to a variation in x about the nominal composition.

The high resolution of ID31 allowed detailed structural analysis to be performed despite a mass fraction of ∼50 % of the 1111 phase. The change in unit cell volume is again anisotropic, reminiscent of the case for $TbFeAsO_{0.9}F_{0.1}$, and in line with the layered nature of the structure with c changing by ∼3 % compared to a change in a of ∼1 % over the temperature range. The bond lengths change by similar amounts over the measured temperature range with approximately linear thermal expansions. The Ho–As bond variation with temperature may have a small curvature and a thermal expansion more similar in form to the expansion of the unit cell parameters, although this effect is small relative to the error in the bond lengths (see Figure 4.35b). The tetrahedral angle α has a negative dependency on temperature. This can be interpreted as the layers moving together as the temperature decreases; the holmium layer gets close to the FeAs layer, which also becomes thinner as the tetrahedral angle increases. The decrease in a will be accommodated as the FeAs bond lengths decrease with temperature, outweighing the increase in α with decreasing temperature.

Neutron diffraction measurements display two sets of magnetic reflections which can be attributed to impurities, no magnetic reflections from the 1111 phase are observed. the data were not of sufficient quality for good structural analysis of the sample and would not support refinement of all the phases present as found by synchrotron x-ray diffraction.

4.7 Attempted synthesis of other 1111 materials

Attempts at the synthesis of yttrium and uranium-containing materials were unsuccessful, with no evidence of the 1111 phase from any of the syntheses attempted, the conditions of which are listed in Table 4.14. The products of attempts with yttrium

Table 4.14: Synthesis conditions of attempts at Y and U-containing 1111 materials

M	x	Pressure (GPa)	Temp. (°C)	Time (min)
Y	0.1	8	1200	60
	0.1	10	1250	120
	0.1	12	1250	60
	0.1	10	1250	120
	0.1	10	1250	60
	0.1	10	1100	120
	0.1	10	1300	120
	0.1	10	1100	120
	0.1	10	1300	60
	0.1	10	1250	120
U	0.1	8	1150	60
	0.1	10	1250	90
	0.1	2	1250	60

consisted of YAs and complex mixtures of various unidentified oxides and arsenides. Yttrium is similar in size to holmium, however it does not appear that the 1111 structure for yttrium is as stable relative to a mixture of other phases as the holmium 1111 material. Multi-phase, $YFeAsO_{1-\delta}$ containing samples have since been synthesised elsewhere with synthesis conditions cited as 5 GPa pressure with 1 h heating at 1000 °C yielding a superconductor with a reported T_c of 46.5 K.[184] This, combined with the similarity in chemical properties of Y^{III} and Ho^{III}, would suggest that fluoride doped Y 1111 materials should be attainable.

Three synthesis attempts with uranium all resulted in samples dominated by UO_2 with small amounts of UAs_2 and no evidence of the presence of the 1111 phase.

4.8 Overall discussion

4.8.1 Synthesis and stoichiometry

The properties of these materials seem to be sensitive to synthetic conditions. Tb and Dy materials were initially synthesised at higher pressures and shorter times than the finally optimised conditions, and the difference in nominal synthetic environments may be expected to produce samples with slightly different properties. In the event, even repeated conditions resulted in varying samples. There are several factors which contribute to said variation; the synthesis method must be examined.

To prepare samples with a given x, a relatively large amount of 'iron mixture' for that x was prepared[3] and kept in a glove box, to be combined with the appropriate amount of RAs for each press run. Any inhomogeneity in the iron mixture would cause a variation in the actual starting composition. The synthesis conditions themselves are not exactly their nominal values, pressure and temperature are inferred from calibrations of the load and parameters of the electrical circuit involving the graphite heater. Variations in the setup of the octahedral and cubic assembly will effect the nature of the heating circuit, so some random variation about the nominal conditions exists, which can effect samples which are sensitive to their synthetic environment. The largest single variable of the synthesis conditions is the temperature, which varies by an estimated 10 % for identical electrical readings of the heating circuit.

The nature of the starting materials proved of critical importance to the quality of the products, different batches of RAs starting material had a noticeable effect, of several batches which appeared identical by laboratory PXRD each would produce samples of consistently higher or lower phase purity, on average. This can be seen in the holmium samples, where a new batch of HoAs was used for samples numbered from Ho17 onwards. Sample Ho18 was synthesised under conditions identical to those used for samples Ho13 and Ho14, two of the highest quality samples, and yet no evidence of the presence of the 1111 phase was seen, the most obvious phase in Ho18 was unreacted HoAs (Table 4.10).

After early attempts to synthesise various doping levels for each R, this work focused on samples with $x = 0.1$. Previous work on the large rare earth containing analogues has established an upper limit of fluoride solubility of $x \approx 0.25$ and we did indeed find $x = 0.2$ samples more difficult to synthesise than $x = 0.1$. An interesting observation, however, is that the parent materials are also more difficult to synthesise than those with $x = 0.1$. Attempts at the Tb and Dy-containing parent compounds resulted in oxygen-deficient superconductors, and attempts at fluoride-free holmium-containing materials were not successful. It appears that a small amount of fluoride in the system acts to facilitate synthesis, (that fluoride may help ion mobility and act as a mineraliser is a known phenomenon[185]). Fewer stoichiometries have been synthesised as smaller rare earths have been used, the synthesis becomes more difficult as the size of the rare earth ion decreases.

[3] *e.g.* for $x = 0.1$ the iron mixture was made from a molar ratio of 7Fe : $6Fe_2O_3$: $1FeF_2$, to be combined with $20R$As.

4.8.2 Structural variation with temperature

Measurements of the structure of combined samples with temperature were only carried out for $TbFeAsO_{0.9}F_{0.1}$ and $HoFeAsO_{0.9}F_{0.1}$. The two materials display similar behaviours with tetragonal $P4/nmm$ symmetry maintained to the lowest temperatures measured. There has been relatively little work on the late rare earth 1111 oxypnictides for comparison but Li *et al.* indicate a resistive anomaly in TbFeAsO at ~100 K in their report on the thorium-doped system.[140] This is suggestive of the same transition to orthorhombic symmetry as is observed in the early rare earth containing materials. Our results show that this transition is suppressed by doping as is the case in earlier materials.

There is a steady increase of unit cell volume with temperature of similar magnitude for both materials, and the majority of this increase is similarly taken up by the c axis increase in both cases, with a smaller part attributed to the a axis increase. A diagram displaying the fractional increase of the unit cell parameters of both materials is shown in Figure 4.39 for ease of comparison. It is expected that the behaviour of

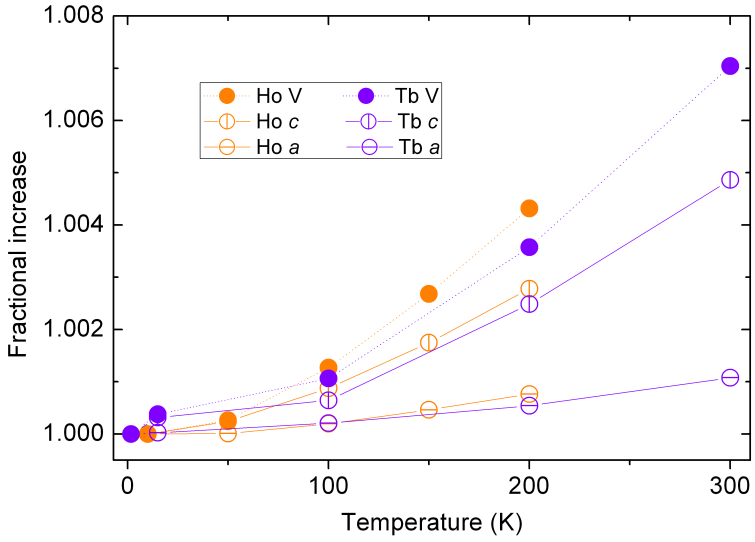

Figure 4.39: Thermal expansion of $TbFeAsO_{0.9}F_{0.1}$ and $HoFeAsO_{0.9}F_{0.1}$ unit cell parameters with temperature. Tb data from GEM is shown in purple and Ho data from ID31 is shown in orange.

$DyFeAsO_{0.9}F_{0.1}$ would be similar. The lack of structural transition suggests that the materials that have been measured are not in the low-doped area of the superconducting region, if the phase diagram for the earlier materials (Figure 4.2) is taken to continue largely unchanged across the group, however this assumption is open to debate.

4.8.3 Structure-property correlations

Repeated attempts at $x = 0.1$ materials with Tb and Ho were made in order to generate enough material to perform neutron diffraction measurements within a reasonable time (this was not attempted for dysprosium due to its high absorption coefficient for neutrons). The accompanying variations in sample properties allowed systematic studies of properties in materials with similar stoichiometries. The origins of the variation of physical properties are discussed earlier, we attribute any changes (in unit cell parameter, T_c, *etc.*) to variations in doping levels *i.e.* actual values of x, brought about by changes in synthetic environment. We cannot measure x but we can measure the physical properties dependent on x. The unit cell parameters for Tb and Ho materials are given in Table 4.4 and Table 4.12 respectively. There is a clear trend between the unit cell parameters of these materials and their superconducting properties. Figure 4.40 shows the mutual dependence of T_c and unit cell parameters. Both materials have similar positive dT_c/dV values of 11 and 7 K Å^{-3} for Tb and Ho

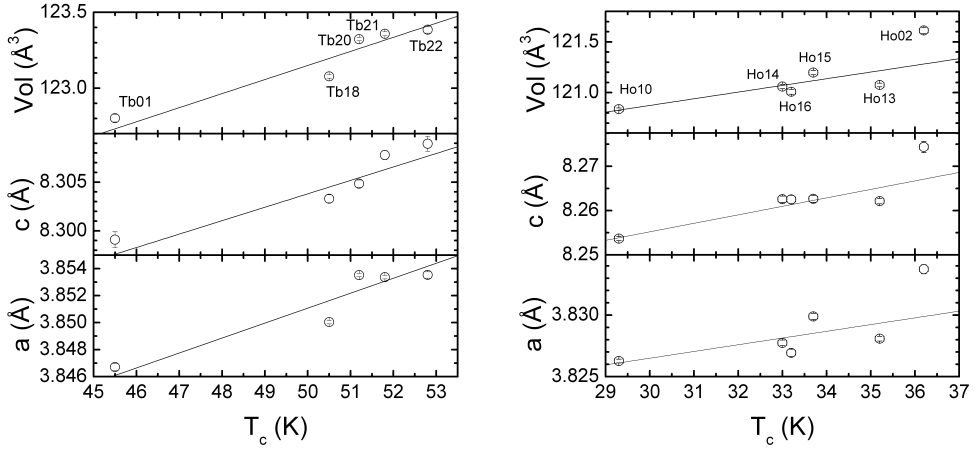

(a) $TbFeAsO_{0.9}F_{0.1}$ **(b)** $HoFeAsO_{0.9}F_{0.1}$

Figure 4.40: Comparison of unit cell parameters vs. T_c for samples of nominal composition $TbFeAsO_{0.9}F_{0.1}$ (a) and $HoFeAsO_{0.9}F_{0.1}$ (b).

respectively. The cause of the change in volume is isotropic, with a and c parameters changing by similar percentages in both materials. The materials were synthesised with nominal $x = 0.1$, which is on or just under the optimum doping level in other 1111 fluoride-doped materials. Since overdoped samples have not been reported for any of these materials it is reasonable to suggest the samples with higher T_c's have higher fluoride content, implying increasing fluoride doping has a positive effect on the unit cell volume. The maximum T_c sample for both rare earth metals has a much lower phase purity than the other samples, a 49 % mass fraction for terbium sample Tb18

and a 40 % mass fraction for holmium sample Ho02. Both have a T_c 1 K higher than other samples with nominally the same compositions but higher mass fractions (~80 % for Tb samples and 50–60 % for Ho samples). This is likely to be an indication that the level of fluoride doping is reaching its limit and supports the claim that the maximum accessible T_c's for these materials have been achieved.

4.8.4 RFeAsO$_{1-x}$F$_x$ series overview

The properties of these latest three 1111 fluoride doped superconductors allow a greater insight into the nature of of the entire RFeAsO$_{1-x}$F$_x$ series. The maximum T_c attained has not increased after SmFeAsO$_{1-x}$F$_x$, and our results show a suppression of the superconductive transition as the rare earth ionic radius and unit cell volume decrease. The variation of maximum T_c for members of the RFeAsO$_{1-x}$F$_x$ with their unit cell volume and Fe–As–Fe tetrahedral angle, α are shown in Figure 4.41. The figure shows

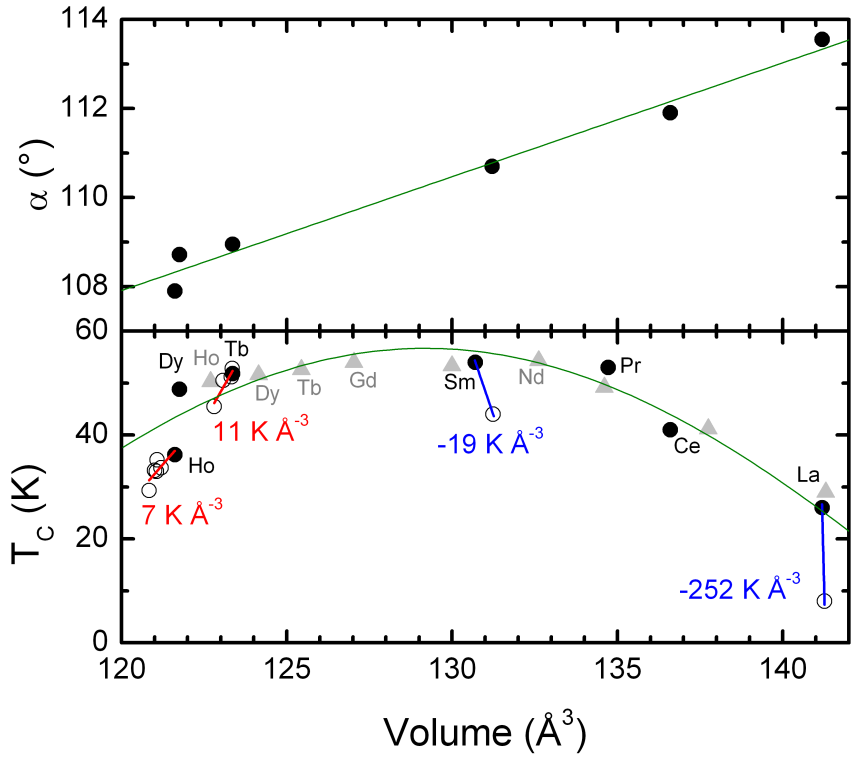

Figure 4.41: Variation of α (upper panel) and superconducting T_c (lower panel) for different 1111 materials. Circles represent RFeAsO$_{1-x}$F$_x$ [117, 119, 186, 187] and triangles RFeAsO$_{1-\delta}$[184, 188]. Filled circles represent T_c(max). dT_c/dV values are given in red and blue and are derived from the data for underdoped samples (empty circles) for R = La[186], Sm[187], Tb and Ho (this work). The T_c(max) data for RFeAsO$_{1-x}$F$_x$ are fitted with a green line as described in the main text.

a monotonic variation of α with unit cell volume across the group.[4] The T_c shows an increase across early members of the rare earth series then decreases in value for the late rare earth containing materials. The maximum T_c data are fit by Equation 4.1

$$T_c(max) = T_c(max)_0 \cos(A(\alpha - \alpha_0)) \tag{4.1}$$

giving a global maximum, $T_c(max)_0 = 57\,K$ at $\alpha_0 = 110.4°$ (the fitting parameter $A = 0.03$). This is close to the ideal tetrahedral angle of 109.5°. There are two observations regarding dT_c/dV which must be made: Firstly, values of dT_c/dV for sets of materials with one R metal but various x values are positive for the late rare earth materials. This is in contrast to the values for the early rare earth analogues which are negative (red and blue in Figure 4.41 respectively). The values in blue are reported for samples synthesised at nominally different compositions whilst the values in red were attempts at identical nominal compositions. Secondly, ignoring x, across the R series there is a global switch from negative dT_c/dV for the various early rare earth materials to positive values for the later R, shown by the cosine fit in green.

The first observation can be explained by a reversal of the fluoride-doping effect: F^- ions have a smaller ionic radius than O^{2-} ions (1.17 Å compared to 1.24 Å) so the ion-size effect should make the unit cell smaller as it does in early rare earth materials (the T_c increases with doping and the unit cell volume decreases, resulting in a negative dT_c/dV). This is not the only way in which fluoride substitution effects the unit cell volume, for every substitution an electron is doped into the FeAs layer, formally a reduction of Fe^{II} to Fe^{I}. The magnitude of this electron-doping effect on unit cell volume depends on the nature of the bands at the Fermi surface, which is informed by the geometry of the FeAs layer. All five iron d-orbitals are partially occupied, and we can consider the decrease in α from a simple crystal field point of view. At one extreme, *i.e.* with $\alpha = 180°$, iron is in a square-planar coordination and at the other extreme, with $\alpha = 0°$, iron is effectively linear. A schematic diagram of the d-orbital splitting is shown in Figure 4.42. The members of t_2 and e sets of orbitals cross over in terms of energy at the tetrahedral angle so some real change in the electronic structure is expected. If the-electron doping effect becomes more important than the ion-size effect for later R, fluoride doping could have a positive effect on the unit cell volume.

This reversal of the fluoride doping effect on the volume does not necessarily explain the trend in T_c(max) across the series. There is a maximum in T_c apparently brought

[4] the angle α did not show a trend with T_c within sets of $TbFeAsO_{1-x}F_x$ or $HoFeAsO_{1-x}F_x$ materials.

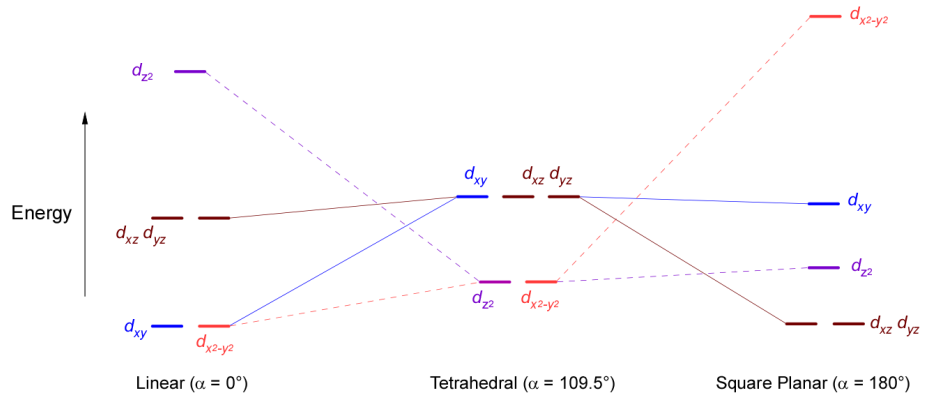

Figure 4.42: Crystal field splitting of *d*-orbitals moving from square-planar (right) through tetrahedral (centre) to linear coordinations.

about by lattice effects at or near the tetrahedral angle. Previous work has claimed that there is a steady rise in T_c with decreasing angle as the Fe ions are brought closer together,[127] the results of this work suggest that this is not the case as there is a drop off in T_c for smaller α. Claims of a global cross-family maximum at the ideal tetrahedral angle have been made before[189] and are supported by Figure 4.41, which demonstrates a maximum in the 1111 family.

Superconductivity in the iron arsenides is multiband, as mentioned above all five iron *d*-orbitals are partially occupied, and all five are involved in superconductivity,[190] so a similar argument can be made as is applied to the reversal in fluoride-doping behaviour. Figure 4.42 suggests the energies of the *d*-orbitals may be closest to each other at or just above $\alpha = 109.5°$, and this could give a maximum accessible T_c. We must bear in mind that this is a very simple schematic and the reality is more complex with the Fe ions close enough together to interact. An alternative possibility is that the allowed maximum T_c continues to increase across the series but in turn the solubility of fluoride in the system decreases, and a downturn in T_c is simply due to the inaccessibility of optimally doped samples, not a real effect of decreasing unit cell volume and angle α. The first argument is supported by the real reversal in fluoride doping demonstrating a significant crossover in the band structure at T_c(max); the fluoride doping effect on the lattice reverses for the same reason that the T_c decreases for small rare earths.

After superconductivity is induced by electron doping it appears the maximum T_c is fairly robust relative to x for the early rare earth materials, implying that the importance of electron doping may not be to provide charge carriers, but instead to suppress the 'pair breaking' magnetic ordering of the iron. Once this magnetic order

is suppressed it is the lattice effects which govern T_c. This is supported by the large pressure dependency of T_c(max) of $LaFeAsO_{1-x}F_x$,[182] which must be brought about solely by lattice effects since doping levels do not change. A decrease in T_c with pressure is predicted for holmium and terbium materials on the basis of our values for dT_c/dV for these materials, and a similar effect should exist for all the smaller rare earth 1111 superconductors (*i.e.* those beyond samarium). The fall in phase purity for the highest T_c Tb and Ho-containing samples (Table 4.4, Table 4.12) may indicate that the upper limit of fluoride doping is being reached, implying that some of the decline in observed T_c is indeed due to inaccessibility of optimally doped samples. The reality is probably a combination of both this effect and a crossover in the band structure leading to a suppression of T_c below $\alpha = 109.5°$. If the holmium and terbium materials are on the borderline of sufficient doping for superconductivity, the Tb materials are nearly optimally doped as their T_c's are comparable with T_c(max) for earlier materials. The holmium materials are of lower phase purity and fall below the curve of the rest of the series in Figure 4.41, probably the limiting factor in the T_c of the holmium material is the accessibility of optimally doped samples, while lattice effects play a small part in the suppressed T_c's.

4.9 Conclusions

From the synthesis of three new oxypnictide superconductors and the subsequent analysis of their properties, several conclusions can be drawn; for the materials themselves and the 1111 series as a whole. The newly-synthesised superconductors reported in this work are similar to each other, and share some similarities with the early 1111 superconductors: materials with nominal $x = 0.1$ are superconducting (as are Tb and Dy-containing $x = 0.2$ materials), and show no tetragonal to orthorhombic phase transition at low temperatures. Both Tb and Ho-containing materials show similar structural temperature dependence. No magnetic ordering is observed in these superconducting phases down to 1.7 K. The highest T_c's have occurred in materials of lower phase purity than is possible for materials with slightly lower T_c's, suggesting that we have reached the maximum accessible T_c for these materials and that the upper limit for fluoride doping decreases across the R series. A downturn in maximum T_c is observed for the heavier rare earth containing 1111 materials. T_c(max) = 52.8, 48.5 and 36.2 K for $TbFeAsO_{0.9}F_{0.1}$, $DyFeAsO_{0.9}F_{0.1}$, and $HoFeAsO_{0.9}F_{0.1}$ respectively.

There are differences between these and the early 1111 materials, principally that dT_c/dV is opposite in sign to previous examples. The cause of this difference, as well as the downturn in T_c for the series exhibited by these latest three members, is

put down a significant change in the electronic structure which can be simply viewed as a reversal in the order of the energies of the iron d-orbitals on crossing the ideal tetrahedral angle. Pressure-dependent superconducting property measurements would be useful in confirming the dT_c/dV values, we would expect a negative dependency of T_c on pressure for Tb, Dy, and Ho-containing materials.

From a practical point of view, the increase in difficulty of stabilising the 1111 phase for smaller R can clearly be seen by the number and quality of samples synthesised for each R. Yttrium is similar in size and chemistry to holmium but no evidence of the 1111 phase was found in ten attempts at $YFeAsO_{0.9}F_{0.1}$. Three attempts with the larger actinide uranium were also unsuccessful.

As a second class of High-T_c superconductors, comparisons have been and will continue to be drawn between the iron-based superconductors and the cuprates. the superconductivity in each material appears to be two-dimensional, with charge-reservoir layers between electronically active layers. Both materials exhibit a spin density wave which is eliminated by doping, followed by the emergence of superconductivity indicating competition between superconducting and magnetically ordered ground states in both systems. This gives rise to the similar form of the phase diagrams of both classes of material. High-temperature superconductivity has been investigated in iron arsenides for almost two years and the maximum T_c has not increased beyond 60 K, That T_c was attained within a few months. This suggests that, certainly within the known families of iron-based superconductor, the maximum possible T_c has already been achieved. This is not to say that other families of iron-based superconductor, yet to be discovered, will be subject to this maximum.

Chapter 5

General conclusions

High-pressure synthesis affords increased reactivities and solid state reaction kinetics, and can stabilise materials which are not accessible at ambient pressure. Materials synthesised at high pressures may include elements with high coordination numbers and unusual oxidation states. Chemical doping levels and solid solution ranges can often be increased using high pressures, and substitution of different elements may be possible. Materials containing rare earth elements offer a good opportunity for substitution, since the chemistry of the rare earths is not very variable and their ionic radii decrease uniformly across the series of elements. When perovskites include *A*-site rare earth elements, this decrease in size results in decreasing tolerance factors with the substitution of heavier *R*, and higher pressures are usually necessary to stabilise the materials. This can be seen in the synthesis pressures of the $R\mathrm{NiO_3}$ series. Similarly, late rare earth substitution in the $R\mathrm{FeAsO_{1-}}_x\mathrm{F}_x$ series has been achieved, with high-pressure synthesis conditions allowing the FeAs tetrahedral layers to contract and maintain the tetragonal 1111 structure as the *R*O layers decrease in size.

High-pressure synthesis may yield new materials with interesting properties different to those of samples synthesised at ambient pressure. Differences in properties are brought about either through simple lattice effects as seen in the 1111 materials, or through the different chemical properties of substitute elements. Potentially interesting materials which may be accessible at high pressures need not be limited to simple analogues of materials accessible at ambient pressure. Entirely new materials and material types may be discovered, the ability to stabilise metastable materials presented by high-pressure synthesis techniques ensures such methods remain exciting and important in field of materials chemistry.

The perovskite $\mathrm{LaPdO_3}$ has been synthesised under a range of pressures above 6 GPa. It contains $\mathrm{Pd}^{\mathrm{III}}$ ions, an oxidation sate of palladium which is usually unstable. The structure of this material has been established at temperatures between room temperature and 7 K by time-of-flight neutron diffraction at GEM at ISIS. No structural

phase transition is seen in this temperature range, in agreement with the lack of transitions displayed by resistivity and magnetisation measurements. The material is orbitally ordered with a tetragonal compression of the PdO_6 octahedra, the short bonds of each octahedron are oriented in the direction of the c unit cell axis. This distortion and orbital ordering persists throughout the temperature range investigated resulting in an O'-type orthorhombic structure. The most promising candidate for an analogue of this material is $NdPdO_3$. Praseodymium has the ability to adopt a +4 oxidation state and the formation of PrO_2 competes with the oxidation of $Pr_2Pd_2O_5$. Neodymium is the next largest rare earth and $NdPdO_3$ may be accessible at high oxygen pressures.

The 1111 family of iron-based superconductors, RFeAs$O_{1-x}F_x$, has been extended to encompass three new high-T_c superconductors containing the late rare earth metals R = Tb, Dy and Ho. All three materials were synthesised under high pressures. This has allowed the trend in T_c to be examined as the Fe–As–Fe tetrahedral angle (a key factor in the superconducting properties of these materials) moves through the ideal of 109.5°. A downturn in T_c is seen and a reversal of dependence of the unit cell volume on x compared to the early R-containing materials, a demonstration of the effects a simple decrease in the size of one ion can have on the properties across a series. The low phase purity of the holmium-containing samples suggests the lower size limit for R substitution is close to being reached. Investigations into possible magnetic ordering of the rare earth ions at low temperatures have not shown any magnetic ordering of the superconducting phases, the detection of magnetic ordering of the impurity phases has demonstrated the impressive sensitivity of the central facility instruments. Pressure-dependent measurements of the superconducting properties of these materials would be useful to confirm any lattice effects on T_c.

Publications of work in this thesis

High pressure synthesis of late rare earth RFeAs(O,F) superconductors; R = Tb and Dy

Jan-Willem G. Bos, George B. S. Penny, Jennifer A. Rodgers, Dmitry A. Sokolov, Andrew D. Huxley and J. Paul Attfield.

High pressure synthesis of late rare earth RFeAs(O,F) superconductors; R = Tb and Dy†

Jan-Willem G. Bos,[ab] George B. S. Penny,[ab] Jennifer A. Rodgers,[ab] Dmitry A. Sokolov,[ac] Andrew D. Huxley[ac] and J. Paul Attfield*[ab]

Received (in Cambridge, UK) 19th May 2008, Accepted 6th June 2008
First published as an Advance Article on the web 30th June 2008
DOI: 10.1039/b808474b

New TbFeAs(O,F) and DyFeAs(O,F) superconductors with critical temperatures T_c = 46 and 45 K and very high critical fields, ≥ 100 T, have been prepared at 1100–1150 °C and 10–12 GPa, demonstrating that high pressure may be used to synthesise late rare earth derivatives of the recently reported RFeAs(O,F) (R = La–Nd, Sm, Gd) high temperature superconductors.

A breakthrough in high temperature superconductivity has recently occurred with the discovery that rare earth oxypnictides RFeAsO (first reported for R = La, Ce, Pr, Nd, Sm and Gd)[1] can show critical temperatures surpassed only by the high-T_c cuprates. These materials have a tetragonal, layered crystal structure as depicted in the inset to Fig. 1. Superconductivity has been induced by the partial substitution of fluoride into the RO layers, which leads to electron doping (reduction of iron) in the electronically active FeAs slabs. The first report of superconductivity was in $LaFeAsO_{1-x}F_x$ samples with T_c values up to 26 K,[2] increasing to 43 K at 4 GPa pressure.[3] Superconductivity has subsequently been induced in the other members of the RFeAsO series using fluoride doping, with ambient pressure T_c values of 41 K for R = Ce,[4] 52 K for Pr[5] and Nd,[6] 43–55 K for Sm samples,[7] and 36 K for Gd.[8]

High pressure and temperature synthesis is known to stabilise many late rare earth analogues of early rare earth solid compounds. This approach has been used to explore the stabilisation of TbFeAs(O,F) and DyFeAs(O,F) phases. Polycrystalline samples of nominal compositions $RFeAsO_{1-x}F_x$ (R = Tb, Dy; x = 0, 0.1, 0.2) were synthesised from stoichiometric amounts of RAs, Fe_2O_3, FeF_2 and Fe. TbAs and DyAs were prepared from a stoichiometric mixture of the elements heated to 500 °C for 5 h and then 900 °C for 10 h in an evacuated quartz tube. All chemicals were obtained from Sigma Aldrich with at least 99.9% purity. The reactants were mixed and ground in a glove box, sealed in a BN capsule, and subjected to pressures of 10 GPa (R = Tb) or 12 GPa (R = Dy) using a Walker two-stage multianvil within a 1000 tonne press. Once at pressure, the samples were heated to 1100–1150 °C in 10 min, held at this temperature for 20 min, and then quenched to room temperature, followed by release of the pressure. The products were dense, black, sintered polycrystalline pellets and were characterised by powder X-ray diffraction, (Fig. 1) magnetisation (Fig. 2) and resistivity (Fig. 3) measurements.‡

The R = Tb samples all contained the tetragonal RFeAsO type phase with traces of TbAs (Fig. 1). The synthesis of DyFeAsO was unsuccessful but $DyFeAsO_{1-x}F_x$ phases were obtained for x = 0.1, and 0.2 with DyAs also present.[1] All four fluoride-doped samples show both magnetic and resistive superconducting transitions, with critical temperatures of 40–46 K. Fig. 2 shows that the samples are bulk superconductors, with some reduction from the theoretical full diamagnetism due to the presence of impurities and field penetration into small grains. The refined lattice parameters and T_c values are shown in Table 1. We also synthesised a new $TbFeAsO_{0.9}$ analogue of the reported oxygen-deficient $RFeAsO_{0.85}$ superconductors at 10 GPa.[9] This sample is superconducting with T_c = 50 K; further details will be reported elsewhere.

The resistivities show clear transitions to zero resistance (Fig. 3) with a smooth negative curvature of the resistivity in the normal state. This differs from data for other superconducting oxypnictides that appear to show higher temperature transitions.[10] Changes in this behaviour are theoretically predicted to be very

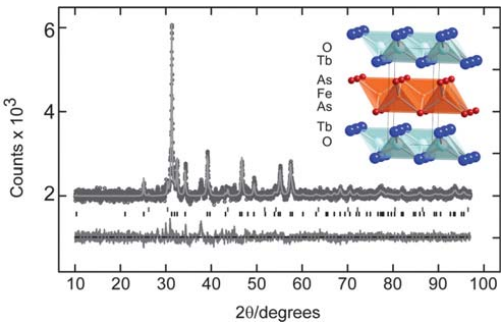

Fig. 1 Rietveld fit to the X-ray diffraction profile of $TbFeAsO_{0.9}F_{0.1}$, with Bragg reflection markers shown below those for the minority phase TbAs. An additional impurity peak is observed at 38° 2θ. Refinement residuals are R_{wp} = 2.63%, R_p = 2.00% and χ^2 = 1.64 for 24 variables. Atom positions (x, y, z) and isotropic-U values; Tb ($\frac{1}{4}$, $\frac{1}{4}$, 0.1447(4)), 0.003(1) Å^2; As ($\frac{1}{4}$, $\frac{1}{4}$, 0.6654(6)), 0.009(2) Å^2; Fe ($\frac{3}{4}$, $\frac{1}{4}$, $\frac{1}{2}$), 0.003(1) Å^2; O,F ($\frac{3}{4}$, $\frac{1}{4}$, 0), 0.07(1) Å^2. The inset shows the structure.

[a] *Centre for Science at Extreme Conditions, University of Edinburgh, King's Buildings, Mayfield Road, Edinburgh, UK EH9 3JZ. E-mail: j.p.attfield@ed.ac.uk; Fax: +44 131 651 7049; Tel: +44 131 651 7229*
[b] *School of Chemistry, University of Edinburgh, King's Buildings, West Mains Road, Edinburgh, UK EH9 3JJ*
[c] *SUPA, School of Physics, University of Edinburgh, King's Buildings, Mayfield Road, Edinburgh, UK EH9 3JZ*

† Electronic supplementary information (ESI) available: Plots of the fitted X-ray diffraction profile and resistivity for $DyFeAsO_{0.9}F_{0.1}$. See DOI: 10.1039/b808474b

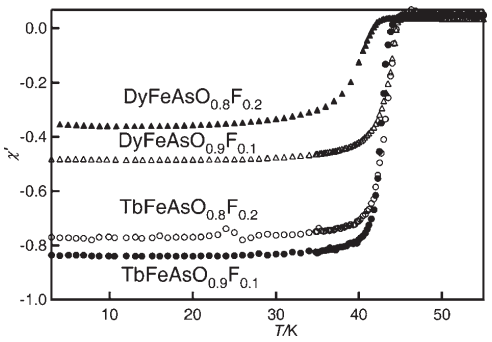

Fig. 2 Ac magnetic volume susceptibility *vs.* temperature plot for RFeAs(O,F) (R = Tb, Dy) samples; $\chi' = -1$ corresponds to full diamagnetism.

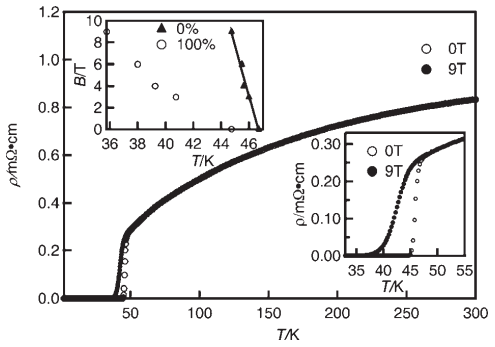

Fig. 3 Temperature dependence of the resistivity of $TbFeAsO_{0.8}F_{0.2}$. The lower inset shows the superconducting transitions in zero and 9 T fields, and the upper inset shows the onset (0%) of the transition and the zero resistance point (100%) indicative of the upper critical field (B_{c2}). The coherence length is obtained from the fit to the latter values.

Table 1 Cell parameters and volume and T_c values from the onset of diamagnetism and the resistive transition mid-point for RFeAs(O,F)

RFeAs(O,F)	a/Å	c/Å	Volume/ Å^3	$T_c(\chi_{ons})$/ K	$T_c(\rho_{mid})$/ K
TbFeAsO	3.8632(8)	8.322(3)	124.20(8)	—	—
$TbFeAsO_{0.9}F_{0.1}$	3.8634(3)	8.333(1)	124.38(3)	45.5	43.8
$TbFeAsO_{0.8}F_{0.2}$	3.860(2)	8.332(6)	124.2(2)	45.2	45.9
$DyFeAsO_{0.9}F_{0.1}$	3.8425(3)	8.2837(8)	122.30(3)	45.3	45.4
$DyFeAsO_{0.8}F_{0.2}$	3.8530(3)	8.299(1)	123.21(2)	43.0	43.0

sensitive to competing energy scales controlling the physics of these materials.[11] The resistive transition width increases with magnetic field for all samples as observed in other oxypnictides,[12] consistent with a large anisotropy of the critical field, reflecting the structural and electronic anisotropy. The upper critical field B_{c2} increases to 9 T in <2 K below T_c for $TbFeAsO_{0.8}F_{0.2}$ (Fig. 3 upper inset) and, in BCS (Bardeen–Cooper–Schrieffer) theory neglecting paramagnetic limitation, this corresponds to B_{c2} exceeding 100 T at low temperatures. Taking the onset of the transition to give the upper critical field for superconductivity in the most favourable direction (parallel to the FeAs planes) an upper estimate for the superconducting coherence length perpendicular to this direction is 13(1) Å. This corresponds to the geometric mean of the in-plane and out-of-plane coherence lengths. Given that the anisotropy is large, the out-of-plane value is therefore likely to be significantly smaller than the FeAs layer spacing, demonstrating that superconductivity is strongly 2-dimensional. The zero resistance transition field has a noticeably more marked upward curvature at low field than observed for the transition onset. This might reflect a transition to a vortex liquid state, which is well known in the high-T_c copper oxide superconductors, or be an indication of multiple band superconductivity as established in MgB_2.[13]

The T_c values of the $RFeAsO_{1-x}F_x$ (R = Tb, Dy, x = 0.1, 0.2) samples do not differ greatly and there is no clear trend in the lattice parameters with x, showing that the actual range of doping may be more limited that in the nominal compositions. Further work will be needed to determine the precise range of x and optimise phase purity. It is notable that the T_c values of TbFeAs(O,F) and DyFeAs(O,F) are comparable to those of the early R = Ce, Pr, Nd, Sm materials. The lower value of 36 K reported for GdFeAs(O,F)[8] suggested that superconductivity might be suppressed as the rare earth size decreases, but the present results show that the superconducting properties change little between Ce and Dy. It will be important to explore further RFeAs(O,F) superconductors of the heavy rare earths to discover how superconductivity develops across the entire series.

Notes and references

‡ Powder X-ray diffraction data were collected on a Bruker AXS D8 diffractometer using Cu Kα_1 radiation. Data were recorded at $10 \leq 2\theta \leq 100°$ with a step size of 0.007° for Rietveld analysis. The ac magnetic susceptibility was measured from 3 to 50 K with a field of 0.5 Oe oscillating at 117 Hz using a Quantum Design superconducting quantum interference device magnetometer. The electrical resistivity was measured by the conventional four-probe method between 1.7 and 300 K using a Quantum Design physical property measurement system.

1 P. Quebe, L. J. Terbuchte and W. Jeitschko, *J. Alloys Compd.*, 2000, **302**, 70.
2 Y. Kamihara, T. Watanabe, M. Hirano and H. Hosono, *J. Am. Chem. Soc.*, 2008, **130**, 3296.
3 H. Takahashi, K. Igawa, K. Arii, Y. Kamihara, M. Hirano and H. Hosono, *Nature*, 2008, **453**, 376.
4 G. F. Chen, Z. Li, D. Wu, G. Li, W. Z. Hu, J. Dong, P. Zheng, J. L. Luo and N. L. Wang, *Phys. Rev. Lett.*, 2008, **100**, 247002.
5 Z.-A. Ren, J. Yang, W. Lu. W. Yi, G.-C. Che, X.-L. Dong, L.-L. Sun and Z.-X. Zhao, unpublished results, arXiv:0803.4283.
6 Z.-A. Ren, J. Yang, W. Lu, W. Yi, X.-L. Shen, Z.-C. Li, G.-C. Che, X.-L. Dong, L.-L. Sun, F. Zhou and Z.-X. Xhao, *Europhys. Lett.*, 2008, **82**, 57002.
7 X. H. Chen, T. Wu, G. Wu, R. H. Liu, H. Chen and D. F. Fang, *Nature*, 2008, **453**, 761; Z.-A. Ren, W. Lu, J. Yang, W. Yi, X.-L. Shen, Z.-C. Li, G.-C. Che, X.-L. Dong, L.-L. Sun, F. Zhou and X.-X. Zhao, *Chin. Phys. Lett.*, 2008, **25**, 2215R. H. Liu, G. Wu, T. Wu, D. F. Fang, H. Chen, S. Y. Li, K. Liu, Y. L. Xie, X. F. Wang, R. L. Wang, L. Ding, C. He, D. L. Feng and X. H. Chen, unpublished results, arXiv:0804.2105.
8 P. Cheng, L. Fang, H. Yang, X. Zhu, G. Mu, H. Luo, Z. Wang and H.-H. Wen, *Sci. China, Ser. G*, 2008, **51**, 719.
9 Z.-A. Ren, G.-C. Che, X.-L. Dong, J. Yang, W. Lu, W. Yi, X.-L. Shen, Z.-C. Li, L.-L. Sun, F. Zhou and Z.-X. Zhao, *Europhys. Lett.*, 2008, **83**, 17002.
10 G. F. Chen, Z. Li, D. Wu, J. Dong, G. Li, W. Z. Hu, P. Zheng, J. L. Luo and N. L. Wang, *Chin. Phys. Lett.*, 2008, **25**, 2235.
11 K. Haule and G. Kotliar, unpublished results, arXiv:0805.0722.
12 F. Hunte, J. Jaroszynski, A. Gurevich, D. C. Larbalestier, R. Jin, A. S. Sefat, M. A. McGuire, B. C. Sales, D. K. Christen and D. Mandrus, *Nature*, 2008, **453**, 903.
13 V. H. Dao and M. E. Zhitomirsky, *Eur. Phys. J. B*, 2005, **44**, 183.

Suppression of the superconducting transition of $R\mathbf{FeAsO}_{1-x}\mathbf{F}_x$ (R = Tb, Dy, and Ho)

Jennifer A. Rodgers, George B. S. Penny, Andrea Marcinkova, Jan-Willem G. Bos, Dmitry A. Sokolov, Anna Kusmartseva, Andrew D. Huxley and J. Paul Attfield.

Reproduced with permission from Physical Review B (Condensed Matter and Materials Physics), volume 80, 052508 (2009).

Suppression of the superconducting transition of $R\mathrm{FeAsO}_{1-x}\mathrm{F}_x$ (R=Tb, Dy, and Ho)

Jennifer A. Rodgers,[1,2] George B. S. Penny,[1,2] Andrea Marcinkova,[1,2] Jan-Willem G. Bos,[1,2] Dmitry A. Sokolov,[1,3] Anna Kusmartseva,[1,2] Andrew D. Huxley,[1,3] and J. Paul Attfield[1,2,*]

[1]*Centre for Science at Extreme Conditions, University of Edinburgh, King's Buildings, Mayfield Road, Edinburgh EH9 3JZ, United Kingdom*

[2]*School of Chemistry, University of Edinburgh, Edinburgh EH9 3JJ, United Kingdom*

[3]*SUPA, School of Physics, University of Edinburgh, Edinburgh EH9 3JZ, United Kingdom*

(Received 31 July 2009; published 28 August 2009)

A suppression of superconductivity in the late rare-earth $R\mathrm{FeAsO}_{1-x}\mathrm{F}_x$ materials is reported. The maximum critical temperature (T_c) decreases from 51 K for R=Tb to 36 K for $\mathrm{HoFeAsO}_{0.9}\mathrm{F}_{0.1}$, which has been synthesized under 10 GPa pressure. This suppression is driven by a decrease in the Fe-As-Fe angle below an optimum value of 110.6°, as the angle decreases linearly with unit-cell volume (V) across the $R\mathrm{FeAsO}_{1-x}\mathrm{F}_x$ series. A crossover in electronic structure around this optimum geometry is evidenced by a change in sign of the compositional dT_c/dV, from negative values for previously reported large R materials to positive for $\mathrm{HoFeAsO}_{0.9}\mathrm{F}_{0.1}$.

DOI: 10.1103/PhysRevB.80.052508 PACS number(s): 74.62.Dh, 74.62.Bf, 74.70.Dd

Rare earth (R) oxypnictides RFeAsO (Ref. 1) were recently discovered to superconduct when doped, with critical temperatures surpassed only by the high-T_c cuprates. Several families of superconducting iron pnictides have subsequently been discovered.[2] These all have layered structures containing AsFeAs slabs with Fe tetrahedrally coordinated by As. The main types are the 1111 materials based on RFeAsO or MFeAsF (M=Ca,Sr,Ba), the 122 phases $M\mathrm{Fe}_2\mathrm{As}_2$, and the 111 AFeAs (A=Li,Na) family. The related binaries FeX (X=Se,Te) are also superconducting.

The electron-doped 1111 materials $R\mathrm{FeAsO}_{1-x}\mathrm{F}_x$ and $R\mathrm{FeAsO}_{1-\delta}$ materials remain prominent as they have the highest T_c's, up to 56 K, and allow lattice and doping effects to be investigated through variations in the R^{3+} cation size and the anion composition. A strong lattice effect is evident at the start of the rare-earth series, as T_c rises from 26 K for $\mathrm{LaFeAsO}_{1-x}\mathrm{F}_x$ to 43 K under pressure,[3,4] and to a near-constant maximum 50–56 K in the $R\mathrm{FeAsO}_{1-x}\mathrm{F}_x$ and $R\mathrm{FeAsO}_{1-\delta}$ series for R=Pr to Gd,[5–10] but whether lattice effects ultimately enhance or suppress superconductivity for the late R's has been unclear. The late rare-earth $R\mathrm{FeAsO}_{1-x}\mathrm{F}_x$ materials and the oxygen-deficient $R\mathrm{FeAsO}_{1-\delta}$ superconductors require high-pressure synthesis, leading to significant challenges as single phase samples are difficult to prepare, and accurate analyses of cation stoichiometries and O and F contents are difficult. To investigate the effect of the lattice for later R, we have synthesized multiple samples of $R\mathrm{FeAsO}_{0.9}\mathrm{F}_{0.1}$ (R=Tb, Dy, and Ho) under varying high-pressure conditions. Here we report superconductivity in $\mathrm{HoFeAsO}_{0.9}\mathrm{F}_{0.1}$ for which the maximum T_c of 36 K is markedly lower than in the previous R analogs. This is part of a systematic suppression of superconductivity by the smaller, late R cations. $\mathrm{HoFeAsO}_{0.9}\mathrm{F}_{0.1}$ also shows a reversal in the sign of the compositional dT_c/dV (V=unit-cell volume) compared to the early R materials, confirming that the decreasing R size has a significant effect on the bands contributing to the Fermi surface.

Polycrystalline ceramic $R\mathrm{FeAsO}_{1-x}\mathrm{F}_x$ samples (R=Tb, Dy, and Ho) were synthesized by a high-pressure method and investigated by powder x-ray diffraction, magnetization, and conductivity measurements.[11] Initial results for $R\mathrm{FeAsO}_{1-x}\mathrm{F}_x$ (R=Tb and Dy) were published elsewhere.[12] Both materials were found to be superconducting with maximum T_c's of 46 and 45 K, respectively. Little difference in superconducting properties between samples with nominal compositions of x=0.1 and 0.2 were observed, and the x=0.2 materials were generally of lower phase purity, and so the x=0.1 composition was used in subsequent syntheses. The best samples typically contain ~80% by mass of the superconducting phase with residual nonsuperconducting $R_2\mathrm{O}_3$ and RAs phases also present. The sample purity and superconducting properties are not sensitive to synthesis pressure over a range that moves to higher pressures as R decreases in size; R=Tb and Dy superconductors were respectively prepared at 7–10 and 8–12 GPa, heating at 1050–1100 °C. Repeated syntheses of $\mathrm{TbFeAsO}_{1-x}\mathrm{F}_x$ gave several samples with higher T_c's than the above value, the highest value is T_c(max)=51 K (Fig. 1). Further $\mathrm{DyFeAsO}_{1-x}\mathrm{F}_x$ samples did not show higher transitions than before, so we conclude that T_c(max) in this system is 45 K.

Tetragonal $\mathrm{HoFeAsO}_{0.9}\mathrm{F}_{0.1}$ was obtained from reactions at 10 GPa pressure and the properties of six $\mathrm{HoFeAsO}_{0.9}\mathrm{F}_{0.1}$ samples prepared under varying conditions are summarized

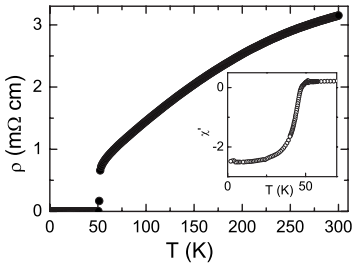

FIG. 1. Resistivity and (inset) susceptibility data for an optimum sample of $\mathrm{TbFeAsO}_{0.9}\mathrm{F}_{0.1}$, showing a sharp superconducting transition at T_c=51 K. The sample was prepared at 7 GPa and 1050 °C.

TABLE I. Synthesis conditions (all samples were synthesized at 10 GPa), refined lattice parameters and volume, T_c's, mass fractions, and superconducting volume fractions for $HoFeAsO_{1-x}F_x$ samples.

Sample	t_{synth} (hr)	T_{synth} (°C)	a (Å)	c (Å)	Vol (Å^3)	T_c (K)	Mass frac. (%)	Diamag. frac. (%)
1	2	1150	3.8246(3)	8.254(1)	120.74(3)	29.3	75	70
2	2	1100	3.8272(2)	8.2649(8)	121.06(2)	33.0	74	85
3	1	1150	3.8258(5)	8.264(2)	120.96(4)	33.2	73	76
4	3	1100	3.8282(5)	8.261(2)	121.07(5)	33.7	84	74
5	2	1100	3.8282(2)	8.2654(7)	121.13(2)	35.2	81	57
6	2	1100	3.8297(7)	8.270(2)	121.30(7)	36.2	58	46

in Table I. Crystal structure refinements and phase analysis were carried out by fitting powder x-ray diffraction data (Fig. 2).[13] Magnetization measurements demonstrate that all six $HoFeAsO_{1-x}F_x$ samples are bulk superconductors with T_c's of 29–36 K (Fig. 3). Resistivities show smooth high-temperature evolutions without apparent spin-density wave anomalies. The transitions to the zero resistance state have widths of less than 4 K.

Although all of the samples in Table I have the same starting composition, small variations in synthesis pressure and temperature result in a dispersion in x around the nominal 0.1 value for the $HoFeAsO_{1-x}F_x$ phase and corresponding variations in superconducting properties. T_c increases to a maximum value, T_c(max), at the upper solubility limit of x in $RFeAsO_{1-x}F_x$ systems,[7] and this is consistent with the observation that the superconducting phases in samples 1, 3, and 4, which are heated at high temperatures or for longer times and so are likely to have a slightly lower F content, have lower T_c's (average 32.1 K) than the other three samples, made under nominally identical "optimum" conditions, which have average T_c=34.8 K. Sample 6 shows the highest T_c=36.2 K and the lowest proportion of the $HoFeAsO_{1-x}F_x$ phase and a correspondingly low diamagnetic volume fraction. This demonstrates that the sample is at the upper limit of the superconducting composition range and so gives a realistic T_c(max) for the $HoFeAsO_{1-x}F_x$ system.

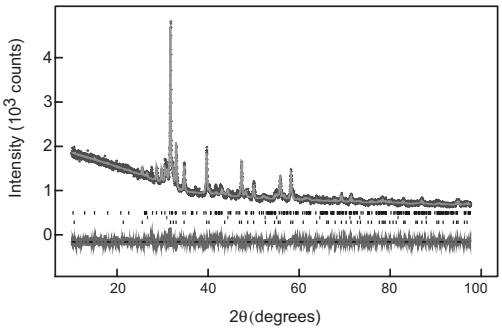

FIG. 2. Fitted x-ray diffraction profile for $HoFeAsO_{0.9}F_{0.1}$ (sample 5) at room temperature. The Bragg markers (from top to bottom) are for the minority phases, Ho_2O_3 and HoAs, and for $HoFeAsO_{0.9}F_{0.1}$.

Although the doping values x for the high-pressure $RFeAsO_{1-x}F_x$ samples are not known precisely, comparing ensembles of samples with similar phase purities made under similar conditions reveals a clear suppression of superconductivity by lattice effects for heavier R. For example, all of our $TbFeAsO_{1-x}F_x$ superconductors have higher T_c's (five $TbFeAsO_{1-x}F_x$ samples, T_c=45–51 K) than all of the $HoFeAsO_{1-x}F_x$ materials (in Table I). The T_c(max) values of 51, 45, and 36 K for $RFeAsO_{1-x}F_x$ with R=Tb, Dy, and Ho, respectively, thus represent the trend correctly.

Figure 4 shows a plot of the maximum critical temperatures, T_c(max), against unit-cell volume for many reported $RFeAsO_{1-x}F_x$ and $RFeAsO_{1-\delta}$ systems and our above materials. T_c(max) rises slowly as cell volume decreases for R=La to Pr and then shows a broad maximum, between R=Pr and Tb in the $RFeAsO_{1-x}F_x$ materials, before falling rapidly as R changes from Tb to Dy to Ho. This trend is not seen in the reported $RFeAsO_{1-x}$ superconductors, where T_c(max) remains approximately constant,[14,15] apparently because they have larger cell volumes than their $RFeAsO_{1-x}F_x$ analogs (see Fig. 4).

The size of the R^{3+} cation tunes the electronic properties through variations in the geometry of the FeAs slab. A trend between the As-Fe-As (or equivalent Fe-As-Fe) angle and T_c has been reported for the early R materials.[16] The upper panel of Fig. 4 shows representative reported values for optimal $RFeAsO_{1-x}F_x$ superconductors including our R=Tb, Dy, and Ho materials. This demonstrates that the angle decreases monotonically with R size and so does not show a universal correlation with T_c(max). The T_c(max) variation in the $RFeAsO_{1-x}F_x$ series is described by a simple $\cos(\phi - \phi_0)$ function, shown in Fig. 4, where the value of the As-

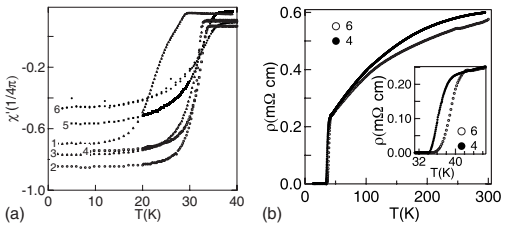

FIG. 3. Superconductivity measurements for $HoFeAs_{0.9}F_{0.1}$; (a) ac magnetic volume susceptibility for the six samples; (b) resistivities for samples 4 and 6.

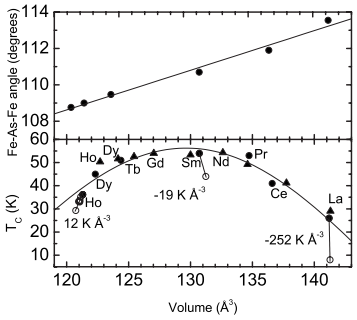

FIG. 4. Variation in Fe-As-Fe angle ϕ (upper panel) and superconducting T_c (lower panel) with unit-cell volume for different $R\mathrm{FeAsO}_{1-x}\mathrm{F}_x$ (circles) (Refs. 19, 22, 5, 7, and 12) and $R\mathrm{FeAsO}_{1-\delta}$ (triangles) (Refs. 14 and 15). T_c(max) points are shown as filled symbols. The fit of equation $T_c(\mathrm{max})=T_c(\mathrm{max})_0\cos A(\phi-\phi_0)$ with parameters $T_c(\mathrm{max})_0=56$ K, $A=0.03$, and $\phi_0=110.6°$ is also shown. dT_c/dV values are derived from the data for suboptimally doped materials (open symbols) in the R=La (Ref. 19), Sm (Ref. 7), and Ho (this Brief Report) systems.

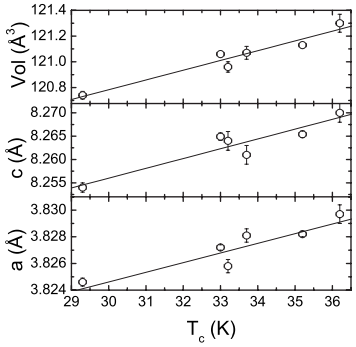

FIG. 5. Variations in T_c with the tetragonal unit-cell parameters and volume for the six $\mathrm{HoFeAsO}_{1-x}\mathrm{F}_x$ samples in Table I.

Fe-As angle corresponding to the global maximum T_c, $\phi_{\max}=110.6°$, is close to the ideal 109.5° value for a regular FeAs_4 tetrahedron. All five of the Fe 3d bands are partially occupied and contribute to the Fermi surface of the iron arsenide superconductors through hybridization with As 4s and 4p states.[17] Decreasing the tetrahedral angle through 109.5° marks the crossover from tetragonal compression to elongation of the FeAs_4 tetrahedra. In a crystal-field model, this reverses the splittings of the t_2 and e d-orbital sets and so a significant crossover in the real electronic structure is likely to occur near 109.5°.

Evidence for the above crossover also comes from a discovered change in the sign of the compositional dT_c/dV near optimum doping in the $R\mathrm{FeAsO}_{1-x}\mathrm{F}_x$ systems.[18] The unit-cell parameters and volume for the six $\mathrm{HoFeAsO}_{1-x}\mathrm{F}_x$ samples in Table I show a positive correlation with T_c (Fig. 5), in contrast to early R=La (Ref. 19) and Sm (Ref. 7) analogs, where lattice parameters and volume decease with increasing T_c. The T_c, V points for near-optimally doped R=La, Sm, and Ho $R\mathrm{FeAsO}_{1-x}\mathrm{F}_x$ superconductors are shown in Fig. 4 together with the derived dT_c/dV values. dT_c/dV for a single $R\mathrm{FeAsO}_{1-x}\mathrm{F}_x$ system follows the overall trend in $dT_c(\mathrm{max})/dV$ for different R's, changing from a negative value at large R=La to a small positive slope at R=Ho.

The compositional dT_c/dV for a given $R\mathrm{FeAsO}_{1-x}\mathrm{F}_x$ system reflects two competing effects of variations in the fluoride content x on the lattice volume. F^- is slightly smaller than O^{2-} so the anion substitution effect gives a negative contribution to the compositional dT_c/dV, independent of R. The concomitant effect of doping electrons into the Fe d bands tends to expand the lattice (and increase T_c), but the magnitude of this positive dT_c/dV term depends on the nature of the bands at the Fermi surface. The observed shift from negative to positive dT_c/dV as R changes from La to Ho shows that the decreasing size of the R^{3+} cation leads to significant changes in the Fermi surface, with volume-expanding (antibonding) bands more prominent for smaller R. Calculations have confirmed that the electronic structure near the Fermi level is sensitive to such small changes in the As z coordinate (equivalent to changing the Fe-As-Fe angle).[20] Small changes in the contributions of the d bands are likely to be particularly important in a multigap scenario for superconductivity, as evidenced in gap measurements of $\mathrm{TbFeAsO}_{0.9}\mathrm{F}_{0.1}$ and other iron arsenide materials.[21]

In summary, our analysis of multiple samples of $R\mathrm{FeAsO}_{1-x}\mathrm{F}_x$ (R=Tb, Dy, and Ho) superconductors demonstrates that the maximum critical temperature falls from 51 K for R=Tb to 36 K for the previously unreported Ho analog. Hence, the effect on the lattice of substituting smaller late rare earths in the $R\mathrm{FeAsO}_{1-x}\mathrm{F}_x$ lattice suppresses superconductivity. This lattice control appears to be through tuning of the interatomic angles in the FeAs layer, with the optimum angle being 110.6°, near the ideal tetrahedral value. The compositional dT_c/dV changes sign around the optimum angle evidencing significant changes in the Fermi surface. It appears difficult to increase the critical temperatures above 56 K in 1111 type iron arsenide materials through tuning lattice effects, although the possibility of higher T_c's in other structure types remains open.

We acknowledge EPSRC, the Royal Society of Edinburgh and the Leverhulme trust for support.

*Corresponding author; j.p.attfield@ed.ac.uk

[1] P. Quebe, L. J. Terbuchte, and W. Jeitschko, J. Alloys Compd. **302**, 70 (2000).
[2] J. W. Lynn and P. Dai, Physica C **469**, 469 (2009).
[3] Y. Kamihara, T. Watanabe, M. Hirano, and H. Hosono, J. Am. Chem. Soc. **130**, 3296 (2008).
[4] H. Takahashi, K. Igawa, K. Arii, Y. Kamihara, M. Hirano, and H. Hosono, Nature (London) **453**, 376 (2008).
[5] Z. A. Ren, J. Yang, W. Lu, W. Yi, G. C. Che, X. L. Dong, L. L. Sun, and Z. X. Zhao, Mater. Res. Innovations **12**, 105 (2008).
[6] Z. A. Ren, J. Yang, W. Lu, W. Yi, X. L. Shen, Z. C. Li, G. C. Che, X. L. Dong, L. L. Sun, F. Zhou, and Z. X. Zhao, EPL **82**, 57002 (2008).
[7] X. H. Chen, T. Wu, G. Wu, R. H. Liu, H. Chen, and D. F. Fang, Nature (London) **453**, 761 (2008).
[8] Z. A. Ren, W. Lu, J. Yang, W. Yi, X. L. Shen, Z. C. Li, G. C. Che, X. L. Dong, L. L. Sun, F. Zhou, and Z. X. Zhao, Chin. Phys. Lett. **25**, 2215 (2008).
[9] R. H. Liu, G. Wu, T. Wu, D. F. Fang, H. Chen, S. Y. Li, K. Liu, Y. L. Xie, X. F. Wang, R. L. Yang, L. Ding, C. He, D. L. Feng, and X. H. Chen, Phys. Rev. Lett. **101**, 087001 (2008).
[10] P. Cheng, L. Fang, H. X. Yang, X. Zhu, G. Mu, H. Luo, Z. Wang, and H. Wen, Sci. China, Ser. G **51**, 719 (2008).
[11] Samples were synthesized from stoichiometric amounts of *R*As, Fe_2O_3, FeF_2, and Fe, using a Walker multianvil module within a 1000 ton press. The products were dense, black, sintered polycrystalline pellets. Powder x-ray diffraction data were collected on a Bruker AXS D8 diffractometer using Cu Kα_1 radiation. Data were recorded at $10 \leq 2\theta \leq 100°$ with a step size of 0.007° for Rietveld analysis. ac magnetic susceptibility was measured from 3 to 50 K with a field of 0.5 Oe oscillating at 117 Hz using a Quantum Design SQUID magnetometer. Electrical resistivity was measured by a four-probe method between 1.7 and 300 K using a Quantum Design physical property measurement system and an APD cryogenics closed cycle refrigeration unit with an in-house built sample stage.
[12] J.-W. G. Bos, G. B. S. Penny, J. A. Rodgers, D. A. Sokolov, A. D. Huxley, and J. P. Attfield, Chem. Commun. **31**, 3634 (2008).
[13] $HoFeAsO_{0.9}F_{0.1}$ has a tetragonal structure (space group $P4/nmm$; results from fit shown in Fig. 2; goodness of fit $\chi^2 = 1.60$, residuals; $R_{wp} = 3.94\%$, $R_p = 3.02\%$; cell parameters $a = 3.8282(2)$ Å, $c = 8.2654(7)$ Å; atom positions $[x, y, z]$ and isotropic temperature (U) factors; Ho $[\frac{1}{4}, \frac{1}{4}, 0.1454(4)]$, 0.044(2) Å^2; As $[\frac{1}{4}, \frac{1}{4}, 0.6659(5)]$, 0.029(2) Å^2; Fe $(\frac{3}{4}, \frac{1}{4}, \frac{1}{2})$, 0.014(2) Å^2; O,F $(\frac{3}{4}, \frac{1}{4}, 0)$, 0.26(2) Å^2). The secondary Ho_2O_3 phase is in a high-pressure *B*-type rare-earth oxide modification, space group $C2/m$, $a = 13.841(2)$ Å, $b = 3.4984(5)$ Å, $c = 8.608(1)$ Å, $\beta = 100.08(1)°$.
[14] K. Miyazawa, K. Kihou, P. M. Shirage, C. H. Lee, H. Kito, H. Eisaki, and A. Iyo, J. Phys. Soc. Jpn. **78**, 034712 (2009).
[15] J. Yang, X. L. Shen, W. Lu, W. Yi, Z. C. Li, Z. A. Ren, G. C. Che, X. L. Dong, L. L. Sun, F. Zhou, and Z. X. Zhao, New J. Phys. **11**, 025005 (2009).
[16] J. Zhao, Q. Huang, C. de la Cruz, S. Li, J. W. Lynn, Y. Chen, M. A. Green, G. F. Chen, G. Li, Z. Li, J. L. Luo, N. L. Wang, and P. Dai, Nature Mater. **7**, 953 (2008).
[17] D. J. Singh and M.-H. Du, Phys. Rev. Lett. **100**, 237003 (2008).
[18] The compositional dT_c/dV quantifies the changes in T_c and unit-cell volume V due to variations in doping level x at constant (atmospheric) pressure, and is complementary to the pressure-induced dT_c/dV at constant x. Both derivatives are negative for $LaFeAsO_{1-x}F_x$, and we thus predict a positive pressure-induced dT_c/dV (pressure suppression of superconductivity) for $HoFeAsO_{1-x}F_x$.
[19] Q. Huang, J. Zhao, J. W. Lynn, G. F. Chen, J. L. Luo, N. L. Wang, and P. Dai, Phys. Rev. B **78**, 054529 (2008).
[20] S. Lebègue, Z. P. Yin, and W. E. Pickett, New J. Phys. **11**, 025004 (2009).
[21] K. A. Yates, K. Morrison, J. A. Rodgers, G. B. S. Penny, J. W. G. Bos, J. P. Attfield, and L. F. Cohen, New J. Phys. **11**, 025015 (2009).
[22] G. F. Chen, Z. Li, D. Wu, G. Li, W. Z. Hu, J. Dong, P. Zheng, J. L. Luo, and N. L. Wang, Phys. Rev. Lett. **100**, 247002 (2008).

Nomenclature

AC Alternating current

BCS Refers to Bardeen, Cooper and Schrieffer's theory of superconductivity, and superconductors which obey it.

CDW Charge density wave

CMR Colossal magnetoresistance

CO Charge order/charge ordering

DAC Diamond anvil cell

DC Direct current

DIA From 'diamond'. Applies to a specific press design which converts uniaxial to cubic triaxial pressure

ESRF European Synchrotron Radiation Facility

FWHM Full width at half maximum

GEM General materials diffractometer

GSAS General structure and analysis system

H_c Critical field, the magnetic field above which superconducting properties are lost by a material

HRTEM High-resolution transmission electron microscope

ILL Institut Laue-Langevin

MPMS Magnetic properties measurement system

OEL Octahedron edge length

PND Powder neutron diffraction

PPMS Physical properties measurement system

PSD Position sensitive detector

PTFE Polytetrafluoroethane

PXRD Powder x-ray diffraction

SAED Selected-area electron diffraction

SDW Spin density wave

SQUID Superconducting quantum interference device

$\mathbf{T_C}$ Curie temperature - the temperature at which the spins ferromagnets become ordered

$\mathbf{T_N}$ Néel temperature - the temperature at which the spins antiferromagnets become ordered

$\mathbf{T_c}$ Superconducting transition temperature: the temperature below which a material becomes superconducting.

TEL Truncation edge length

Z Atomic number

Bibliography

[1] M. I. McMahon and R. J. Nelmes, Chem. Soc. Rev. **35**, 1341 (2006).

[2] W. Nellis, A. Louis, and N. Ashcroft, Phil. Trans. R. Soc. London A **356**, 119 (1998).

[3] V. Struzhkin, R. Hemley, H. Mao, and Y. Timofeev, Nature **390**, 382 (1997).

[4] L. Gao, Y. Y. Xue, F. Chen, Q. Xiong, R. L. Meng, D. Ramirez, C. W. Chu, J. H. Eggert, and H. K. Mao, Phys. Rev. B **50**, 4260 (1994).

[5] S. Klotz, T. Strässle, R. J. Nelmes, J. S. Loveday, G. Hamel, G. Rousse, B. Canny, J. C. Chervin, and A. M. Saitta, Phys. Rev. Lett. **94**, 025506 (2005).

[6] I. D. H. Oswald, I. Chataigner, S. Elphick, F. P. A. Fabbiani, A. R. Lennie, J. Maddaluno, W. G. Marshall, T. J. Prior, C. R. Pulham, and R. I. Smith, CrystEngComm. **11**, 359 (2009).

[7] P. McMillan, Nat. Mater. **1**, 19 (2002).

[8] A. R. West, *Basic Solid State Chemistry* (Wiley, 1999).

[9] E. Ito and E. Takahashi, J. Geophys. Res. B **94**, 10637 (1989).

[10] G. Demazeau, C. Parent, M. Pouchard, and P. Hagenmüller, Mater. Res. Bull. **7**, 913 (1972).

[11] B. L. Chamberland, Solid State Commun. **5**, 663 (1967).

[12] J. A. Rodgers, A. J. Williams, and J. P. Attfield, Z. Naturforsch., B: Chem. Sci. **61**, 1515 (2006).

[13] M. Murakami, K. Hirose, K. Kawamura, N. Sata, and Y. Ohishi, Science **304**, 855 (2004).

[14] G. Jonker and J. Vansanten, Physica **16**, 337 (1950).

[15] M. Gilleo, Acta Crystallogr. **10**, 161 (1957).

[16] P. Forsbergh, Phys. Rev. **76**, 1187 (1949).

[17] J. Wang, J. Neaton, H. Zheng, V. Nagarajan, S. Ogale, B. Liu, D. Viehland, V. Vaithyanathan, D. Schlom, U. Waghmare, et al., Science **299**, 1719 (2003).

[18] T. Kimura, S. Kawamoto, I. Yamada, M. Azuma, M. Takano, and Y. Tokura, Phys. Rev. B **67** (2003).

[19] A. Glazer, Acta Crystallogr., Sect. B: Struct. Sci. **B 28**, 3384 (1972).

[20] V. M. Goldschmidt, Naturwissenschaften **14**, 477 (1926).

[21] P. Woodward, Acta Crystallogr., Sect. B: Struct. Sci. **53**, 44 (1997).

[22] J. Longo, P. Raccah, and J. Goodenough, J. Appl. Phys. **39**, 1327 (1968).

[23] E. O. Wollan and W. C. Koehler, Phys. Rev. **100**, 545 (1955).

[24] A. Belik, S. Iikubo, K. Kodama, N. Igawa, S. Shamoto, S. Niitaka, M. Azuma, Y. Shimakawa, M. Takano, F. Izumi, et al., Chem. Mater. **18**, 798 (2006).

[25] W. C. Koehler, E. O. Wollan, and M. K. Wilkinson, Phys. Rev. **118**, 58 (1960).

[26] A. Urushibara, Y. Moritomo, T. Arima, A. Asamitsu, G. Kido, and Y. Tokura, Phys. Rev. B **51**, 14103 (1995).

[27] M. Uehara, S. Mori, C. Chen, and S. Cheong, Nature **399**, 560 (1999).

[28] C. Zener, Phys. Rev. **82**, 403 (1951).

[29] A. Millis, P. Littlewood, and B. Shraiman, Phys. Rev. Lett. **74**, 5144 (1995).

[30] C. Chaillout, A. Santoro, J. Remeika, A. Cooper, G. Espinosa, and M. Marezio, Solid State Commun. **65**, 1363 (1988).

[31] S. Pei, J. D. Jorgensen, B. Dabrowski, D. G. Hinks, D. R. Richards, A. W. Mitchell, J. M. Newsam, S. K. Sinha, D. Vaknin, and A. J. Jacobson, Phys. Rev. B **41**, 4126 (1990).

[32] A. Sleight, J. Gillson, and P. Bierstedt, Solid State Commun. **17**, 27 (1975).

[33] R. Cava, B. Batlogg, J. Krajewski, R. Farrow, L. Rupp, A. White, K. Short, W. Peck, and T. Kometani, Nature **332**, 814 (1988).

[34] M. Braden, W. Reichardt, E. Elkaim, J. Lauriat, S. Shiryaev, and S. Barilo, Phys. Rev. B **62**, 6708 (2000).

[35] H. Kamerlingh Onnes, Comm. Phys. Lab. Univ. Leiden **122** (1911).

[36] W. Meissner and R. Ochsenfeld, Naturwissenschaften **21**, 787 (1933).

[37] J. Bardeen, L. Cooper, and J. Schrieffer, Phys. Rev. **108**, 1175 (1957).

[38] J. Gavaler, Appl. Phys. Lett. **23**, 480 (1973).

[39] J. Bednorz and K. Muller, Z. Phys. B **64**, 189 (1986).

[40] M. Wu, J. Ashburn, C. Torng, P. Hor, R. Meng, L. Gao, Z. Huang, Y. Wang, and C. Chu, Phys. Rev. Lett. **58**, 908 (1987).

[41] K. Tanigaki, T. Ebbesen, S. Saito, J. Mizuki, J. Tsai, Y. Kubo, and S. Kuroshima, Nature **352**, 222 (1991).

[42] G. R. Darling, A. Y. Ganin, M. J. Rosseinsky, Y. Takabayashi, and K. Prassides, Phys. Rev. Lett. **101**, 136404 (2008).

[43] J. Nagamatsu, N. Nakagawa, T. Muranaka, Y. Zenitani, and J. Akimitsu, Nature **410**, 63 (2001).

[44] F. Bloch, Z. Phys. A **52**, 555 (1929).

[45] E. Maxwell, Phys. Rev. **78**, 477 (1950).

[46] H. Fröhlich, Phys. Rev. **79**, 845 (1950).

[47] J. Bardeen, Phys. Rev. **79**, 167 (1950).

[48] R. J. Cava, R. B. van Dover, B. Batlogg, and E. A. Rietman, Phys. Rev. Lett. **58**, 408 (1987).

[49] H. Maeda, Y. Tanaka, M. Fukutomi, and T. Asano, Jpn. J. Appl. Phys., Part 2 **27**, L209 (1988).

[50] Z. Sheng and A. Hermann, Nature **332**, 138 (1988).

[51] A. Schilling, M. Cantoni, J. Guo, and H. Ott, Nature **363**, 56 (1993).

[52] P. Dai, B. Chakoumakos, G. Sun, K. Wong, Y. Xin, and D. Lu, Physica C **243**, 201 (1995).

[53] J. Jorgensen, Phys. Today **44**, 34 (1991).

[54] P. Anderson, Science **235**, 1196 (1987).

[55] P. Monthoux and D. Pines, Phys. Rev. Lett. **69**, 961 (1992).

[56] P. Monthoux, A. V. Balatsky, and D. Pines, Phys. Rev. B **46**, 14803 (1992).

[57] H. Won, Y. Morita, and K. Maki, Phys. Status Solidi B **244**, 4371 (2007).

[58] E. Dagotto, Rev. Mod. Phys. **66**, 763 (1994).

[59] P. Decarli and J. Jamieson, Science **133**, 1821 (1961).

[60] P. Bridgman, Proc. Roy. Soc. Lond. Math. Phys. Sci. **203**, 1 (1950).

[61] F. Bundy, H. Hall, H. Strong, and R. Wentorf, Nature **176**, 51 (1955).

[62] H. Bovenkerk, F. Bundy, H. Hall, H. Strong, and R. Wentorf, Nature **184**, 1094 (1959).

[63] H. Hall, Rev. Sci. Instrum. **31**, 125 (1960).

[64] C. Weir, E. Lippincott, A. Van Valkenburg, and E. Bunting, J. res. Nat. Bur. Stand. A **63**, 55 (1959).

[65] A. Van Valkenburg, Rev. Sci. Instrum. **33**, 1462 (1962).

[66] L. Merrill and W. Bassett, Rev. Sci. Instrum. **45**, 290 (1974).

[67] R. Forman, S. Block, J. Barnett, and Piermari.GJ, Science **176**, 284 (1972).

[68] A. Jayraman, Rev. Mod. Phys. **55**, 65 (1983).

[69] H. Hall, Rev. Sci. Instrum. **29**, 267 (1958).

[70] E. C. Lloyd, U. O. Hutton, and D. P. Johnson, J. Res. Nat. Bur. Stand. **63C**, 59 (1959).

[71] M. Wakatsuki, K. Ichinose, and T. Aoki, Jpn. J. Appl. Phys. **10**, 357 (1971).

[72] H. Huppertz, Z. Kristallogr. **219**, 330 (2004).

[73] N. Kawai, Proc. Jpn. Acad. **42**, 385 (1966).

[74] N. Kawai and S. Endo, Rev. Sci. Instrum. **41**, 1178 (1970).

[75] N. Kawai, M. Togaya, and A. Onodera, Proc. Jpn. Acad. **49**, 623 (1973).

[76] Y. Palyanov, A. Khokhryakov, Y. Borzdov, A. Sokol, V. Gusev, G. Rylov, and N. Sobolev, Geol. Geophiz. **38**, 882 (1997).

[77] A. Prikhna and A. Borimsky, J. Cryst. Growth **26**, 129 (1974).

[78] A. Ohtani, A. Onodera, and N. Kawai, Rev. Sci. Instrum. **50**, 308 (1979).

[79] E. Ohtani, T. Irifune, W. Hibberson, and A. Ringwood, High Temp. - High Pressures **19**, 523 (1987).

[80] D. Walker, M. Carpener, and C. Hitch, Am. Mineral. **75**, 1020 (1990).

[81] R. E. Dinnebier and S. J. Billinge, *Powder Diffraction Theory and Practice* (RSC Publishing, 2008).

[82] A. Fitch, J. Res. Natl. Inst. Stand. Technol. **109**, 133 (2004), 3rd Conference on Accuracy in Powder Diffraction, Gaithersburg, MD, APR 22-25, 2001.

[83] A. Hannon, Nucl. Instrum. Meth. A **551**, 88 (2005), symposium on Applications of Linear and Area Detectors for X-Ray and Neutron Diffraction and Spectroscopy held at the E-MRS Fall Meeting, Warsaw, POLAND, SEP 06-10, 2004.

[84] H. Rietveld, J. Appl. Crystallogr. **2**, 65 (1969).

[85] A. Larson and R. B. Von Dreele, Los Alamos National Laboratory Report **86**, 748 (1994).

[86] J. Rodriguez-Carvajel, Physica B **192**, 55 (1993).

[87] D. Chen, J. Brug, and R. Goldfarb, IEEE Trans. Magn. **27**, 3601 (1991).

[88] S.-J. Kim, S. Lemaux, G. Demazeau, J.-Y. Kim, and J.-H. Choy, J. Am. Chem. Soc. **123**, 10413 (2001).

[89] J. Torrance, P. Lacorre, A. Nazzal, E. Ansaldo, and C. Niedermayer, Phys. Rev. B **45**, 8209 (1992).

[90] J. Garcia-Munoz, J. Rodriguez-Carvajal, P. Lacorre, and J. Torrance, Phys. Rev. B **46**, 4414 (1992).

[91] P. Lacorre, J. Torrance, J. Pannetier, A. Nazzal, P. Wand, and T. Huang, J. Solid State Chem. **91**, 225 (1991).

[92] J. Perez-Cacho, J. Blasco, J. Garcia, M. Castro, and J. Stankiewicz, J. Phys.: Condens. Matter **11**, 405 (1999).

[93] J. Alonso, M. Martinez-Lope, M. Casais, J. Garcia-Munoz, M. Fernandez-Diaz, and M. Aranda, Phys. Rev. B **64**, 094102 (2001).

[94] V. Dyakonov, F. N. Bukhanko, V. I. Kamenev, E. E. Zubov, M. Arciszewska, W. Dobrowolski, V. Mikhaylov, R. Puźniak, A. Wiśniewski, K. Piotrowski, et al., Phys. Rev. B **77**, 214428 (2008).

[95] Y. Takeda, F. Kanamaru, M. Shimada, and M. Koizumi, Acta Crystallogr., Sect. B: Struct. Sci. **32**, 2464 (1976).

[96] J. Bell, D. Hall, and T. Waters, Acta Crystallogr. **21**, 440 (1966).

[97] B. Craven and D. Hall, Acta Crystallogr. **14**, 475 (1961).

[98] A. Tressaud, M. Wintenberger, N. Bartlett, and P. Hagenmuller, C. R. Acad. Sci. Paris **282**, 1069 (1976).

[99] F. Langlais, G. Demazeau, J. Portier, A. Tressaud, and P. Hagenmuller, Solid State Commun. **29**, 473 (1979).

[100] A. Sleight, Mater. Res. Bull. **3**, 699 (1968).

[101] G. Kramer and M. Jansen, J. Solid State Chem. **114**, 206 (1995).

[102] G. Kramer, E. Hagele, N. Wagner, and M. Jansen, Z. Anorg. Allg. Chem. **622**, 1027 (1996).

[103] B. Chen, D. Walker, and B. Scott, Chem. Mater. **9**, 1700 (1997).

[104] J. P. Attfield, Acta Crystallogr., Sect. B: Struct. Sci. **44**, 563 (1988).

[105] J. P. Attfield and G. Ferey, J. Solid State Chem. **80**, 286 (1989).

[106] R. V. Panin, N. R. Khasanova, A. M. Abakumov, E. V. Antipov, G. Van Tendeloo, and W. Schnelle, J. Solid State Chem. **180**, 1566 (2007).

[107] G. Demazeau, I. Omeran, M. Pouchard, and P. Hagenmuller, Mater. Res. Bull. **11**, 1449 (1976).

[108] Y. Wang, D. Walker, B. Chen, and B. Scott, J. Alloys Compd. **285**, 98 (1999).

[109] A. Tressaud, S. Khairoun, J. Dance, and P. Hagenmuller, Z. Anorg. Allg. Chem. **517**, 43 (1984).

[110] S. Kim, S. Lemaux, G. Demazeau, J. Kim, and J. Choy, J. Mater. Chem. **12**, 995 (2002).

[111] B. Toby, J. Appl. Crystallogr. **34**, 210 (2001).

[112] K. Sreedhar, J. Honig, M. Darwin, M. Mcelfresh, P. Shand, J. Xu, B. Crooker, and J. Spalek, Phys. Rev. B **46**, 6382 (1992).

[113] P. Woodward, T. Vogt, D. Cox, A. Arulraj, C. Rao, P. Karen, and A. Cheetham, Chem. Mater. **10**, 3652 (1998).

[114] Y. Kamihara, T. Watanabe, M. Hirano, and H. Hosono, J Am Chem Soc **130**, 3296 (2008).

[115] Y. Kamihara, H. Hiramatsu, M. Hirano, R. Kawamura, H. Yanagi, T. Kamiya, and H. Hosono, J. Am. Chem. Soc. **128**, 10012 (2006).

[116] T. Watanabe, H. Yanagi, T. Kamiya, Y. Kamihara, H. Hiramatsu, M. Hirano, and H. Hosono, Inorg. Chem. **46**, 7719 (2007).

[117] G. F. Chen, Z. Li, D. Wu, G. Li, W. Z. Hu, J. Dong, P. Zheng, J. L. Luo, and N. L. Wang, Phys. Rev. Lett. **100**, 247002 (2008).

[118] Z.-A. Ren, J. Yang, W. Lu, W. Yi, X.-L. Shen, Z.-C. Li, G.-C. Che, X.-L. Dong, L.-L. Sun, F. Zhou, et al., Europhys. Lett. **82** (2008).

[119] Z. A. Ren, J. Yang, W. Lu, W. Yi, G. C. Che, X. L. Dong, L. L. Sun, and Z. X. Zhao, Mater. Res. Innovations **12**, 105 (2008).

[120] Z.-A. Ren, W. Lu, J. Yang, W. Yi, X.-L. Shen, Z.-C. Li, G.-C. Che, X.-L. Dong, L.-L. Sun, F. Zhou, et al., Chin. Phys. Lett. **25**, 2215 (2008).

[121] P. Cheng, L. Fang, H. Yang, X. Zhu, G. Mu, H. Luo, Z. Wang, and H. Wen, Sci. China, Ser. G **51**, 719 (2008).

[122] S. A. J. Kimber, D. N. Argyriou, F. Yokaichiya, K. Habicht, S. Gerischer, T. Hansen, T. Chatterji, R. Klingeler, C. Hess, G. Behr, et al., Phys. Rev. B **78**, 140503 (2008).

[123] M. L. Tacon, M. Krisch, A. Bosak, J.-W. G. Bos, and S. Margadonna, Phys. Rev. B **78**, 140505 (2008).

[124] R. H. Liu, G. Wu, T. Wu, D. F. Fang, H. Chen, S. Y. Li, K. Liu, Y. L. Xie, X. F. Wang, R. L. Yang, et al., Phys. Rev. Lett. **101**, 087001 (2008).

[125] Z.-A. Ren, G.-C. Che, X.-L. Dong, J. Yang, W. Lu, W. Yi, X.-L. Shen, Z.-C. Li, L.-L. Sun, F. Zhou, et al., Europhys. Lett. **83**, 17002 (4pp) (2008).

[126] J. Yang, Z.-C. Li, W. Lu, W. Yi, X.-L. Shen, Z.-A. Ren, G.-C. Che, X.-L. Dong, L.-L. Sun, F. Zhou, et al., Supercond. Sci. Technol. **21** (2008).

[127] J. Zhao, Q. Huang, C. de la Cruz, S. Li, J. W. Lynn, Y. Chen, M. A. Green, G. F. Chen, G. Li, Z. Li, et al., Nat. Mater. **7**, 953 (2008).

[128] S. Margadonna, Y. Takabayashi, M. T. McDonald, M. Brunelli, G. Wu, R. H. Liu, X. H. Chen, and K. Prassides, Phys. Rev. B **79**, 014503 (2009).

[129] A. S. Sefat, A. Huq, M. A. McGuire, R. Jin, B. C. Sales, D. Mandrus, L. M. D. Cranswick, P. W. Stephens, and K. H. Stone, Phys. Rev. B **78**, 104505 (2008).

[130] C. Wang, Y. K. Li, Z. W. Zhu, S. Jiang, X. Lin, Y. K. Luo, S. Chi, L. J. Li, Z. Ren, M. He, et al., Phys. Rev. B **79**, 054521 (2009).

[131] H.-H. Wen, G. Mu, L. Fang, H. Yang, and X. Zhu, Europhys. Lett. **82** (2008).

[132] G. Wu, H. Chen, Y. L. Xie, Y. J. Yan, T. Wu, R. H. Liu, X. F. Wang, D. F. Fang, J. J. Ying, and X. H. Chen, Phys. Rev. B **78**, 092503 (2008).

[133] K. Kasperkiewicz, J.-W. G. Bos, A. N. Fitch, K. Prassides, and S. Margadonna, Chem. Commun. p. 707 (2009).

[134] G. Mu, B. Zeng, X. Zhu, F. Han, P. Cheng, B. Shen, and H.-H. Wen, Phys. Rev. B **79**, 104501 (2009).

[135] S. Matsuishi, Y. Inoue, T. Nomura, H. Yanagi, M. Hirano, and H. Hosono, J. Am. Chem. Soc. **130**, 14428 (2008).

[136] X. Zhu, F. Han, P. Cheng, G. Mu, B. Shen, L. Fang, and H.-H. Wen, Europhys. Lett. **85** (2009).

[137] Y. Xiao, Y. Su, R. Mittal, T. Chatterji, T. Hansen, C. M. N. Kumar, S. Matsuishi, H. Hosono, and T. Brueckel, Phys. Rev. B **79**, 060504 (2009).

[138] G. Wu, Y. L. Xie, H. Chen, M. Zhong, R. H. Liu, B. C. Shi, Q. J. Li, X. F. Wang, T. Wu, Y. J. Yan, et al., J. Phys.: Condens. Matter **21** (2009).

[139] C. Wang, L. Li, S. Chi, Z. Zhu, Z. Ren, Y. Li, Y. Wang, X. Lin, Y. Luo, S. Jiang, et al., Europhys. Lett. **83** (2008).

[140] L.-J. Li, Y.-K. Li, Z. Ren, Y.-K. Luo, X. Lin, M. He, Q. Tao, Z.-W. Zhu, G.-H. Cao, and Z.-A. Xu, Phys. Rev. B **78**, 132506 (2008).

[141] M. Rotter, M. Tegel, D. Johrendt, I. Schellenberg, W. Hermes, and R. Poettgen, Phys. Rev. B **78** (2008).

[142] K. Sasmal, B. Lv, B. Lorenz, A. M. Guloy, F. Chen, Y.-Y. Xue, and C.-W. Chu, Phys. Rev. Lett. **101** (2008).

[143] H. S. Jeevan, Z. Hossain, D. Kasinathan, H. Rosner, C. Geibel, and P. Gegenwart, Phys. Rev. B **78** (2008).

[144] N. Ni, S. Nandi, A. Kreyssig, A. I. Goldman, E. D. Mun, S. L. Bud'ko, and P. C. Canfield, Phys. Rev. B **78** (2008).

[145] P. M. Shirage, K. Miyazawa, H. Kito, H. Eisaki, and A. Iyo, Appl. Phys. Express **1** (2008).

[146] A. S. Sefat, R. Jin, M. A. McGuire, B. C. Sales, D. J. Singh, and D. Mandrus, Phys. Rev. Lett. **101**, 117004 (2008).

[147] M. Pfisterer and G. Nagorsen, Z. Naturforsch., B: Chem. Sci. **35**, 703 (1980).

[148] M. S. Torikachvili, S. L. Bud'ko, N. Ni, and P. C. Canfield, Phys. Rev. Lett. **101**, 057006 (2008).

[149] P. L. Alireza, Y. T. C. Ko, J. Gillett, C. M. Petrone, J. M. Cole, G. G. Lonzarich, and S. E. Sebastian, J. Phys.: Condens. Matter **21**, 012208 (2009).

[150] H. Kotegawa, H. Sugawara, and H. Tou, J. Phys. Soc. Jpn. **78**, 013709 (2009).

[151] H. Fukazawa, N. Takeshita, T. Yamazaki, K. Kondo, K. Hirayama, Y. Kohori, K. Miyazawa, H. Kito, H. Eisaki, and A. Iyo, J. Phys. Soc. Jpn. **77**, 105004 (2008).

[152] A. Kreyssig, M. A. Green, Y. Lee, G. D. Samolyuk, P. Zajdel, J. W. Lynn, S. L. Bud'ko, M. S. Torikachvili, N. Ni, S. Nandi, et al., Phys. Rev. B **78** (2008).

[153] W. Yu, A. A. Aczel, T. J. Williams, S. L. Bud'ko, N. Ni, P. C. Canfield, and G. M. Luke, Phys. Rev. B **79** (2009).

[154] Q. Huang, Y. Qiu, W. Bao, M. A. Green, J. W. Lynn, Y. C. Gasparovic, T. Wu, G. Wu, and X. H. Chen, Phys. Rev. Lett. **101** (2008).

[155] A. A. Aczel, E. Baggio-Saitovitch, S. L. Budko, P. C. Canfield, J. P. Carlo, G. F. Chen, P. Dai, T. Goko, W. Z. Hu, G. M. Luke, et al., Phys. Rev. B **78** (2008).

[156] S. Takeshita, R. Kadono, M. Hiraishi, M. Miyazaki, A. Koda, S. Matsuishi, and H. Hosono, Phys. Rev. Lett. **103**, 027002 (2009).

[157] H. Chen, Y. Ren, Y. Qiu, W. Bao, R. H. Liu, G. Wu, T. Wu, Y. L. Xie, X. F. Wang, Q. Huang, et al., Europhys. Lett. **85** (2009).

[158] X. F. Wang, T. Wu, G. Wu, R. H. Liu, H. Chen, Y. L. Xie, and X. H. Chen, New J. Phys. **11** (2009).

[159] M. Rotter, M. Pangerl, M. Tegel, and D. Johrendt, Angew. Chem. **47**, 7949 (2008).

[160] N. Ni, M. E. Tillman, J.-Q. Yan, A. Kracher, S. T. Hannahs, S. L. Bud'ko, and P. C. Canfield, Phys. Rev. B **78**, 214515 (2008).

[161] J.-H. Chu, J. G. Analytis, C. Kucharczyk, and I. R. Fisher, Phys. Rev. B **79**, 014506 (2009).

[162] X. C. Wang, Q. Q. Liu, Y. X. Lv, W. B. Gao, L. X. Yang, R. C. Yu, F. Y. Li, and C. Q. Jin, Solid State Commun. **148**, 538 (2008).

[163] M. J. Pitcher, D. R. Parker, P. Adamson, S. J. C. Herkelrath, A. T. Boothroyd, R. M. Ibberson, M. Brunelli, and S. J. Clarke, Chem. Commun. pp. 5918–5920 (2008).

[164] J. H. Tapp, Z. Tang, B. Lv, K. Sasmal, B. Lorenz, P. C. W. Chu, and A. M. Guloy, Phys. Rev. B **78**, 060505 (2008).

[165] D. R. Parker, M. J. Pitcher, P. J. Baker, I. Franke, T. Lancaster, S. J. Blundell, and S. J. Clarke, Chem. Commun. pp. 2189–2191 (2009).

[166] G. F. Chen, W. Z. Hu, J. L. Luo, and N. L. Wang, Phys. Rev. Lett. **102**, 227004 (2009).

[167] R. Juza and K. Langer, Z. Anorg. Allg. Chem. **361**, 58 (1968).

[168] G. Hagg and A. Kindstrom, Z. Phys. Chem. B **22**, 453 (1933).

[169] F.-C. Hsu, J.-Y. Luo, K.-W. Yeh, T.-K. Chen, T.-W. Huang, P. M. Wu, Y.-C. Lee, Y.-L. Huang, Y.-Y. Chu, D.-C. Yan, et al., Proc. Natl. Acad. Sci. U. S. A. **105**, 14262 (2008).

[170] T. M. McQueen, Q. Huang, V. Ksenofontov, C. Felser, Q. Xu, H. Zandbergen, Y. S. Hor, J. Allred, A. J. Williams, D. Qu, et al., Phys. Rev. B **79**, 014522 (2009).

[171] S. Margadonna, Y. Takabayashi, M. T. McDonald, K. Kasperkiewicz, Y. Mizuguchi, Y. Takano, A. N. Fitch, E. Suard, and K. Prassides, Chem. Commun. p. 5607 (2008).

[172] K.-W. Yeh, T.-W. Huang, Y.-L. Huang, T.-K. Chen, F.-C. Hsu, P. M. Wu, Y.-C. Lee, Y.-Y. Chu, C.-L. Chen, J.-Y. Luo, et al., Europhys. Lett. **84** (2008).

[173] Y. Mizuguchi, F. Tomioka, S. Tsuda, T. Yamaguchi, and Y. Takano, Appl. Phys. Lett. **93**, 152505 (2008).

[174] S. Medvedev, T. M. McQueen, I. A. Troyan, T. Palasyuk, M. I. Eremets, R. J. Cava, S. Naghavi, F. Casper, V. Ksenofontov, G. Wortmann, et al., Nat. Mater. **8**, 630 (2009).

[175] S. Margadonna, Y. Takabayashi, Y. Ohishi, Y. Mizuguchi, Y. Takano, T. Kagayama, T. Nakagawa, M. Takata, and K. Prassides, Phys. Rev. B **80**, 064506 (2009).

[176] H. Kang, P. Dai, J. Lynn, M. Matsuura, J. Thompson, S. Zhang, D. Argyriou, Y. Onose, and Y. Tokura, Nature **423**, 522 (2003).

[177] S. Li, C. de la Cruz, Q. Huang, Y. Chen, J. W. Lynn, J. Hu, Y.-L. Huang, F.-C. Hsu, K.-W. Yeh, M.-K. Wu, et al., Phys. Rev. B **79**, 054503 (2009).

[178] J. W. Lynn and P. Dai, Physica C **469**, 469 (2009).

[179] W. Bao, Y. Qiu, Q. Huang, M. A. Green, P. Zajdel, M. R. Fitzsimmons, M. Zhernenkov, S. Chang, M. Fang, B. Qian, et al., Phys. Rev. Lett. **102**, 247001 (2009).

[180] Y. Qiu, W. Bao, Q. Huang, T. Yildirim, J. M. Simmons, M. A. Green, J. W. Lynn, Y. C. Gasparovic, J. Li, T. Wu, et al., Phys. Rev. Lett. **101**, 257002 (2008).

[181] J. Zhao, Q. Huang, C. de la Cruz, J. W. Lynn, M. D. Lumsden, Z. A. Ren, J. Yang, X. Shen, X. Dong, Z. Zhao, et al., Phys. Rev. B **78**, 132504 (2008).

[182] H. Takahashi, K. Igawa, K. Arii, Y. Kamihara, M. Hirano, and H. Hosono, Nature **453**, 376 (2008).

[183] F. Hunte, J. Jaroszynski, A. Gurevich, D. C. Larbalestier, R. Jin, A. S. Sefat, M. A. McGuire, B. C. Sales, D. K. Christen, and D. Mandrus, Nature **453**, 903 (2008).

[184] J. Yang, X.-L. Shen, W. Lu, W. Yi, Z.-C. Li, Z.-A. Ren, G.-C. Che, X.-L. Dong, L.-L. Sun, F. Zhou, et al., New J. Phys. **11** (2009).

[185] M. Doran, B. Cockbain, A. Norquist, and D. O'Hare, Dalton Trans. p. 3810 (2004).

[186] Q. Huang, J. Zhao, J. W. Lynn, G. F. Chen, J. L. Luo, N. L. Wang, and P. Dai, Phys. Rev. B **78**, 054529 (2008).

[187] X. H. Chen, T. Wu, G. Wu, R. H. Liu, H. Chen, and D. F. Fang, Nature **453**, 761 (2008).

[188] K. Miyazawa, K. Kihou, P. M. Shirage, C.-H. Lee, H. Kito, H. Eisaki, and A. Iyo, J. Phys. Soc. Jpn. **78** (2009).

[189] C.-H. Lee, A. Iyo, H. Eisaki, H. Kito, M. T. Fernandez-Diaz, T. Ito, K. Kihou, H. Matsuhata, M. Braden, and K. Yamada, J. Phys. Soc. Jpn. **77** (2008).

[190] D. J. Singh and M.-H. Du, Phys. Rev. Lett. **100**, 237003 (2008).